FIXED-BED COLUMN TREATMENT OF TEXTILE DYE WASTEWATER BY SILICON NITRIDE DERIVED FROM SAND, COFFEE HUSK AND MACADAMIA NUTSHELLS

NDUNG'U SAMUEL NG'ANG'A (MSc.)
I84/21737/2021

A RESEARCH THESIS SUBMITTED IN FULFILLMENT OF THE REQUIREMENTS FOR THE AWARD OF THE DEGREE OF DOCTOR OF PHILOSOPHY IN CHEMISTRY IN THE SCHOOL OF PURE AND APPLIED SCIENCES OF KENYATTA UNIVERSITY

NOVEMBER, 2025

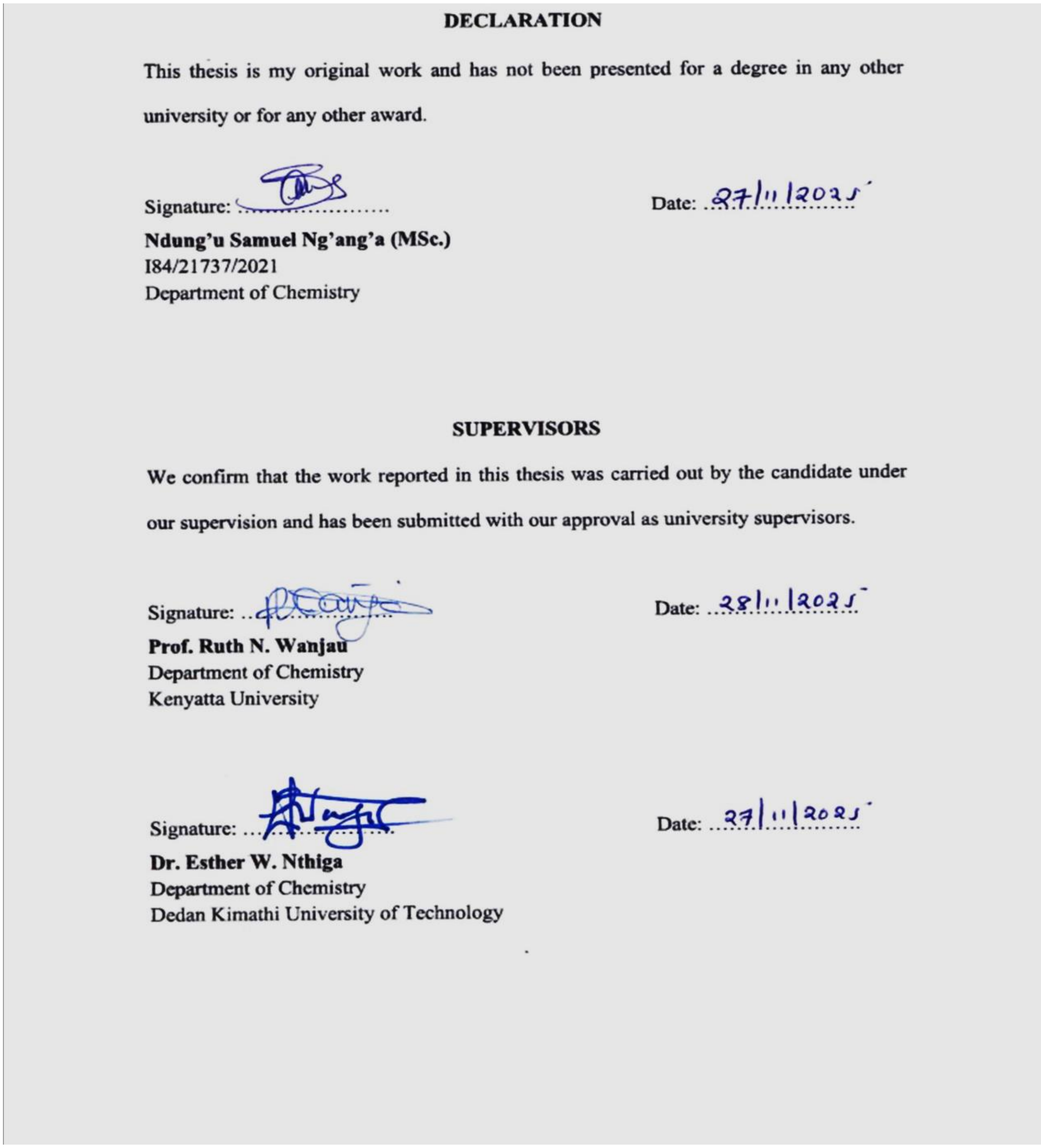

DECLARATION

This thesis is my original work and has not been presented for a degree in any other university or for any other award.

Signature: …………………… Date: 27/11/2025

Ndung'u Samuel Ng'ang'a (MSc.)
I84/21737/2021
Department of Chemistry

SUPERVISORS

We confirm that the work reported in this thesis was carried out by the candidate under our supervision and has been submitted with our approval as university supervisors.

Signature: …………………… Date: 28/11/2025

Prof. Ruth N. Wanjau
Department of Chemistry
Kenyatta University

Signature: …………………… Date: 27/11/2025

Dr. Esther W. Nthiga
Department of Chemistry
Dedan Kimathi University of Technology

DEDICATION

This research is dedicated to family members for their love, constant support, prayers and encouragement throughout my PhD studies.

ACKNOWLEDGEMENTS

After several years of research work, this PhD study comes to completion. My gratitude to God for bestowing upon me the strength, good health and His abundant grace that has enabled me to complete this PhD work. I acknowledge, with sincere appreciation, my academic guardians, Prof. Ruth N. Wanjau and Dr. Esther W. Nthiga for their excellent supervision, inspiration, tireless intellectual and technical guidance throughout the research period. Thank you for offering yourself to mentor and guide me from the inception of this research work. I am also grateful to Kenyatta University (KU) administration for giving me a chance to undertake my PhD studies. To the lecturers and technical staff departments of Chemistry, Food Nutrition and Dietetics (Kenyatta University), Dedan Kimathi University of Technology, Nyeri, United States International University-Africa and Geothermal Development Company, Nakuru, thank you for your invaluable support during data collection and production of this thesis document. I am also thankful to Prof. Joel M. Gichumbi of the Department of Physical Sciences, Chuka University for his valuable inputs in putting this manuscript in order.

To my entire family, thank you for your understanding even at the times when my attention for you went divided. Special thanks to my parents Luke Ndung'u and Juliah Njoki, my siblings (Jane, Ruth, Sharon and Francis) and all my nieces and nephews. Finally, my gratitude goes to all colleagues and/or friends for their wise counsel, prayers, support, critiques and insights throughout the study especially during consolidating and proofreading of this manuscript.

GOD BLESS YOU ALL

TABLE OF CONTENTS

LIST OF TABLES

LIST OF FIGURES

ABBREVIATIONS, ACRONYMS AND SYMBOLS

ANOVA	One-way analysis of variance
ASTM	American Society for Testing and Materials
BBS	Bamburi Beach sand
CHB	Coffee husk biochar
CICS	Crescent Island Crater sand
CR	Congo red
EDX	Energy Dispersive X-Ray
EPZA	Export Processing Zone Authority
ES-1	Extracted silica from Marine National Park sand
ES-2	Extracted silica from Bamburi Beach sand
ES-3	Extracted silica from Crescent Island Crater sand
FE-SEM	Field Emission Scanning Electron Microscope
FT-IR	Fourier Transform Infra-Red Radiation
ICDD	International Centre for Diffraction Data
JCPDS	Joint Committee on Powder Diffraction Standards
KIA	Kenya Investment Authority
MB	Methylene blue
MDGs	Millennium Development Goals
MLA	Mineral Liberation Analyzer
MNB	Macadamia nutshell biochar
MNPS	Marine National Park sand
MO	Methyl orange
MOH	Ministry of Health
MOH-MCG	Ministry of Health-Machakos County Government
NEMA	National Environment Management Authority
RCH	Raw coffee husk
RMN	Raw macadamia nutshell
SDGs	Sustainable Development Goals
Si_3N_4	Silicon Nitride
SN-1	Silicon Nitride 1
SN-2	Silicon Nitride 2
SN-3	Silicon Nitride 3
SN-4	Silicon Nitride 4
SN-5	Silicon Nitride 5
SN-6	Silicon Nitride 6
TGA	Thermal Gravimetric Analysis
UNEP	United Nation Environment Program
UNICEF	United Nations Children’s Fund
UN Water	United Nations Water
UV-Vis	UV-Visible Spectroscopy
WHO	World Health Organization
WWAP	World Water Assessment Programme
XRD	X-Ray Diffraction
XRF	X-Ray Fluorescence

ABSTRACT

To address the challenge of increased demand for clean water globally, there is a need to treat the available wastewater. Textile dyes are carcinogenic and their discharge to the environment has been reported to degrade the esthetic properties of water bodies. It is imperative to assess textile dye levels in wastewater as well as decontamination to ascertain its safety. Conventional purification processes suffer from limitations in terms of efficiency, cost effectiveness and environmental effect. Attention has recently shifted to adsorption as an economical technique for textile dyes removal using low-cost adsorbents. Silicon nitride contains positively and negatively charged surface capable of adsorbing cationic and anionic pollutants from water. This research studied the use of silicon nitride adsorbent prepared from extracted silica from sand and biochars from macadamia nutshell and coffee husk wastes in textile dye wastewater treatment. The silica extraction from the raw sand was carried out via alkali fusion process. The biochars were obtained by pyrolytic treatment of their raw biomass materials at 300 °C for 5 hours then acid leached. Both the biochar and extracted silica materials were used in the silicon nitride (Si_3N_4) adsorbents synthesis in an ammonia (NH_3) environment. The prepared materials were characterized by the use of X-Ray Diffractometer (XRD), Thermogravimetric Analyzer (TGA), Scanning Electron Microscope (SEM), Fourier Transform Infrared (FT-IR), X-Ray Fluorescence (XRF) and Energy Dispersive X-Ray (EDX). The findings indicated that the raw sand contain quartz (SiO_2), microcline (K (Al, Fe) Si_3O_8), calcite ($CaCO_3$) and clinochlore ($(Mg, Fe)_6(Si, Al)_4O_{10}(OH)_8$)). The extracted silica (ES) results showed a pure and amorphous composites with siloxane (Si-O-Si) and silanol (Si-OH) groups. The acid treatment and alkali fusion improved the silica (SiO_2) content to > 80 % with other oxide impurities decreased to < 1 %. The biochar results showed an amorphous, pure and porous carbon structure with aromatic bonds (C=C). The spectroscopic analysis of silicon nitride (Si_3N_4) adsorbents showed porous and thermally stable adsorbents with α-Si_3N_4 and β- Si_3N_4 phases, functional groups of silicon-nitrogen (Si-N), silanol (Si-OH) and silicon-nitrogen-silicon (Si-N-Si) which were hydroxylated in an aqueous media to give silazane ($Si_2=NH_2^+$) and silanolate ($Si\text{-}O^-$) adsorbent sites for congo red (CR), methylene blue (MB) and methyl orange (MO) dyes removal. Adsorption capacity ranged from 26.93 ± 0.03 mg/g to 31.77 ± 0.15 mg/g at optimal conditions for the dyes removal. The equilibrium and kinetic plots indicated that Langmuir, Dubinin-Radushkevich and Pseudo-second-order models ($R^2 > 0.9$) were more suitable in explaining the chemisorption process. The adsorption-desorption studies using 1.0×10^{-1} M NaOH and 1.0×10^{-1} M HCl showed that the SN-5 adsorbent can be re-used repeatedly with minimal loss. The column sorption studies gave a maximum column capacity of 50.76 ± 0.17 mg/g (MO), 47.01 ± 0.14 mg/g (MB) and 52.56 ± 0.04 mg/g (CR) at 4 mL/min, 7 cm and 50 mg/L optimal values. The column data obtained from the breakthrough curves conformed with Yoon-Nelson and Thomas models ($R^2 > 0.9$) in describing fixed-bed operations. The column performance showed that SN-5 had a lower efficacy using spiked water samples than using model solutions with column adsorption capacity ranging from 38.92 ± 0.08 mg/g to 46.38 ± 0.05 mg/g. The column regeneration showed a good reusability of the SN-5 adsorbent in textile dye wastewater treatment. The research findings report silicon nitride as a potential adsorbent that can be applied in purification of water to safe levels both at household and industrial scale.

CHAPTER ONE

INTRODUCTION

1.1 Introduction overview

The chapter describes a detailed information on the vitality of safe water for life sustenance, water quality and quantity, textile dyes wastewater in Kenya, their dangers in relation to the environment degradation and the need to look for greener and affordable water purification methods to curb the existing environmental menace.

1.2 Background information

Safe water is important for domestic consumption, peoples' health, agricultural and economic growth (Jaime *et al.*, 2018; Ndambiri and Rotich, 2018). It is therefore necessary to provide this vital resource to the public for a healthier community (Kümmerer *et al*., 2019). Due to an increased demand of safe water every dawn, its scarcity has remained a global problem (Goutam *et al.,* 2020). Majority of people worldwide (about 2 billion) are deprived of quality water (UNICEF and WHO, 2019). Kenya is greatly affected by this global problem where 27 % of her people obtain it from unimproved bodies (Boateng *et al.,* 2018). This is worsened due to rapid urbanization, population and economic growth making it difficult addressing the issue as well as provision of adequate sanitation facilities (Mulwa *et al.,* 2021). With the housing issue being the key agenda of the current Kenya kwanza regime (Kinyanjui, 2023), this will absolutely affect the demand for drinking water and additional costs for water purification. Approximately, 40 % of Kenyan urban people have accessed to piped water while others acquire water from community suppliers and via illegitimate connections exposing users to different water related illnesses (Osiemo *et al.,* 2019). In Nairobi alone, clean water shortage of about 170,000 m^3 (23 % of the total requirement) is experienced every day (Ombuna *et al.,* 2017).

The rapid industrial and population growth, anthropogenic stress, unskillful exploitation of water resources and unplanned urban development has increased toxic materials to the immediate ecosystem (Kumar *et al.,* 2019). Most of the technologies available for treatment of domestic water are expensive and as a result people consume as it is or find alternatives from the community water suppliers whose quality is compromised (Gurung *et al.,* 2019). Pollution has affected quality of water due to discharge of vast organic and inorganic pollutants (Ndung'u *et al.,* 2022). Dyes are among the contaminants present in water bodies with their common sources being the food, cosmetics, textiles, plastics, paper and paint industries among others (Arora *et al.,* 2019; Unugul and Nigiz, 2020). These industries utilize dyes to colour their end products (Litefti *et al.,* 2019). Because of this, loads of coloured wastewater are produced due to huge water consumption at various dyeing and finishing steps (Gadekar and Ahammed, 2016). In fact, for every one (1) ton of a textile product processed, about 200 to 270 tons of water is utilized with most of it leaving as a wastewater (Kloster *et al.,* 2023). Also, during the dyeing process, 50 % of dye is lost to the environment as a waste (Ali and Mohammed, 2021).

The people perception on quality of water is impressively influenced by color, the first recognizable contaminant in water (Patel, 2018). The existence of textile dyes even at low concentration values (1 mg/L) is highly visible (Mishra and Soni, 2016; Ali and Mohammed, 2021). In fact, the human eye can detect dyes even at 0.005 mg/L (Maghanga *et al.,* 2017). The direct discharge of this highly coloured wastewater into the nearby water bodies like streams and rivers greatly influences the visibility and quality of water, making it esthetically nasty (Jain *et al.,* 2020). This is due to their complex aromatic structures and molecular weight that make them non-biodegradable leading to toxicity and contamination of water by colour (Litefti *et al.*, 2019; Kakhki *et al.*, 2020). They cause environmental havoc by the formation of toxic aromatic amines through various metabolic activities in plants and animals (Şentürk and Yıldız, 2020). These textile effluents also contain high concentration of inorganic chemicals such as acids, hydrogen peroxide, alkalis, heavy metals, surfactants and dispersing agents (Mani *et al.*, 2019). This makes them toxic, mutagenic and carcinogenic (Rosanti *et al.,* 2022). They have inhibiting effects on the process of photosynthesis to water plants, due to reduced light penetration lowering oxygen levels in water thus affecting the aquatic ecosystem (Mcyotto *et al.,* 2021).

Majority of these factories have wastewater treatment plants but because of overproduction, they are overwhelmed in treating the effluents making their way to the nearby water bodies (Niinimäki *et al.,* 2020). For example, the plant located at the EPZ textile industry (Athi river), Machakos treats about 6,500 m^3 of textile effluent per day against the current discharge of 10,000 m^3 (EPZA, 2016). Therefore, this means that the plant is overworked and therefore not effective in treating its wastes to allowed levels that is safe to the surrounding community when discharged to river Athi (Wafula *et al.,* 2020). This has caused health and livelihood threats for the people consuming the water from this river (Aywa, 2017). The textile dye wastewater treatment is therefore crucial to avoid any possible risks to the environment and legal aftermaths (Wawrzkiewicz and Hubicki, 2016). Also, to sustainably overcome global water scarcity, textile dye polluted water has to be reclaimed using effective treatment methods, re-used and re-cycled (Sani and Abdullahi, 2017).

In some industries, conventional treatment methods such as nanotechnology (Mittal *et al.*, 2019), microbial technology (Parmar and Shukla, 2018), ion exchange (Pismenskaya *et al.*, 2020), coagulation-flocculation (Gadekar and Ahammed, 2016), electrochemical (Gerçel, 2015) are employed for dye wastewater treatment. Among them, adsorption has remained most appropriate due to its easiness in application, cost effectiveness and environmentally friendliness (Rosanti *et al.*, 2022). Low-cost adsorbents of banana peels (Jawad *et al.*, 2018), kaolinite clay (Aroke *et al.*, 2020) and saw dust (Jan *et al.*, 2022) among others have been reported in decontamination of textile dyes in wastewater. However, from the literature, no information is reported on an adsorbent that is capable of decontaminating both cationic and anionic dye species from wastewater. Studies report silicon nitride synthesis via hydrothermal procedures using rice husk (silica source) and sugar bagasse (carbon source) and their adsorption potential using batch experiments (Adamu *et al.*, 2017). The present work sought to synthesize Si_3N_4 adsorbent using silica extracted from raw sand, biochars from coffee husk and macadamia nutshells and evaluate its efficiency in column uptake of selected textile dyes from wastewater.

Biochar is a carbon product of pyrolytic treatment of a raw biomass under limited supply of oxygen (Suman and Gautam, 2017). Biochar has received immense interest due to its unique structural properties which vary widely in their chemical composition, large surface area, cost effectiveness, porosity, high cation exchange capacity, availability in large quantities and environmentally friendly (Yaashikaa *et al.*, 2020). This makes them widely used in vast fields such as in water purification as adsorbents (Al-Alwadhi *et al.,* 2022), in agriculture for soil amendment, ion exchange capacity and nutrients retention (Fachini *et al.,* 2021).

Fixed-bed column adsorption is an efficient, effective and a popular approach for water purification (Nguyen *et al.,* 2021). Columns are advantageous over batch due to their high flow rates which increases the column capacity and breakthrough times (Gupta *et al.,* 2016). Parameters of removal efficiency, fractional bed utilization, mass transfer zone, column capacity and effluent volume among others are determined from the breakthrough curves to evaluate the column performance (Ndung'u *et al.,* 2022). Various optimization parameters of column height, influent concentration, flow rate and particle size on the effect of breakthrough curves are usually investigated (Iheanacho *et al.,* 2021). The time data from the column uptake studies is analyzed using various kinetic models such as Adams-Bohart model (Dlamini *et al.,* 2021), Thomas model (Patel, 2019, Babazadeh *et al.,* 2021), Yoon-Nelson model (Silva *et al.,* 2020), Clark model (Sazali *et al.,* 2020) and Bed Depth Service Time model (Jaime *et al.,* 2018) among others.

Desorption studies are important because they regenerate the used adsorbents enhancing re-use and reduces the used adsorbent disposal problems (Farias *et al.,* 2018). Various agents such as alkalis, acids and salts are reported for desorption studies with the use of acid and alkali eluents rated most efficient (Munagapati and Kim, 2016). This study also investigated the reusability of the adsorbents using different eluents.

1.3 Statement of the problem

In Kenya, cities like Nairobi and local municipalities such as Mavoko constitute the largest source of both untreated and treated wastewater effluents (Wafula *et al.,* 2020). This has increased production of wastewater discharges with ineffective and inadequate treatment resources (Wakhungu, 2019). Kenyan textile industries such as Export Processing Zone (EPZ) in Machakos county produces about 1.5 million pieces of fabric of different blends, colours and prints every month (KIA, 2021). About 20 % of these coloured textile dyes used in these industries is lost to nearby water reserves without treatment (Khaleque and Roy, 2016). The dye wastes presence in water is detrimental to human and animal wellbeing owing to their carcinogenic and mutagenic nature (Lellis *et al.,* 2019). The majority of textile industries have treatment plants to treat the textile dye wastewater but because of overproduction, the wastewater is improperly treated making their way to the nearby water bodies (Niinimäki *et al.,* 2020).

Although strict regulations are already in position, the public outcry on quality of water in river Athi is witnessed as these discharges has made the river turn coloured posing a health hazard to the ecosystem (Aywa, 2017; Wafula *et al.,* 2020). Local communities have raised concerns that the water they use from the river for their livelihood has turned pink (Nzuma, 2021). The farm produce grown using the highly coloured water from the river is sold in the markets within Machakos county and its environs which is detrimental to the consumers hence the need for an urgent intervention (Owiti, 2022). This could be the reason why Machakos County was ranked among the counties leading in cancer cases (Waitara *et al.,* 2021). According to the ministry of health in Machakos County (MOH-MCG 2023) report, the highest prevalence was in Mwala sub-county attributed by the consumption of the heavily polluted water from river Athi, the main source of water for their domestic consumption. The cancer cases are increasing every dawn due to the exposure to chemicals such as textile dyes (MOH, 2023). The prevalence of cancer-related diseases in Kenya was reported to be 42,116 and mortality rate was 27,092 in the year 2020 (WHO, 2020).

In addition, coffee husk and macadamia nutshell wastes, given their abundance, is reported to be of concern upon their disposal to the environment. Coffee husks cause stinking and agglomeration especially during the rainy seasons (Ayalew and Aragaw, 2020). Macadamia nutshells, due to their hardness and durability, may cause harm to human beings and animals as well as acting as breeding ground for disease causing pathogens like mosquitos (Mutunga *et al.*, 2020). Therefore, coming up with greener and cost-effective ways of value adding such wastes in silicon nitride (Si_3N_4) adsorbent synthesis for dye wastewater treatment before their discharged to the water bodies is important.

1.4 Justification of the study

The textile industry plays vitally in global economic growth but also contributes significantly to pollution because of the release of dye-containing effluents (Dastgerdi *et al.*, 2020). The textile dyes are toxic, persistent and cancer-causing, posing serious environmental and health risks (Adegoke and Bello, 2015). Therefore, this demands for an economical, sustainable and innovative treatment ways in mitigation of the menace. The emerging techniques for textile dye wastewater decontamination entail physical or chemical treatments that are pricy, energy consuming and generate large quantities of sludge containing unsafe by-products (Parmar and Shukla, 2018).

Adsorption has continued to be the most suitable technique for textile dye wastewater treatment owing to its high efficiency and cost-effectiveness in nature (Jain *et al.*, 2020). However, most researches are reported on the sorption of textile dyes by batch mode limiting the usability of the adsorbents in an industrial scale containing high load of textile dye wastewater (Bennani *et al.*, 2015). Fixed-bed column treatment is a practical and scalable approach commonly used in water treatment processes. Investigating the performance of waste-derived silicon nitride adsorbent in this set-up assesses its real-world applicability. Also, understanding its efficiency and reusability in fixed-bed columns is critical for the evaluation of the adsorbent long-term sustainability and economic feasibility. If proven effective, its usability could be adopted by the textile industries and other sectors as a sustainable and efficient wastewater treatment method. The current problem revolves around the need for an effective, economically viable and environmentally friendly adsorbent for dyes uptake from an aqueous media.

The Si_3N_4 adsorbent is reported for adsorption of pollutants such as tetracycline (Sharma *et al.*, 2020) and fluoride ions (Adamu *et al.*, 2017). While silica, biochar from coffee husk and macadamia nutshell waste materials have shown promise as potential precursors for the adsorbent synthesis, their utilization in a Si_3N_4-based adsorbent for batch mode and fixed-bed column mode sorption studies remains largely unexplored. The use of silicon nitride adsorbents can potentially reduce the need for chemical coagulants in dye wastewater treatment, contributing to a reduction in chemical usage and associated costs.

There is therefore a pressing need to assess the potential of a Si_3N_4 adsorbent derived from extracted silica from sand, biochar from coffee husks and macadamia nutshells for the sorption studies of selected textile dyes from an aqueous media.

This research contributes to environmental sustainability (MDG 7) as it aligns with the global trend towards sustainable and environmentally friendly wastewater treatment technologies. It addresses the need of coming up with novel, eco-friendly and inexpensive solutions to address industrial pollution challenges. This will ensure good health and well-being (SDG 3), clean water and sanitation (SDG 6), industry, innovation and infrastructure (SDG 9), sustainable cities and communities (SDG 11), responsible consumption and production (SDG 12) and climate action (SDG 13).

1.5 Hypotheses

i. Silica extracted from raw sand and biochar from coffee husk and macadamia nutshell wastes can be used in the preparation of Si_3N_4 adsorbent for sorption of selected textile dyes in both model and environmental water samples.
ii. The uptake of MO, CR and MB dyes is affected by pH, agitation time, dosage, bed height, concentration and volumetric flow rate.
iii. The Si_3N_4 adsorbent can be reused with a high regeneration efficiency.

1.6 Objectives

1.6.1 General objective

To investigate the potential of Si_3N_4 adsorbent derived from extracted silica from sand, biochar from coffee husks and macadamia nutshells for fixed-bed column adsorption studies of MO, CR and MB dyes from both a model and environmental water samples.

1.6.2 Specific objectives

i. To characterize raw sand, extracted silica (ES), raw and biochar samples from coffee husks and macadamia nutshells and Si_3N_4 adsorbents using XRF, FT-IR, TGA, SEM, XRD and EDX.
ii. To determine the batch optimal dosage, agitation time, pH and initial concentration for CR, MO and MB dyes uptake.
iii. To determine the removal capacities, adsorption mechanisms and re-usability of Si_3N_4 adsorbents on sorption of the CR, MB and MO textile dyes from water.
iv. To determine the fixed-bed column optimal bed height, influent concentration and volumetric flow rate for CR, MB and MO dyes adsorption.
v. To determine maximum bed capacity and kinetic parameters using column isotherms for uptake of the CR, MO and MB dyes.
vi. To determine column performance of the Si_3N_4 adsorbents using environmental water samples.

1.7 Significance of the study

The outcomes of the work will aid in coming up with greener and sustainable adsorbent materials for textile dye wastewater treatment. This will greatly ensure that majority of people especially those living close to the textile industries are accessible to safe water in line with SDG 6. The use of waste materials like sand, coffee husks and macadamia nutshells for the synthesis of silicon nitride adsorbents lines up with the basis of circular economy and resource efficiency. This approach repurposes waste materials that would otherwise contribute to environmental burdens. The findings from this study can be used by authorities in informing in decision making and policy formulation.

1.8 Scope and limitations

The textile wastewater contains vast contaminants of microbes, heavy metal ions and dyes among other inorganic and organic species. However, due to cost and time restrictions, the study focused only on the selected textile dyes (MO, MB and CR). The effects of other interfering ions and water turbidity were not considered. The study was limited to both model and environmental water samples from river Athi without considering seasons. The sand was strictly collected from Crescent Island Crater (Nakuru), Bamburi Beach (Mombasa) and Marine National Park (Kilifi). The study used coffee beans and macadamia nuts without considering their varieties, seasons, age or geographical regions. Only the husks and nutshell wastes were considered.

CHAPTER TWO

LITERATURE REVIEW

2.1 Literature review highlights

The chapter highlights the status of water scarcity, pollution and treatment, a review of the similar materials investigated, methods used for fabrication and characterization of the materials, the expected mechanisms for adsorption, reported efficiencies of both batch and column studies, and regeneration studies. The chapter further critics the reported work and identifies the existing literature gaps. Further, adsorption and kinetics data models for both batch and column studies used by other researchers have been reviewed.

2.2 Water scarcity and sanitation

Accessing safe drinking water and good sanitation systems is a vital asset for a flourishing society as well as a thriving economy (Mulwa *et al.*, 2021). Water, which covers almost 70 % of the earth is the most vital constituents needed for survival (Gusain *et al.*, 2020). The existing water reserves from various sources are important as they provide livelihood to the ecosystem (Masakha *et al.*, 2017; Ndung'u *et al.*, 2021). Increased global demand for safe water has been escalated by rapid population growth, climate change and industrial advancements (Kümmerer *et al.*, 2019). The twenty-first (21st) century global challenge is to surmount the problem of water scarcity for a healthier ecosystem (Goutam *et al.*, 2020). The SDG 6 aims at having all communities with an access to affordable and safe water for domestic consumption. In its target 3 and 4, the SDG aims at tackling the problem of water scarcity and quality by safeguarding sustainable supply of freshwater via its use and re-use for personal hygiene (UN WWAP, 2017). However, this target has not been achieved globally especially in third world countries.

According to a report by UNICEF and WHO (2019), 2.2 billion people are unable to access safely managed drinking water, with approximately 4.2 billion and 3 billion lacking safely managed sanitation systems and basic handwashing amenities. Also, about 663 million people depend on water from unprotected sources leading to water-related diseases (WHO, 2017). In Kenya, about 40 % of her population in urban regions access piped water throughout the day (Osiemo *et al.,* 2019) with the rest obtaining it from illegal connections and private vendors to meet their daily needs exposing them to water-related diseases (Sarkar, 2020).

The UN WWAP (2017) report that over 80 % of effluent wastewater is produced globally and discharged to the immediate surrounding without any purification. In Kenya, the challenges of contaminated water cannot be underestimated (Mulwa *et al.,* 2021). The increased production rate of wastewater every dawn with inadequate purification resources by most Kenyan industries and improper discharge systems has led to effluent release into the water systems (Wafula *et al.,* 2020). This eventually compromises the water quality and quantity (Dinu *et al.,* 2017). Access to safe water is crucial to infectious diseases control and prevention (Anim and Ofori-Asenso, 2020). This has been the key preventive measures for controlling the spread of Corona Virus Disease (COVID-19) making it more difficult for the third world countries to curb the disease due to water scarcity leading to more fatalities (Boretti, 2022).

The highly coloured water witnessed in river Athi due to heavy discharge of industrial effluents by industries has become a public outcry and has greatly affected the quality of water (UNEP, 2018). Emphasis on the need for continued quality monitoring for water in the river and use of data for enforcement of laws on environmental pollution by NEMA is necessary (Nzuma, 2021). Also, there is a need to come up with cleaner alternatives to treat these polluted water reserves so as to promote use and re-use.

2.3 Textile dyes and industries

Prolonged use of textile dyes by industries generates large quantities of toxic-colored industrial effluents (Mohammadi and Veisi, 2018). An estimate of more than 100, 000 dyes exist globally (Mani *et al.,* 2019). A significant proportion of these textile dyes get their way to the surrounding via industrial effluents (Dovi *et al.,* 2021). The dyes are classed differently based on their colour index, chemical structure and/or uses (Adegoke and Bello, 2015). They are classed into anionic, non-ionic and cationic groups, where each class contains many dyes (Elwakeel *et al.,* 2020). Acid and direct dyes are anionic dyes which are negatively charged mainly due carboxylic acid (-COOH) and sulphonic acid ($-SO_3H$) groups (Kumar *et al.,* 2021). The cationic dyes are because of protonated amine groups and non-ionic dyes depending on their dissociation in aqueous media (Omer *et al.,* 2017). The cationic and anionic dyes such as congo red, maxilon red, methyl orange, crystal violet and methylene blue among others are classes of dyes employed in textile industries (Cheruiyot *et al.,* 2019; Khurram *et al.,* 2020; Şentürk and Yıldız, 2020).

Textile dyes contain chromophores and auxochromes (Kumar *et al.,* 2021). The chromophores are such as azo (-N=N-), carbonyl (-C=O), nitroso (-N=O), imino (-C=N-), thiocarbonyl (-CH=S), nitro (-NO_2) and ethenyl (-C=C-) among others (Wawrzkiewicz and Hubicki, 2015; Affat, 2021). These chromophoric groups imparts the dye colour by undergoing strong n-π and π-π electronic transitions in the UV-Visible area (Ngulube *et al.,* 2017). The auxochromes such as carboxyl (-COOH), sulfonate (-SO_3H), amine (-NH_2) and hydroxyl (-OH) (Kumar *et al.,* 2021) intensifies the dye colour by altering the overall energy of the electron aromatic system (Aroke *et al.,* 2020). Textile effluents may also be loaded with heavy metals such as cobalt, chromium, zinc, lead and copper in trace amounts produced during the dyeing steps (Ngulube *et al.,* 2017). The dye auxochromic groups dissociate easily in aqueous media since they are weakened by the structural stability imparted by the chromophore conjugation and a high degree of dye aromaticity (Mcyotto *et al.*, 2021). Discharging such wastewater laden with dyes and heavy metals into the nearby water sources affects the water quality (Aigbe *et al.*, 2021).

Kenyan textile industries such as Thika Cloth Mills (Thika), Export Processing Zone (Athi River) and Rivatex East African Limited (Eldoret) are among the industries known to produce large amounts of coloured effluents due to huge production of fabrics daily (Maghanga *et al.,* 2017; Krishnan *et al.,* 2019). For example, Thika cotton mills processes about 650,000 meters of fabric every month in different blends, colours and prints (Waithaka, 2017). Rivatex East African Limited processes more than 70 bales of cotton fabrics in a day (Krishnan *et al.,* 2019). The Export Processing Zone (EPZ) in Machakos produces about 1.5 million pieces of fabrics every month (KIA, 2021). Most of these industries have wastewater treatment plants for treating their colored effluents but due to overproduction, they are overwhelmed hence end up releasing the effluents to the nearby water bodies (Bidu *et al.*, 2021). The EPZ wastewater treatment plant (Athi river), Machakos treats about 6,500 m^3 of wastewater per day against the total wastewater discharge of 10,000 m^3 in a day (EPZA, 2016). This makes the wastewater plant ineffective in treating its wastes to permissible limits before discharged to river Athi (Wafula *et al.,* 2020). The river over the last 15 years has become stinky, filthy and has green-colored water with litter wastes scattered all over its banks (UNEP, 2018). The local communities consume water from this highly polluted river leading to increased prevalence of water-related diseases (Aywa, 2017). Therefore, there is a need to continue monitoring the quality of water in river Athi.

The methylene blue (MB), congo red (CR) and methyl orange (MO) dyes are among the most used in textile industries (Khurram *et al.,* 2020). They are reviewed in the following sub-sections.

2.3.1 Methylene blue

Methylene blue, MB ($C_{16}H_{18}ClN_3S$), a cationic thiazine dye is employed in coloring of wool, cotton, silk and paper (Çatlıoğlu *et al.*, 2021). The dye is also commonly used in food processing, tannery, cosmetics and pharmaceutical industries among others (Saini *et al.*, 2018). The dye has been reported in industrial effluents at varying concentrations (Hurairah *et al.*, 2020). The dye has hetero-polyaromatic structure (Figure 2.1), which presents a strong inhibitive role for biodegradation (Liu *et al.*, 2019). The MB dye is reported to be harmful as it has effects such as tissue necrosis, cyanosis, heart rate, vomiting, jaundice, reproductive system, dermatitis, brain kidney, quadriplegia, problems in the liver, respiratory tract and central nervous system (Patel *et al.,* 2019).

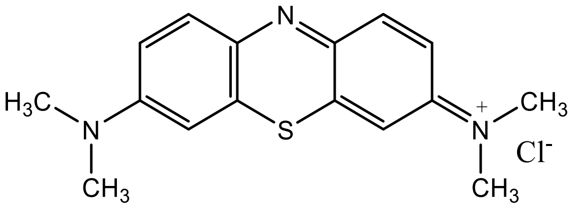

Figure 2.1: A chemical structure of methylene blue dye (Omer *et al.,* 2017)

2.3.2 Congo red

The congo red (CR) dye ($C_{32}H_{22}N_6Na_2O_6S_2$), a diazo anionic dye has a complex aromatic structure and varied molecular structures that differ in their pH in the aqueous solutions (Zhou *et al.,* 2018). It is generated from the dyestuff manufacturing industries such as leather, textile, printing and paper industries among others (Priyadarshini *et al.,* 2020). Degradation of this dye in wastewater is difficult due to its complex structure (Dovi *et al.,* 2021). The CR dye is lethal to plants and animals and thus its presence in water streams should be a great concern as it is detrimental to health and the entire ecosystem (Conrad *et al.,* 2016). Consumption of wastewater containing congo red is detrimental to health as it destroys the liver, human blood system with other symptoms such as breathing difficulties, diarrhoea, nausea and vomiting (Zhang *et al.,* 2018). The CR dye structure is represented in Figure 2.2.

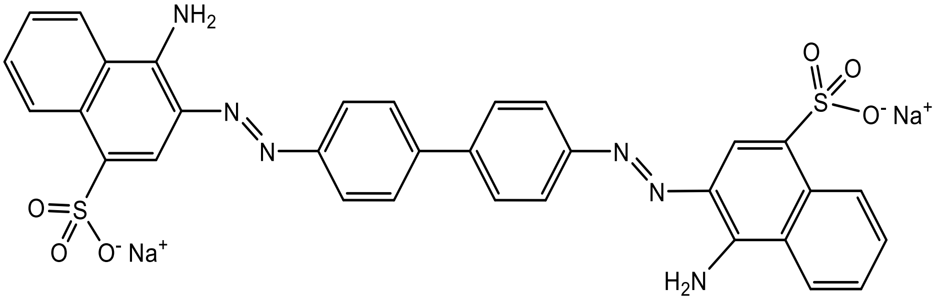

Figure 2.2: A chemical formula of congo red dye (Zare *et al.,* 2015)

2.3.3 Methyl orange

Methyl orange (MO) dye ($C_{14}H_{14}N_3NaO_3S$) is an azo, water-soluble dye with a very high colorability when dissolved in water (Wu *et al.,* 2021). It is widely employed in research, textiles and other industrial products (Qu *et al.,* 2020). MO dye is stable, toxic, mutagenic and carcinogenic (Zhao *et al.,* 2017). The hazardous and non-biodegradability nature of the dye is due to the stable aromatic rings in its structure (Shah *et al.,* 2021) as shown by Figure 2.3. The dye enters the human body system, get metabolized by intestinal micro-organisms into aromatic amines which causes intestinal cancer (Smita *et al.,* 2016).

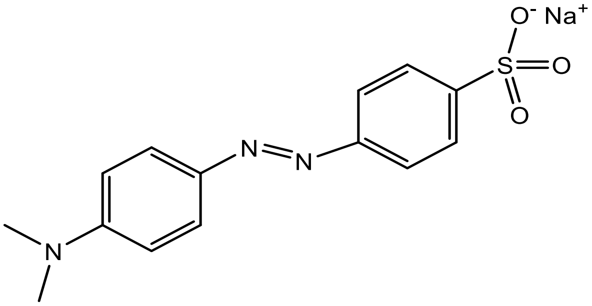

Figure 2.3: A methyl orange dye structure (Fortunate and Misael, 2016)

2.4 Wastewater treatment technologies

The choice of the technique of treating textile dye wastewater is determined by the chemical nature of the dye, equipment, the expense of the chemicals needed, the immediate environment and the maintenance (Parmar and Shukla, 2018). The various technologies of ion exchange, electrochemical treatment, adsorption, chemical coagulation and flocculation are among the available techniques for dye wastewater treatment. They are reviewed in the following sub-sections.

2.4.1 Electrochemical process

The electrochemical treatment is reported for efficient decontamination of hazardous inorganic and organic substances such as heavy metal ions and dyes among others (Giwa *et al.,* 2018). The technique relies on the migration of the ions from one solution to another through charged membranes under an applied electricity without the introduction of any chemicals (Wu *et al.,* 2019). During the process, the pollutants are damaged by means of both direct and indirect oxidation procedures (Körbahti and Demirbüken, 2017). This is summarized by Figure 2.4.

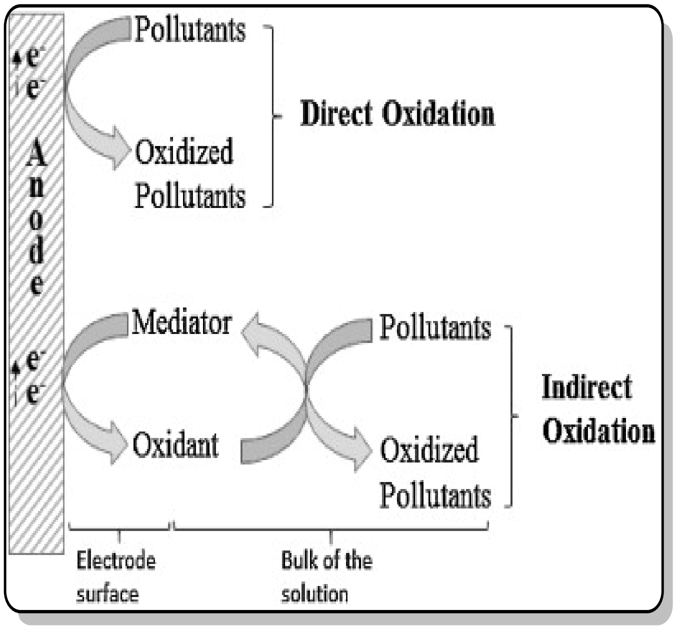

Figure 2.4: Direct and indirect oxidation diagram **(**Abbas *et al.,* 2019)

The major demerit of the method is that it cannot be used in many rural areas because the equipment requires electricity which is costly (Parmar and Shukla, 2018).

2.4.2 Ion exchange

The technique is an effective and versatile tool for the dye wastewater treatment (Yang *et al.,* 2015). The ion exchange resins are made of functionalized gel-like or porous polymers that remove the exchanged ions from a mixture (Arslan *et al.*, 2016). They are classed on the basis of counter-ion charge; anion exchanger or cation exchanger (Wawrzkiewicz and Hubicki, 2015). The anion-exchanger resins contain functional groups that have positive charge while cation-exchanger resins have negatively charged groups (Pismenskaya *et al.*, 2020). Their affinity is dependent on the structure, the charge and the size of the ion (Jatoi *et al.*, 2021). Therefore, the technique is used for removal of anionic and cationic dye wastewater (Khan *et al.*, 2017). The effluent is passed through the ion exchanger resin till all the active sites get saturated (Zhang *et al*., 2020).

Ion exchangers are characterized by low operation costs, outstanding sorption capacity, cheap regenerated chemicals, low energy requirement and well-maintained resin beds that last for a longer period without replacement (Wawrzkiewicz and Hubicki, 2016). However, commercially available resins are relatively pricy and therefore various affordable alternatives need to be explored for textile dye wastewater treatment (Hassan and Carr, 2018).

2.4.3 Chemical coagulation-flocculation

The technique entails the addition of coagulants such as ferric chloride, polyferric sulfate, cationic polyacrylamide, anionic polyacrylamide, aluminum chloride, polyferric chloride, magnesium chloride, aluminum sulfate, polyaluminum chloride and lime for effective decolourization of the textile dye wastewater (Mcyotto *et al.,* 2021). The dyes removal is based not on the partial degradability of the dyes and therefore no production of potential toxic intermediates (Gadekar and Ahammed, 2016). The coagulants interact with the dye molecules forming coagulates/flocs which are later precipitated out by either filtration, flotation, settling or any other physical technique (Mani *et al.,* 2019).

The primary setback is that some highly soluble and low molecular weight dyes might not effectively be removed (Liu *et al.,* 2019). Also, the technique generates large amounts of sludge making their treatment and disposal very expensive (Kumar *et al.,* 2019). Therefore, the choice of the coagulant to be used is essential for improvement of water quality and reducing the environmental menace (Mcyotto *et al.,* 2021).

2.4.4 Adsorption

The technique involves chemical and/or physical interactions of the analyte and the sorbent surface (Gawande *et al.,* 2017). It is a widely recognized surface phenomenon for an effective uptake of vast pollutants (Aigbe *et al.,* 2021). This makes the technique an attractive treatment technology (Gupta *et al.,* 2016). The technique has received a great attention due to low maintenance costs, easy in operation, low energy requirements, high efficiency and safety (Aminu *et al.,* 2020; Rosanti *et al.,* 2022). Low-cost materials such as banana peels (Jawad *et al.,* 2018), walnut shells (Dovi *et al.,* 2021) and coffee husks

(Njeri *et al.,* 2023) among others have been employed in remediation of textile dye wastewater. Table 2.1 shows different adsorbents for uptake of CR, MB and MO dyes.

Table 2.1: The equilibrium adsorption capacity for different selected adsorbents

Adsorbent	Dye	Adsorption capacity (mg/g)	Reference
Banana peel	Congo red	1.73	(Mondal and Kar, 2018)
Geopolymer	Methylene blue	20.22	(Maingi *et al.*, 2017)
Kaolinite clay	Methyl orange	3.48	(Aroke *et al.*, 2020)
Silica gel (Amino-functionalized)	Congo red	5.37	(Farias *et al.*, 2018)
Orange peel	Methyl orange	4.41	(Rosanti *et al.*, 2022)
	Methylene blue	10.96	
Mahagoni bark (Activated carbon)	Methyl orange	6.07	(Ghosh *et al.*, 2020)
Pine bark	Congo red	1.60	(Litefti *et al.*, 2019)
Saw dust	Methylene blue	5.46	(Jan *et al.*, 2022)

The Si_3N_4 is reported as an excellent adsorbent in decontamination of various pollutants such as flouride ions and tetracycline from an aqueous media via batch mode with a higher efficiency and reusability (Adamu *et al.,* 2017: Sharma *et al.*, 2020). This study sought to synthesize the adsorbent using sand, coffee husk and macadamia nutshell wastes and investigate its effectiveness in fixed-bed column dye wastewater treatment.

2.5 Silicon nitride (Si_3N_4)

Silicon nitride is employed in vast fields due to its outstanding thermomechanical properties, chemical inertness, corrosion resistance and high thermal conductivity among others (Qadri *et al.,* 2016). The material has a rigid structure with strong covalent bonds (Sharma *et al.,* 2018). These features make the material suitable for many applications which include ball bearings, nanocomposites and optoelectronic devices among others (Farzana *et al.,* 2018). Silicon nitride occurs in two phases, an alpha (α) form (trigonal) which is stable at a lower temperature and beta (β) form (hexagonal) stable at higher temperatures (Parrillo *et al.,* 2021). The Figure 2.5 shows the Si_3N_4 phases.

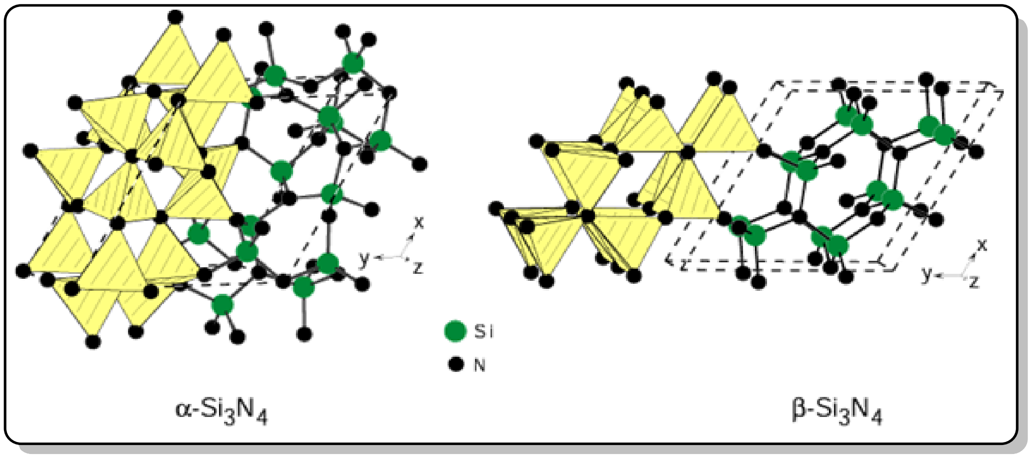

Figure 2.5: Silicon nitride (Si_3N_4) phases (Fayomi *et al.*, 2020)

Several techniques such as metallurgy method (Tran *et al.*, 2021), oxide-assisted growth (Zhao *et al.*, 2021), direct nitridation of silicon (Liu *et al.*, 2017; Jin *et al.*, 2019), electrochemical method (Vishnu *et al.*, 2018), combustion synthesis (Li *et al.*, 2022), chemical vapour deposition (Liu *et al.*, 2018) and carbothermal reduction-nitridation of amorphous silica (Abdulhameed *et al.*, 2018) amongst others are reported for silicon nitride (Si_3N_4) synthesis. Carbothermal reduction-nitridation is the most cost-effective technique for large-scale synthesis (Zhi *et al.*, 2019). This is because it utilizes vast low-cost materials for the Si_3N_4 synthesis (Rajarao and Veena, 2016). The synthesis is carried out in an ammonia (NH_3) environment as shown in Equation 2.1 (Wan, 2013).

$$3SiO_{2(s)} + 6C_{(s)} + 4NH_{3(g)} \longrightarrow Si_3N_{4(s)} + 6CO_{(g)} + 6H_{2(g)} \qquad (2.1)$$

Various materials such as rice husks (Parrillo *et al.*, 2021), wheat husks (Qadri *et al.*, 2016), computer monitors (Maroufi *et al.*, 2018) and rice straw (Ma *et al.*, 2020) among others are reported as silica sources. Also, sugarcane bagasse (Abdulhameed *et al.*, 2018), carbon black (Ji *et al.*, 2014) and carbon nanotubes (Zhi *et al.*, 2019) among others are reported as carbon sources during the Si_3N_4 synthesis. The study of silica from sand, biochars from coffee husk and macadamia nutshell wastes as silica and carbon precursor materials for Si_3N_4 synthesis and its potential in dyes uptake has not been explored.

2.5.1 Silica

Silica (SiO_2) is a potential mineral applied in vast fields (Ishmah *et al.*, 2020). It is obtained mainly in amorphous, gel and crystalline forms (Todkar *et al.*, 2016). The amorphous silica is employed industrially in different fields such as electronics, healthcare, textiles, cement, glass, paper, concrete, cosmetics, rubber, wastewater treatment and ceramics amongst others (Ismail *et al.*, 2020; Setyoningrum *et al.*, 2020). The emergence of technological discoveries has increased the need for different kinds of silica such as in sol, precipitated, fumed and gel forms (Arunmetha *et al.*, 2015). This is due to the exceptional features such as environmentally friendliness, chemical stability, high purity, easy in biocompatibility and fabrication for use in vast industries (Wahyudi *et al.,* 2013; El-Sawy *et al.,* 2021). The amorphous silica is found from biogenic marine organisms, minerals and agricultural wastes such as coconut husks (Anuar *et al.*, 2018), rice husks (Qadri *et al.,* 2016), beach sand (Ismail *et al.,* 2020), sugar bagasse (Norsuraya *et al.,* 2016; Fardhyanti *et al.,* 2018) and fly ash coal wastes (Cheng *et al.,* 2018).

The natural sand is an abundant material that is found in coastal oceans, seas, beaches and the fresh shallow lakes (Ismail *et al.,* 2020). It is formed by erosion and weathering processes forming finer sand deposits (Gallop *et al.,* 2020). Also, marine animals such as diatomaceous earth (Kemp *et al.,* 2021) and siliceous sponges (Drozdov *et al.,* 2021) among other siliceous organisms undergo biogenic decomposition that form part of the sand deposits (Rampe *et al.*, 2023). The sand aggregates comprise of quartz (SiO_2) which are in crystalline forms such as cristobalite and tridymite (Munasir *et al.*, 2018), micro- and crypto-crystalline polymorphs (Antolik and Daria, 2021), strained quartz polymorphs (Hasdemir *et al.,* 2012) and glassy volcanic materials (Pavlenko *et al.,* 2014). The sand is usually in impure form with oxide impurities such as titanium (IV) oxide (TiO_2), magnesium (II) oxide (MgO), potassium oxide (K_2O) and aluminium (III) oxide (Al_2O_3) among others (Munasir *et al.*, 2018).

The polymorphs (siltstone, phyllite, opal, quartzite, chalsedony, granite, gneiss, chert and granodiorite among others) contain silicate mineral components with an active silica which is prone to alkali-silica chemical dissolution reactions (Hasdemir *et al.,* 2012; Moreira *et al.,* 2021). The crystal structure of the partly crystalline polymorphs is lost when heated in activating agents such as alkali solutions to form soluble silicates which are used for amorphous silica synthesis (Lin *et al.*, 2020; Luthfiah *et al.*, 2021; Meftah *et al.*, 2023).

The amorphous silica is hydrophilic in nature because of its attached hydroxyl (-OH) groups on the surface (Ismail *et al.*, 2021). Various silica extraction methods such as electrocoagulation (Zhang *et al.*, 2019), hydrothermal (Thahir *et al.*, 2019), sol-gel (Zulfiqar *et al.*, 2016) and alkaline fusion (Ishmah *et al.*, 2020) have been reported. Alkaline fusion chemical extraction is reported the most effective method due to its easy in silica synthesis even at low temperatures (Azzahra *et al.*, 2020).

2.5.1.1 Alkali fusion

Alkali fusion is conducted by fusing the particles with an alkali solution at a certain temperature and then crystalize the molecules into nano-size (Wahyudi *et al.*, 2013). The method entails breaking the bonds in the raw sand using activating solutions such as potassium hydroxide (KOH), sodium carbonate (Na_2CO_3) and sodium hydroxide (NaOH), then binding the silicon with oxygen to obtain the amorphous silica (Ishmah *et al.*, 2020). This method involves three main steps: first is to prepare a silicate solution using alkaline solutions such as KOH or NaOH (Firdaus *et al.*, 2020). This is expressed by Equation 2.2 and the mechanism is as reported by Novita and Idris (2022) with slight modifications (Figure 2.6).

$$SiO_{2(s)} + 2NaOH_{(aq)} \longrightarrow Na_2SiO_{3(aq)} + H_2O_{(l)} \qquad (2.2)$$

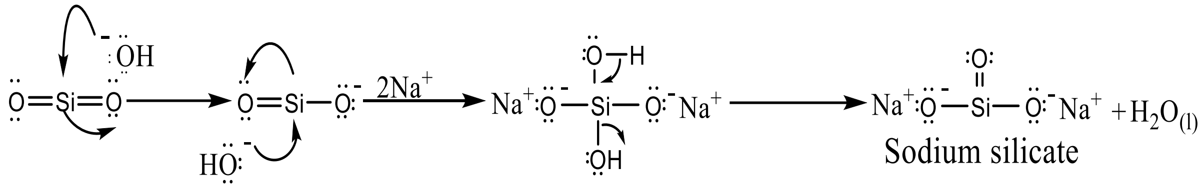

Figure 2.6: The mechanism of sodium silicate formation

The acid such as HCl solution is then reacted with sodium silicate (Na_2SiO_3) forming silica gel ($Si(OH)_4$) residue and sodium chloride solution which is subsequently filtered out (Meftah *et al.,* 2023). Adding the acid solution to the precursor solution increases the proton (H^+) concentration in the silicate solution causing siloxy (Si-O−) groups hydrolysis to form silanol groups (Si-OH), which are further hydrolyzed forming siloxane bonds (Si-O-Si), a silica polymer growth (tetraortosilicate acid) (Rahmayanti *et al.,* 2020; Huljana *et al.,* 2021). This is as expressed by Equation 2.3 and Figure 2.7.

$$Na_2SiO_{3(aq)} + H_2O_{(l)} + 2HCl_{(aq)} \longrightarrow Si(OH)_{4(s)} + 2NaCl_{(aq)} \qquad (2.3)$$

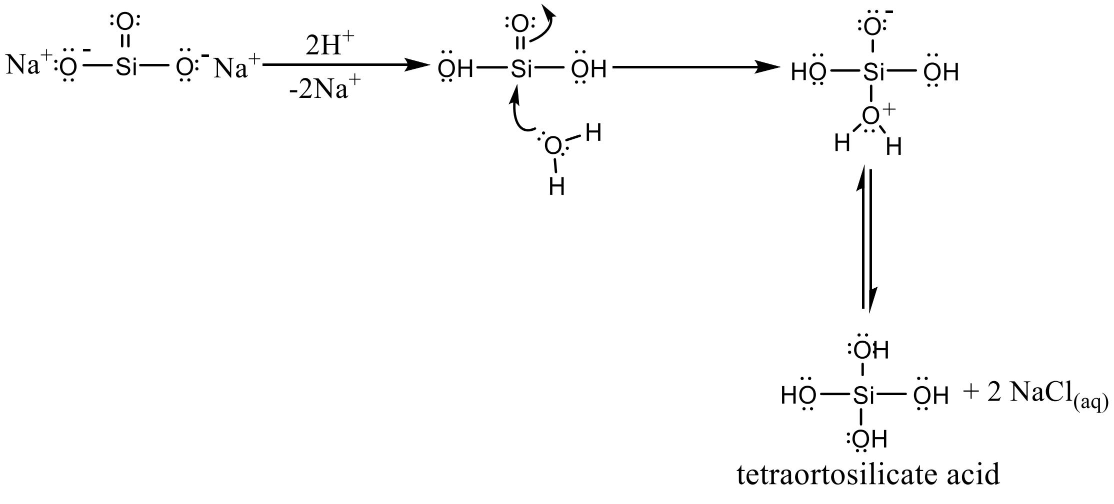

Figure 2.7: The mechanism for the formation of silica gel (Ishmah *et al.,* 2020)

The silica gel formed is then heated forming an amorphous silica (SiO_2) as expressed in Equation 2.4 and Figure 2.8.

$$Si(OH)_{4\,(s)} \longrightarrow SiO_{2\,(s)} + 2H_2O_{\,(l)} \qquad (2.4)$$

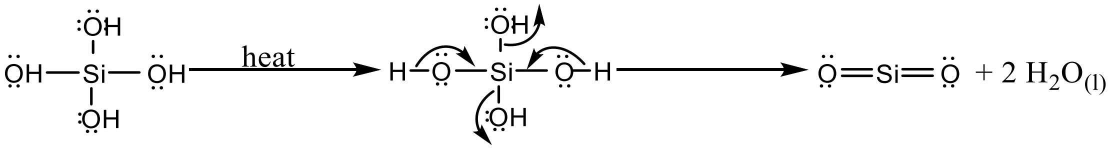

Figure 2.8: A reaction mechanism for silica gel heating (Firdaus *et al.*, 2020)

2.5.2 Coffee husks

Kenya produces about 50, 000 tons of coffee beans yearly (Duguma *et al.,* 2022). The processing of coffee generates significant amount of husk wastes to about 25.5 % of the total weight (Ayalew and Aragaw, 2020). Approximately, 0.18 tons of the coffee husk wastes are produced in every 1 ton of coffee fruits harvested (Harshananda *et al.,* 2020). The husk residues have limited applications and their continued accumulated volumes at the milling centers impact negatively to the surrounding (Kanyiri and Waswa, 2017).

Most of the coffee husks are disposed to the environment with no care causing pollution, especially in developing countries (Hoseini *et al.,* 2021). Efforts of finding alternative technologies to exploit the waste in solving the menace is beneficial because of its abundance globally (Cheruiyot *et al.,* 2019). The waste has been employed as adsorbents in textile dyes remediation such as methyl red (Njeri *et al.,* 2023), methylene blue (Krishna Murthy *et al.,* 2020) and brown R (Harshananda *et al.,* 2020) among others. The study sought to use biochar (as carbon source) from coffee husk wastes in the synthesis of Si_3N_4 adsorbent for textile dye wastewater treatment.

2.5.3 Macadamia nuts

The macadamia nuts farming has increased in the Africa Eastern region due to their improved prices comparing to other cash crops like tea and coffee (Mutunga *et al.,* 2020). In Kenya, the nuts are grown in many parts of the country such as Kiambu (7 %), Murang'a (17.2 %), Nyeri (5.8 %), Kirinyaga (4.4 %), Embu (36.5 %), Meru (11.8 %), Tharaka Nithi (5.5 %), Machakos (7.8 %), Baringo (2.4 %) and Trans Nzoia (0.9 %) among other regions (Wasilwa *et al.,* 2019). Because of the increase in macadamia nut production, the disposal of their nut shells has become a major bother at the processing facilities due to their hardness and durability (Wongcharee *et al.,* 2019).

The biggest challenge experienced by macadamia nutshell processing factories in Kenya is the mechanism of developing greener techniques to handle the residual wastes (Mutunga *et al.,* 2020). This bio-waste's have been value added as adsorbents by scientists for the uptake of water pollutants such as heavy metal ions and dyes among others in different forms (Honorato *et al.*, 2017; Kamau *et al.*, 2020). The study utilized macadamia nutshell biochar as a carbon source in silicon nitride adsorbent synthesis.

2.6 Adsorptive ability of silicon nitride (Si_3N_4) adsorbent

Silicon nitride (Si_3N_4) is reported to adsorb organic compounds and ions such as fluoride ions (Adamu *et al.,* 2017), tetracycline (Sharma *et al.,* 2020) and some amino acids (Awsiuk *et al.,* 2013). This is because of the hydroxylation of Si_3N_4 surface structure in aqueous media yielding basic silazane ($Si_2{=}NH$) and acidic silanol (Si-OH) groups which then make the surface charged (Shi *et al.*, 2014). This is as shown in Equation 2.5 and Figure 2.9.

$$\underset{\text{(Tertiary amine)}}{Si_3N_{(s)}} + H_2O_{(l)} \longrightarrow \underset{\text{(basic silazane group)}}{Si_2{=}\ddot{N}H_{(s)}} + \underset{\text{(acidic silanol)}}{Si\underset{\cdot\cdot}{\ddot{O}}H_{(s)}} \qquad 2.5$$

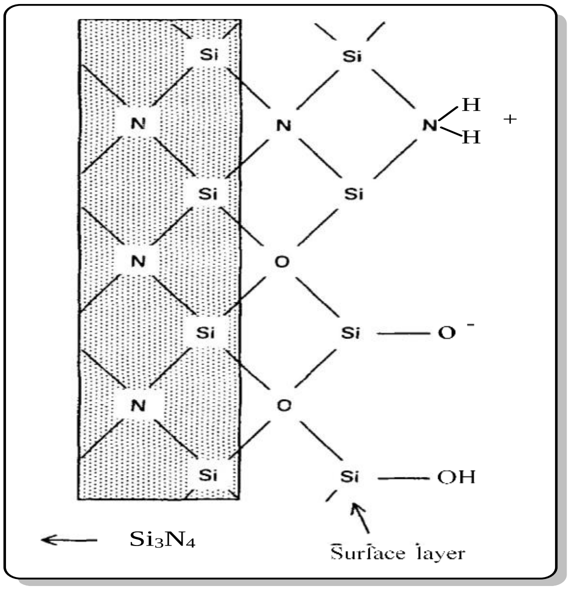

Figure 2.9: Hydroxylated silicon nitride (Si_3N_4) surface structure (Hackley and Malghan, 1994)

The proposed mechanism of formation of silazane and silanol groups (Figure 2.10) is as described by Cazako *et al.* (2018) with modifications.

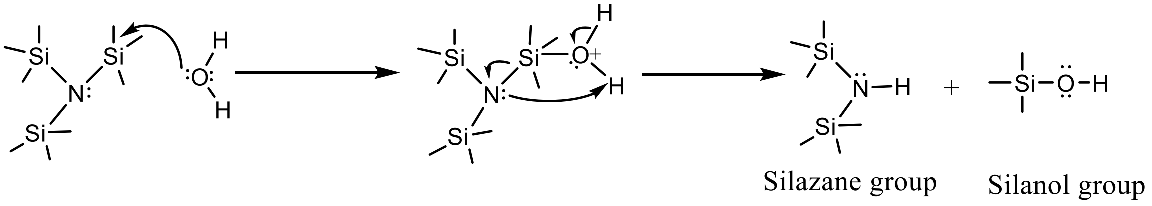

Figure 2.10: Reaction mechanism of silazane and silanol group formation

The mechanism of hydroxylation of silicon nitride (Si_3N_4) surface is given by Figure 2.11.

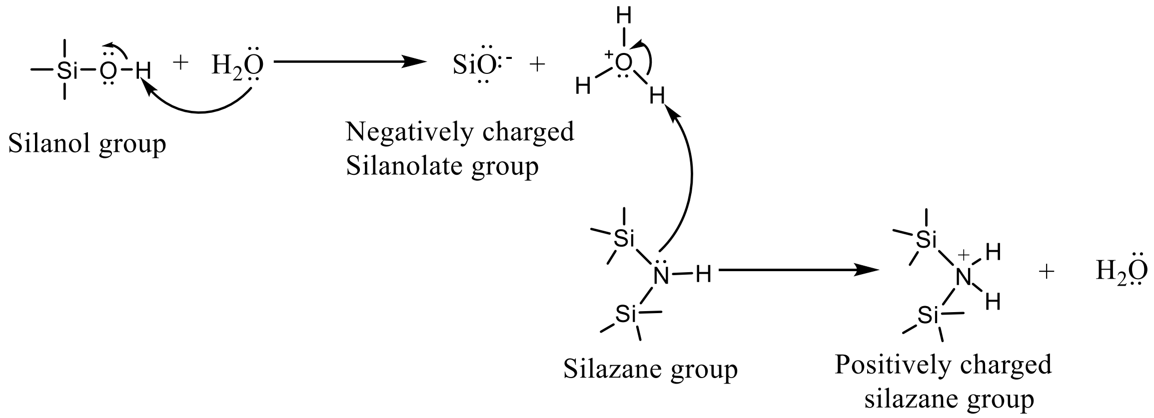

Figure 2.11: Surface hydroxylation mechanism

The binding sites on the silicon nitride surface makes the material suitable for decontamination of vast inorganic and organic species from contaminated water. Adamu *et al.* (2017) prepared silicon nitride adsorbents by hydrothermal process using rice husk silica source and sugar bagasse carbon source for flouride ions decontamination. Sharma *et al.* (2020) prepared doped silicon nitride material for the tetracycline removal from an aqueous media. In another study, the adsorbent was chemically modified with organo-silanes of (3-aminopropyl) trimethoxysilane and 3-glycidoxypropyl) trimethoxysilane for protein adsorption via covalent bonding or by physical adsorption (Awsiuk *et al.,* 2013). The study prepared silicon nitride adsorbent using silica extracted from sand, biochar from coffee husk and macadamia nutshell wastes for treatment of textile dye wastewater.

2.7 Adsorption mechanism

The mechanism of the dyes uptake is mainly by electrostatic interactions and dipole-dipole hydrogen bonding as described by Manzar *et al.* (2019) and Bahrudin *et al.* (2020) with major modifications to fit the adsorbent being investigated as shown in Figure 2.12.

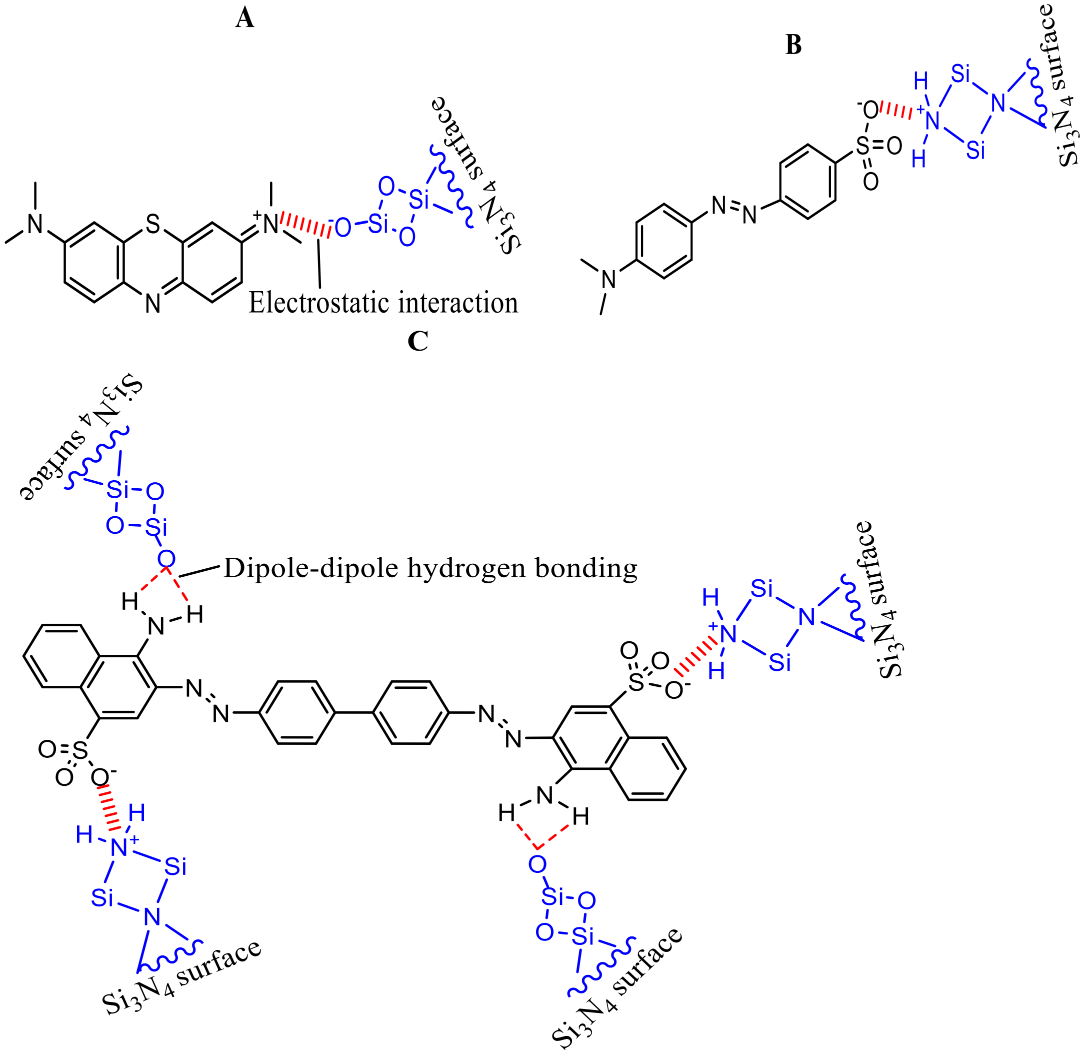

Figure 2.12: Adsorption mechanism of MB (A), MO (B) and CR (C) onto Si_3N_4 adsorbent

2.8 Batch adsorption studies

The batch adsorption are studies that provide information about the adsorbent performance at equilibrated conditions before application in a larger scale set up (Sazali *et al.,* 2020). Batch adsorption processes have several gains as it is cost-effective, greener, simple and easy in practice (Ndung'u *et al.,* 2021). The major disadvantage is that only a lower pollution load is decontaminated, hence, hardly employed for industrial purposes (Patel, 2020). The batch is employed with various process parameters of particle size, temperature, agitation speed, dosage, pH, analyte concentration and agitation time among others (Mutunga *et al.,* 2020; Priyadarshini *et al.,* 2020). The current study reviewed pH, adsorbent dosage, agitation time and initial concentration parameters which are discussed in the sub-sections 2.8.1- 2.8.4.

2.8.1 pH

The dye solution pH is essential because it affects the sorption processes by altering the binding sites charge and the dyes degree of ionization (Benzekri *et al.,* 2018; Mashkoor and Nasar, 2019). The methylene blue (MB), being a cationic dye, its extent of uptake is greatly influenced by pH of its solution and the adsorbent net charge (Saini *et al.,* 2018). The uptake occurs primarily because of electrostatic attractions between the sorbent surface and the cationic dyes (Ahmad *et al.,* 2020). At a lower pH value, H^+ ions and the cationic dyes compete stiffly for the binding sites resulting to a lower uptake (Chang *et al.,* 2016). At pH values beyond optimal, the adsorbent becomes negatively charged, which leads to improved sorption of MB dye molecules via attractive forces enhancing its uptake (Jawad *et al.,* 2018).

The MO and CR anionic dyes removal is highest at strongly acidic media (Jain *et al.*, 2020; Abdul Rahim *et al.*, 2021). This is because of the fact that, at a lower solution pH, the positively charged adsorbent interacts strongly with the dye sulphonate groups ($-SO_3^-$) (Simonescu *et al.*, 2021). As the pH is increased, the dyes uptake is decreased due to competition between the sulphonate ($-SO_3^-$) dye groups and the hydroxyl (OH^-) ions in a basic medium (Khan *et al.*, 2020).

Bellifa *et al.* (2017) report a pH of 1.00 as optimal for maximum removal of MO dyes using bentonite adsorbent. Hachani *et al.* (2017) obtained similar optimal pH values on their study on CR dyes adsorption onto raw date pits adsorbent. A pH value of 10.00 was obtained for MB dyes uptake using geopolymer and peanut shell adsorbents (Maingi *et al.*, 2017; Islam *et al.*, 2019). According to Tahazadeh *et al*. (2021), a pH of 11.00 was optimum for removal of MB dyes using cellulose acetate (CA)-based nanocomposite adsorbent.

2.8.2 Agitation time

The residence time is essential in uptake of dyes as it alters the kinetics of adsorption (Ahmad and Ansari, 2021). Generally, the dye removal is rapid at initial times then equilibrium state (Toumi *et al.*, 2021). At initial stages of adsorption, the dyes are rapidly removed as the adsorbent surfaces have enough active centers available for adsorption (Simonescu *et al.*, 2021). As the agitation time exceed optimal, the active sites become exhausted and consequently lowers the sorption process (Mondal and Kar, 2018). Also, as more adsorbent centers are occupied by the dyes, it becomes hard to occupy the unoccupied sites because of repulsion forces between the dyes adsorbed and the dyes present in the solution (Arora *et al.*, 2019).

Abualnaja *et al.* (2021) reported that 60 minutes were enough to attain maximum equilibrium for sorption of MO onto poly (Acrylonitrile-co-Styrene) and carbon nanotubes. A maximum MB dyes removal uptake onto Fe-modified banana peel was attained at an adsorption time of 50 minutes (Çatlıoğlu *et al.*, 2021). Muniyandi and Govindaraj (2021) reported similar optimal value during their study on MB adsorption onto activated carbon from a palm shell. The uptake of CR dyes using porous γ-alumina nanoshells reached equilibrium within 30 minutes (Al-Salihi *et al.*, 2022).

2.8.3 Adsorbent dosage

The influence of dosage on the uptake process is important as it avails the adsorbent sites and surface area for the dyes uptake (Ahmad and Mirza, 2017). The uptake of dyes increases with increasing dosage to optimum levels due to increased binding sites available for adsorption (Jan *et al.*, 2022). The uptake decreases as the adsorbent dose is increased beyond optimal (Mondal and Kar, 2018). This is due to an increased overlap of the adsorbent particles causing screening effect which reduces the number of effective sites (Aminu *et al.*, 2020). Also, at higher dosages, the dye molecules in the dye solution are inadequate to fully interact with all the adsorbent sites lowering their uptake (Goswami and Dey, 2022).

The optimal dosage of 20 mg was reported for the uptake of MO dyes onto the Mn-doped CuO-nanoparticles (Sharifpour *et al.*, 2019). Adsorbent dosage for MO adsorption by magnetic Fe/MCM-41 adsorbent attained maximum sorption at 30 mg (Albayati *et al.*, 2017). The uptake of MB dyes using empty fruit bunch-derived activated carbon adsorbent was maximum at optimal dosage of 30 mg (Egbosiuba *et al.*, 2020). An optimal dosage of 15 mg was reported for the uptake of MO using copper modified nanoalum (Kakhki *et al.*, 2020). Shittu *et al.* (2019) registered an optimum dosage of 10 mg for sorption of MB onto a novel surfactant functionalized porous graphitic carbon.

2.8.4 Initial concentration

The parameter influences the adsorbent performance significantly (Paclijan *et al.*, 2021). An increased concentration improves dye uptake to maximum values beyond which a plateau or a slight decrease is observed (Smita *et al.*, 2016). An increase in dyes uptake could be because of increased mass transfer driving power with increase in dye concentrations (Omokpariola and Otuosorochi, 2020). The dyes are adsorbed to specific adsorbent sites at lower concentration which continue being used up upon increasing the dyes concentration (Maingi *et al.*, 2017; Ojedokun and Bello, 2017). In higher concentrations beyond optimal, the dyes uptake decreases as the available adsorbent sites are completely used up leaving more dye ions in the solution (Rondina *et al.*, 2019).

Mirzaei *et al.* (2020) reported that MO dyes sorption onto NaX/MgO-TiO_2 nanocomposite was maximum at 50 mg/L. Uptake of CR dyes by L-cysteine/rGO/PANI nanocomposite was 92 % at an optimal value of 30 mg/L (Razzaq *et al.*, 2021). Tan *et al.* (2021) registered an uptake of 22.72 mg/g at 30 mg/L for MB dyes removal using polysaccharide composites. The efficiency of CR dyes uptake onto water hyacinth was > 90 % at 50 mg/L (Ali and Mohammed, 2020).

2.9 Adsorption isotherm studies

The equilibrium isotherms describe the mechanisms of dyes uptake at equilibrium (Oyarce *et al.,* 2021). The isotherm modelling is based on assumption of homogeneity or heterogeneity of the adsorbents on possible interactions with the dye molecules (Alharby *et al.,* 2021). Several isotherms such as Langmuir (Ndung'u *et al.,* 2021), Dubinin-Radushkevich (Lemraski *et al.,* 2021), Freundlich (Cheruiyot *et al.,* 2019) and Temkin (Jadhav and Thorat, 2022) among others are reported. The study employed Langmuir, Dubinin-Radushkevich and Freundlich models and are briefly discussed.

2.9.1 Langmuir isotherm model

The model investigates the adsorbent properties in terms of affinity and removal capacity for the dyes (Xu *et al.,* 2019)**.** It also describes monolayer interactions which are chemisorption in nature (Rosanti *et al.*, 2022). Its linear form is shown by Equation 2.6.

$$\frac{\mathrm{C_e}}{\mathrm{q_e}} = \frac{\mathrm{C_e}}{\mathrm{q_m}} + \frac{1}{\mathrm{K_L q_m}} \qquad (2.6)$$

Where q_e and q_m is the respective experimental and calculated sorption capacity (mg/g), K_L (L/g): the constant and C_e (mg/L): the concentration at equilibrium. A linear plot of $\frac{\mathrm{C_e}}{\mathrm{q_e}}$ against $\mathrm{C_e}$ are employed to obtain $\mathrm{Q_m}$, b and $\mathrm{K_L}$.

The uptake studies of MB dyes using *Dipterocarpus alatus* fruit adsorbent fitted best in Langmuir model (Patawat *et al.,* 2020). Abdul Rahim *et al.* (2021) reports similar conclusions with CR dyes uptake onto coconut wastes. The uptake of MO dyes using populous leaves adsorbent conformed to the Langmuir isotherm (Shah *et al.,* 2021).

2.9.2 Freundlich isotherm model

The model's assumption is on multilayer interactions and an exclusively physisorption process (Shittu *et al.*, 2019). The expression is shown by the Equation 2.7.

$$\ln q_e = \ln K_F + \frac{1}{n} \ln C_e \qquad (2.7)$$

Where $\frac{1}{n}$ (adsorbent heterogeneity), K_F (sorption capacity, mg/g) and n (adsorption intensity) parameters are calculated from linear plots of $\ln q_e$ against $\ln C_e$.

2.9.3 Dubinin-Radushkevich isotherm model

The model is employed to examine the effect of the adsorbent micropore structure on the uptake process (Hu and Zhang, 2019). The model assumes micropore filling mechanism onto heterogeneous and homogenous surfaces (Chen, 2015). Its linear expression is shown by Equation 2.8.

$$\ln q_e = \ln q_m - K_{D-R}\varepsilon^2 \qquad (2.8)$$

Where q_m and q_e (mg/g): the respective calculated and experimental uptake capacity, K_{D-R} (mol^2/kJ^2): the constant and ε: the Polanyi potential. The q_m and K_{D-R} are determined by a plot of a graph of $\ln q_e$ versus ε^2.

The value Polanyi potential (ε) is determined using the expression in Equation 2.9.

$$\varepsilon = RT\ln\left(1 + \frac{1}{C_e}\right) \qquad (2.9)$$

Where R (8.314 J/mol/K): the molar gas constant, C_e (mg/L): the dye concentration at equilibrium and T (K): absolute temperature.

The model is employed to differentiate the chemisorption and physisorption processes (Elwakeel *et al.*, 2020). The adsorption energy (E) is determined using Equation 2.10.

$$E = \frac{1}{\sqrt{-2K_{D-R}}} \tag{2.10}$$

The magnitude of free energy (E) is employed to govern the uptake mechanism. When its value is < 8 kJ/mol, physisorption process dictates and when > 8 kJ/mol, chemisorption predominates (Muralisankar *et al.*, 2018).

The adsorption of MB dyes using poly (vinylidene fluoride) and poly (acrylonitrile) nanofibers conformed to the Dubinin-Radushkevich model (Paclijan *et al.,* 2021). The MB dyes uptake onto copper nanoparticles gave mean free energy (E) of 100 - 129.1 kJ/mol implying a chemisorption process (Sebeia *et al.,* 2019).

2.10 Adsorption kinetic studies

Kinetics of adsorption plays an important role as it offers vital information about mechanisms and dynamics of sorption (Ghosh *et al.*, 2020; Abualnaja *et al.*, 2021). Various models such as Intraparticle diffusion (Maingi *et al.*, 2017), Pseudo-first-order (Silva *et al.,* 2020), Elovich (Duhan and Kaur, 2019) and Pseudo-second-order (Lacin and Aroguz, 2020) among others are reported. The time data for CR, MB and MO dyes uptake was analyzed using Pseudo-second-order, Elovich and Pseudo-first-order models which are discussed in the following sub-sections.

2.10.1 Pseudo-first-order kinetic model

The assumption is that the dyes uptake is physisorption in nature controlled by diffusion rate limiting step (Mittal *et al.,* 2019). Also, the rate of dyes uptake is proportional to the binding sites (Babazadeh *et al.,* 2021). The linearized expression is shown by Equation 2.11.

$$\ln\left(q_e - q_t\right) = \ln q_e - K_1 t \tag{2.11}$$

Where q_e (mg/g) and q_t (mg/g): the respective uptake capacity at equilibrium and at time (t) while K_1 (min^{-1}): the rate constant.

2.10.2 Pseudo-second-order kinetic model

The model assumes a chemisorption process as the rate-governing step in dyes uptake (Abdul Rahim *et al.,* 2021). The expression is shown by Equation 2.12.

$$\frac{t}{q_t} = \frac{1}{k_2\, q_e^2} + \frac{1}{q_e}\, t \tag{2.12}$$

The q_t (mg/g) and k_2 (mg/g/min) (rate constant) values are obtained from t/q_t against time (t) linear plots.

Staroń *et al.* (2019) report Pseudo-second-order as the best fit model for MB dyes adsorption using *raphia* fiber adsorbent. The uptake of MO dyes using modified halloysite was governed by Pseudo-second-order model (Lacin and Aroguz, 2020). Ojedokun and Bello (2017) reported similar findings during their CR dyes uptake studies onto activated carbon from guava leaves. The studies of MO dyes uptake onto watermelon shells and neem leaves adsorbents showed the highest R^2 of 0.9224 and 0.9979 with $Q_{e,\ cal}$ of 3.37 mg/g and 6.69 mg/g respectively all fitting Pseudo-second-order model (Sani and Abdullahi, 2017).

2.10.3 Elovich kinetic model

The model's assumption is on the basis of energetic heterogeneity of the adsorption sites in a multilayer adsorption (Silva *et al.*, 2020). It is employed to determine the kinetic rate constants (adsorption rate and desorption rate) (Kandisa *et al.*, 2018). The Elovich kinetic model linearized form is expressed by Equation 2.13.

$$q_t = \frac{1}{\beta}\ln(\alpha\beta) + \frac{1}{\beta}\ln_t \qquad (2.13)$$

Where β (g/mg) and α (mg/g/min) are the respective desorption and adsorption rate constants. The rate values are obtained from linear plots of q_t versus $\ln_t$.

2.11 Fixed-bed column adsorption studies

Most researches are reported on the removal of textile dyes by batch mode (Mohammad *et al.,* 2016). This limits the usability of the adsorbents in an industrial scale containing high loads of textile dye wastewater (Bennani *et al.,* 2015). Large volumes of coloured wastewater are treated in the columns (Şentürk and Yıldız, 2020). The fixed-bed column operations can be employed in design and operation of fixed-bed industrial plants (Reddy and Nirmala, 2014; Patel *et al.*, 2019).

The fixed-bed column operations allow purification of large loads of wastewater before their discharge to the environment (Dotto and McKay, 2020). Columns are advantageous compared to batch since influent continuous flow is maintained thereby increasing the adsorbent capacity (Gupta *et al.,* 2016). It is worth to note that, before examining the feat of an adsorbent in a fixed-bed column adsorber, preliminary batch studies are done to determine its maximum adsorption capacity at equilibrated optimal conditions (Patel, 2020). The set-up of a column is shown by Figure 2.13.

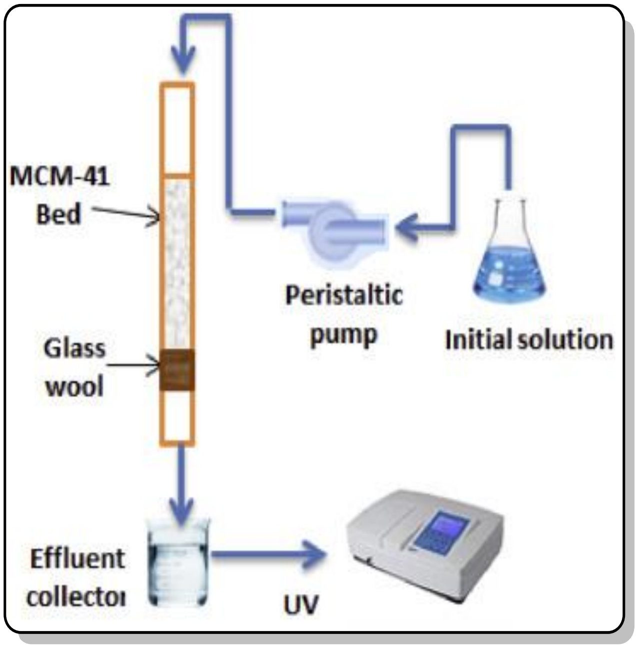

Figure 2.13: A Fixed-bed column (Alardhi *et al.*, 2020)

In fixed-bed columns, the uptake of the adsorbate at different conditions is explained by the use of breakthrough curves which give a profile of the sorption process (Chowdhury *et al.,* 2015; Ndung'u *et al.,* 2022). The Figure 2.14 is a breakthrough curve showing different phases of column adsorption.

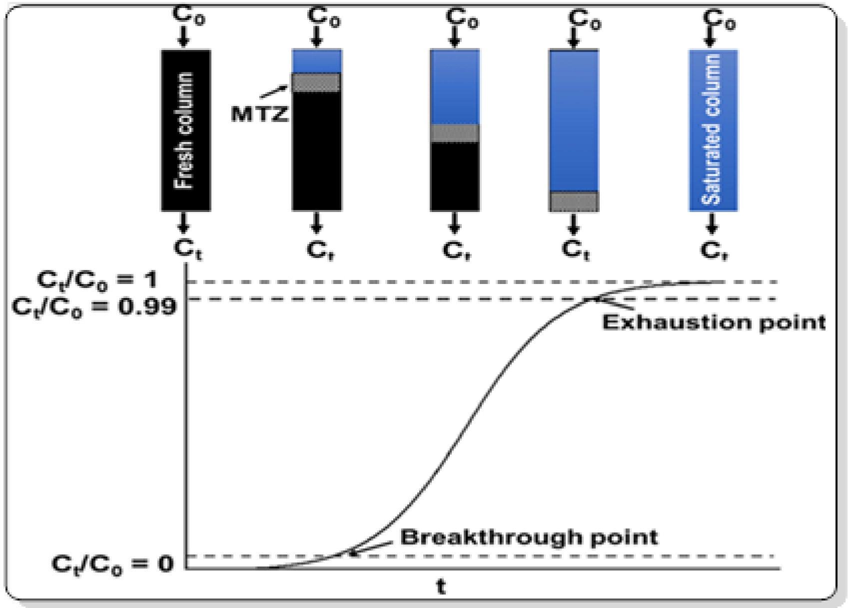

Figure 2.14: A breakthrough curve (Matharage *et al.*, 2025)

Breakthrough curves prediction are important tools that provide guide during designing of adsorption systems (Lemus *et al.*, 2017; Ratnamala *et al.* 2023). A breakthrough curve consists of a saturated zone, mass transfer zone and exhaustion zone (Ndung'u *et al.*, 2022). Initially, column sorption of the dyes is rapid due to less dye molecules present at the upper layers (Gupta *et al.*, 2016). The adsorbent sites get saturated as they are completely occupied following the previous adsorptions (Cundari *et al.*, 2019).

The analyte moves to the unadsorbed part of the adsorbent in the fixed-bed column (mass transfer zone) where most adsorption occur (Chowdhury *et al.*, 2015). Later, the fixed-bed column becomes saturated completely and hence, no adsorption (Patel, 2019). At saturation point, the ratio of influent and effluent concentration is 1 ($C_t/C_o = 1$) (Ndung'u *et al.*, 2022).

Table 2.2 illustrates column capacity of various adsorbent materials for fixed-bed column studies of MO, CR and MB dyes at optimal conditions.

Table 2.2: The column capacity of selected adsorbents

Adsorbent	Dye	Column capacity (mg/g)	Reference
Clay@Fe_2O_3 nanocomposites	Methylene blue	34.69	(Aboussabek *et al.*, 2024)
Water hyacinth (phosphoric acid treated)	Congo red	15.21	(Kalai and Suganthi, 2019)
Chitosan-Clinoptilolite Composite (surfactant modified)	Methyl orange	32.09	(Babazadeh *et al.*, 2021)
Gulmohar leaf powder (Activated)	Congo red	31.64	(Patel, 2018)
Sewage-sludge biochar	Methyl orange	42.30	(Al-Mahbashi *et al.*, 2022)
Corncob biochar (Nano zero-valent Iron (nZVI) coated)	Methylene blue	15.00	(Ding *et al.*, 2022)

The study of silicon nitride (Si_3N_4) as an adsorbent in fixed-bed column adsorption studies for textile dye wastewater treatment has not been explored. The effect of breakthrough curves on fixed-bed column operations is guided by the experimental parameters of influent concentration, volumetric flow rate and bed height (Ali and Mohammed, 2021; Hummadi *et al.*, 2022).

2.12 Effect of fixed-bed column process conditions

In order to design a fixed-bed column process, prediction of breakthrough curves and column capacity of the adsorbents under a set of operating column conditions is important (Isiuku and Horsfall, 2017). Various column parameters of influent concentration, volumetric flow rate, pH, column bed height and adsorbent particle size among others are important in evaluation of the column efficacy in an industrial or pilot scale (Patel, 2019). The study focused on bed height, influent concentration and flow rate which are reviewed in the following sub-sections.

2.12.1 Volumetric flow rate

The breakthrough curves are generally achieved faster with higher volumetric flow rates (Chafi *et al.*, 2016). Adsorption is high at lower volumetric flow rate as the time of contact is more sufficient for the interaction of the adsorbent sites with the dyes (Raj *et al.*, 2020). At high flow rates, the dyes uptake is lower due to inadequate residence time and mass diffusion of dyes in the column leading to a faster column saturation (Yunnen *et al.*, 2017). This result in decreasing amount of dye molecules being adsorbed by the adsorbents (Marzbali and Esmaieli, 2017; Thuong *et al.*, 2019).

The maximum column efficiency of 35.1 % was obtained on MB dyes sorption onto Moroccan clay adsorbent at an optimal flow rate value of 4 mL/min (Bennani *et al.*, 2015).

2.12.2 Bed height

The uptake of dye molecules in a column depends on the adsorbent amount (Akbar *et al.*, 2020). As bed height increases, the adsorbent surface area and breakthrough time is also increased providing more active sites for the dyes uptake (Alardhi *et al.*, 2020). The improved capacity of the adsorbent material at high bed heights enhances the dyes removal making it possible to decontaminate more volumes of dye wastewater (Selambakkannu *et al.,* 2019). If the bed height is lowered, the dosage in the column decreases, thus a decreased column bed capacity (Ali and Mohammed, 2021). The breakthrough curve slope decreases with increased bed height, leading to a greater mass transfer zone (Muliwa *et al.*, 2016).

A breakthrough and saturation times of 142.4 minutes and 294.4 minutes respectively was obtained at an optimal bed height of 7 cm for MB dyes sorption using cellulose cellet adsorbent (Nica *et al.*, 2020).

2.12.3 Influent concentration

The effect of effluent concentration is important in column adsorption as it affects the adsorbent saturation (Baharlouei *et al.,* 2018). The breakthrough times decrease with increasing influent concentration (Thuong *et al.*, 2019). At lower influent concentrations, the breakthrough time significantly increases and a better column performance is achieved (Banerjee *et al.*, 2017). This is because of a lower competition between dye molecules being adsorbed and the binding sites due to a decreased mass transfer driving force (Şentürk and Yıldız, 2020). An increase in influent concentration heightens the concentration gradient and therefore a higher mass transfer driving power of the dye molecules to the adsorption sites (Gopal *et al.,* 2016). The breakthrough curve slope becomes steeper and therefore a decrease in breakthrough and saturation time (Dastgerdi *et al.,* 2020). This results to a faster saturation of the binding sites resulting to a reduced adsorption zone length which lowers the dye removal capacity (Hummadi *et al.,* 2022).

Reddy and Nirmala (2014) during their research studies on CR dyes sorption onto bengal gram seed husk adsorbent reported highest adsorption at low influent concentration. A similar trend was reported by Patel *et al.* (2019) during their studies on column uptake of MB dyes using guava leaf powder adsorbent.

2.13 Column dynamic modelling

In order to assess the kinetics (dynamics) of column adsorption behavior, the column sorption behavior is followed at different column parameters to investigate their influence on the column capacity (Patel, 2019). The Adams-Bohart, Thomas and Yoon-Nelson models are commonly used to model the column time data (Ndung'u *et al.,* 2022). They are reviewed in the following sub-sections.

2.13.1 Thomas model

The column model is employed to determine the adsorbent column capacity and predict the breakthrough curves which assumes a Langmuir and Pseudo second-order isotherm mechanisms (Dlamini *et al.,* 2021; Iheanacho *et al.,* 2021). The linearized form is given by Equation 2.14.

$$\ln\left(\frac{C_o}{C_t}-1\right)=k_{TH}Q_o\frac{m}{Q}-k_{TH}C_ot \tag{2.14}$$

Where $\mathrm{C_o}$ and $\mathrm{C_t}$ (mg/L) is the respective influent and effluent concentration**,** m (g): dosage (g), Q (mL/min): flow rate, $\mathrm{k_{TH}}$ (ml/mg/min): rate constant, $\mathrm{Q_o}$ (mg/g): calculated column capacity. The parameters of $\mathrm{Q_o}$ and $\mathrm{k_{TH}}$ are determined from a plot of $\ln\left(\frac{\mathrm{C_o}}{\mathrm{C_t}} - 1\right)$ against time (t).

2.13.2 Yoon-Nelson model

The model assumption is that the amount of dyes adsorbed is half at the 50 % column breakthrough within a period of time ($t_{1/2}$) (Nica *et al.,* 2020). Its expression is presented by Equation 2.15.

$$\ln\left(\frac{\mathrm{C_t}}{\mathrm{C_o}-\mathrm{C_t}}\right) = \mathrm{k_{YN}}\mathrm{t} - \tau\mathrm{k_{YN}} \tag{2.15}$$

Where τ (min): the time needed for a 50 % ($C_t/C_0 \approx 0.5$) breakthrough and $\mathrm{k_{YN}}$ ($\mathrm{min^{-1}}$): the rate constant. The τ and $\mathrm{k_{YN}}$ parameters are calculated from $\ln\left(\frac{\mathrm{C_t}}{\mathrm{C_o}-\mathrm{C_t}}\right)$ against time (t) linear plots.

The Yoon-Nelson parameters can be employed to determine the column capacity at 50 % column breakthrough using Equation 2.16 (Bharathi and Ramesh, 2013; Gopal *et al.,* 2016; Hummadi *et al.,* 2022).

$$\mathrm{Q_{o\,(YN)}} = \frac{\mathrm{C_o Q_\tau}}{1000\mathrm{m}} \tag{2.16}$$

Where $\mathrm{Q_{o\,(YN)}}$: the column capacity (mg/g).

2.13.3 Adams-Bohart model

According to the model, the dyes uptake rate is proportional to the column capacity at saturation (Patel, 2018). The expression is given by Equation 2.17.

$$\ln\left(\frac{C_t}{C_o}\right) = K_{AB}C_o t - \frac{K_{AB}N_o Z}{U_o} \tag{2.17}$$

Where Z (cm): the bed height, t (minutes): the flow time, K_{AB} (L/mg/min): rate constant, N_o (mg/L): column capacity per unit volume and U_o (cm/min): the superficial velocity. The $\ln\left(\frac{C_t}{C_o}\right)$ against time (t) linear graphs are employed to calculate K_{AB} and N_o.

The adsorbent column capacity at saturation can be obtained from Adams-Bohart model parameters using Equation 2.18.

$$Q_{AB} = \frac{N_o}{1000} \tag{2.18}$$

Where Q_o (mg/g) is the column capacity per unit mass.

The MO dyes fixed-bed column uptake onto chitosan-clinoptilolite composite best fitted Yoon-Nelson and Thomas models at optimal column optimization parameters (Babazadeh *et al.,* 2021). The column studies of MB dyes onto H_3PO_4-activated carbon fibers gave a $R^2 > 0.99$ for Thomas and Yoon-Nelson column models (Silva *et al.,* 2020). Similar conclusions were made by Mohammad *et al.* (2016) during their column studies for CR dyes uptake onto tea waste adsorbent.

2.14 Methods of analysis

Several analytical instruments such as Nuclear Magnetic Resonance (NMR) spectroscopy (Meng *et al.,* 2020), X- Ray Diffraction (XRD) (Al-Salihi *et al.,* 2022), Thermal Gravimetric Analysis (TGA) (Yang *et al.,* 2023), Fourier Transformed Infrared (FT-IR) spectroscopy (Ndung'u *et al.,* 2021; Njeri *et al.,* 2023), Transmission Electron Microscopy (TEM) (Chen *et al.,* 2023), X-Ray Fluorescence (XRF) (Aboussabek *et al.,* 2024), Scanning Electron Microscope-Energy Dispersive X-Ray (SEM-EDX) (Hummadi *et al.,* 2022) and UV-Visible spectroscopy (Khurram *et al.,* 2020; Kloster *et al.,* 2023) are used for analysis. The study involved the use of FT-IR, UV-Visible, SEM-EDX, XRF, XRD and TGA which are briefly discussed in the following sub-sections.

2.14.1 Fourier Transform Infra-Red (FT-IR) spectroscopy

The technique is non-destructive, with gains over other techniques such as a small sample size use, ease in sample preparation and fast analysis (Chen *et al.,* 2014). The FT-IR utilizes IR radiation causing molecular bond vibration and rotation which gives IR spectra at specific wavenumbers (Cui *et al.,* 2017). These FT-IR spectra exhibit characteristic absorption frequencies of varied intensities for different functional groups in a sample (Gonciarz *et al.,* 2020). The Figure 2.15 shows a diagram for FT-IR.

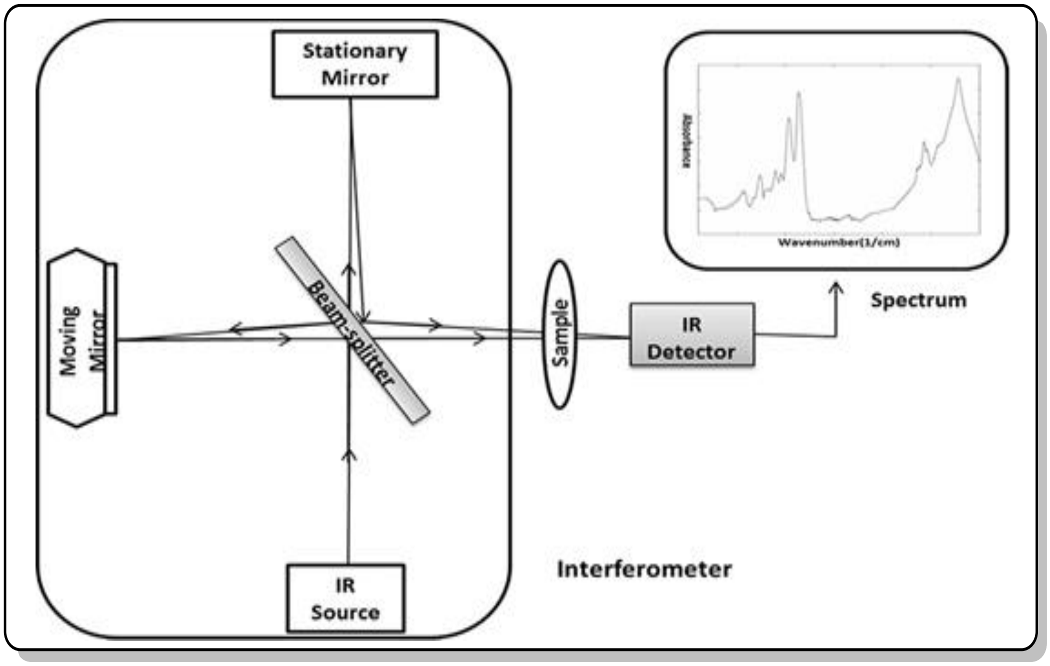

Figure 2.15: The Fourier Transform Infra-Red (FT-IR) instrument components **(**Faghihzadeh *et al.*, 2016)

2.14.2 UV-Visible (UV-Vis) spectroscopy

The ultra-violet (UV) spectroscopy utilizes light in the ultraviolet, visible and infra-red ranges (Verma and Mishra, 2018). It is the most employed technique in analysis as a rapid, simple, accurate, precise, specific and applicable to small quantities of compounds (Chakraborty *et al.,* 2018). The technique measures the absorbance of light passing through the test sample as a function of wavelength dependent on the molecules present (Singh, 2020). The schematic diagram of UV-Visible spectrophotometer is summarized by Figure 2.16.

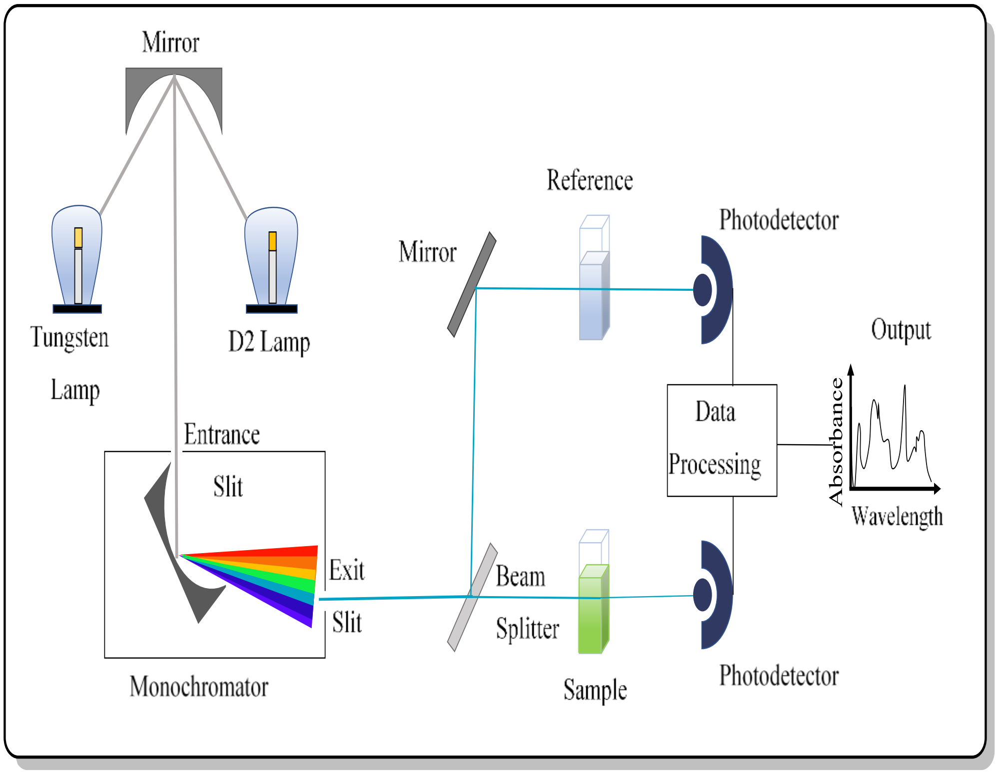

Figure 2.16: Components of UV-Visible spectrophotometer
(Rocha *et al.*, 2018)

2.14.3 Scanning Electron Microscope (SEM) spectroscopy

The technique helps to understand better the micromorphology of the sample materials (Nie *et al.*, 2015). The SEM spectroscopy uses beam of electrons that interacts with the sample and scatters to produce a signal which provides information about topological image and relative composition (Han *et al.*, 2018). The SEM instrument is mostly hyphenated together with Energy Dispersive X-Ray (EDX) detectors as an additional tool for semi-quantitative analysis (Abd Mutalib *et al.*, 2017). The Figure 2.17 shows a SEM diagram with all its components.

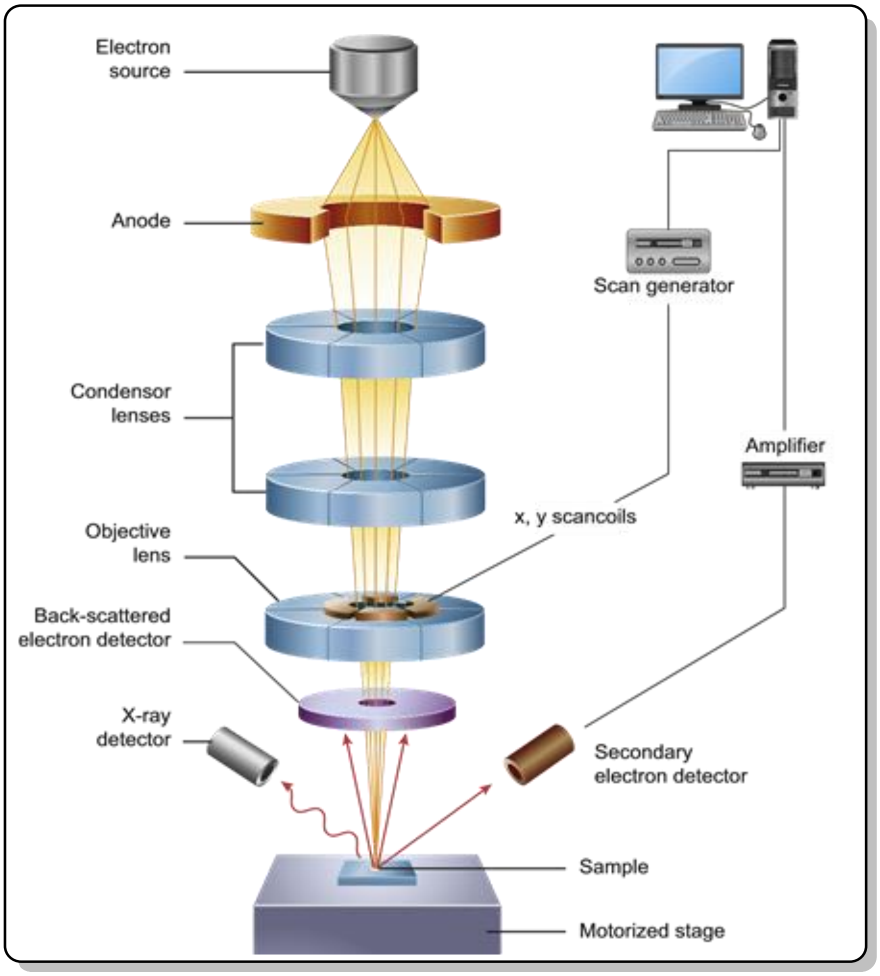

Figure 2.17: Schematic view of Scanning Electron Microscope (SEM) components (Inkson, 2016)

2.14.4 X-Ray Fluorescence (XRF) spectroscopy

This is a versatile tool in trace elements analysis (Potter and Brand, 2019). The technique is based on the principle of wavelength-dispersive, which states that atoms emit X-Ray photon energy that can be estimated (Oyedotun, 2018). The energies of the emitted X-Rays are then used for elements identification in a sample (Marguí *et al.*, 2014). The Figure 2.18 is a diagram of XRF spectrometer.

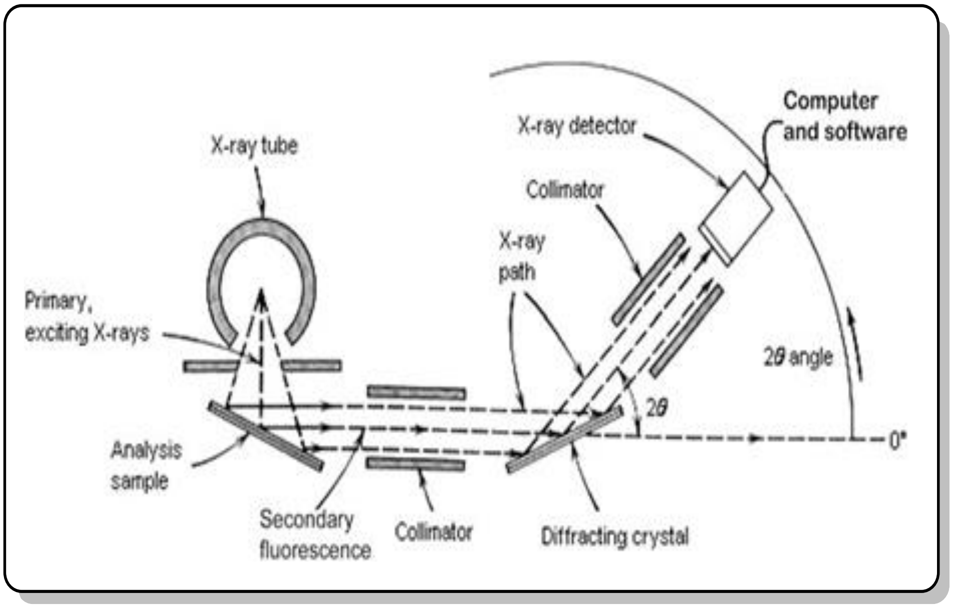

Figure 2.18: X-Ray Fluorescence spectrometer **(**Shackley, 2011)

2.14.5 X-Ray Diffraction (XRD) spectroscopy

The technique is a non-destructive, which performs quick quantitative and qualitative analysis of multi-component and pure substances with minimal sample preparation (Khan *et al.,* 2020). It is used in determining the element proportions of the sample, degree of crystallinity and its structural state (Titus *et al.,* 2019). The diagram for the XRD components is shown by Figure 2.19.

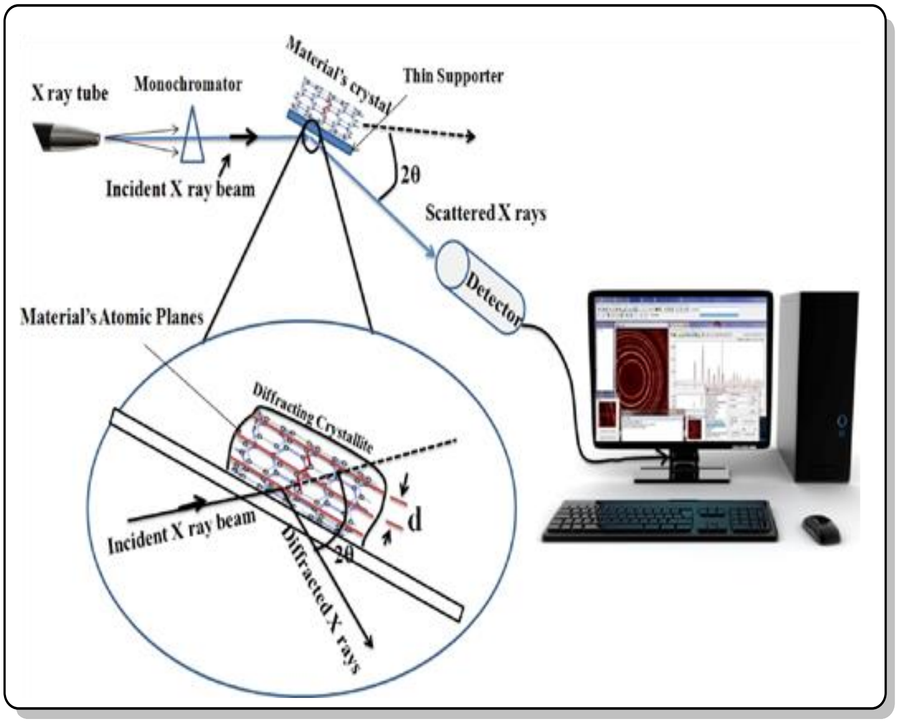

Figure 2.19: Components of an X-Ray Diffraction (XRD) instrument (Das *et al.*, 2014)

2.14.6 Thermal Gravimetric Analysis (TGA)

The technique is employed in characterization of samples by scrutinizing the changes in their physical properties mostly weight under a controlled-temperature system (Xiao *et al.*, 2020). The results are interpreted from TGA thermograms plotted between the change in mass and temperature (Akash and Rehman, 2020). The diagram of a thermogravimetric analyzer is shown by Figure 2.20.

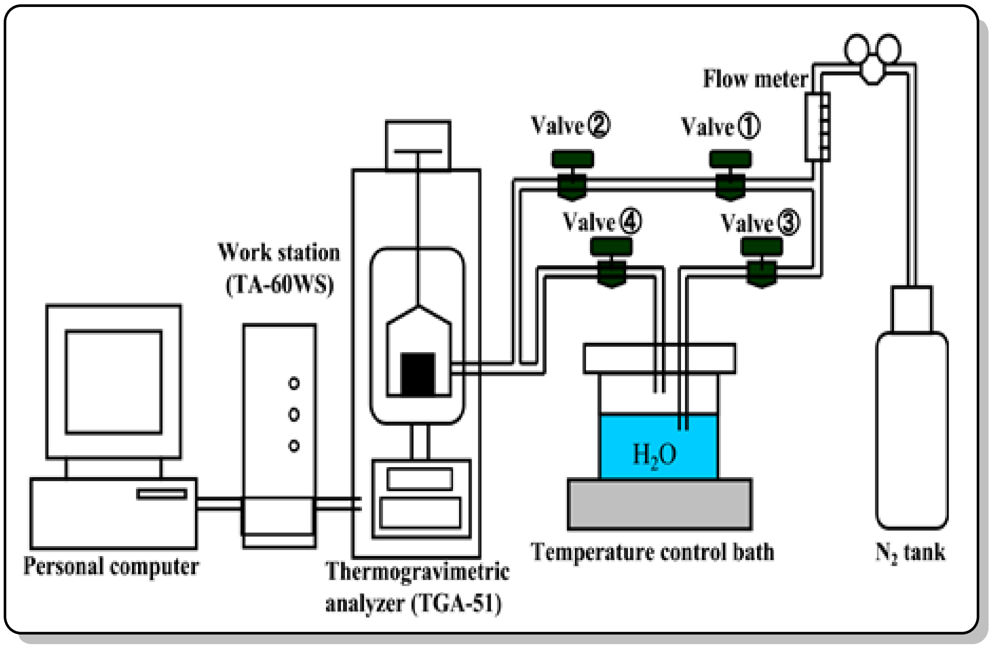

Figure 2.20: Components of a Thermal Gravimetric Analyzer (TGA) (Zhang *et al.*, 2017)

2.15 Regeneration studies

In adsorption technology, it's imperative to regenerate the spent adsorbent material in order to reduce the treatment cost and prevent harmful wastes from getting into the environment (Aigbe *et al.,* 2021). The process is performed by mixing a suitable eluent with the dye loaded adsorbent, agitated for a pre-determined time and filtrated to obtain the amount of the desorbed dyes (Shakoor and Nasar, 2018). An effective eluent should desorb dyes without causing damage to the adsorbent structure (Daneshvar *et al.*, 2017).

Several eluents such as hydrochloric acid (Hou *et al.*, 2021), ethanol (Sharifpour *et al.*, 2019), sulphuric acid (Baharlouei *et al.*, 2018), methanol (Parimelazhagan *et al.*, 2022), acetic acid (Munagapati and Kim, 2016) and sodium hydroxide (Dovi *et al.*, 2021) among others have been used in dyes desorption studies. The 0.5 M HCl eluent showed high desorption ability of 97 % for MB dyes from MB loaded chitosan/montmorillonite composites (El-Kousy *et al.*, 2020). The desorption studies of MO dyes from MO loaded water-soluble polymers showed that 0.01 M NaOH solution was an excellent eluent for desorption (Oyarce *et al.*, 2021). Munagapati and Kim (2016) made similar conclusion from a series of eluent solutions.

CHAPTER THREE

MATERIALS AND METHODS

3.1 Chapter overview

The chapter communicates the experimental design that was used, the research study area, instrumentation, chemicals and apparatus used, sample preparation and pre-treatment, silica extraction, biochar preparation, silicon nitride preparation and characterization of the prepared samples. Batch optimization for MO, MB and CR dyes removal using Si_3N_4 adsorbents, equilibrium, kinetics and desorption studies are also discussed in this chapter. Fixed-bed column optimization, dynamics of column adsorption and column regeneration in both model and environmental water samples from river Athi are discussed.

3.2 Research design

The research study employed an experimental design. This approach evaluates the adsorptive efficiency and performance of the synthesized silicon nitride adsorbent under optimized experimental conditions. In batch preliminary tests, the parameters of pH, adsorbent dosage, agitation time and initial concentration were optimized to determine maximum adsorption capacity and adsorption mechanism. The fixed-bed column experiments tested on the adsorbent’s behavior under dynamic and practical treatment set-ups. This approach offered reliable data for comparing the adsorbent column performance at optimal conditions and establishing the scalability of silicon nitride adsorbent for real-world textile dye wastewater treatment. This is summarized by the Figure 3.1.

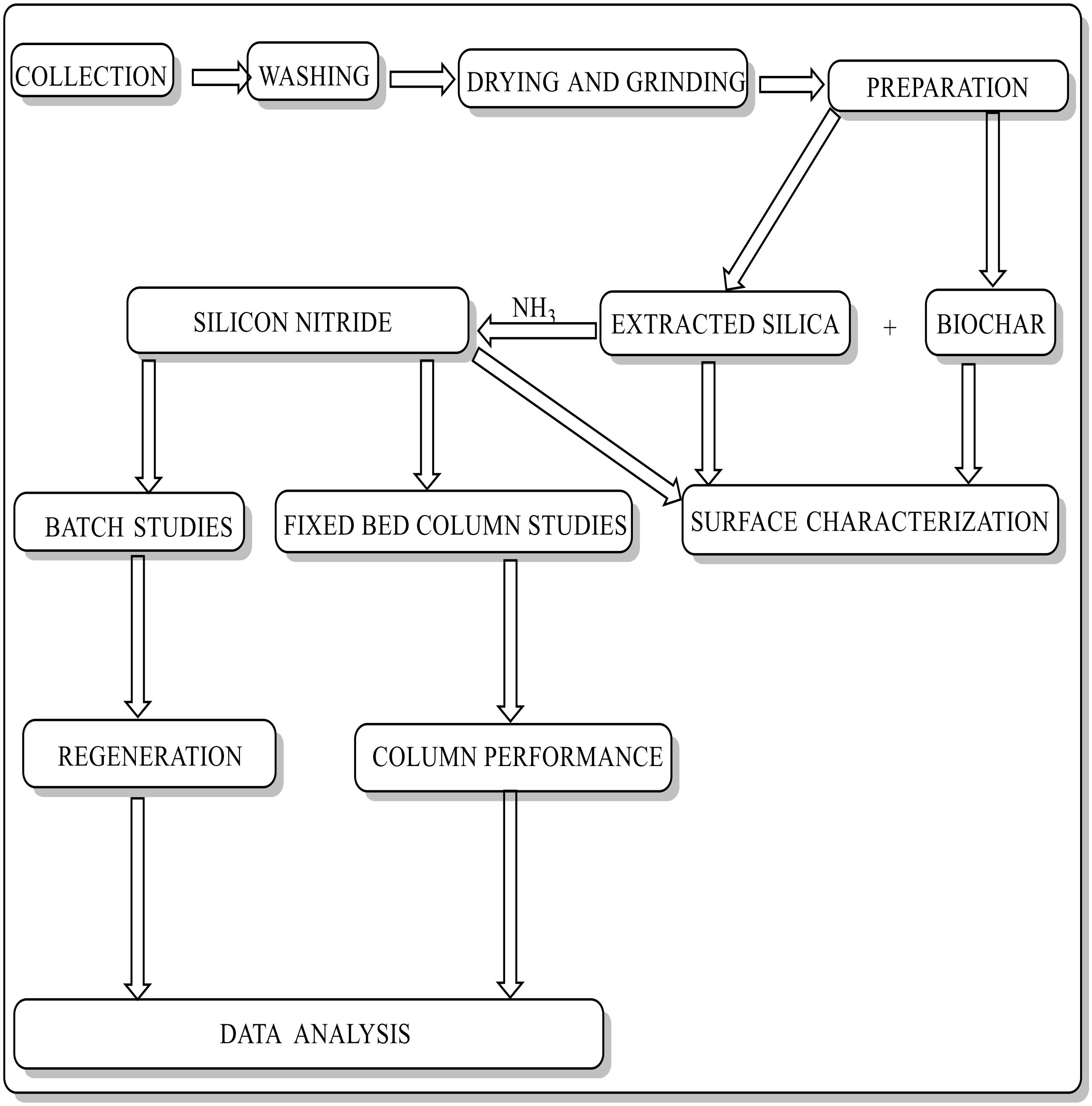

Figure 3.1: The research design

3.3 Study area

The sand samples were collected from the Bamburi Beach (-3.98822’S, 39.73678’E) in Mombasa County, Crescent Island Crater in Lake Naivasha catchment (-0.7775384’S, 36.371476’E) in Nakuru County and Marine National Park (-3.2596385’S, 40.1337541’E) in Malindi, Kilifi County. The coffee husk and macadamia nutshell wastes were randomly collected in Othaya, Nyeri County (-0.551751’S, 36.944703’E).

The environmental water samples collection was restricted to river Athi in Mavoko constituency, Machakos county. The Mavoko area is 25 Km Southeast of Nairobi Central Business District (CBD) and a hub for rapid industrial advancements with industries such as the Export Processing Zone Authority (EPZA) near Athi River town (Aywa, 2017). The EPZA is on the river Athi banks with co-ordinates of -1.355374’S, 37.050251’E (Wafula *et al.,* 2020). The part of river Athi is shown by Figure 3.2.

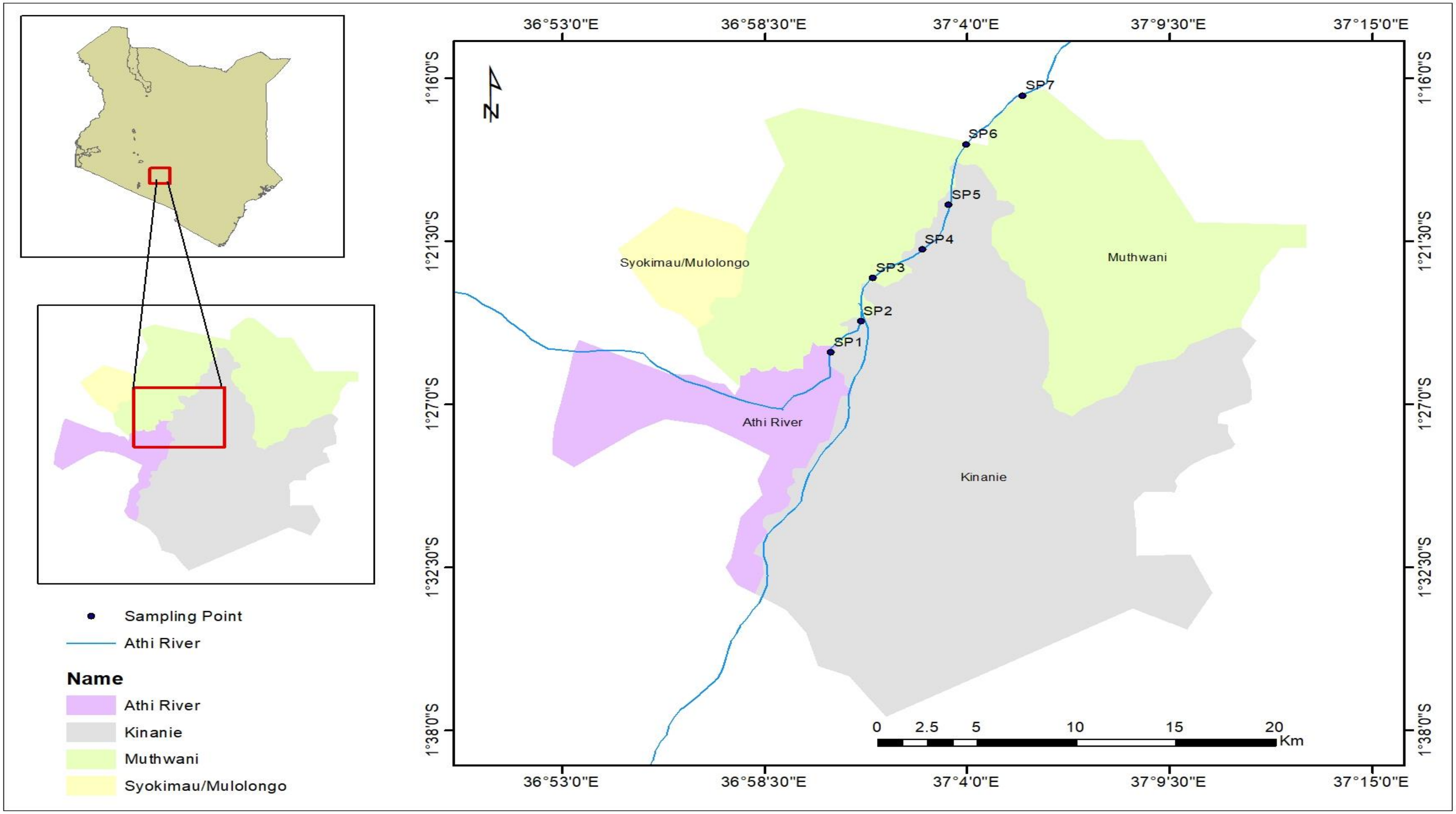

Figure 3.2: Location of river Athi showing different sampling stations

3.4 Chemicals, reagents and solvents

Analar (> 99.5 % purity) grade chemicals, reagents and solvents were used in the study. Ammonium solution (NH_4OH), Congo red ($C_{32}H_{22}N_6Na_2O_6S_2$), Acetic acid ($CH_3COOH$), Methylene blue ($C_{16}H_{18}ClN_3S$), Sodium acetate ($C_2H_3O_2Na$), Methyl orange ($C_{14}H_{14}N_3NaO_3S$), Hydrochloric acid (HCl), Potassium chloride (KCl), Nitric (V) acid (HNO_3), Ammonium acetate ($C_2H_7O_2N$) and Sodium hydroxide (NaOH) were obtained from Sigma Aldrich limited (Kobian outlet in Nairobi). Distilled water used during the research study was prepared from the Kenyatta University (KU) chemistry laboratories.

3.5 Apparatus and equipment

The glassware and plastic bottles were soaked in 10 % HNO_3 overnight and then scrubbed using a scotch brush. They were then washed using hot water containing detergent, soaked in aqua regia (1 % HNO_3 / 3 % HCl) overnight, rinsed with distilled water and air-dried.

The equipment and instruments used were X-Ray Diffractometer, XRD (Rigaku MiniFlex II; made in Tokyo, Japan), Thermogravimetric Analyzer (TGA-50 SHIMADZU), Drying oven (WTC binder FD53), X-Ray Fluorescence (XRF) spectrophotometer (Bruker S1 Titan 600, Tracer 5/CTX), Lab-line mechanical reciprocating shaker (SSL_2 Harrogate, UK), Distiller (WSB 14), Fourier Transform Infra-red (FT-IR) spectrophotometer (IR Tracer-100; made in Japan), UV-Visible spectrophotometer (Specord 200 model, Analytik Jena), Magnetic stirrer with hot plate (WH240-HT), Thermostat-controlled muffle furnace (MC5-12 Biobase), Field Emission-

Scanning Electron Microscope, FEI ESEM (Vega3 Tescan LMH), Peristaltic pump (Longer-BT100), pH meter (PHS-3C), Grinding mill (Retsch SR 200), Pulveriser rock grinding machine (Retsch RS 200), Test sieve (BK-TS 200) and Analytical weighing balance (ATX224 Shimadzu).

3.6 Adsorbent preparation

3.6.1 Sample collection and pre-treatment

The sample collection procedure for the sand samples was borrowed from Olando *et al.* (2020) with slight adjustments. Each of the sand sample was taken from a composite by harmonizing three (3) sub-samples on a 0 - 15 cm depth from a site of 5 × 5 km grid. The composite (500.00 g) was stored in tightly closed and cleaned polythene containers. The macadamia nutshell and coffee husk wastes were collected by random sampling. The sand, coffee husk and macadamia nutshell waste samples were moved to Kenyatta University (KU) chemistry laboratories. The sand samples were sun dried and all visible impurities eliminated, sieved and then oven-dried for 12 hours at 80 °C. Then, they were ground to a fine powder and kept in containers labelled Marine National Park sand (MNPS), Bamburi Beach sand (BBS) and Crescent Island Crater sand (CICS). The coffee husk and macadamia nutshell wastes were washed using distilled water, sliced to pieces and oven-dried for 1 day at 105 °C till all moisture is eliminated. They were ground and sieved to a fine powder and kept in containers labelled raw coffee husk (RCH) and raw macadamia nutshell (RMN) respectively awaiting subsequent experiments.

3.6.2 Silica extraction by alkali fusion

The silica extraction procedure was as carried out by Setyoningrum *et al.* (2020) with slight modifications. The raw sand powders (100.00 g) were soaked in HCl acid (2 M) in glass beakers (500 mL) for about 12 hours. Then, filtration of the mixture followed and the residues thoroughly cleaned with distilled water and then oven-dried for 24 hours at 105 °C to a constant mass. Then, 5 M of NaOH alkaline solution (400 mL) was introduced to the sand residue followed by heating while stirring at 105 °C for about 4 hours. The silicate (Na_2SiO_3) filtrate was filtrated out from the unreacted sand residues by the use of Whatmann filter paper No. 1. Addition of HCl acid solution (2 M) to the silicate solution was slowly done and the mixture left overnight at a room temperature (25 °C) forming a white silica gel. The gel was filtrated out, washed thoroughly using distilled water and then heated in an oven at 105 °C to form amorphous silica. The extracted silica yield (%) was determined using the Equation 3.1.

$$\text{Silica yield (\%)} = \frac{\text{Extracted silica mass(g)}}{\text{Sand sample mass (g)}} \times 100 \tag{3.1}$$

The silica extracted was stored in containers labelled ES-1 (Extracted silica from Marine National Park sand), ES-2 (Extracted silica from Bamburi Beach sand) and ES-3 (Extracted silica from Crescent Island Crater sand) awaiting subsequent experiment (sub-section 3.6.4). The raw sand and extracted silica samples were characterized using XRD, FT-IR and XRF.

3.6.3 Preparation of biochar

A 20.00 g of RCH and RMN powders were first oven-dried for 1 day at 105 °C to eliminate all the moisture and the constant weight recorded. The pyrolytic treatment of the biomass materials was done in a muffle furnace at a 3.00 kW power output, frequency (50 Hz), heating rate (10 °C/min) and voltage (220 V). The powders were placed in a ceramic crucible of 10.20 cm (internal width), 15.50 cm (internal length) and 5.50 cm (internal height) with a ceramic lid and pyrolyzed at 300 °C for 5 hours (Fachini *et al.*, 2021). They were then pulverized to a fine powder and weighed. The biochar yield (%) was calculated as a biochar mass to dried sample mass ratio expressed as a percentage (Equation 3.2).

$$\text{Yield (\%)} = \frac{\text{Mass of biochar}}{\text{Mass of the dried sample}} \times 100 \tag{3.2}$$

Part of the biochar sample was treated with a 3 M HCl acid solution for about 3 hours to eliminate inorganic materials (Alvarez *et al.,* 2016). The excess acid was eliminated by washing the final biochar materials using distilled water, then oven drying them overnight at 105 °C. The final material was then stored in airtight bottles labelled coffee husk biochar (CHB) and macadamia nutshell biochar (MNB) respectively awaiting characterization and subsequent experiment as described in sub-section 3.6.4.

The proximate analysis of the other part of the biochar materials was performed according to the gravimetric method of the ASTM (D1762-84) standard methods.

3.6.3.1 Biochar moisture content

The biochar sample (1.00 g) in a crucible was oven-dried at a temperature of 105 °C for 1 day. The material was cooled and the percentage moisture content determined using the Equation 3.3.

$$\text{Moisture } (\%) = \frac{(\text{Initial biochar mass} - \text{Final biochar mass})}{\text{Initial biochar mass}} \times 100 \tag{3.3}$$

3.6.3.2 Biochar volatile matter

A 1.00 g biochar in a top closed ceramic crucible was heated at 300 °C for 1 hour in a muffle furnace. The % content was determined by the use of Equation 3.4.

$$\text{Volatile matter } (\%) = \frac{\text{Initial biochar mass} - \text{Final biochar mass}}{\text{Initial biochar mass}} \times 100 \tag{3.4}$$

3.6.3.3 Biochar ash content

A biochar (1.00 g) was placed in an open-top crucible. The biochar loaded crucibles were heated to 300 °C for about 3 hours to complete the ashing process. The final material was reweighed and the ash percentage content was by the use of using Equation 3.5.

$$\text{Ash } (\%) = \frac{\text{Final ash mass}}{\text{Initial biochar mass}} \times 100 \tag{3.5}$$

3.6.3.4 Biochar fixed carbon content

The raw biomass samples (1.00 g) were put in a crucible and weighed. The material was oven dried and the final product re-weighed to determine the percentage moisture content as described in sub-section 3.6.3.1. The biochar sample was then divided into two portions in separate crucibles and reweighed. The volatile matter and ash content was determined as described in sub-sections 3.6.3.2 and 3.6.3.3 respectively. The fixed carbon content (%) was determined using the Equation 3.6.

$$\text{Fixed carbon } (\%) = 100 - (\%\text{ moisture content} + \%\text{ Volatile matter} + \%\text{ Ash}) \quad (3.6)$$

3.6.4 Preparation of silicon nitride (Si_3N_4) adsorbents

The Si_3N_4 adsorbents were prepared first by carbothermal reduction followed by nitridation as reported by Maroufi *et al.* (2018) and Abdulhameed *et al.* (2018) with slight adjustments. The synthesis was carried out using digestion bombs constructed locally at the school of engineering, Kenyatta University. The bombs were of stainless steel (SS-316) make with a cylindrical body of a total length of 105 mm, external diameter of 38 mm and internal diameter of 23.5 mm. The bomb top lid material had a 23.5 × 1.5 × 22 mm (thread length) and 39 mm (total length).

Each of biochar powders (CHB and MNB) was mixed separately with the extracted silica (ES-1, ES-2 and ES-3) in stoichiometric ratios (3:2) and the mixture placed in their respective digestion bombs. The bombs were closed tightly and heated at 300 °C in a muffle furnace for 12 hours. A 28 % v/v of NH_4OH solution (200 mL) was added, bombs tightly closed again and heating progressed for another 12 hours at the same temperature (300 °C). The resulting six adsorbent products were left to cool, ground and stored in containers labeled SN-1, SN-2, SN-3, SN-4, SN-5 and SN-6, representing different biochar–silica combinations.

3.7 Characterization of the samples

The adsorbent thermal stability was investigated using Thermal Gravimetric Analyzer (TGA), surface functional groups were characterized by the use of Fourier Transform Infra-Red (FT-IR) spectrophotometer, surface morphology and elemental constitution using Scanning Electron Microscope-Energy Dispersive X-Ray (SEM-EDX), chemical composition using X-Ray Fluorescence (XRF) and crystallinity using X-Ray Diffraction (XRD).

3.7.1 The FT-IR analysis

The sample materials were characterized by the use of FT-IR (IR Tracer-100, SHIMADZU, Japan) spectrophotometer at a set mid-IR range (4000 cm^{-1} - 400 cm^{-1}). Each of the dried samples (1.00 mg) and 500.00 mg of potassium bromide (Merck, spectroscopic grade) were mixed by the use of a pestle in an agate mortar. The mixture was then ground to a fine powder, vacuum pressed for about 10 minutes forming a pellet disk of about 2 mm (internal diameter). The disks were run at 4 cm^{-1} (resolution) with an average of 10 scans for a single spectrum. All the FT-IR spectra were obtained as a plot of transmittance (% T) against wave number (cm^{-1}).

3.7.2 The SEM-EDX analysis

The surface characterization was determined using Field Emission Scanning Electron Microscope, FEI ESEM (Vega3 Tescan LMH model) coupled with EDAX Sapphire Si (Li) EDS detectors together with a MLA software. The powdered samples were pressed, coated and mounted on the aluminum stubs using carbon tapes. They were then loaded onto a sample holder, placed on the SEM instrument and analyzed at 20.0 kV (accelerating voltage).

3.7.3 The TGA analysis

The thermal stability of silicon nitride adsorbents was tested using Thermogravimetric Analyzer (TGA-50 SHIMADZU) on a Thermal analysis work station (TA-60WS) analyzer. The analysis was done by heating the samples using alumina crucibles under a continuous flow of purged inert nitrogen gas (50 mL/min) using a gas flow controller (FC-60 A, SHIMADZU, made in Japan). A heating rate (15 °C/min) was employed with a 10.00 mg of the sample mass at a varied scanning temperature (0 °C - 600 °C). This was followed by cooling process using an automatic blower instrument (BLW-50 SHIMADZU, Kyoto Technology, Japan).

3.7.4 The XRF analysis

The chemical constitution of the raw sand and the extracted silica (ES) was determined using an automated X-Ray Fluorescence spectrometer (Bruker S1 Titan 600, Tracer 5/CTX). The energy was first calibrated to make sure that the peak energies are correctly bound to specific elements. The sample materials were packed into the sample cups with no use of rubber gloves to prevent zinc contamination. The sample cups were then sealed using plastic thin films and analysis performed at a scanning time of 180 seconds per sample. The results were generated from a computer coupled to XRF.

3.7.5 The XRD analysis

The phase analysis was performed using X-Ray Diffractometer, XRD (Rigaku MiniFlex II made in Tokyo, Japan) equipped with Cu Kα radiation source (λ 1.5406 Å). The instrument was set at an accelerating voltage (45 kV), step size (0.02) and an applied current (40 mA). A 5.00 g of each powdered sample was poured onto a sample holder and evenly distributed so that all four corners of the holder are filled. A clean glass slide was used to package the sample onto the cavity firmly to avoid it falling out, deform or slide. A clean single-edge razor blade with a steel or aluminium spine was used to remove any surplus powder by holding it carefully at a 45 ° angle and scraping it. The sample was then scanned from 3 ° to 90 ° 2θ (two theta) at 2 degrees per minute scan rate. The per steps was 3 seconds and running time was 1 hour.

3.8 Preparation of stock solutions

The preparation of stock solution (1000 mg/L) was carried out by dissolving 1.00 g of the respective dye solids in $C_2H_7O_2N$ (CR and MO dyes) and $C_2H_3O_2Na$ (MB dyes) buffer medium to maintain constant ionic power. Serial dilutions were then done from the stock dye solution to obtain working dye solutions with their pH monitored using 1.0×10^{-1} M HCl or NaOH solutions. The working solutions were freshly prepared in each of the experiment.

3.9 Batch adsorption studies

The impact of optimization parameters on MO, MB and CR dyes uptake was investigated at a room temperature (298 K) by batch mode using plastic (100 mL) screw cap bottles. The pH effect (1.00 - 14.00), initial concentration (10 - 150 mg/L), agitation time (10 -

130 minutes) and dosage (5.00 - 40.00 mg) were varied in a 20 mL of the test dye solution. This was carried out in triplicate at 150 revolutions per minute (rpm) by adjusting a particular parameter while others are kept constant. The amount of dyes adsorbed was determined using a UV-Visible spectrophotometer (double beam) at a maximum absorbance wavelength (λ_{max}) of 450 nm (MO), 600 nm (MB) and 500 nm (CR) determined experimentally as shown in appendix I. The amount of dyes adsorbed per unit adsorbent mass was determined using Equation 3.7.

$$q_e = \frac{(C_i - C_e)V}{M} \tag{3.7}$$

where C_i and C_e (mg/L) are respective initial and final concentration, M (g): adsorbent dosage, q_e: amount adsorbed (mg/g) at equilibrium and V: solution volume (mL).

3.9.1 Optimization of pH

3.9.1.1 Point of zero charge (pH_{pzc}) studies

To obtain the pH_{pzc} value of Si_3N_4 adsorbents, 50 mL of distilled water was taken in 100 mL screw cap bottles. The pH adjustments of water were done from pH 1.00 to pH 10.00 as the initial pH using 1.0×10^{-1} M NaOH and 1.0×10^{-1} M HCl solutions. Then, a mass of 0.10 g for each of the adsorbent was added to the screw cap bottles and agitated for 1 day at 150 rpm. The resultant mixture was then filtrated and the pH of water at equilibrium was taken and considered as final pH. The graph of (Initial - Final) ΔpH against initial pH was then plotted. The ΔpH at which it is zero was considered as point of zero charge (pH_{pzc}) value.

3.9.1.2 Calibration of pH meter

To perform pH meter calibration, the electrode was first conditioned with 1.0×10^{-1} M KCl aqueous solution. A pH = 4.00, 7.00 and 10.00 buffer preparation was carried out by dissolving their respective tablets in distilled water (200 mL). The pH meter calibration was then performed and the procedure repeated prior to any dye solution pH adjustments.

3.9.1.3 Obtaining the pH values

The pH impact on CR, MO and MB uptake process by different adsorbents was examined by conducting measurements at 1.00, 3.00, 5.00, 7.00, 9.00, 11.00 and 13.00 pH values at 298 K. A mass of 20.00 mg of each of the Si_3N_4 adsorbent was then added to 20 mL of each 20 mg/L CR, MO and MB dye solution in plastic bottles and the mixture agitated on a Lab-line mechanical reciprocating shaker set at 150 rpm for 1 hour. Then, filtration of the resultant mixture was done and the residual amount of the dyes in the filtrate analyzed.

3.9.2 Effect of agitation time

The MO, CR and MB dyes uptake was investigated at various agitation times using 20.00 mg of Si_3N_4 adsorbents in 20 mg/L dye solutions (20 mL) at optimal pH of 1.00 (MO and CR) and pH 11.00 (MB) and agitation speed (150 rpm). The resultant mixtures were agitated for 10 minutes, then samples filtered out and the dye amount in the supernatant solution determined. The subsequent experiments were performed at varied agitation times of 30, 50, 70, 90, 110 and 130 minutes.

3.9.3 Effect of dosage

To determine the influence of dosage on sorption of MO, CR and MB dyes, varied dosages (5.00 mg - 40.00 mg) of each of the adsorbent was put in the respective plastic bottles containing 20 mg/L dye solutions at optimal pH values. The mixture was agitated for 50 minutes to achieve equilibrium, withdrawn, then filtered and the dyes amount determined.

3.9.4 Effect of initial concentration

The influence of sorption of the dyes onto Si_3N_4 adsorbents was examined by varying the dye concentrations (10 - 150 mg/L) at optimal pH values. A 20 mL of 10, 30, 50, 70, 90, 110, 130 and 150 mg/L MO, CR and MB dye solutions were put in 100 mL screw cap plastic bottles and 30.00 mg optimal dosage of each of the adsorbents added. The mixtures were agitated at optimal agitation time (50 minutes), agitation speed (150 rpm) at 298 K. The dye solutions were then filtered out and the amount of dyes in the test solution analyzed.

3.10 Adsorption isotherms

The Langmuir, Dubinin-Radushkevich and Freundlich isotherms (Equations 2.6, 2.7. 2.8, 2.9 and 2.10) were employed in modelling the experimental data to obtain the maximum sorption capacity of Si_3N_4 adsorbents at optimal initial concentration, agitation time, pH and dosage at a room temperature (298 K).

3.11 Adsorption kinetics

The rate constants for CR, MO and MB dyes sorption onto Si_3N_4 adsorbents were determined using Pseudo-second-order, Elovich models and Pseudo-first-order (Equations 2.11, 2.12 and 2.13). A 20 mL of 50 mg/L for each of the dye solution at pH = 1.00 (MO and CR) and pH = 11.00 (MB) and optimal dosage (30.00 mg) were agitated at 150 rpm and at time intervals of 10 minutes to 250 minutes. The dye amount in the supernatant solution was then analyzed.

3.12 Batch regeneration studies

The batch desorption experiments were carried out using 1.0×10^{-1} M HCl, distilled water, 1.0×10^{-1} M NaOH and 1.0×10^{-1} M CH_3COOH eluents. A 30.00 mg of Si_3N_4 adsorbents was added to the 100 mL screw cap bottles having 20 mL of 50 mg/L MO, MB and CR dye solutions and shaken using a mechanical shaker at optimal agitation time. The amount of dyes adsorbed was then determined. The dye-loaded Si_3N_4 adsorbents were then washed with distilled water and then oven-dried at 80 ^{o}C for 1 hour. The dried loaded adsorbents were transferred to clean dried screw cap plastic bottles. The desorption experiments were done by adding 1.0×10^{-1} M NaOH eluent (20 mL) to the loaded adsorbents and then shaken for a pre-determined agitation time. The amount of dyes desorbed was analyzed. The procedure was repeated for other eluents. The best eluents were employed for subsequent cycles (upto 6th cycle). The desorption capacity was calculated by using Equation 3.8.

$$q_d = \frac{V\,(C_f)}{M} \tag{3.8}$$

Where q_d: amount of dyes desorbed at equilibrium (mg/g), V: eluent volume (mL), C_f: dye concentration desorbed (mg/L) and M: dye saturated adsorbent weight (g).

3.13 Column adsorption experiments

A glass column (25 cm in length and 1 cm internal diameter) was packed with glass wool supporting layers at both ends and equipped with a peristaltic pump (Longer-BT100) for fixed-bed column experiments. The column packed with SN-5 adsorbent was wetted using distilled water to eliminate any trapped air in the adsorbent particles. The effluent analyte was collected at pre-defined time intervals (0 - 600 minutes). The effect of influent concentration (50 mg/L - 90 mg/L), bed height (3 - 7 cm) and volumetric flow rate (4 - 6 mL/min) on the column capacity, breakthrough and saturation time was studied. The resultant solution was analyzed for the amount of dyes adsorbed. All the column experiments were replicated thrice.

3.13.1 Optimization of volumetric flow rate

The MO, MB and CR analyte of 50 mg/L was pumped to each of the columns loaded with SN-5 adsorbent (3 cm) at 4, 5 and 6 mL/min varied flow rates. The dye effluent solutions were taken at time interval of 20 minutes and the amount of supernatant solution was analyzed at 298 K.

3.13.2 Optimization of bed height

The MO, MB and CR dyes (50 mg/L) were introduced into columns of varied bed heights (3, 5 and 7 cm) for SN-5 adsorbent at an optimal flow rate (4 mL/min). The dye effluent solution was taken at varied time intervals (0 - 600 minutes) and its concentration determined.

3.13.3 Optimization of influent concentration

The influent concentration effect (50 mg/L - 90 mg/L) on column sorption of MO, MB and CR dyes onto SN-5 adsorbent was examined at optimal value of 4 mL/min and 7 cm. The amount of dyes in the effluent solution was analyzed.

3.14 Column dynamic modelling

The experimental column data obtained at optimal parameters (4 mL/min, 7 cm and 50 mg/L) for MO, MB and CR dyes sorption onto the SN-5 adsorbent was modelled using Yoon-Nelson, Thomas and Adams-Bohart models (Equations 2.14, 2.15, 2.16, 2.17 and 2.18). This was done to determine the maximum column capacity and sorption mechanism of the Si_3N_4 adsorbent. The model with the highest R^2 values best fitted the column data.

3.15 Data analyses

The quantity of dyes adsorbed is equal to the area under the breakthrough curve calculated by using Equation 3.9.

$$Q_{total} = \frac{Q}{1000} \int_{t=0}^{t_{total}} C_{ads} dt \tag{3.9}$$

Where t_{total} (minutes): the total flow time at saturation, Q (mL/min): the volumetric flow rate, C_{ads} (mg/L): the concentration adsorbed at a given time t (minutes).

The experimental column capacity (Q_{exp}) can be determined from the Equation 3.10.

$$Q_{exp} = \frac{Q_{total}}{m} \tag{3.10}$$

Where m is dosage (g).

The effluent volume, V_{eff} (mL) at saturation time is determined using Equation 3.11.

$$V_{eff} = Qt_{total} \tag{3.11}$$

The total dyes sent through the column (M_{total}) is determined using Equation 3.12.

$$M_{total} = \frac{C_o V_{eff}}{1000} \tag{3.12}$$

Where C_o is the initial influent concentration.

The column removal efficiency (%) is calculated as shown by Equation 3.13.

$$R.E\,(\%) = \frac{Q_{total}}{M_{total}} \times 100 \tag{3.13}$$

3.16 Column performance using environmental water samples

The environmental water samples were obtained from river Athi, Mavoko, Machakos county. They were taken randomly from seven different sampling points along the shores of the river. Five samples of 1 L were taken from each sampling point and concentrated HNO_3 acid (5 mL) solution added to each water sample, bottles sealed and samples were transported to Kenyatta University laboratories. A 100 mL of the water sample from each of the sampling point was placed in a beaker. The analysis of the amount of each of the dye solution found in environmental water samples was determined. Then, known concentration (50 mg/L) of MO, MB and CR dye standards were individually spiked into each of the water sample. The spiked water sample was loaded in the column containing SN-5 adsorbent (at an optimal bed height of 7 cm). Each of the water sample (3 L) was introduced into the column at an optimal flow rate (4 mL/min). The effluent analyte samples were collected at specified time interval of 20 minutes and the amount of dyes in the effluent determined. The retained dyes in the adsorbent were stripped with 1.0×10^{-1} M NaOH or 1.0×10^{-1} M HCl eluent solutions.

3.17 Column regeneration studies

The 1.0×10^{-1} M HCl or 1.0×10^{-1} M NaOH eluents were passed through the column containing the SN-5 dye loaded adsorbent at 4 mL/min. The effluents exiting the column were collected at different pre-determined time intervals and the amount of dyes desorbed analyzed. After the elution process, distilled water was then pumped through the column to wash the fixed-bed until the pH neared neutral. The regenerated fixed-bed was utilized for the next adsorption/desorption cycle. The experiments were carried out up to fourth cycle using the same bed to check on its sustainability for repeated use. The column regeneration efficiency was calculated using Equation 3.14.

$$\text{Regeneration efficiency (\%)} = \frac{\mathrm{C_{des}}}{\mathrm{C_{ads}}} \times 100 \qquad (3.14)$$

Where, $\mathrm{C_{ads}}$ and $\mathrm{C_{des}}$ (mg/L) are the respective dye concentration adsorbed and desorbed.

3.18 Statistical analysis

The experimental data obtained was subjected to one-way ANOVA tests using Fisher least significance difference (LSD) method in minitab software version 17 to test on the significance difference of the mean values at $\alpha = 0.05$ p-value.

CHAPTER FOUR

RESULTS AND DISCUSSION

4.1 Results and discussion overview

The chapter discusses the results on percentage yield and characterization of raw sand, extracted silica, biochar and silicon nitride adsorbents. The results of CR, MO and MB dyes batch optimization parameters (pH, dosage, initial concentration and agitation time), equilibrium (adsorption capacity), kinetics and desorption studies using the Si_3N_4 adsorbents are reported. The impact of process parameters on column adsorption (bed height, influent concentration and volumetric flow rate) were also investigated for CR, MO and MB dyes. The dynamics (kinetics) of column adsorption and column performance using environmental water samples from river Athi are also discussed.

4.2 Characterization of raw sand

The raw sand from Marine National Park, Bamburi Beach and Crescent Island Crater was analyzed using X-Ray Diffractometer (XRD), X-Ray Fluorescence spectrometer (XRF) and Fourier Transform Infra-Red (FT-IR) spectrophotometer. The findings for the characterization studies are discussed in sub-section 4.2.1, 4.2.2 and 4.2.3.

4.2.1 The XRD characterization

The raw sand was analyzed using XRD to determine their crystalline phases. The relative intensity is represented in counts per second (cps). The XRD patterns of sand from Marine National Park, Bamburi Beach and Crescent Island Crater are shown in Figure 4.1.

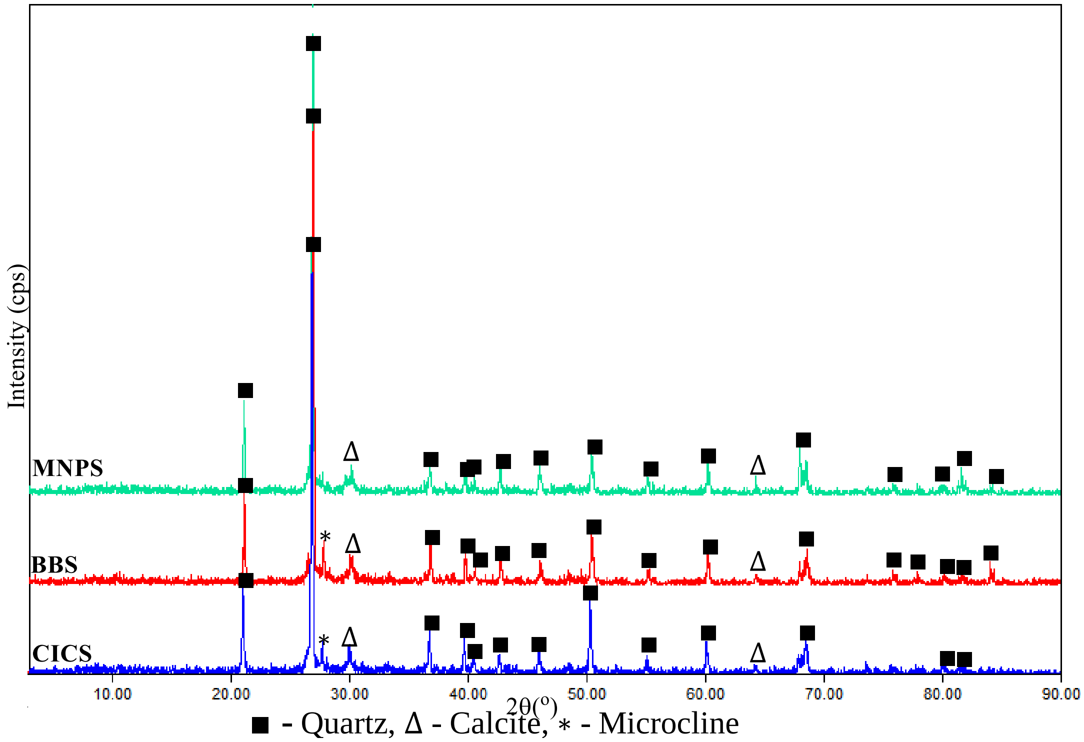

Figure 4.1: The XRD pattern of Marine National Park sand (MNPS), Bamburi Beach sand (BBS) and Crescent Island Crater sand (CICS)

According to the XRD diffractograms (Figure 4.1), the main mineral phases of the MNPS, BBS and CICS samples were quartz (SiO_2) (JCPDS-ICDD file No. 46-1045), calcite ($CaCO_3$) (JCPDS-ICDD file No. 47-1743) and microcline ($K (Al, Fe) Si_3O_8$) (JCPDS-ICDD file No. 19-0932). A minor mineral phase of clinochlore ($(Mg, Fe)_6(Si, Al)_4O_{10}(OH)_8$)) (JCPDS-ICDD file No. 07-0078), although its crystal planes does not appear in the XRD patterns, is also suggested to be present in BBS and CICS samples by the Match! software version 3.14 Build 238. A characteristic peak at 2θ 26.7 ° (MNPS), 26.4 ° (BBS) and 26.8 ° (CICS) indicates the high crystallinity of the quartz phase (El-Sawy *et al.*, 2021). The presence of other diffraction peaks at around 2θ 21 °, 36 °, 39 °, 40 °, 43 °, 46 °, 50 °, 55 °, 60 °, 68 ° and 81 ° with lower intensity are also indicative of quartz phase (Meftah *et al.*, 2023). The dominant peaks at 29.2 ° and 65.9 ° (MNPS);

28.9 °, 29.9 ° and 65.8 ° (BBS); 28.6 °, 29.8 ° and 66.1 ° (CICS) corresponded to microcline and calcite minerals respectively (Munasir *et al.*, 2015; Meftah and Mahboub, 2019; Benchaa *et al.*, 2021).

Based on the outcomes in Figure 4.1, it can be deduced that silica, calcite and microcline minerals are the main components of the raw sand samples under investigation. This agrees with the findings of Munasir *et al.* (2015) and Meftah and Mahboub (2019) during their studies on the silica nanopowder synthesis from silica sand and spectroscopic analysis of sand dune minerals respectively. The raw sand materials were chemically treated using HCl acid solution (sub-section 3.6.2) and outcomes are shown in Figure 4.2.

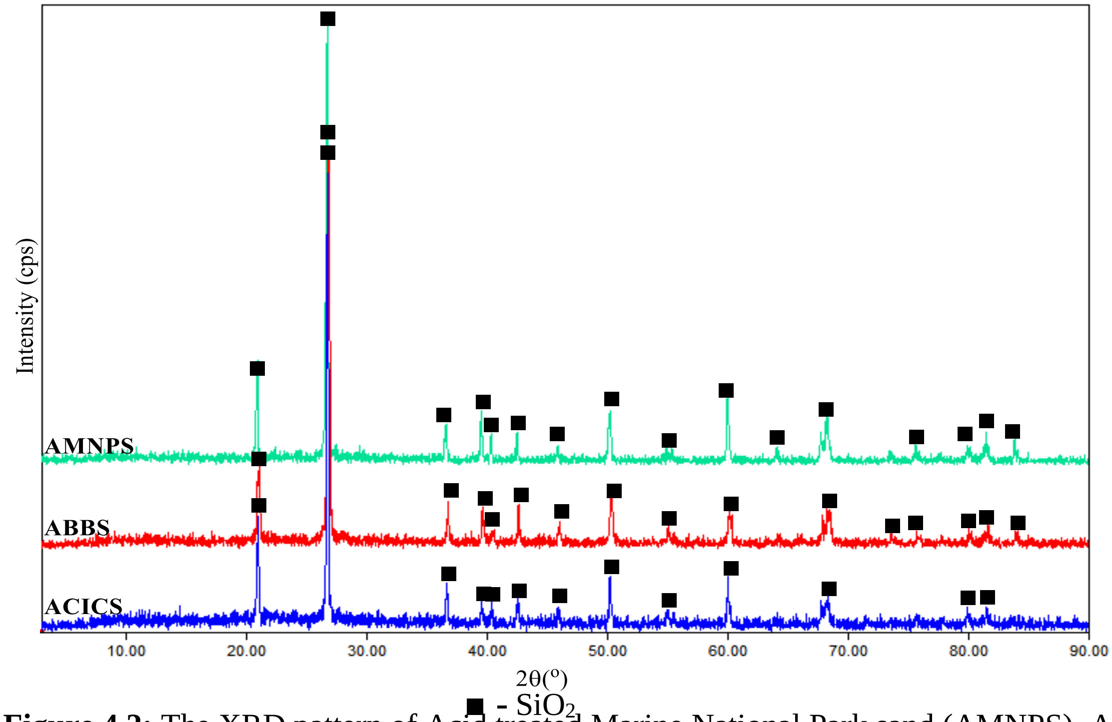

Figure 4.2: The XRD pattern of Acid treated Marine National Park sand (AMNPS), Acid treated Bamburi Beach sand (ABBS) and Acid treated Crescent Island Crater sand (ACICS)

From the results in Figure 4.2, the XRD diffractograms for AMNPS, ABBS and ACICS showed the diffraction peaks for quartz only. The disappearance of peaks at 29.2 ° and 65.9 ° (MNPS); 28.9 °, 29.9 ° and 65.8 ° (BBS); 28.6 °, 29.8 ° and 66.1 ° (CICS) for microcline and calcite minerals showed that HCl solution leached the mineral impurities to negligible amounts. This implied that the purification process eliminated the major impurities in the sand (Bousbih *et al.,* 2020). The peak intensity recorded at 2θ 26.7 °, 26.4 ° and 26.8 ° for MNPS, BBS and CICS respectively increased after the acid leaching. This was also observed for the other diffraction peaks. This can be explained by an eventual impurity reduction in the sand samples (Kheloufi *et al.,* 2011). The position of the 2θ (^{o}) values for quartz phase in all the XRD spectra remained the same as that of MNPS, BBS and CICS. This showed that acid leaching did not alter the quartz phases in the sand samples (Afriani *et al.*, 2019).

The results showed quartz as the dominant phase for the AMNPS, ABBS and ACICS materials after acid leaching. The findings agree to those reported by Kheloufi *et al.* (2011) during their studies on elimination of impurities from sand by leaching.

4.2.2 The XRF characterization

The chemical constitution of the raw sand before and after acid leaching was determined by XRF analysis. The outcomes are tabulated in Table 4.1 and 4.2.

Table 4.1: Mean percentage of chemical constitution of MNPS, BBS and CICS

Oxide (%)	MNPS	BBS	CICS
		(Mean ± S.D)	
SiO_2	78.32 ± 0.81^{b}	83.46 ± 0.39^{a}	66.89 ± 0.41^{c}
Fe_2O_3	1.03 ± 0.25^{bc}	2.56 ± 0.07^{ab}	3.17 ± 0.91^{a}
Na_2O	0.94 ± 0.09^{ab}	0.79 ± 0.47^{ab}	1.01 ± 0.36^{a}
ZrO_2	0.89 ± 0.16^{a}	0.14 ± 0.05^{a}	0.29 ± 0.07^{a}
K_2O	1.06 ± 0.23^{b}	3.54 ± 0.14^{a}	1.98 ± 0.36^{ab}
MgO	0.34 ± 0.12^{c}	1.29 ± 0.07^{b}	2.07 ± 0.02^{a}
MnO_2	0.17 ± 0.06	nd	nd
TiO_2	0.33 ± 0.25	nd	0.28 ± 0.02
Al_2O_3	1.08 ± 0.01^{c}	3.62 ± 0.34^{b}	9.89 ± 0.29^{a}
ZnO	0.08 ± 0.01^{a}	0.43 ± 0.05^{a}	0.19 ± 0.01^{a}
CaO	5.09 ± 0.03^{bc}	6.48 ± 1.01^{b}	8.96 ± 0.24^{a}

nd – not detected

mean values with same letter (s) within the same row are not significantly different (One-way ANOVA, Fisher LSD-test, $\alpha = 0.05$)

KEY

MNPS: Marine National Park sand **BBS:** Bamburi Beach sand

CICS: Crescent Island Crater sand

Table 4.2: Mean percentage of chemical constitution of AMNPS ABBS and ACICS

Oxide (%)	AMNPS	ABBS	ACICS
		(Mean ± S.D)	
SiO_2	83.23 ± 0.14^{b}	88.14 ± 0.06^{a}	77.82 ± 0.37^{c}
Fe_2O_3	0.88 ± 0.03^{a}	1.95 ± 0.05^{a}	1.81 ± 0.15^{a}
Al_2O_3	0.95 ± 0.06^{b}	1.59 ± 0.22^{b}	5.18 ± 0.26^{a}
CaO	1.28 ± 0.01^{b}	3.04 ± 0.03^{a}	2.78 ± 0.79^{ab}

mean values with same letter (s) within the same row are not significantly different (One-way ANOVA, Fisher LSD-test, $\alpha = 0.05$)

KEY

AMNPS: Acid treated Marine National Park sand **ABBS:** Acid treated Bamburi Beach sand

ACICS: Acid treated Crescent Island Crater sand

From the results in Table 4.1, the silica content was 78.32 ± 0.81 %, 83.46 ± 0.39 % and 66.89 ± 0.41 % with lower amount of oxide impurities (< 10 %) for MNPS, BBS and CICS respectively. Before acid leaching, the silica content was higher (> 75 %) in MNPS and BBS than in CICS. This could be due the presence of silica components from biogenic decomposition of siliceous marine organisms' shells which form the sand deposits in the beach sands (Rampe *et al.,* 2023). The content of calcium oxide (CaO) in the raw sand could be due to calcite ($CaCO_3$) mineral in the sand samples (Hachem *et al.*, 2023). Also, iron, magnesium, potassium and aluminium oxide contents could indicate the presence of minerals such as clinochlore $(Mg, Fe)_6(Si, Al)_4O_{10}(OH)_8$) and microcline (K (Al, Fe) Si_3O_8) in the silica matrix. This is in tandem with the XRD results (Figure 4.1).

The acid treatment of the sand samples increased the silica content to 83.23 ± 0.14 %, 88.14 ± 0.06 % and 77.82 ± 0.37 % for AMNPS, ABBS and ACICS respectively while the amount of the other oxide components reduced (Table 4.2). This showed that silica was the main constituent of the sand. The purification resulted to mass decreasing of the sand samples by 9.99 % (AMNPS), 8.32 % (ABBS) and 9.10 % (ACICS). The yellowish-white colour was observed in the sand samples after acid treatment. This could be due to the remaining iron content in the sand samples after leaching process (Alyosef *et al.,* 2014). The findings showed that the samples obtained were pure with minimal mass loss (< 10 %).

The XRF findings are coherent with those reported by Meftah *et al.* (2023) during their studies on extraction of silica nanoparticles from dunes sand.

4.2.3 The FT-IR characterization

The MNPS, BBS and CICS was characterized using FT-IR at a mid IR range of 4000 - 400 cm^{-1}. The findings are presented in Figure 4.3.

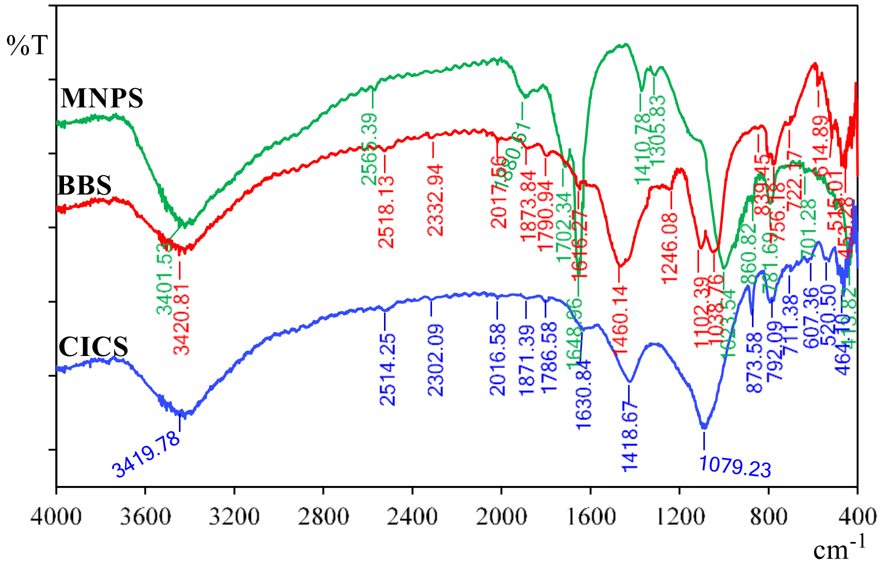

Figure 4.3: The FT-IR spectrum of Marine National Park sand (MNPS), Bamburi Beach sand (BBS) and Crescent Island Crater sand (CICS)

The results in Figure 4.3 revealed broad bands at 3401.53 cm^{-1}, 3420.81 cm^{-1} and 3419.78 cm^{-1} which corresponded to -OH stretch mode of water (H_2O) molecules in the raw sand (Zouaouid and Gheriani, 2018; Meftah *et al.*, 2023). The absorbance at 1648.96 cm^{-1}, 1616.27 cm^{-1} and 1630.84 cm^{-1} is due to flexion mode of -OH groups (Aziz *et al.*, 2019). The absorbance at 2565.39 cm^{-1} and 1410.78 cm^{-1} (MNPS); 2518.13 cm^{-1} and 1460.14 cm^{-1} (BBS); 2514.25 cm^{-1} and 1418.67 cm^{-1} (CICS) is attributed to asymmetrical and symmetrical stretch modes of CO_3^{2-} groups (Meftah and Mahboub, 2019). This was confirmed by peaks at 1702.34 cm^{-1}, 1790.94 cm^{-1} and 1786.58 cm^{-1} respectively for C=O stretch mode vibrations (Hachem *et al.*, 2023). The absorption peaks at 860.82 cm^{-1} and

701.28 cm^{-1} (MNPS); 839.45 cm^{-1} and 722.17 cm^{-1} (BBS); 873.58 cm^{-1} and 711.38 cm^{-1} (CICS) could be due to CO_3^{2-} out-of-plane and in-plane bend modes respectively (Mahdadi *et al.,* 2016). This suggested calcite ($CaCO_3$) mineral presence in the sand samples.

The distinguished peaks at 1023.54 cm^{-1} and 781.69 cm^{-1} (MNPS), 1038.76 cm^{-1} and 756.18 cm^{-1} (BBS) and 1079.23 cm^{-1} and 792.09 cm^{-1} (CICS) were due to the asymmetrical and symmetrical stretch modes of the siloxane (Si-O-Si) groups respectively (Yang *et al.,* 2023). The absorbance observed at 614.89 cm^{-1} and 607.36 cm^{-1} corresponded to Si-O-Fe and Si-O-Mg stretch modes (Beddiaf *et al.,* 2015). The peaks at 515.01 cm^{-1} and 520.50 cm^{-1} was ascribed to Si-O-Al stretch vibrations (Abdelhak *et al.,* 2014). This could be due clinochlore and microcline mineral components in the silica matrix (Jovanovski and Makreski, 2016). The absorbance at 413.82 cm^{-1}, 453.28 cm^{-1} and 464.10 cm^{-1} was ascribed to Si-O-Si bend mode (Yue *et al.,* 2018). The FT-IR studies therefore agree with XRD results (Figure 4.1) that the components of MNPS, BBS and CICS are clinochlore ($(Mg, Fe)_6(Si, Al)_4O_{10}(OH)_8)$), calcite ($CaCO_3$), quartz ($SiO_2$) and microcline (K (Al, Fe) Si_3O_8). Mahdadi *et al.* (2016) reported similar findings during their studies on determination of main compositions and color of Ouargla (Algeria) dune sand. The FT-IR results for acid treated sand samples are presented by the Figure 4.4.

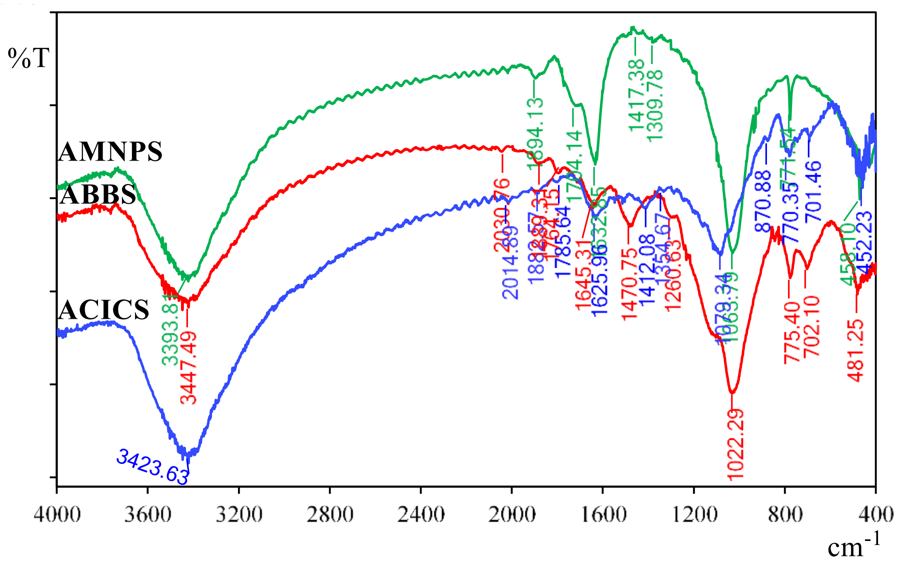

Figure 4.4: The FT-IR spectrum of Acid treated Marine National Park sand (AMNPS), Acid treated Bamburi Beach sand (ABBS) and Acid treated Crescent Island Crater sand (ACICS)

As shown by the results in Figure 4.4, the absorbance at 1063.79 cm^{-1}, 1022.29 cm^{-1} and 1079.34 cm^{-1}; 771.54 cm^{-1}, 775.40 cm^{-1} and 770.35 cm^{-1}; 458.10 cm^{-1}, 481.25 cm^{-1} and 452.23 cm^{-1} for AMNPS, ABBS and ACICS respectively are indicative of quartz in the sand. The results compare to those reported for MNPS, BBS and CICS (Figure 4.3). All the peaks showed shifting to higher or lower values. Also, there was increase in peak intensity for 3393.81 cm^{-1}, 3447.49 cm^{-1} and 3423.63 cm^{-1}, 1063.79 cm^{-1} 1022.29 cm^{-1} and 1079.34 cm^{-1}. These changes are due to reduced impurities in the sand (Rampe *et al.*, 2023).

The peak intensity for 1417.38 cm^{-1} and 1704.14 cm^{-1} (AMNPS), 1470.75 cm^{-1} and 1764.15 cm^{-1} (ABBS), 1412.08 cm^{-1} and 1785.64 cm^{-1} (ACICS) was lower than that of MNPS, BBS and CICS respectively. Also, peaks at 2565.39 cm^{-1} (MNPS); 2518.13 cm^{-1}, 515.01 cm^{-1} and 614.89 cm^{-1} (BBS); 2514.25 cm^{-1}, 520.50 cm^{-1} and 607.36 cm^{-1} (CICS) disappeared after acid treatment. This showed that acid treatment led to elimination of calcite, clinochlore and microcline mineral impurities to negligible amounts.

The FT-IR results for AMNPS, ABBS and ACICS show quartz dominating the raw sand. These results corroborate those reported by Xiao *et al.* (2015) on their studies on alumina and silicon carbide preparation. The highly pure sand was used in silica extraction.

4.3 Characterization of extracted silica

The results on the percentage yield and spectroscopic analysis of the extracted silica (ES-1, ES-2 and ES-3) are discussed in sub-sections 4.3.1, 4.3.2, 4.3.3 and 4.3.4.

4.3.1 The percentage yield

The silica powder was extracted via alkali fusion route described in sub-section 3.6.2 and its mean percentage yield is presented in Table 4.3.

Table 4.3: Mean % yield of extracted silica

Mean %Yield	**ES-1**	**ES-2**	**ES-3**
		(Mean ± S.D, n=3)	
	35.01 ± 0.11^{b}	40.49 ± 0.06^{a}	31.95 ± 0.26^{c}

mean values with same letter (s) within the same row are not significantly different (One-way ANOVA, Fisher LSD-test, $\alpha = 0.05$)

KEY

ES-1: Extracted silica from MNPS **ES-2:** Extracted silica from BBS

ES-3: Extracted silica from CICS

From the results above (Table 4.3), the extracted silica (ES) yield from Marine National Park sand (ES-1), Bamburi Beach sand (ES-2) and Crescent Island Crater sand (ES-3) was 35.01 ± 0.11 %, 40.49 ± 0.06 % and 31.95 ± 0.26 %. The lower yield content (< 50 %) showed that the crystalline quartz dominated the raw sand samples. The results showed that ES-2 gave the highest yield followed by ES-1 and ES-3 in that order. This could be due to variations in local geological characteristics of the sand samples.

Also, the yield for extracted silica (ES-1 and ES-2) was higher than ES-3. This could be due the silica content from the shells of marine organisms which is eventually deposited to the beach sand sediments (Kemp *et al.,* 2021). The higher yield from the beach sands commensurate with the higher silica content in their raw sand materials respectively (XRF results). This implied that silica extraction is influenced by the silica content in their raw sand (Setyoningrum *et al.,* 2020). The findings are in tandem to those reported by Rahmayanti *et al.* (2020) during their silica synthesis studies from Lapindo mud Sidoarjo.

4.3.2 The XRF characterization

The XRF analysis of the extracted silica from Marine National Park sand (ES-1), Bamburi Beach sand (ES-2) and Crescent Island Crater sand (ES-3) was done at a scan time of 180 seconds. The outcomes are presented in Table 4.4.

Table 4.4: Mean percentage of chemical constitution of ES-1, ES-2 and ES-3

Oxide (%)	**ES-1**	**ES-2**	**ES-3**
		(Mean ± S.D, n=3)	
SiO_2	90.16 ± 0.47^b	94.75 ± 0.48^a	84.34 ± 0.45^c
Fe_2O_3	0.51 ± 0.02^a	0.99 ± 0.09^a	0.82 ± 0.03^a
Al_2O_3	0.05 ± 0.01^a	0.09 ± 0.01^a	0.04 ± 0.01^a
CaO	nd	0.25 ± 0.04	nd

nd – not detected
mean values with same letter (s) within the same row are not significantly different
(One-way ANOVA, Fisher LSD-test, $\alpha = 0.05$)

From the results in Table 4.4, the percentage silica yield was 90.16 ± 0.47 % (ES-1), 94.75 ± 0.48 % (ES-2) and 84.34 ± 0.45 % (ES-3) after alkali fusion. This was increased from 83.23 ± 0.14 %, 88.14 ± 0.06 % and 77.82 ± 0.37 % in their AMNPS, ABBS and ACICS samples respectively. All other oxide components were less than 1 % implying that the alkali fusion extraction process improved not only the amorphous silica content but also further reduced the remaining sand impurities after acid leaching (Munasir *et al.*, 2013). The results are coherent with data registered by Ishmah *et al.* (2020) on silica extraction from Bengkulu beach sand via alkali fusion route.

4.3.3 The XRD characterization

The extracted silica (ES) was analyzed by XRD spectrometer to determine its purity and amorphous nature. The findings are presented by Figure 4.5.

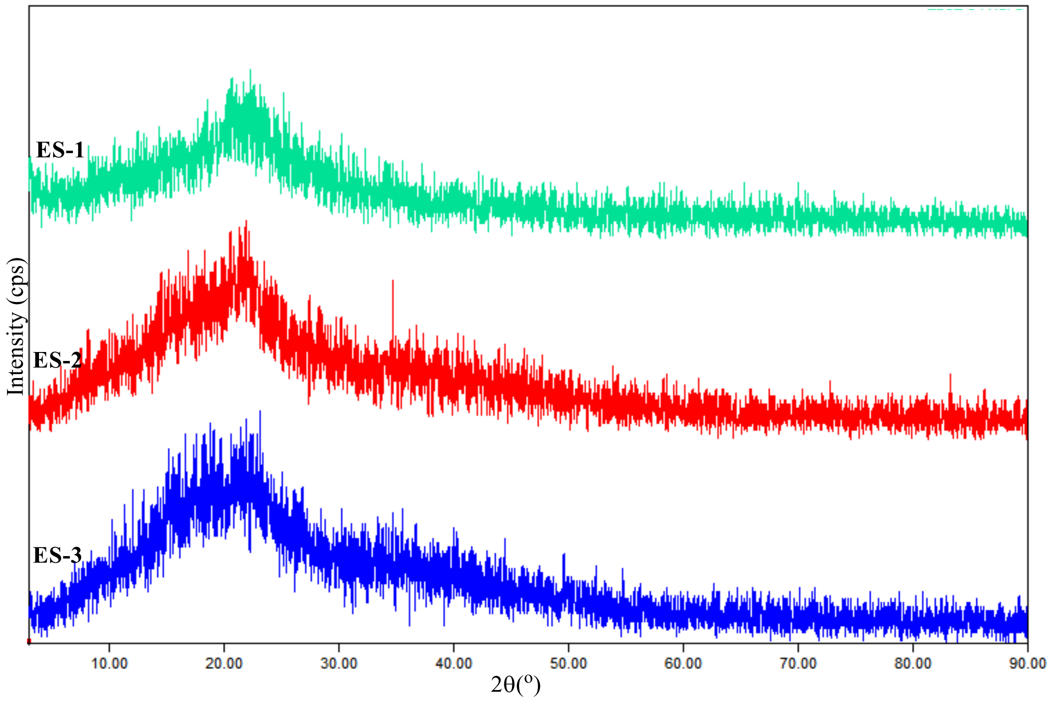

Figure 4.5: The XRD pattern of ES-1, ES-2 and ES-3

The X-Ray Diffraction patterns (Figure 4.5) presented broad diffraction peaks at 2θ = 21.76 ° (ES-1), 20.74 ° (ES-2) and 23.30 ° (ES-3) (JCPDS-ICDD file No. 001-0424). This indicated that the extracted silica was amorphous (Biswas *et al.*, 2018; Ismail *et al.*, 2021). The absence of any other peak showed that the silica extracted was pure (Nayak and Datta, 2020).

The findings showed that the silica extracted from MNPS, BBS and CICS respectively was highly pure and amorphous. The findings corroborate those reported by Firdaus *et al.* (2020) on their studies on extraction of silica from the beach sand for dyes uptake.

4.3.4 The FT-IR characterization

The extracted silica (ES-1, ES-2 and ES-3) was analyzed by FT-IR and the outcomes are presented in Figure 4.6.

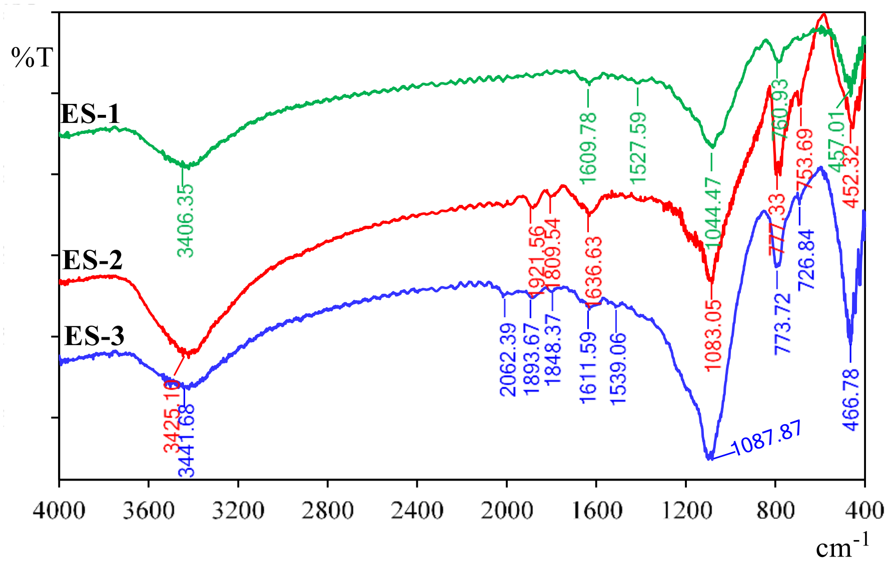

Figure 4.6: The FT-IR spectrum of ES-1, ES-2 and ES-3

The results (Figure 4.6) showed absorbance at 3406.35 cm^{-1}, 3425.10 cm^{-1} and 3441.68 cm^{-1} corresponding to (-OH) stretch modes of silanol (Si-OH) groups and/or adsorbed water on the extracted silica surface (Munasir *et al.*, 2018). This was confirmed by peaks at 1609.78 cm^{-1}, 1636.63 cm^{-1} and 1611.59 cm^{-1} corresponding to -OH bend mode (Ishmah *et al.*, 2020). Absorption peaks at 1044.47 cm^{-1} and 760.93 cm^{-1}, 1083.05 cm^{-1} and 777.33 cm^{-1}, 1087.87 cm^{-1} and 773.72 cm^{-1} was because of asymmetric and symmetric siloxane (Si-O-Si) stretch modes (Mourhly *et al.*, 2015; Thahir *et al.*, 2019). The peaks observed at 457.01 cm^{-1}, 452.32 cm^{-1} and 466.78 cm^{-1} attributed to Si-O-Si bend modes (El-Didamony *et al.*, 2020).

Based on the FT-IR results for ES-1, ES-2 and ES-3, the siloxane (Si-O-Si) and silanol (Si-OH) groups dominated the extracted silica. These results agree to findings reported by Boualem *et al.* (2021) during their studies on nanosilica synthesis using Algerian river sand by alkali fusion method.

The findings for the extracted silica (ES) showed amorphous silica with siloxane (Si-O-Si) and silanol (Si-OH) as important functional groups. This makes the material suitable as a silica source in Si_3N_4 adsorbent synthesis.

4.4 Characterization of biochar

The coffee husk biochar (CHB) and macadamia nutshell biochar (MNB) prepared from their respective raw coffee husk (RCH) and macadamia nutshell (RMN) biomass materials were analyzed by proximate and characterized using XRD, FT-IR and SEM-EDX. The findings of the study are discussed in sub-sections 4.4.1-4.4.5.

4.4.1 Proximate analysis

The proximate analysis of CHB and MNB was performed and the outcomes are presented in Table 4.5.

Table 4.5: Proximate analysis of the coffee husk biochar (CHB) and macadamia nutshell biochar (MNB)

Analysis wt (%)	**CHB**	**MNB**	**p-value ($\alpha = 0.05$)**
	(Mean ± S.D)		
Yield	25.11 ± 0.12	28.19 ± 0.05	0.3553
Moisture	7.45 ± 0.04	5.67 ± 0.03	
Volatile matter	74.80 ± 5.93	71.56 ± 7.61	
Ash	1.02 ± 0.27	0.89 ± 0.14	
Fixed carbon	16.73 ± 2.01	21.88 ± 5.28	

mean values with p-value > 0.05 are not significantly different
(Student t-test, $\alpha = 0.05$)

The results (as tabulated in Table 4.5) showed that 74.80 ± 5.93 % (CHB) and 71.56 ± 7.61 % (MNB) volatile matter was released during the pyrolysis of their respective biomass materials. This showed that all the volatiles trapped within the biomass matrix were eliminated forming biochar with a high carbon content (Bushra and Remya, 2020). The biochar had a carbon and ash content of 16.73 ± 2.01 % and 1.02 ± 0.27 % (CHB), 21.88 ± 5.28 % and 0.89 ± 0.14 % (MNB) respectively. The results indicate that the biochar obtained has a high carbon content and negligible ash amount.

The findings showed a higher fixed carbon content values for CHB and MNB respectively than those reported by Mansuri *et al.* (2018) and Manrique *et al.* (2019) on the proximate analysis studies of biochars from pyrolytic treatment of the macadamia nutshell and coffee husk wastes respectively at different temperatures. This could be due to their varied geographical areas of growth, seasons and maturity.

4.4.2 The FT-IR characterization

The FT-IR characterization for the raw biomass, biochar from coffee husks and macadamia nutshells was carried out at a mid-IR range of 4000 - 400 cm^{-1} and at an average of 10 scans per spectrum. The results are as presented in Figures 4.7 I and II.

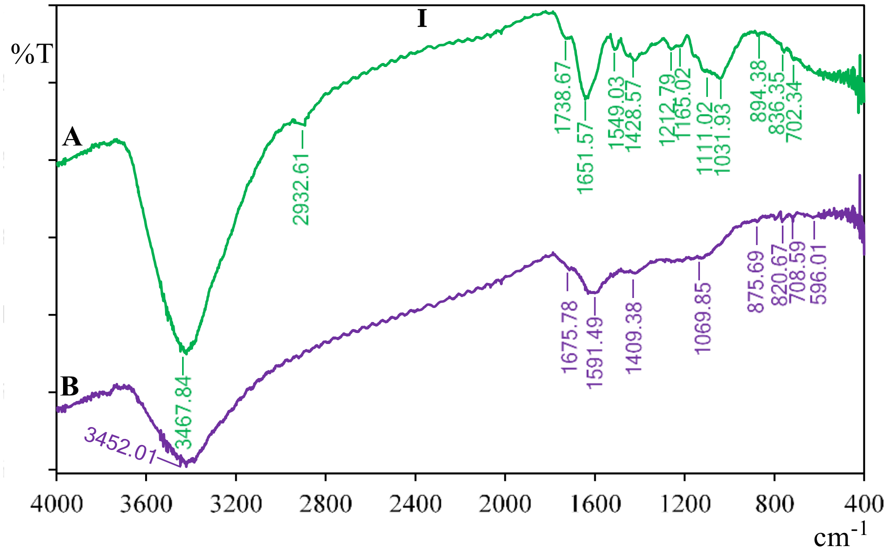

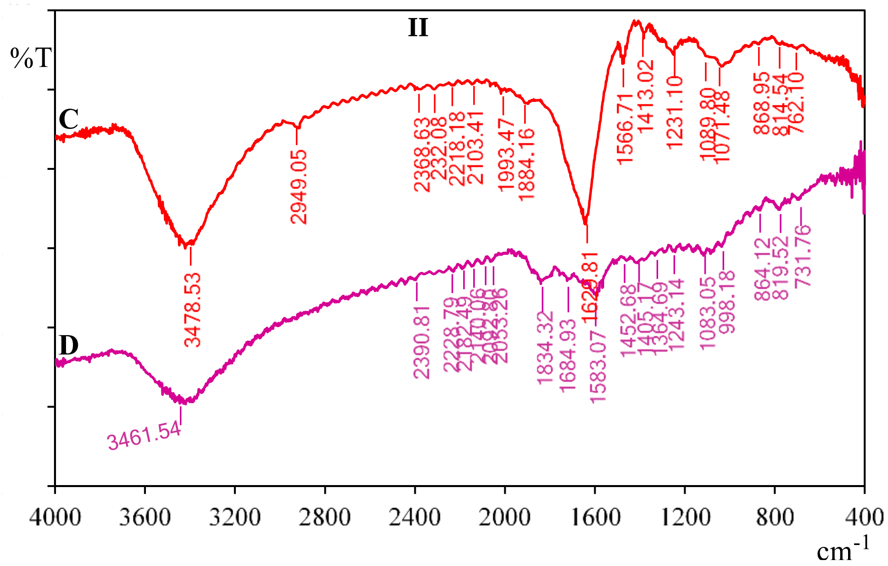

Figure 4.7: The FT-IR spectrum of RCH (A), CHB (B), RMN (C) and MNB (D)

The results in FT-IR spectra of RCH and RMN (Figure 4.7 A and C) showed strong bands at 3467.84 cm^{-1} and at 3478.53 cm^{-1} which indicated free and intermolecular bonded –OH in alcohol, phenol or carboxylic derivative functional groups in polymeric compounds (Alghamdi and El Mannoubi, 2021). The absorbance at 2932.61 cm^{-1} and 2949.05 cm^{-1} was due to methyl (-CH$_3$)/methylene (-CH$_2$-) stretch modes in aliphatic groups (Lemraski *et al.*, 2021). The absorbance at 1651.57 cm^{-1} and 1629.81 cm^{-1} correspond to carbonyl (C=O) groups stretch in carboxylic acid and its derivatives (Ndung'u *et al.*, 2021). The absorbance at 1549.03 cm^{-1} and 1566.71 cm^{-1} could be due to carbon-carbon (C=C) stretch vibration of aromatic hydrocarbons (Mansuri *et al.*, 2018). The absorbance observed at 1428.57 cm^{-1}, 1413.02 cm^{-1} 1212.79 cm^{-1}, 1231.10 cm^{-1}, 1031.93 cm^{-1} and 1071.48 cm^{-1} corresponded to the C-O stretch modes of the carboxylate groups (Njeri *et al.*, 2023). The same peaks at 1031.93 cm^{-1} and 1071.48 cm^{-1} together with peaks at 702.34 cm^{-1} and 762.10 cm^{-1} could also be because of the Si-O-Si stretch modes (Huljana *et al.*, 2021). This corroborated the presence of silica in the raw biomass materials. The absorption at 836.35 cm^{-1} and 814.54 cm^{-1} was ascribed to C=C of aromatic bending modes (Adekanye *et al.*, 2022).

The FT-IR spectra for the biochars (Figure 4.7 B and D) is different from the raw biomass materials. The methyl ($-CH_3$)/methylene ($-CH_2-$) peaks disappeared after pyrolysis indicating the absence of the aliphatic carbon (Chen *et al.,* 2023). The spectra showed clearly distinguished peaks at 1591.49 cm^{-1} and 1583.07 cm^{-1} for C=C groups confirming the aromatic carbon content in the biochar samples (Kabayo *et al.*, 2019). Additionally, a reduced peak intensity for 1409.38 cm^{-1} and 1405.17 cm^{-1} showed reduction of the polymeric compounds containing carboxylic groups. The broad bands at 3452.01 cm^{-1} (CHB) and 3461.54 cm^{-1} (MNB) were due to -OH stretch vibrations of adsorbed water on the biochar surface (Philippou *et al.,* 2019). Also, the absorbance at 1069.85 cm^{-1} (CHB) and 1083.05 cm^{-1} (MNB) decreased in intensity and shifted to higher values. This could be due to the decomposition of the cellulose components during pyrolysis leaving the aromatic carbon and silica components only. The FT-IR spectra didn’t show any other major peaks which showed that there was complete pyrolysis of coffee husk and macadamia nutshell wastes. The findings of the study mirror to those reported by Suman and Gautam (2017) during their studies on pyrolytic treatment of coconut husk biomass at 400 ^{o}C.

The FT-IR outcomes showed peaks at 1591.49 cm^{-1} and 1583.07 cm^{-1} (C=C), 1069.85 cm^{-1}, 1083.05 cm^{-1}, 708.59 cm^{-1} and 731.76 cm^{-1} (Si-O-Si) for CHB and MNB respectively. This imply that carbon and silica dominated the biochar materials.

4.4.3 The XRD characterization

The biochars (CHB and MNB) were prepared by pyrolysis of their respective biomass materials followed by acid leaching. The XRD results are shown in Figures 4.8 I and II.

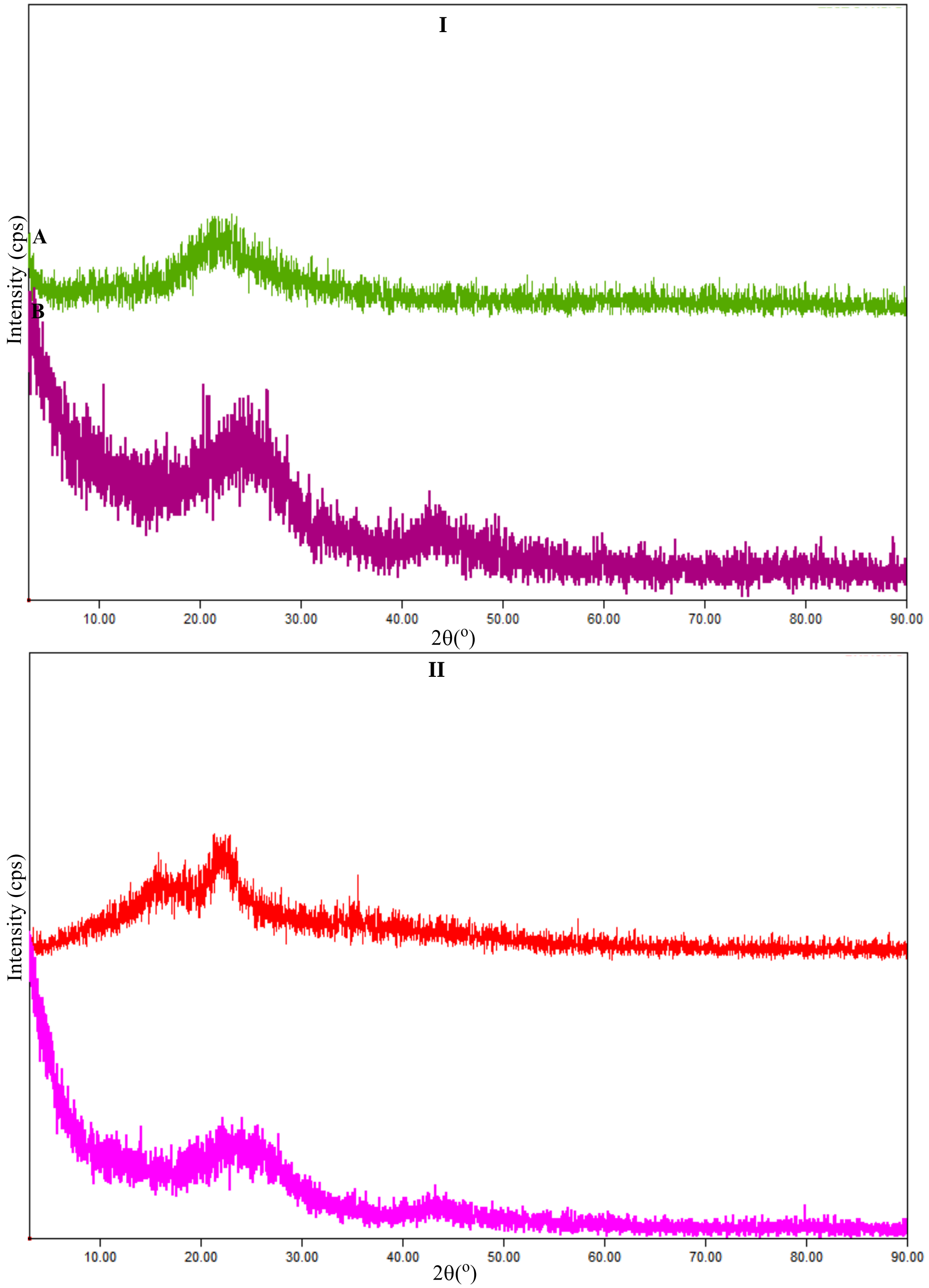

Figure 4.8: The XRD pattern of RCH (A), CHB (B), RMN (C) and MNB (D)

The results in Figure 4.8 A and C showed broad diffraction peaks at 21.97 ° and 22.74 ° for RCH and RMN respectively. This corresponded to a diffraction peak for amorphous cellulose (JCPDS-ICDD file No. 03-0226). The results showed that the raw biomass contains lignin, hemicellulose, pectin and cellulosic materials which are highly amorphous (Mu *et al.*, 2018). The same peaks provide information on amorphous silica in RCH and RMN biomass and their biochars respectively (JCPDS-ICDD file No. 001-0424).

The XRD diffractograms for CHB and MNB show diffraction patterns at $2\theta = 24.14$ ° and $2\theta = 44.73$ °; $2\theta = 25.32$ ° and $2\theta = 43.98$ ° respectively which corresponded to diffuse graphitic peaks in low and high theta regions respectively (JCPDS-ICDD file No. 41-1487). The results showed an amorphous carbon biochar structure (Jagdale *et al.*, 2019). The absence of other diffraction peaks in the diffractograms revealed that the biochar materials had negligible ash contents (Lawrinenko and Laird, 2015).

The findings revealed an amorphous and pure carbon structure of the biochar materials (CHB and MNB). This is in tandem with results reported by Rajarao and Veena (2016) on their research on the silicon nitride and silicon carbide nanopowder synthesis using macadamia nutshell wastes.

4.4.4 The SEM characterization

The SEM analysis of the raw and biochar samples from the coffee husk and macadamia nutshell materials was done and the SEM micrographs obtained are presented in Figures 4.9 A, B, C and D.

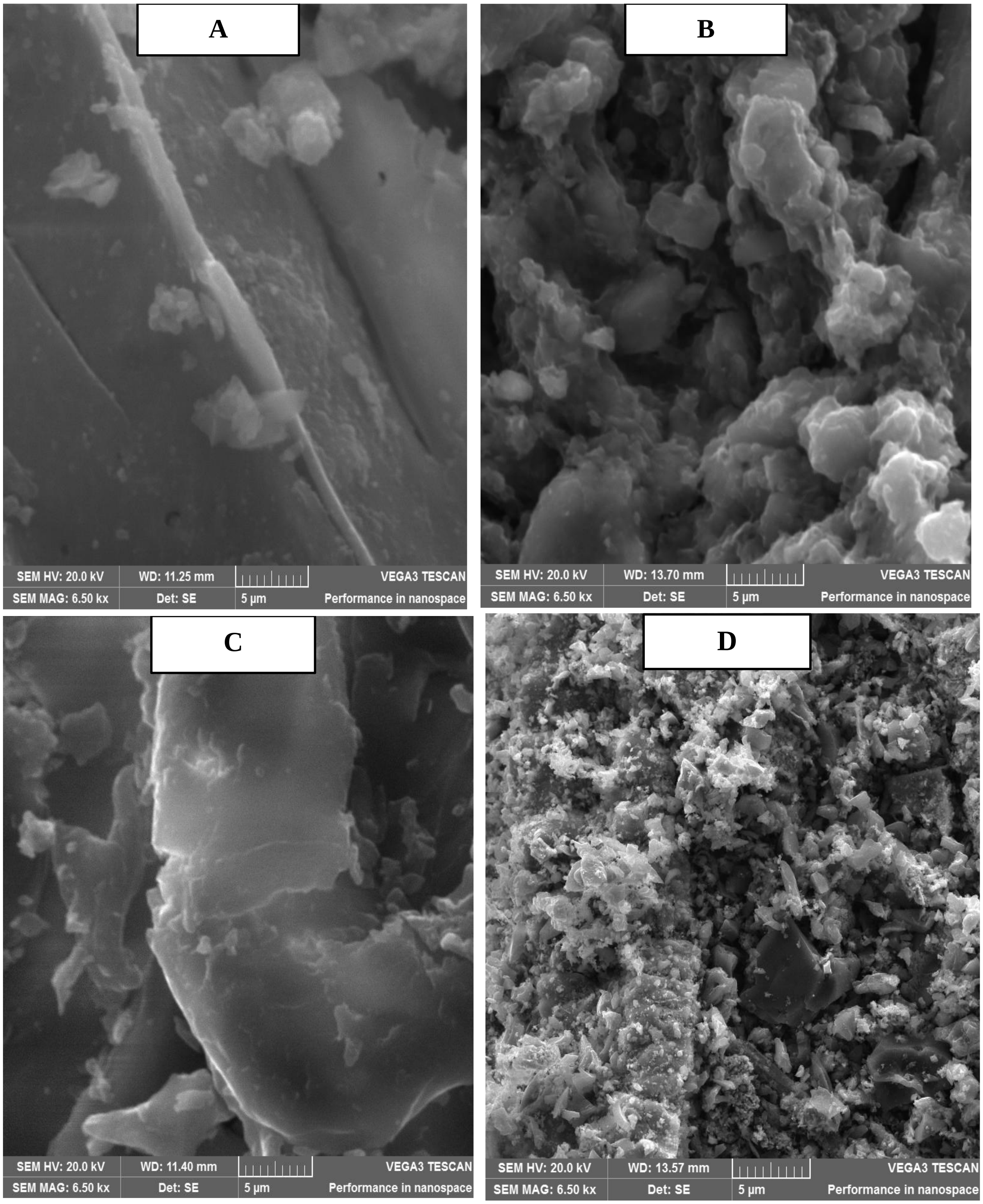

Figure 4.9: The SEM images for RCH (A), CHB (B), RMN (C) and MNB (D)

The SEM results (Figure 4.9) showed changes in the surface texture and morphology of the biochar samples after pyrolysis. The raw biomass surface structure was rigid, regular and less porous (Figure 4.9 A and C). After pyrolysis, the biochar surfaces became rugged and more porous (Figure 4.9 B and D). This is due to the rapid decomposition of volatile components during pyrolysis (Sahoo *et al.,* 2020). This made the biochar surface develop micro pores and cracks making it rough and irregular (Eshun *et al.,* 2019).

This porosity of the biochar carbon structure increased its surface area which could enhance its usability during the Si_3N_4 synthesis. Jagdale *et al.* (2019) reported similar findings on pyrolysis of ground coffee to produce biochar materials as humidity sensors.

4.4.5 The EDX characterization

The EDX analysis of RCH, RMN, CHB and MNB was done to determine their elemental compositions. The results are represented by Figures 4.10 A, B, C and D.

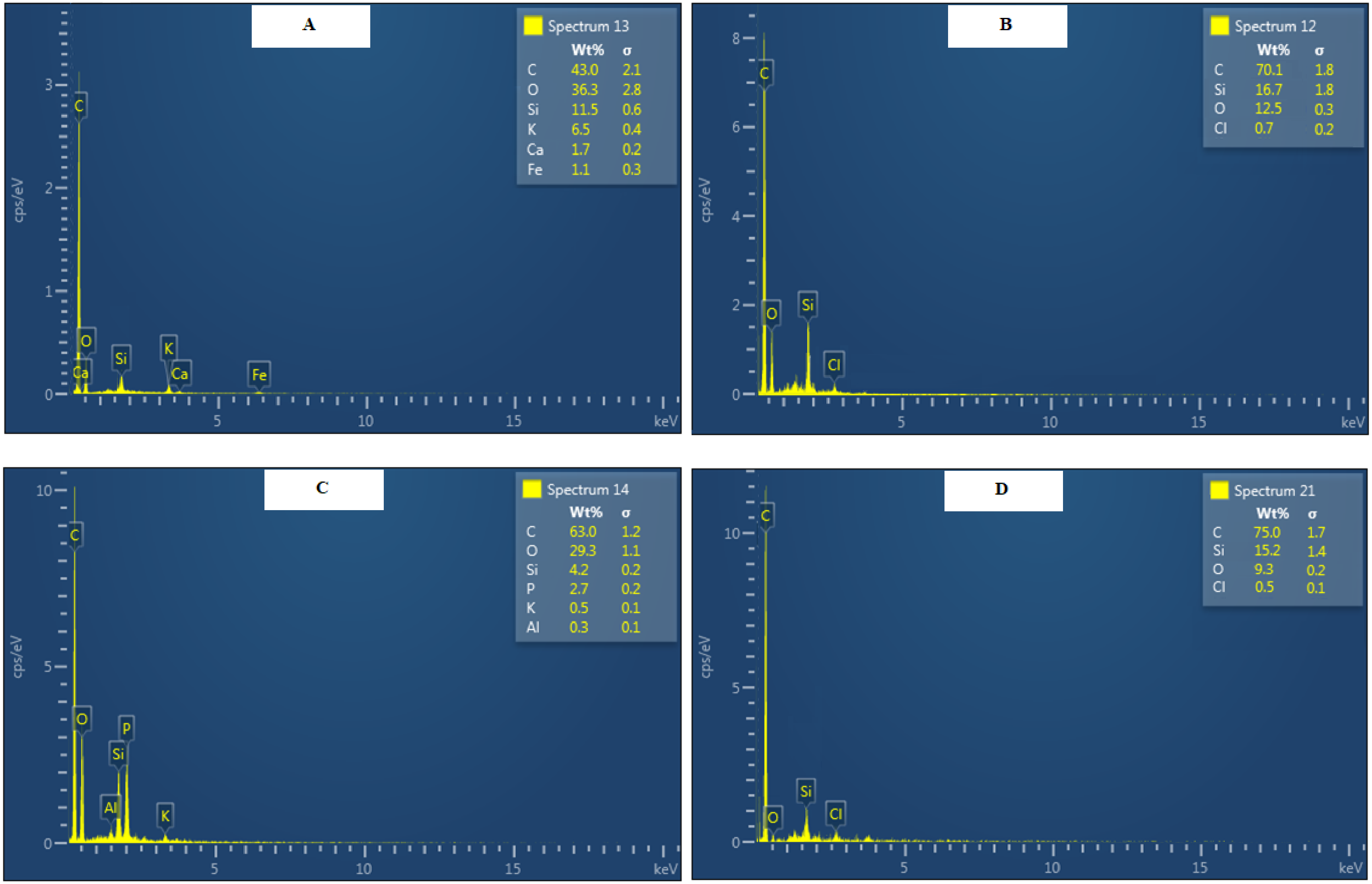

Spectrum 13

	Wt%	σ
C	43.0	2.1
O	36.3	2.8
Si	11.5	0.6
K	6.5	0.4
Ca	1.7	0.2
Fe	1.1	0.3

Spectrum 12

	Wt%	σ
C	70.1	1.8
Si	16.7	1.8
O	12.5	0.3
Cl	0.7	0.2

Spectrum 14

	Wt%	σ
C	63.0	1.2
O	29.3	1.1
Si	4.2	0.2
P	2.7	0.2
K	0.5	0.1
Al	0.3	0.1

Spectrum 21

	Wt%	σ
C	75.0	1.7
Si	15.2	1.4
O	9.3	0.2
Cl	0.5	0.1

Figure 4.10: The EDX spectra of RCH (A), CHB (B), RMN (C) and MNB (D)

From the EDX results in Figure 4.10 A and C, the main elemental composition of RCH and RMN was carbon (43.0 % and 63.0 %), oxygen (36.3 % and 29.3 %) and silicon (11.5 % and 4.2 %) respectively. This showed the presence of carbon (C) and silica (SiO_2) as the main constituents of raw biomass materials. The elemental oxygen could also be as attributed to surface oxides of metallic elements.

The elemental composition of CHB and MNB (Figure 4.10 B and D) was 70.1 % (C), 16.7 % (Si), 12.5 % (O) and 0.7 % (Cl); 75.0 % (C), 15.2 % (Si), 9.3 % (O) and 0.5 % (Cl) respectively. The final biochar showed a higher carbon and silica content with negligible ash contents than their respective raw biomass materials. This showed that pyrolytic treatment followed by acid washing not only decreased the inorganic ash contents from the biochar (Chang *et al.*, 2019) but also increased the carbon content. The chloride contents were detected in the biochar materials. This could be due to residue acid after the materials were washed with distilled water (Abdulhameed *et al.,* 2018).

The EDX results for CHB and MNB materials showed that carbon (C) and silica (SiO_2) dominated the biochar materials. Similar conclusions were made by Tsai *et al.* (2021) on their research studies on the biochar preparation from rice husk. The amorphous and porous carbon structure of the biochar materials with a high silica and carbon contents and negligible ash make the CHB and MNB suitable as carbon and silica precursor materials for the Si_3N_4 adsorbent synthesis.

4.5 Characterization of Si_3N_4 adsorbents

The Si_3N_4 adsorbents were prepared (sub-section 3.6.4) and characterized using XRD, FT-IR, SEM, EDX and TGA. The outcomes are discussed in the subsequent sub-sections.

4.5.1 The FT-IR characterization

The FT-IR analysis of Si_3N_4 adsorbents were recorded at 4000 - 400 cm^{-1} and the findings are presented in Figures 4.11 I and II.

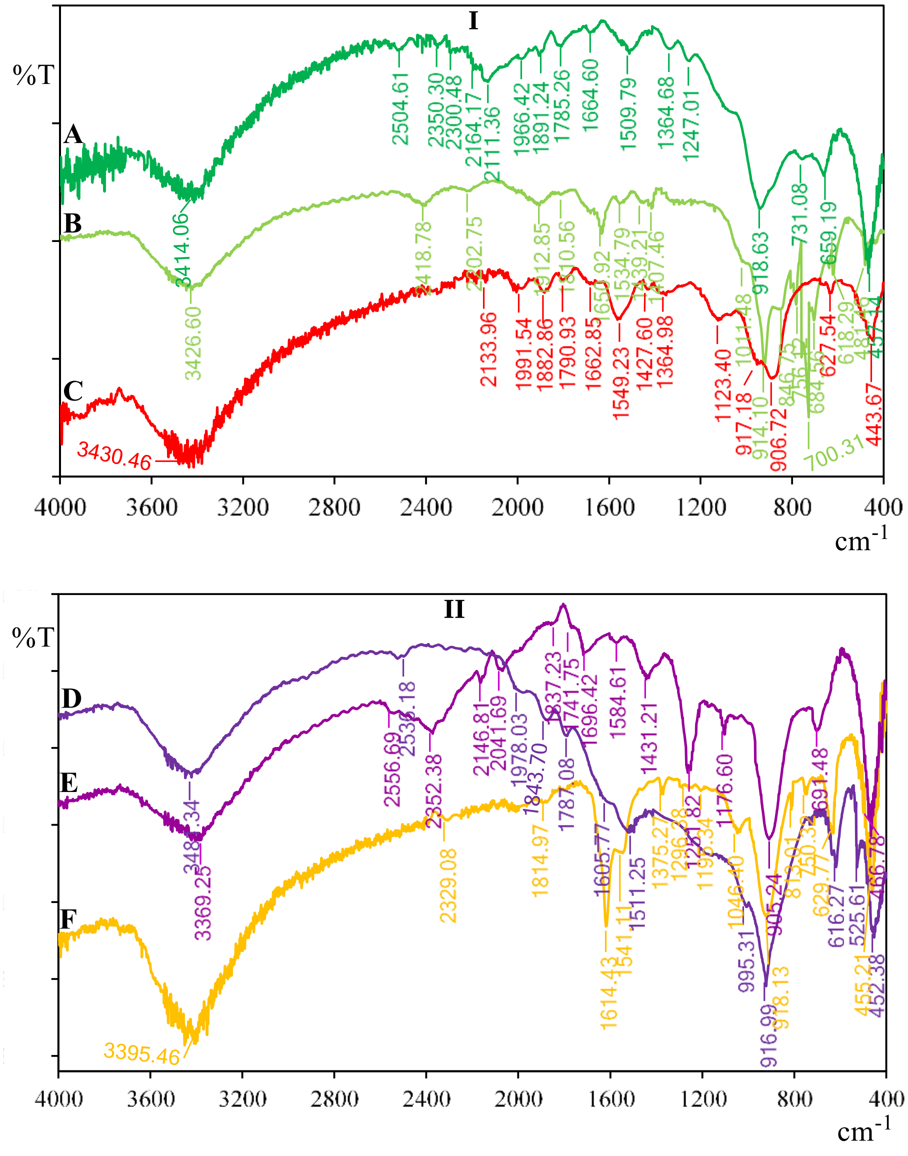

Figure 4.11: The FT-IR spectrum of SN-1 (A), SN-2 (B), SN-3 (C), SN-4 (D), SN-5 (E) and SN-6 (F) adsorbents

The FT-IR spectra of the Si_3N_4 adsorbents (Figure 4.11) showed broad peaks at 3414.06 cm^{-1} (SN-1), 3426.60 cm^{-1} (SN-2), 3430.46 cm^{-1} (SN-3), 3481.34 cm^{-1} (SN-4), 3369.25

cm^{-1} (SN-5) and 3395.46 cm^{-1} (SN-6) ascribed to stretch modes of hydroxyl (OH^-) in silanol (Si-OH) and amine ($-NH_2$) in silazane ($Si_2=NH$) groups on the hydroxylated adsorbent surface (Kobayashi, 2016; Kuddus *et al.*, 2019). This was confirmed by their OH^- and N-H bend modes at 1664.60 cm^{-1} and 1509.79 cm^{-1} (SN-1), 1650.92 cm^{-1} and 1534.79 cm^{-1} (SN-2), 1662.85 cm^{-1} and 1549.23 cm^{-1} (SN-3), 1605.77 cm^{-1} and 1511.25 cm^{-1} (SN-4), 1696.42 cm^{-1} and 1584.61 cm^{-1} (SN-5) and 1614.43 cm^{-1} and 1541.11 cm^{-1} (SN-6) respectively.

The peaks at 1123.40 cm^{-1} (SN-3), 1176.60 cm^{-1} (SN-5) and 1195.34 (SN-6) could be due to Si-O-C stretch vibrations modes (Liang *et al.*, 2020). Predominant peaks at 1011.48 cm^{-1} and 700.31 cm^{-1} (SN-2); 1046.40 cm^{-1} and 750.32 cm^{-1} (SN-6) are indicative of siloxane (Si-O-Si) bonds in the silica residues (Andriayani *et al.*, 2021). The absorbance at 918.63 cm^{-1} (SN-1), 914.10 cm^{-1} (SN-2), 906.72 cm^{-1} (SN-3), 916.99 cm^{-1} (SN-4), 905.24 cm^{-1} (SN-5) and 918.13 cm^{-1} (SN-6) were ascribed to the Si-N-Si stretch modes (Jhansirani *et al.*, 2016). The stretch bands at 846.75 cm^{-1} (SN-2) and 813.01 cm^{-1} (SN-6) could be due to Si-C bonds of silicon carbide residues (Rajarao and Veena, 2016). The peaks at 659.19 cm^{-1} (SN-1), 618.29 cm^{-1} (SN-2), 627.54 cm^{-1} (SN-3), 616.27 cm^{-1} (SN-4), 691.48 cm^{-1} (SN-5) and 629.77 cm^{-1} (SN-6) may ascribe to Si-Si stretch modes (Cui *et al.*, 2015). The absorbance at 457.14 cm^{-1} (SN-1), 481.46 cm^{-1} (SN-2), 443.67 cm^{-1} (SN-3), 452.38 cm^{-1} (SN-4), 466.78 cm^{-1} (SN-5) and 455.21 cm^{-1} (SN-6) are ascribed to Si-N stretch modes (Abdulhameed *et al.*, 2018).

The findings of the study revealed silicon-nitrogen (Si-N), silanol (Si-OH) and silicon-nitrogen-silicon (Si-N-Si) functional groups which when hydroxylated in water give silanolate ($Si\text{-}O^-$) and silazane groups ($Si_2=NH_2^+$) as important adsorption sites for MO, MB and CR dyes sorption. The finding corroborates those reported by Shi *et al.* (2014) during their studies on silicon nitride fiber-PMMA composite fabrication.

4.5.2 The XRD characterization

The Si_3N_4 adsorbents were characterized using the XRD for phase analysis. The XRD spectra obtained are presented in Figures 4.12 I and II.

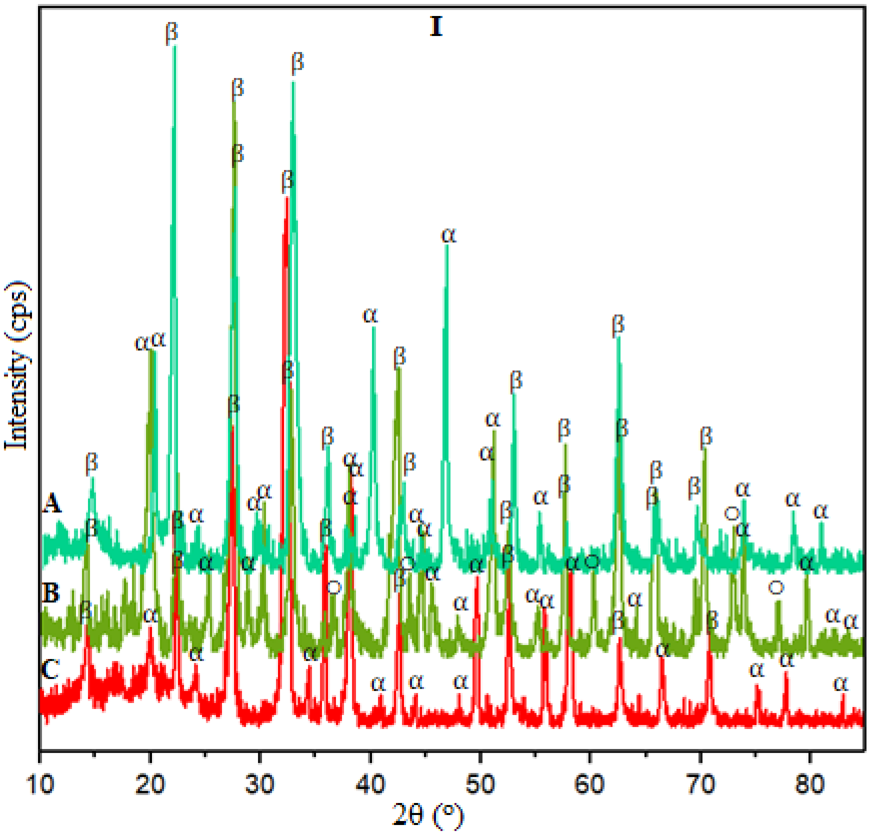

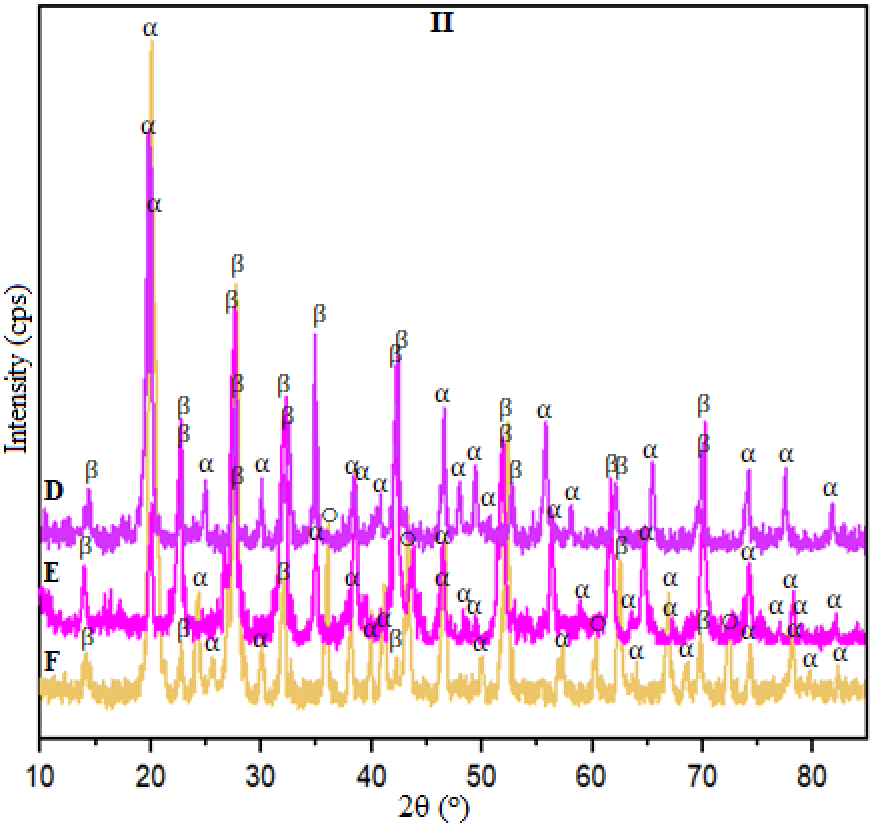

α- Si_3N_4, β- Si_3N_4, ○- SiC

Figure 4.12: The XRD spectrum of SN-1 (A), SN-2 (B), SN-3 (C), SN-4 (D), SN-5 (E) and SN-6 (F) adsorbents

The XRD diffractograms (Figure 4.12) showed that Si_3N_4 was the main phase in all the adsorbents dominated by α-Si_3N_4 as a major phase (JCPDS-ICDD file No. 41-0360) and β- Si_3N_4 (JCPDS-ICDD file No. 33-1160) as a minor phase. The profile Rietveld analysis showed the relative amount of α-Si_3N_4 and β-Si_3N_4 phases in the Si_3N_4 adsorbent as 65.38 % and 34.62 % (SN-1), 50.61 % and 33.25 % (SN-2), 68.97 % and 31.03 % (SN-3), 70.37 % and 29.63 % (SN-4), 54.94 % and 45.06 % (SN-5) and 53.67 % and 34.15 % (SN-6) respectively. The high yield content of α-Si_3N_4 phase could be due to the use of high pure amorphous raw materials for carbothermal reduction and nitridation at low temperatures (Ji *et al.*, 2014).

The silicon carbide (SiC) apparent phase was observed in SN-2 (16.14 %) and SN-6 (12.18 %) dominated by β-SiC (JCPDS-ICDD file No. 75-0254). This could be due to unreacted SiC residues during carbothermal reduction-nitridation process (Vishnu *et al.*, 2018). The broad peak patterns with a high noise level in all the XRD spectra signified that the Si_3N_4 adsorbent was predominantly amorphous (Biesuz *et al.*, 2019).

The findings showed α-Si_3N_4 as the dominant phase in all the XRD patterns which is more favored during the Si_3N_4 adsorbent synthesis at low temperatures. This agrees with the studies reported by Qadri *et al.* (2016) on the silicon nitride synthesis from wheat and rice husks.

4.5.3 The SEM characterization

The SEM images for Si_3N_4 adsorbents were obtained at 20.0 kV (voltage) and 6.50 K X (magnification). The results are as shown in Figures 4.13 A, 4.13 B, 4.13 C, 4.13 D, 4.13 E and 4.13 F.

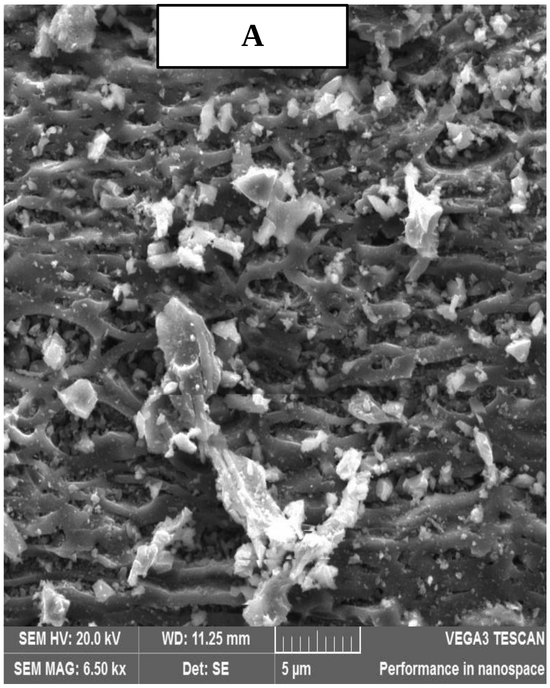
A
SEM HV: 20.0 kV
WD: 11.25 mm
VEGA3 TESCAN
SEM MAG: 6.50 kx
Det: SE
5 μm
Performance in nanospace

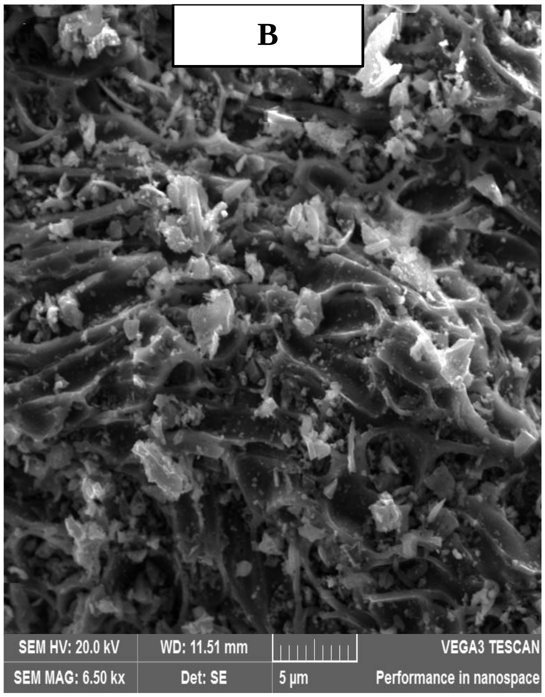
B
SEM HV: 20.0 kV
WD: 11.51 mm
VEGA3 TESCAN
SEM MAG: 6.50 kx
Det: SE
5 μm
Performance in nanospace

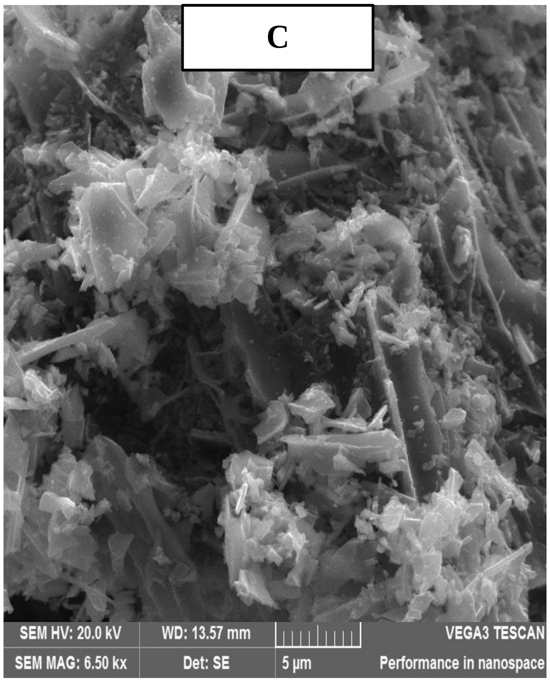
C
SEM HV: 20.0 kV
WD: 13.57 mm
VEGA3 TESCAN
SEM MAG: 6.50 kx
Det: SE
5 μm
Performance in nanospace

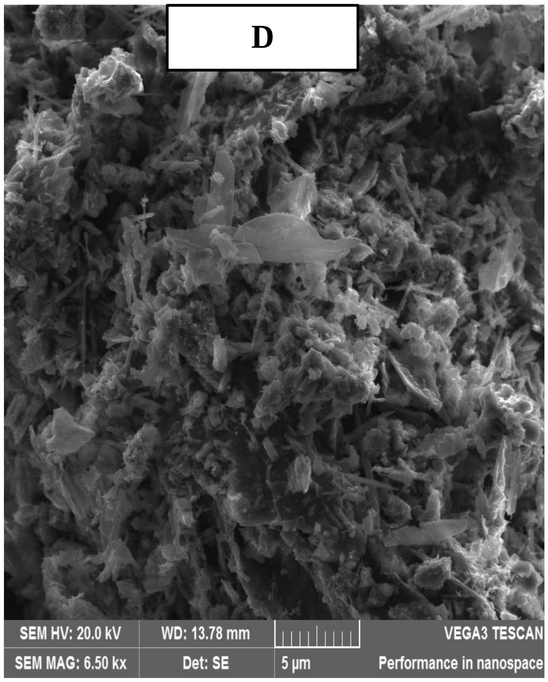
D
SEM HV: 20.0 kV
WD: 13.78 mm
VEGA3 TESCAN
SEM MAG: 6.50 kx
Det: SE
5 μm
Performance in nanospace

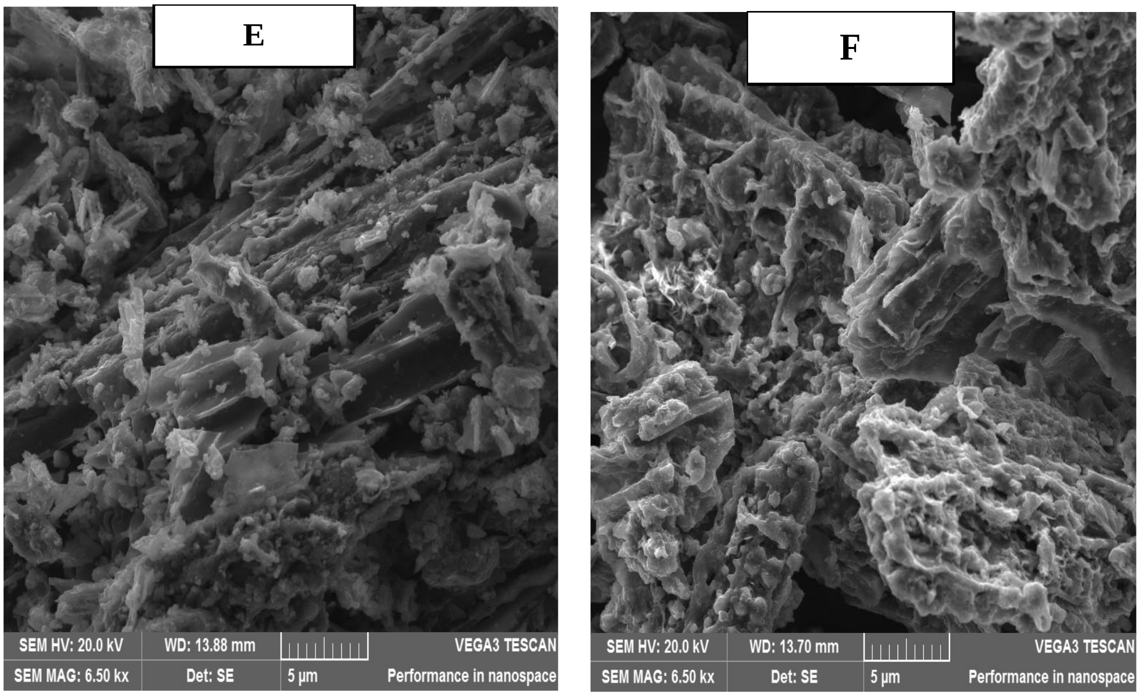

Figure 4.13: The SEM images for SN-1 (A), SN-2 (B), SN-3 (C), SN-4 (D), SN-5 (E) and SN-6 (F) adsorbents

The results in Figure 4.13 showed fiber-like and rod-like micrographs attributed to β-Si_3N_4 and α-Si_3N_4 structures respectively (Ji *et al.*, 2014; Mahmut *et al.*, 2020). As evidenced, there is presence of some crevices and pores on the Si_3N_4 adsorbent surfaces. The results showed the porous nature of the Si_3N_4 adsorbent materials which could increase surface area for the uptake of MB, CR and MO dyes. Similar results are reported by Tao *et al.* (2016) during their study on silicon nitride synthesis from rice husk.

The SN-3 micrographs before and after CR dyes uptake is shown in Figure 4.14 A and 4.14 B.

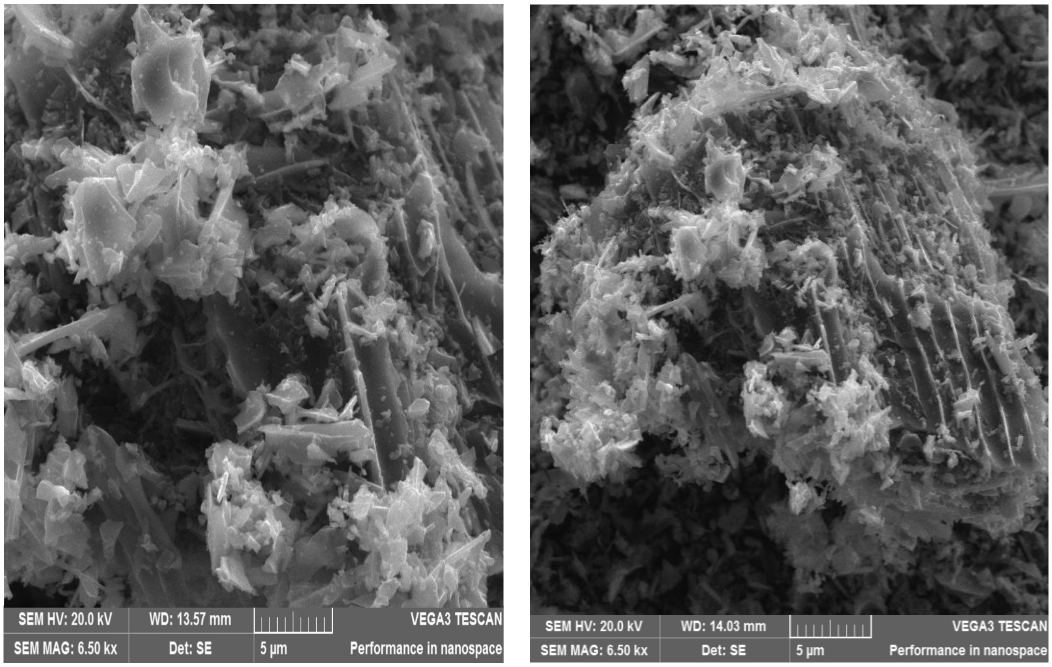

Before adsorption
(A)

After adsorption
(B)

Figure 4.14: The SEM micrographs of SN-3 before (A) and after (B) CR dyes adsorption

The results in Figure 4.14 before and after CR dyes uptake showed significant changes on the SN-3 adsorbent surface. Before sorption (A), the adsorbent surface showed pores of varying sizes and shapes. The CR-loaded adsorbent surface (B) is restrained and less porous caused by the Si_3N_4 adsorbent pores occupied by dye molecules. Similar findings were reported by Litefti *et al.* (2019) on their congo red sorption studies onto pine bark adsorbent.

4.5.4 The EDX characterization

The Si_3N_4 adsorbents elemental constitution was determined and the results are as shown by the Figures 4.15 A, B, C, D, E and F.

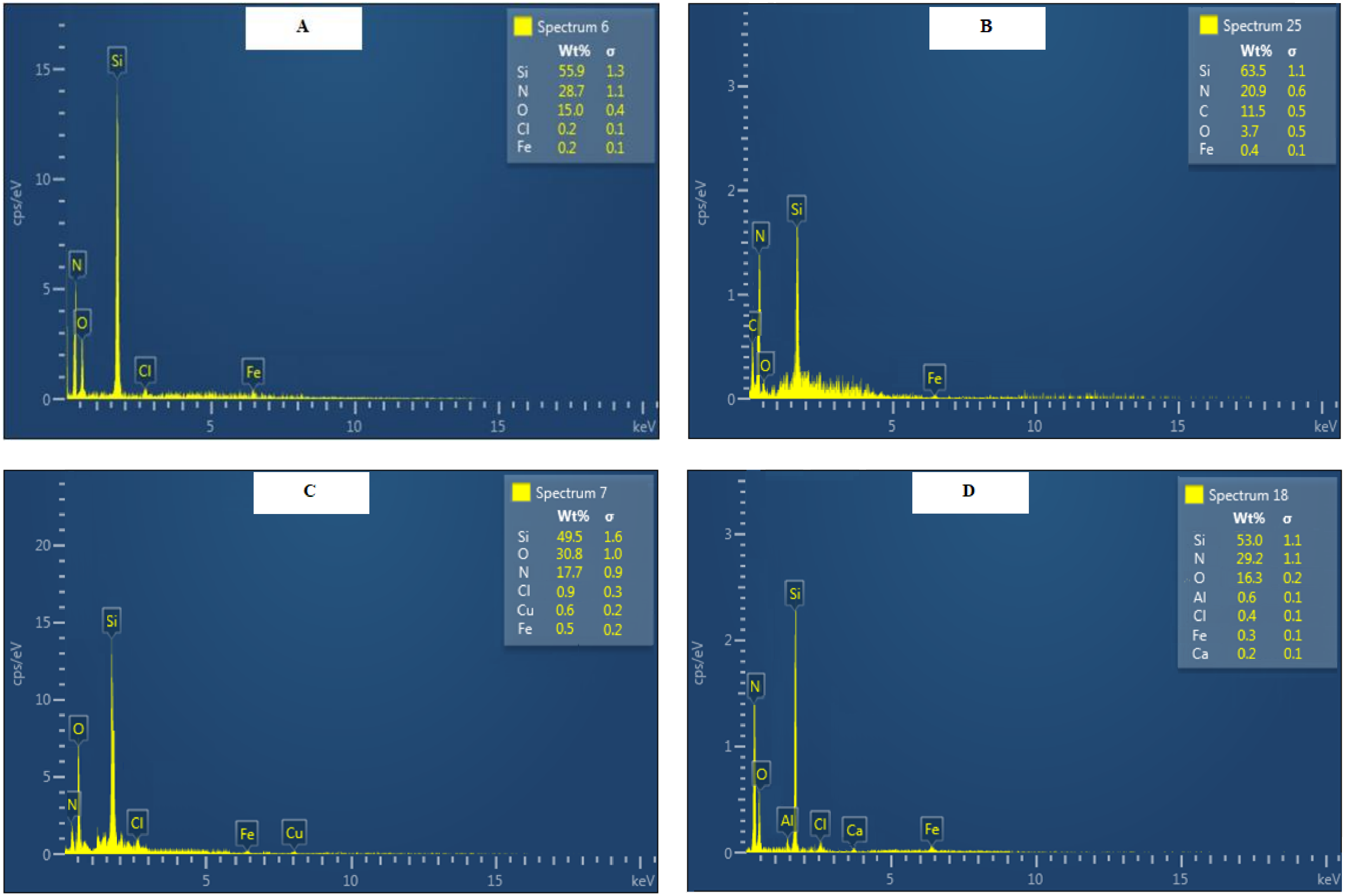
A
Spectrum 6
Wt% σ
Si 55.9 1.3
N 28.7 1.1
O 15.0 0.4
Cl 0.2 0.1
Fe 0.2 0.1
cps/eV
0
5
10
15
keV
Si
N
O
Cl
Fe
B
Spectrum 25
Wt% σ
Si 63.5 1.1
N 20.9 0.6
C 11.5 0.5
O 3.7 0.5
Fe 0.4 0.1
cps/eV
0
1
2
3
5
10
15
keV
Si
N
C
O
Fe
C
Spectrum 7
Wt% σ
Si 49.5 1.6
O 30.8 1.0
N 17.7 0.9
Cl 0.9 0.3
Cu 0.6 0.2
Fe 0.5 0.2
cps/eV
0
5
10
15
20
keV
Si
O
N
Cl
Fe
Cu
D
Spectrum 18
Wt% σ
Si 53.0 1.1
N 29.2 1.1
O 16.3 0.2
Al 0.6 0.1
Cl 0.4 0.1
Fe 0.3 0.1
Ca 0.2 0.1
cps/eV
0
1
2
3
5
10
15
keV
Si
N
O
Al
Cl
Ca
Fe

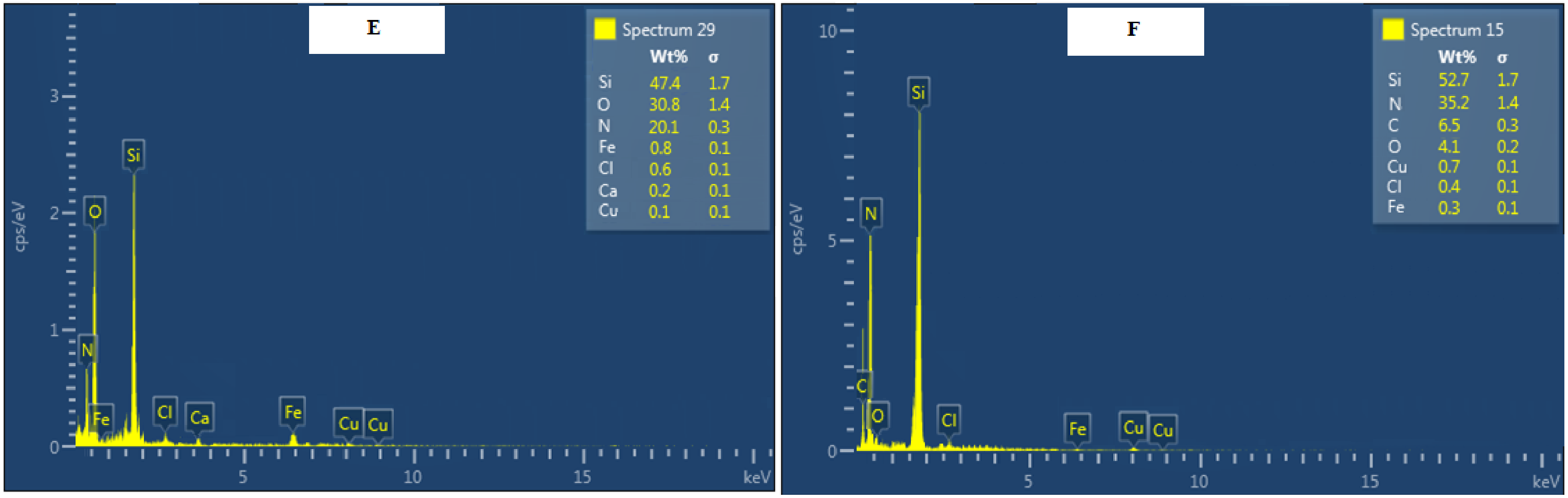

Spectrum 29

	Wt%	σ
Si	47.4	1.7
O	30.8	1.4
N	20.1	0.3
Fe	0.8	0.1
Cl	0.6	0.1
Ca	0.2	0.1
Cu	0.1	0.1

Spectrum 15

	Wt%	σ
Si	52.7	1.7
N	35.2	1.4
C	6.5	0.3
O	4.1	0.2
Cu	0.7	0.1
Cl	0.4	0.1
Fe	0.3	0.1

Figure 4.15: The EDX spectra of SN-1 (A), SN-2 (B), SN-3 (C), SN-4 (D), SN-5 (E) and SN-6 (F) adsorbents

From the results in Figure 4.15, the elemental composition of Si_3N_4 adsorbents was 55.9 % and 28.7 % (SN-1), 63.5 % and 20.9 % (SN-2), 49.5 % and 17.7 % (SN-3), 53.0 % and 29.2 % (SN-4), 47.4 % and 20.1 % (SN-5), 52.7 % and 35.2 % (SN-6) for silicon and nitrogen respectively. The SN-2 and SN-6 adsorbents are characterized by an elemental carbon peak at around 0.21 keV and 0.20 keV respectively which is absent in other adsorbents. This showed the presence of unreacted silicon carbide residues in the adsorbents (Vishnu *et al.*, 2018) and/or contamination from the carbon tapes used to mount the samples (Qadri *et al.*, 2016).

Minor peaks for copper and aluminium could be due to contamination from the copper grid sample holder and corundum tube during the firing process and/or ball milling (Huang *et al.*, 2013). The oxygen content could be due to some silica residues and minor metal oxide components (Abdulhameed *et al.,* 2018) and/or adsorbent surface oxidation during the analysis forming a thin silicon oxynitride layer (Meziani *et al.*, 2016). The chloride contents detected in the Si_3N_4 adsorbents could be due to residue HCl acid (Alpay, 2014) from the biochar samples used for the synthesis of Si_3N_4 adsorbents.

The findings showed silicon, nitrogen and oxygen elements as the main constituents of Si_3N_4 adsorbents. The minor residues of silica, silicon carbide and metal oxide components can be suggested to be present in the adsorbents. This corroborates studies reported by Vishnu *et al.* (2018) on preparation of silicon carbide and its nitridation action.

4.5.5 The TGA characterization

The thermogravimetric analysis of Si_3N_4 adsorbents were obtained at a varied temperature of 0 °C to 600 °C. The TG curves are presented by Figure 4.16.

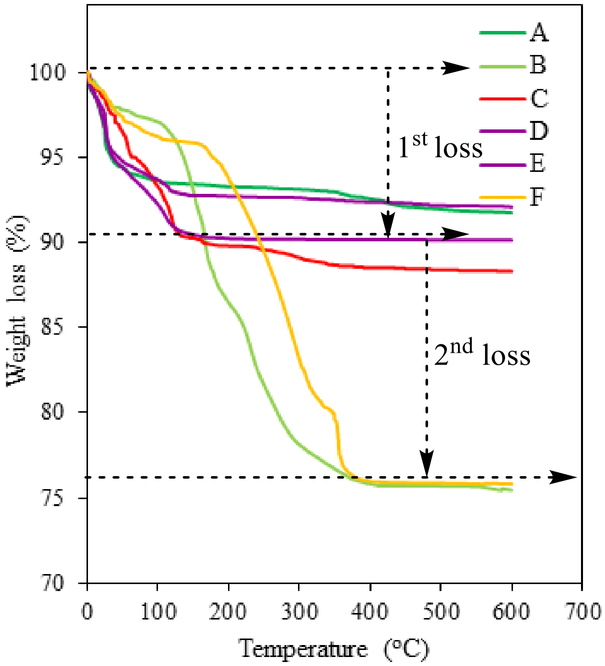

Figure 4.16: The TG curve for SN-1 (A), SN-2 (B), SN-3 (C), SN-4 (D), SN-5 (E) and SN-6 (F) adsorbents

From the results in Figure 4.16, the thermogravimetric analysis (TGA) curves for SN-1, SN-3, SN-4 and SN-5 represents two weight change steps. At the first step from 0 °C to around 150 °C, the weight loss was 6.32 %, 9.63 %, 9.71 % and 7.24 % respectively beyond which no any thermal effect is recorded as the constant weight change is obtained. This could be to the vaporization of adsorbed water (H_2O) molecules onto the adsorbent surfaces after which the adsorbent remains stable (Qiu *et al.*, 2019).

The thermal analysis of SN-2 and SN-6 adsorbents depicted a representative three-stage weight loss profile. A slight weight loss below 200 °C is 3.53 % and 4.74 % respectively attributed to the loss of some adsorbed water (Zhang *et al.*, 2019). The sample degradation then continued to about 450 °C with a maximum weight loss of 18.40 % and 19.18 %. This could be due to depolymerization of silicon carbide residues in the adsorbents (Tishchenko *et al.,* 2015; Kumar *et al.,* 2020). The mass profile was then flat until 600 ^oC. This makes the Si_3N_4 adsorbent thermally stable even at high temperatures and therefore suitable in textile dye wastewater treatment.

The results showed that Si_3N_4 adsorbents are thermally stable at varied temperatures. This is in agreement with findings reported by Sun and Xiao (2017) on their studies on the thermal stability of silicone oil/polystyrene microcapsules.

The characterization of Si_3N_4 adsorbents showed thermally stable and porous adsorbents with α-Si_3N_4, β- Si_3N_4 and β-SiC phases. The FT-IR findings showed silicon-nitrogen (Si-N), silicon-nitrogen-silicon (Si-N-Si) and silanol (Si-OH) functional groups which could be important sites for MO, MB and CR dyes adsorption when hydroxylated in water to silanolate ($Si\text{-}O^-$) and positively charged silazane groups ($Si_2{=}NH_2^+$).

4.6 Batch optimization studies

The impact of dosage, agitation time, pH and concentration on CR, MB and MO dyes uptake were investigated. The outcomes are discussed in sub-section 4.6.1, 4.6.2, 4.6.3 and 4.6.4.

4.6.1 The pH_{pzc} studies and effect of pH on sorption of MO, MB and CR dyes

To study the pH influence on dyes uptake using Si_3N_4 adsorbents, the studies on point of zero charge (pH_{pzc}) were first done as described in sub-section 3.9.1.1. The findings are presented by Figure 4.17.

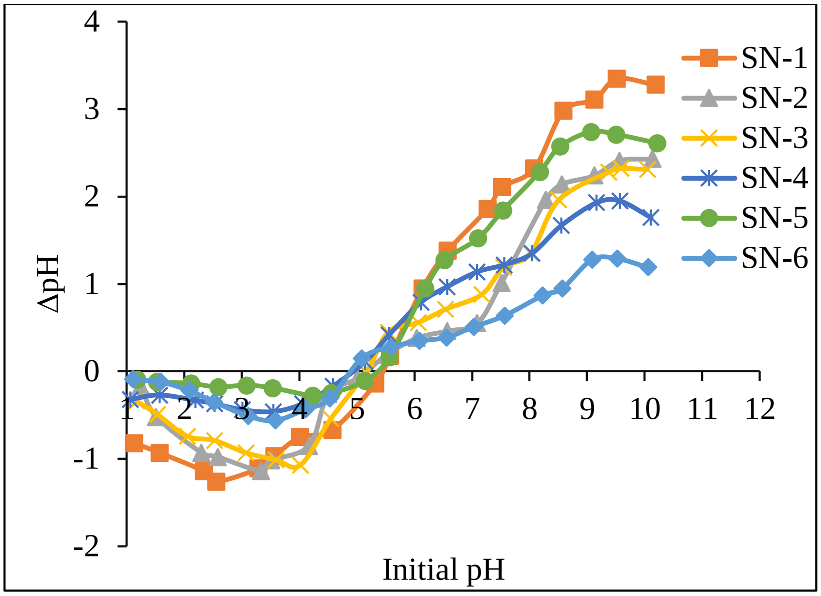

Figure 4.17: Point of zero charge (pH_{pzc})

From the Figure 4.17 above, it is noted that pH_{pzc} values of Si_3N_4 adsorbent are 5.40 (SN-1 and SN-5), 5.20 (SN-2), 4.80 (SN-4 and SN-6) and 5.10 (SN-3). This shows that the net Si_3N_4 adsorbent surface is positive at $pH \leq 5.40$ and negatively charged at $pH \geq 5.40$. This implies that, the uptake of cationic dyes is high at $pH \geq pH_{pzc}$ and that of anionic dyes dominates at $pH \leq pH_{pzc}$ (Gollakota *et al.*, 2021).

The correlation between pH and pH_{pzc} was investigated on sorption of MB, MO and CR dyes onto the Si_3N_4 adsorbents. The results of pH effect on the mean uptake of the dyes are represented in Figures 4.18 A, B and C.

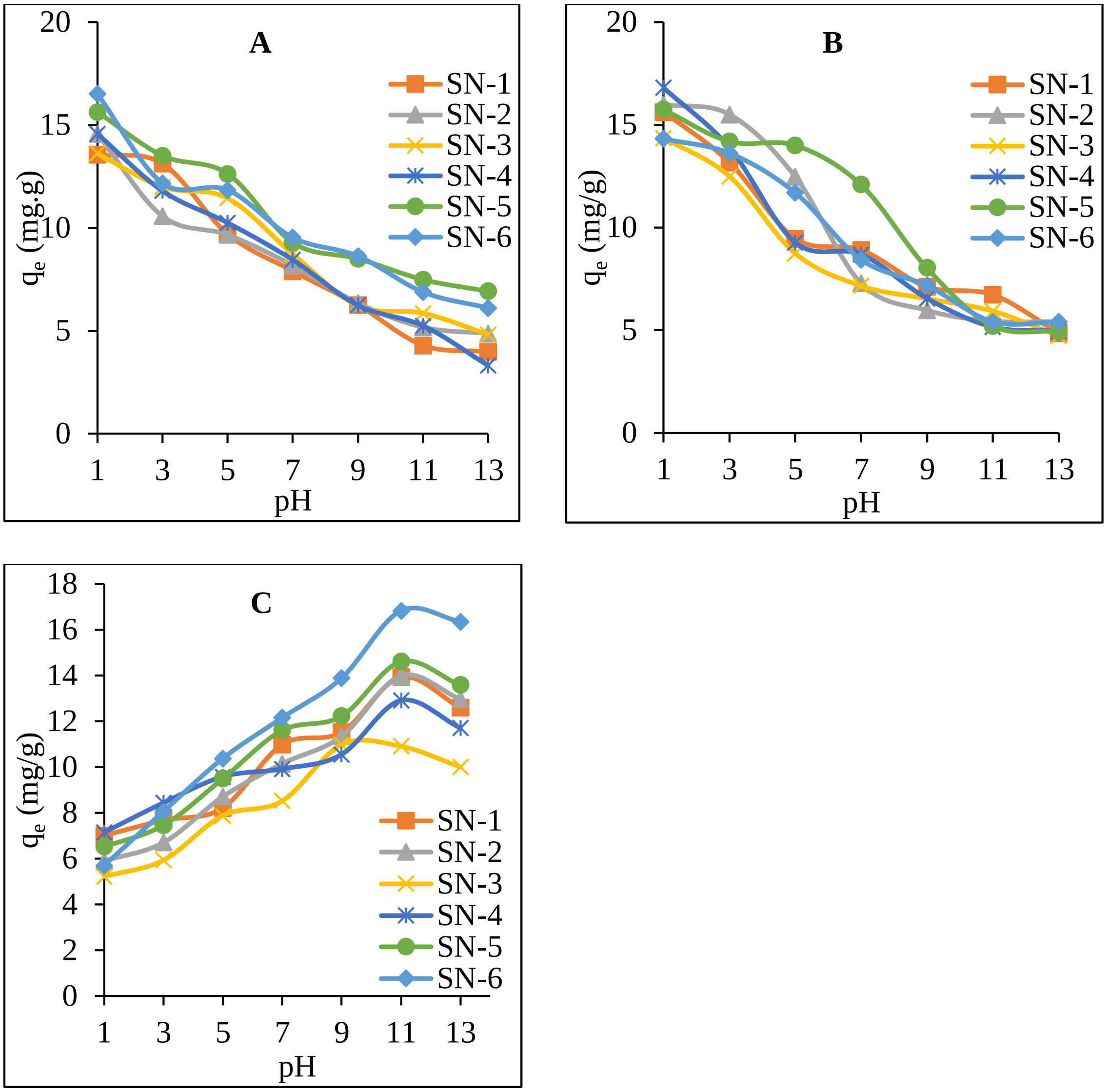

Figure 4.18: Effect of pH on MO (A), CR (B) and MB (C) dyes removal onto Si_3N_4 adsorbents: 20 mg/L; 60 minutes; 20 mg; 298 K; 150 rpm

From the results in Figures 4.18 above, the optimal pH for sorption of MO and CR dyes is pH=1.00 for all the adsorbents. This means that the sorption of MO and CR dyes is best in strongly acidic media. The maximum uptake for MO dyes (Figure 4.18 A) was 13.57 ± 0.06 mg/g (SN-1), 14.55 ± 0.03 mg/g (SN-2), 13.63 ± 0.04 mg/g (SN-3), 14.58 ± 0.01 mg/g (SN-4), 15.64 ± 0.14 mg/g (SN-5) and 16.52 ± 0.05 mg/g (SN-6). The removal of CR dyes at optimum pH (Figure 4.18 B) was 15.70 ± 0.05 mg/g (SN-1), 15.99 ± 0.13

mg/g (SN-2), 14.37 ± 0.08 mg/g (SN-3), 16.81 ± 0.05 mg/g (SN-4), 15.75 ± 0.07 mg/g (SN-5) and 14.33 ± 0.03 mg/g (SN-6). This is as construed in appendices III A and III C. This followed a decrease in dyes uptake with increased in dye solution pH. The number of positive charges onto the surface of the adsorbent were enhanced greatly in strongly acidic solution which favored the dyes uptake (Khaniabadi *et al.*, 2017). At a pH 1.00 ≤ pH_{pzc} 5.40, the H^+ ions in the solution is raised. This initiates the electrostatic repulsions between H^+ ions in the dye solution and the positively charged silazane groups ($Si_2=NH_2^+$) of Si_3N_4 adsorbents. The H^+ ions get complexed by the silanolate groups ($Si-O^-$) and are neutralized (Adamu *et al.*, 2017). This increases the affinity of silazane active sites for MO and CR dye uptake. The adsorption mechanism is that the sulfonate group in the molecular structure of MO and CR dyes ($R-SO_3Na$) first dissociates in aqueous solution to active negatively charged sulfonate groups ($-SO_3^-$) as shown in Equation 4.1 (Subbaiah and Kim, 2016).

$$\text{Dye-SO}_3\text{Na} \xrightarrow{H_2O} \text{Dye-SO}_3^- + \text{Na}^+ \tag{4.1}$$

There are significant electrostatic forces between the $Si_2=NH_2^+$ and the sulphonate groups ($-SO_3^-$) of the MO and CR dye molecules and this leads to maximum adsorption as shown in Equation 4.2.

$$\text{Si}_2\text{=NH}_2^+ + \text{Dye-SO}_3^- \longrightarrow \text{Si}_2\text{=NH}_2\text{-O}_3\text{S-Dye} \tag{4.2}$$

At pH levels ≥ pH_{pzc} 5.40, the dye solution becomes more alkaline as a result of excess OH^- ions causing its competition with the $-SO_3^-$ ions for silazane binding sites. This consequently weakens its adsorption effect (Munagapati and Kim, 2016). The results compare with findings reported by Bellifa *et al.* (2017) and Hachani *et al.* (2017) during their adsorption studies on MO and CR dyes onto bentonite and raw date pits adsorbents respectively.

The uptake of MB dyes (Figure 4.18 C) was 10.97 ± 0.03 mg/g for SN-3 at optimal pH=10.00. On using other adsorbents, the uptake was 13.93 ± 0.09 mg/g (SN-1), 13.99 ± 0.06 mg/g (SN-2), 12.91 ± 0.03 mg/g (SN-4), 14.62 ± 0.01 mg/g (SN-5) and 16.82 ± 0.05 mg/g for (SN-6) at optimal value (pH=11.00). This is as shown in appendix III B. Lower adsorption at lower initial pH ($\leq pH_{pzc}$ 5.40) was because of excess H^+ ions which competed with cationic MB dye molecules for silanolate adsorbent sites. The silanolate functional groups becomes protonated making it to lose affinity for MB dyes uptake. However, at higher pH values ($\geq pH_{pzc}$ 5.40), there is an increased OH^- ions in the solution. This causes a repulsion between OH^- ions and the silanolate ($Si\text{-}O^-$) active sites favoring the sorption of MB molecules. The findings are in tandem with reports by Maingi *et al.* (2017), Islam *et al.* (2019) and Tahazadeh *et al*. (2021) on MB dye sorption using geopolymer, peanut shell and cellulose acetate (CA)-based nanocomposite adsorbents respectively. The pH of 1.00 (MO and CR) and 11.00 (MB) was chosen for subsequent experiments.

4.6.2 Effect of agitation time on sorption of MO, MB and CR dyes

The effect of agitation time on the MO, MB and CR dyes uptake was investigated at varied time intervals of 20 minutes at optimal pH conditions and other parameters (20 mg/L, 20 mg, 298 K and 150 rpm). The outcomes are presented in the Figures 4.19 A, B and C.

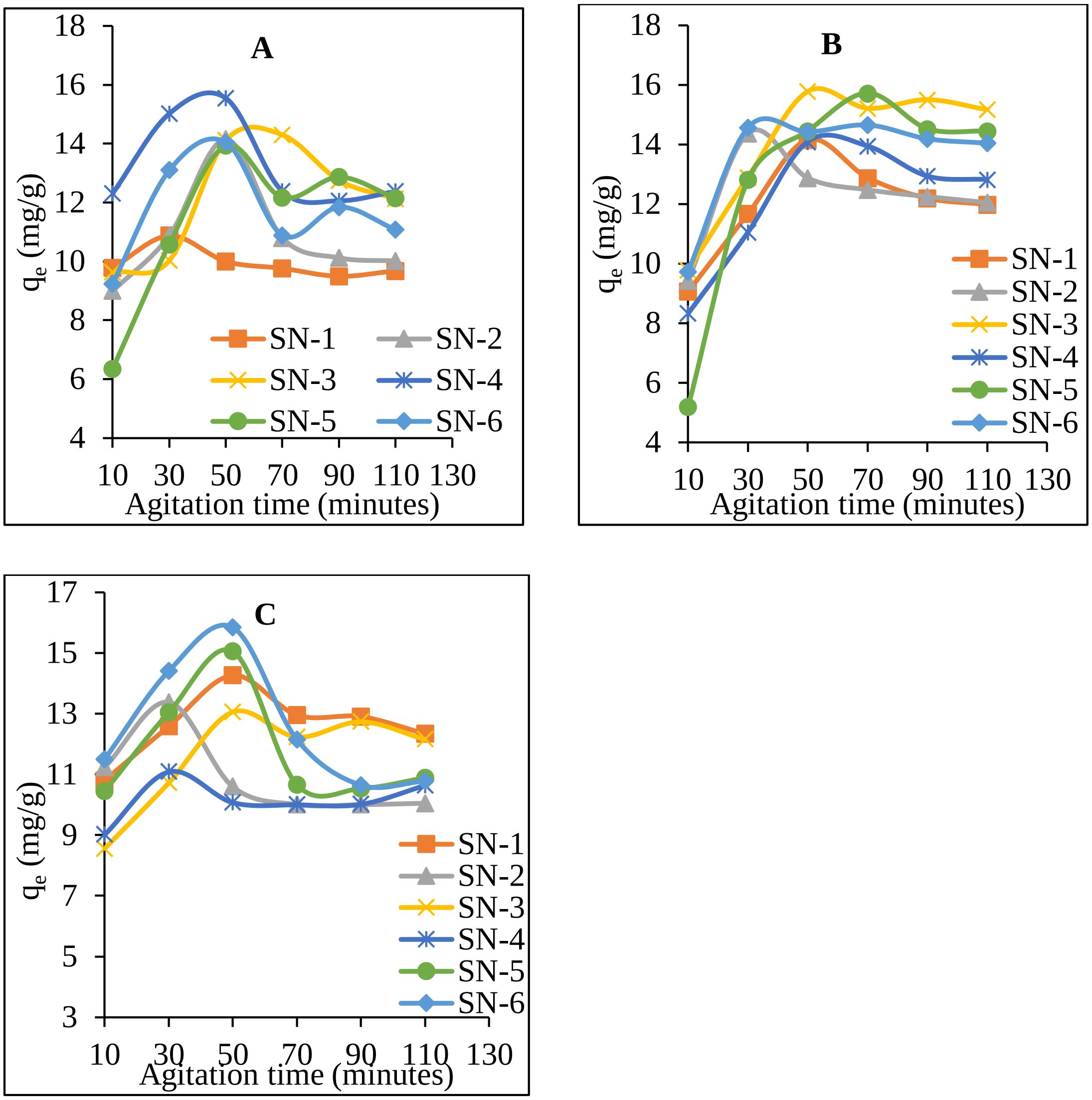

Figure 4.19: Effect of agitation time on MO (A), MB (B) and CR (C) dyes removal onto Si_3N_4 adsorbents: 20 mg/L; pH = 1.00 (MO and CR) and pH = 11.00 (MB); 20 mg; 298 K; 150 rpm

The results (Figure 4.19 A) indicate that the uptake of MO dyes was rapid within the first 30 minutes (SN-1) followed by 40 minutes (SN-4 and SN-6), 50 minutes (SN-2 and SN-5) and 60 minutes (SN-3) with maximum uptake ranging from 10.88 ± 0.02 mg/g to

15.55 ± 0.07 mg/g. The maximum sorption for MB dyes (Figure 4.19 B) ranged from 14.09 ± 0.04 mg/g to 15.78 ± 0.00 mg/g at optimal values of 30 minutes (SN-2), 50 minutes (SN-1, SN-3 and SN-4) and 70 minutes (SN-5 and SN-6). The optimal agitation time for CR dyes (Figure 4.19 C) sorption onto Si_3N_4 adsorbents was 30 minutes (SN-2 and SN-4) and 50 minutes for other adsorbents. The maximum uptake ranged from 11.09 ± 0.11 mg/g to 15.85 ± 0.06 mg/g. This is as shown appendices IV A, IV B and IV C.

The uptake of MO, CR and MB dyes increased with increasing agitation time to equilibrium beyond which no significant change was registered. The rapid dyes uptake at initial adsorption stages was due to the accessibility of vacant binding sites for maximum uptake (Song *et al.*, 2018). Subsequently, the dyes uptake decreased beyond the optimal agitation times as most of the binding sites are used up which do not allow for further dyes uptake to take place (Fadhil and Eisa, 2019; Maia *et al.,* 2021). These findings compare well with those reported by Abualnaja *et al.* (2021), Çatlıoğlu *et al.* (2021), Muniyandi and Govindaraj (2021) and Al-Salihi *et al.* (2022) during their removal studies of MO, MB and CR dyes using poly (Acrylonitrile-co-Styrene) nanocomposites, Fe-modified banana peel, palm shell activated carbon and γ-alumina nanoshell adsorbents. An agitation time of 50 minutes was selected for subsequent experiments.

4.6.3 Effect of adsorbent dosage on sorption of MO, MB and CR dyes

The dosage effect on MB MO and CR dyes uptake was examined at a pH of 1.00 (MO and CR) and pH = 11.00 (MB), 20 mg/L (concentration) and 50 minutes (agitation time) at a room temperature (298 K). The outcomes are presented in Figures 4.20 A, B and C.

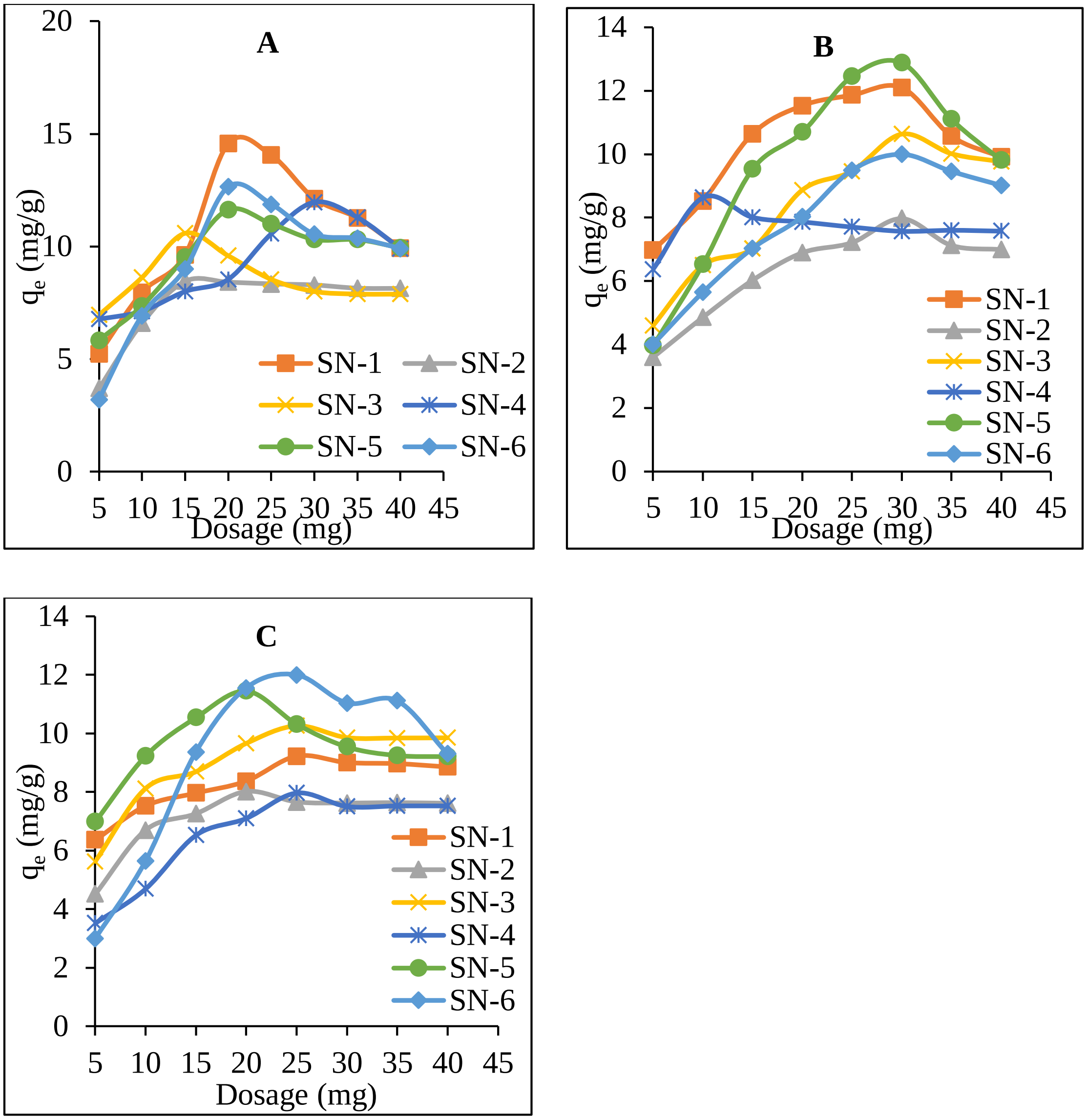

Figure 4.20: Effect of adsorbent dosage on MO (A), MB (B) and CR (C) dyes removal onto Si_3N_4 adsorbents: 20 mg/L; pH = 1.00 (MO and CR) and pH = 11.00 (MB); 50 minutes; 298 K; 150 rpm

The results in Figure 4.20 A showed that the MO dyes uptake was maximum at an optimal dosage of 15 mg (SN-2 and SN-3), 20 mg (SN-1, SN-5 and SN-6) and 30 mg for SN-4 adsorbent.

The amount of MB dyes (Figure 4.20 B) adsorbed increased with increase in dosage (5 mg) to optimal (10 mg) for SN-4 and 30 mg for other adsorbents. The optimum dosage for CR dyes removal (Figure 4.20 C) was 20 mg (SN-2 and SN-5) and 25 mg for other adsorbents beyond which a slight decrease was observed. The maximum mean uptake was highest in SN-1 (14.57 ± 0.27 mg/g), SN-5 (12.88 ± 0.01 mg/g) and SN-6 (11.99 ± 0.01 mg/g) for MO, MB and CR dyes respectively at optimal dosages. This is as shown in appendices V A, V B and V C.

An increase in adsorbent mass increased the binding sites for maximum uptake of the dyes (Tuli *et al.*, 2020; Unugul and Nigiz, 2020). A decreased dyes uptake beyond optimal values could be due to increased overlapping of the binding sites causing screening effect which reduces the number of effective sites (Qu *et al.*, 2020; Jiang *et al.*, 2021). A dosage of 30 mg was used for the subsequent batch experiments. The findings are in tandem with the ones reported by Albayati *et al.* (2017), Sharifpour *et al.* (2019), Shittu *et al.* (2019), Kakhki *et al.* (2020) and Egbosiuba *et al.* (2020) on MO, CR and MB dyes uptake using different adsorbents.

4.6.4 Effect of initial concentration on sorption of MO, MB and CR dyes

The impact of concentration on MO, CR and MB dyes removal onto Si_3N_4 adsorbents was investigated at varied concentrations (10 mg/L to 150 mg/L) and agitated for 50 minutes. The outcomes are shown in Figures 4.21 A, 4.21 B and 4.21 C.

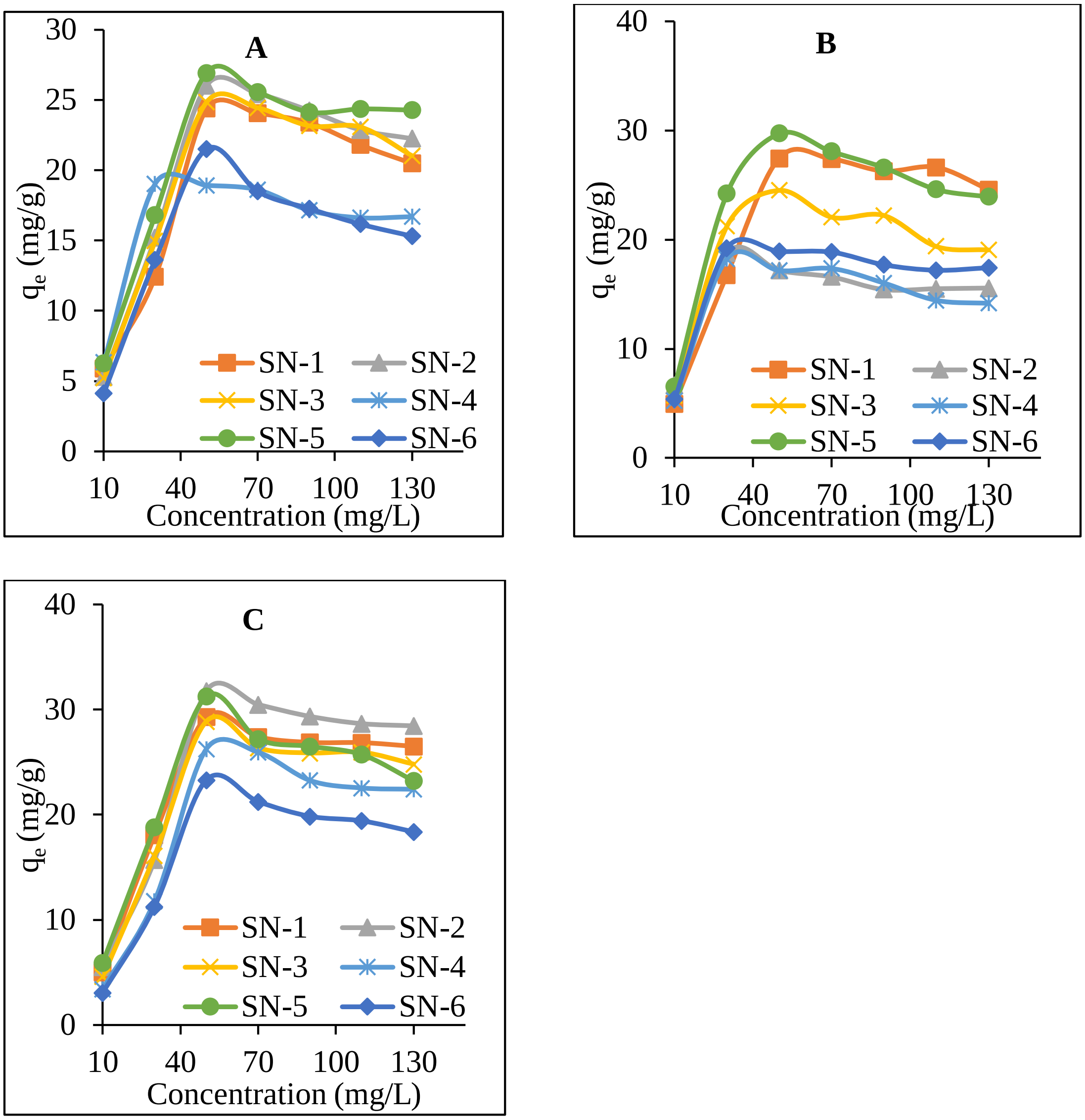

Figure 4.21: Effect of initial concentration on MO (A), MB (B) and CR (C) dyes removal onto Si_3N_4 adsorbents: pH = 1.00 (MO and CR) and pH = 11.00 (MB); 50 minutes; 30 mg; 298 K; 150 rpm

From the outcomes in Figure 4.21 A, the maximum MO dyes uptake ranged from 19.04 ± 0.07 mg/g to 26.93 ± 0.03 mg/g at optimal values of 30 mg/L (SN-4) and 50 mg/L for other adsorbents. The optimal concentration values for MB dyes (Figure 4.21 B) were 30 mg/L (SN-2, SN-4 and SN-6) and 50 mg/L (SN-1, SN-3 and SN-5). The maximum uptake was 27.46 ± 0.09 mg/g (SN-1), 18.79 ± 0.01 mg/g (SN-2), 24.53 ± 0.02 mg/g

(SN-3), 18.25 ± 0.07 mg/g (SN-4), 29.74 ± 0.04 mg/g (SN-5) and 19.21 ± 0.05 mg/g (SN-6). The sorption of CR dyes (Figure 4.21 C) increased to maximum at 50 mg/L for all the adsorbents with uptake ranging from 23.29 ± 0.03 mg/g to 31.77 ± 0.15 mg/g. This is as expounded in appendices VI A, VI B and VI C. This was the followed by a steady state or a decrease in removal uptake.

The trend is described by the fact that, at lower initial concentration values, adsorbent sites are available with less available dye molecules (Youcef *et al.*, 2019). Also, the diffusion rate of dyes at lower concentration values is low; hence only few dye molecules reach the adsorbent sites (Aminu *et al.,* 2020). An increase in concentration with unchanged amount of binding sites leads to an increase in dyes uptake to optimum concentrations (Khan *et al.*, 2022). A decreased dyes uptake beyond optimal values could be due to the binding sites being used up as the dye molecules for a given adsorbent mass is already occupied leaving more unadsorbed in the solution (Rondina *et al.*, 2019; Radoor *et al.*, 2020). An optimal value of 50 mg/L was used for subsequent experiments. The results mirror those reported by Mirzaei *et al.* (2020), Ali and Mohammed (2020), Razzaq *et al.* (2021) and Tan *et al.* (2021) on sorption studies of MO, MB and CR dyes onto NaX/MgO-TiO_2 zeolite nanocomposite, water hyacinth, L-cysteine/rGO/PANI nanocomposite and polysaccharide composite adsorbents respectively.

4.7 Equilibrium studies using adsorption isotherms

The experimental data obtained for MO, CR and MB dyes uptake onto Si_3N_4 adsorbents at optimal conditions was analyzed using Langmuir, Dubinin-Radushkevich and

Freundlich isotherms (Equations 2.6, 2.7. 2.8, 2.9 and 2.10). The outcomes of the study are discussed in the sub-sections 4.7.1, 4.7.2 and 4.7.3.

4.7.1 Adsorption isotherms for MO dyes

The plotting of $\frac{C_e}{q_e}$ against C_e (Langmuir), $\ln q_e$ against $\ln C_e$ (Freundlich) and $\ln q_e$ versus ε^2 (Dubinin-Radushkevich) yields graphs which were employed to determine isotherm parameters and constants. The outcomes are represented in Table 4.6.

Table 4.6: Isotherm models for MO dyes adsorption onto Si_3N_4 adsorbents

Isotherm	Adsorbent	SN-1	SN-2	SN-3	SN-4	SN-5	SN-6
Langmuir	$Q_{m, exp}$ ± S.D (mg/g)	24.38 ± 0.03^{b}	26.01 ± 0.01^{a}	24.84 ± 0.02^{b}	19.04 ± 0.07^{d}	26.93 ± 0.03^{a}	21.52 ± 0.02^{c}
	$Q_{m, cal}$ ± S.D (mg/g)	21.60 ± 0.04^{e}	24.75 ± 0.06^{c}	28.25 ± 0.11^{a}	23.92 ± 0.02^{cd}	25.13 ± 0.05^{bc}	19.53 ± 0.01^{f}
	K_L (L/g)	6.82×10^{-1}	1.61×10^{-1}	1.22×10^{-1}	8.10×10^{-1}	8.82×10^{-1}	6.85×10^{-1}
	R^2	0.9876	0.9702	0.9789	0.9835	0.9993	0.9887
Freundlich	$^{1}/_{n}$	2.73×10^{-1}	2.93×10^{-1}	3.13×10^{-1}	1.74×10^{-1}	3.42×10^{-1}	2.92×10^{-1}
	K_F ± S.D (mg/g)	7.67 ± 0.00^{b}	7.61 ± 0.01^{b}	6.86 ± 0.03^{c}	11.50 ± 0.06^{a}	6.68 ± 0.02^{cd}	5.30 ± 0.00^{d}
	R^2	0.7642	0.5745	0.6443	0.3777	0.7261	0.4464
Dubinin-Radushkevich	$Q_{m, cal}$ ± S.D (mg/g)	32.13 ± 0.04^{bc}	31.53 ± 0.05^{c}	32.18 ± 0.00^{b}	33.30 ± 0.03^{b}	37.58 ± 0.01^{a}	16.54 ± 0.02^{d}
	K_{D-R} (mol^2/kJ^2)	4.10×10^{-2}	3.00×10^{-2}	6.66×10^{-2}	7.25×10^{-2}	1.42×10^{-1}	3.70×10^{-2}
	E ± S.D (kJ/mol)	3.49 ± 0.02^{bc}	4.08 ± 0.01^{a}	2.74 ± 0.03^{c}	2.63 ± 0.00^{c}	1.88 ± 0.02^{d}	3.68 ± 0.01^{ab}
	R^2	0.9118	0.9090	0.8457	0.7986	0.7896	0.9013
Best fit model		Langmuir					

mean values with same letter (s) within the same row are not significantly different
(One-way ANOVA, Fisher LSD-test, α = 0.05)

From the findings in Table 4.6, the experimental data on sorption of MO dyes fitted well in Langmuir model with R^2 of > 0.97 for all the adsorbents. This is as indicated by appendices VII A, VIII A and IX A. The calculated adsorption capacities (Q_m) were 21.60 ± 0.04 mg/g (SN-1), 24.75 ± 0.06 mg/g (SN-2), 28.25 ± 0.11 mg/g (SN-3), 23.92 ± 0.02 mg/g (SN-4), 25.13 ± 0.05 (SN-5) and 19.53 ± 0.01 mg/g (SN-6) which were in tandem with the adsorption capacity obtained from the experimental data. This suggested monolayer interactions of the MO dye molecules with the binding sites that are chemisorption in nature (Rosanti *et al.*, 2022). The findings are in tandem with those registered by the study done by Shah *et al.* (2021) on MO dyes sorption using populous leaves adsorbent.

4.7.2 Adsorption isotherms for MB dyes

The adsorption capacity of Si_3N_4 adsorbents and isotherm constants at equilibrium for MB dyes uptake is given in Table 4.7.

Table 4.7: Isotherm models for MB dyes adsorption onto Si_3N_4 adsorbents

Isotherm	Adsorbent	SN-1	SN-2	SN-3	SN-4	SN-5	SN-6
Langmuir	$Q_{m,\,exp}$ ± S.D (mg/g)	27.46 ± 0.09^{b}	18.79 ± 0.01^{e}	24.53 ± 0.02^{c}	18.25 ± 0.07^{e}	29.74 ± 0.04^{a}	19.21 ± 0.05^{de}
	$Q_{m,\,cal}$ ± S.D (mg/g)	33.22 ± 0.15^{a}	21.46 ± 0.06^{c}	19.69 ± 0.11^{d}	16.03 ± 0.14^{e}	28.09 ± 0.03^{b}	19.96 ± 0.08^{d}
	K_L (L/g)	3.03×10^{-1}	3.00×10^{-1}	8.82×10^{-1}	5.98×10^{-1}	3.48×10^{-1}	6.89×10^{-1}
	R^2	0.9081	0.9896	0.9614	0.9712	0.9973	0.9982
Freundlich	$^{1}/_{n}$	2.92×10^{-1}	1.46×10^{-1}	1.73×10^{-1}	1.79×10^{-1}	1.13×10^{-1}	1.37×10^{-1}
	K_F ± S.D (mg/g)	8.90 ± 0.01^{d}	11.94 ± 0.00^{b}	8.62 ± 0.02^{d}	10.14 ± 0.01^{bc}	15.98 ± 0.03^{a}	10.63 ± 0.00^{c}
	R^2	0.4330	0.2325	0.2826	0.4511	0.4341	0.4169
Dubinin-Radushkevich	$Q_{m,\,cal}$ ± S.D (mg/g)	26.96 ± 0.02^{c}	14.11 ± 0.00^{d}	43.53 ± 0.03^{a}	12.26 ± 0.01^{e}	33.09 ± 0.07^{b}	33.22 ± 0.01^{b}
	K_{D-R} (mol^2/kJ^2)	2.10×10^{-3}	1.95×10^{-2}	2.20×10^{-2}	1.01×10^{-2}	2.62×10^{-2}	2.40×10^{-2}
	E ± S.D (kJ/mol)	15.43 ± 0.00^{a}	5.06 ± 0.01^{c}	4.77 ± 0.02^{cd}	7.04 ± 0.03^{b}	4.37 ± 0.00^{d}	4.56 ± 0.02^{d}
	R^2	0.9923	0.9567	0.7518	0.8021	0.9164	0.8019
Best fit model		Dubinin-Radushkevich	Langmuir				

mean values with same letter (s) within the same row are not significantly different
(One-way ANOVA, Fisher LSD-test, $\alpha = 0.05$)

From the results in Table 4.7, sorption of MB dyes onto Si_3N_4 adsorbents gave $R^2 > 0.96$ in Langmuir isotherm. The results are as construed in appendices VII B, VIII B and IX B. This showed that adsorption best fitted the model dictating a monolayer coverage of MB dyes on the adsorbents surface which is chemisorption in nature (Mohammadi and Veisi, 2018). Also, most of the binding sites have equal affinities toward the MB dyes (Farghali *et al.*, 2021).

For SN-1, the adsorption studies of MB dyes were explained by Dubinin-Radushkevich model with R^2 of 0.9923, $Q_{m, cal}$ of 26.96 ± 0.02 mg/g, $K_{D\text{-}R}$ value of 2.10×10^{-3} mol^2/kJ^2 and E value of 15.43 ± 0.00 kJ/mol which implied that the uptake process was predominated by chemisorption (Muralisankar *et al.*, 2018). Patawat *et al.* (2020), Paclijan *et al.* (2021) and Sebeia *et al.* (2019) reported similar findings during their adsorption studies of MB dyes using *Dipterocarpus alatus* fruit derived activated carbon, PAN and PVDF nanofiber membrane and copper nanoparticles adsorbents.

4.7.3 Adsorption isotherms for CR dyes

The Table 4.8 show the results obtained for the comparison of Langmuir, Dubinin-Radushkevich and Freundlich isotherms for the CR dyes sorption onto Si_3N_4 adsorbents.

Table 4.8: Isotherm models for CR dyes adsorption onto Si_3N_4 adsorbents

Isotherm	**Adsorbent**	**SN-1**	**SN-2**	**SN-3**	**SN-4**	**SN-5**	**SN-6**
Langmuir	$Q_{m,\,exp} \pm$ S.D (mg/g)	29.29 ± 0.03^{b}	31.77 ± 0.15^{a}	28.87 ± 0.07^{b}	26.27 ± 0.08^{c}	31.27 ± 0.13^{a}	23.29 ± 0.03^{d}
	$Q_{m,\,cal} \pm$ S.D (mg/g)	32.36 ± 0.49^{ab}	30.21 ± 0.03^{c}	33.90 ± 0.47^{a}	28.09 ± 0.13^{d}	32.57 ± 0.09^{ab}	28.74 ± 0.26^{d}
	K_L (L/g)	1.30×10^{-1}	1.94×10^{-1}	9.42×10^{-2}	7.67×10^{-2}	1.11×10^{-1}	9.54×10^{-2}
	R^2	0.9643	0.9958	0.9538	0.9822	0.9973	0.9683
Freundlich	$^1/_n$	2.62×10^{-1}	3.50×10^{-1}	4.32×10^{-1}	4.67×10^{-1}	4.76×10^{-1}	4.70×10^{-1}
	$K_F \pm$ S.D (mg/g)	9.99 ± 0.41^{a}	9.23 ± 0.07^{a}	5.83 ± 0.06^{b}	2.99 ± 0.02^{d}	4.58 ± 0.07^{c}	2.96 ± 0.07^{d}
	R^2	0.4480	0.4769	0.5952	0.6501	0.6707	0.5288
Dubinin-Radushkevich	$Q_{m,\,cal} \pm$ S.D (mg/g)	20.35 ± 0.07^{f}	38.88 ± 0.09^{b}	43.07 ± 0.03^{a}	22.39 ± 0.01^{e}	34.32 ± 0.05^{d}	36.11 ± 0.03^{c}
	$K_{D\text{-}R}$ (mol^2/kJ^2)	1.77×10^{-2}	3.05×10^{-2}	4.56×10^{-2}	3.81×10^{-2}	3.58×10^{-2}	4.34×10^{-2}
	E ± S.D (kJ/mol)	5.31 ± 0.00^{a}	4.05 ± 0.08^{ab}	3.31 ± 0.04^{c}	3.62 ± 0.02^{c}	3.74 ± 0.03^{bc}	3.39 ± 0.01^{c}
	R^2	0.6273	0.8355	0.8611	0.8873	0.9043	0.8030
Best fit model		Langmuir					

mean values with same letter (s) within the same row are not significantly different (One-way ANOVA, Fisher LSD-test, $\alpha = 0.05$)

From the outcomes in Table 4.8, correlation coefficients (R^2) of > 0.95 were obtained for Langmuir isotherm. This was corroborated by the closeness of $Q_{m, exp}$ (mg/g) and $Q_{m, cal}$ (mg/g). This implies that the Langmuir gave better regression coefficient than those of Freundlich and Dubinin-Radushkevich as shown by appendices VII C, VIII C and IX C. The values of $K_L < 1$ showed the favorability of CR dye sorption onto the adsorbents (Litefti *et al.*, 2019). The results mirror those reported by Abdul Rahim *et al.* (2021) on uptake studies of CR dyes onto coconut wastes.

From the equilibrium results, the Si_3N_4 adsorbents performance for sorption of CR, MB and MO dyes was chemisorption in nature. This showed that the adsorbent functional groups of silicon-nitrogen-silicon (Si-N-Si) and silanol (Si-OH) were hydroxylated in water to silazane ($Si_2=NH_2^+$) and silanolate groups ($Si\text{-}O^-$) as important adsorption sites for anionic (MO and CR) and cationic MB dyes sorption.

All adsorbents recorded highest uptake capacity for CR dyes. This could be due to more reaction centers of amino ($-NH_2$) and sulphonate ($-SO_3H$) groups in the CR structure increasing the Si_3N_4 adsorbent affinity for the dye ion via electrostatic attractions and dipole-dipole hydrogen bonding.

4.8 Adsorption kinetic studies

The time data at optimized parameters was fitted to Pseudo-second-order, Elovich and Pseudo-first-order models (Equations 2.11, 2.12 and 2.13). The outcomes of the study are discussed in the sub-sections 4.8.1, 4.8.2 and 4.8.3.

4.8.1 Adsorption kinetic studies for MO dyes

The three different kinetic parameters calculated by linear regression of time data for MO dyes sorption onto Si_3N_4 adsorbents are shown in Table 4.9.

Table 4.9: Kinetic parameters for sorption of MO dyes onto Si_3N_4 adsorbents

Model	**Adsorbent**	**SN-1**	**SN-2**	**SN-3**	**SN-4**	**SN-5**	**SN-6**
Pseudo-first-order	$Q_{e,\ exp} \pm$ S.D (mg/g)	15.72 ± 0.04^{ab}	15.01 ± 0.02^{b}	12.47 ± 0.05^{c}	12.29 ± 0.07^{c}	16.04 ± 0.09^{a}	11.63 ± 0.01^{d}
	$Q_{e,\ cal} \pm$ S.D (mg/g)	1.17 ± 0.08^{d}	2.13 ± 0.03^{c}	4.41 ± 0.01^{a}	2.66 ± 0.05^{c}	3.06 ± 0.00^{b}	2.36 ± 0.07^{bc}
	K_1 (min^{-1})	1.10×10^{-3}	6.90×10^{-3}	5.70×10^{-3}	5.60×10^{-3}	7.10×10^{-3}	8.30×10^{-3}
	R^2	0.2105	0.4533	0.6536	0.6232	0.7357	0.6177
Pseudo-second-order	$Q_{e,\ cal} \pm$ S.D (mg/g)	16.08 ± 0.09^{a}	15.53 ± 0.01^{ab}	11.35 ± 0.03^{c}	11.96 ± 0.07^{c}	15.46 ± 0.02^{ab}	11.55 ± 0.04^{c}
	K_2 (mg/g/min)	6.44×10^{-2}	1.19×10^{-2}	9.21×10^{-2}	2.11×10^{-2}	3.17×10^{-2}	3.48×10^{-2}
	R^2	0.9941	0.9908	0.9834	0.9945	0.9982	0.9953
Elovich	$\propto$ (mg/g/min)	1.37×10^{-3}	2.67×10^{-5}	5.78×10^{-11}	1.45×10^{-5}	5.03×10^{-4}	1.71×10^{-15}
	β (g/mg)	4.20×10^{-1}	5.95×10^{-1}	8.36×10^{-1}	6.66×10^{-1}	5.11×10^{-1}	8.75×10^{-1}
	R^2	0.1691	0.5924	0.6780	0.5347	0.7633	0.7054
Best fit model		Pseudo-second-order					

mean values with same letter (s) within the same row are not significantly different
(One-way ANOVA, Fisher LSD-test, $\alpha = 0.05$)

From the findings in Table 4.9, the Pseudo-second-order plots gave correlation coefficients (R^2) closer to unity ($R^2 > 0.98$) comparatively to those of Pseudo-first-order and Elovich plots. This presupposes that MO dyes sorption occurred through chemical interactions (Manzar *et al.,* 2019). The model explain that the uptake process occurred on the adsorbent surface via exchange or sharing of electrons (Cheah *et al.,* 2013).

The K_2 (mg/g/min) values were 6.44×10^{-2} (SN-1), 1.19×10^{-2} (SN-2), 9.21×10^{-2} (SN-3), 2.11×10^{-2} (SN-4), 3.17×10^{-2} (SN-5) and 3.48×10^{-2} (SN-6). The results are as shown in appendices X A, XI A and XII A. The higher K_2 (Pseudo-second-order) values than K_1 (Pseudo-first-order) and $\propto$ (Elovich) values shows that there were strong chemical interactions between the active sites and the dye molecules which improved the rate of adsorption (Abbas *et al.,* 2018). This is coherent to results previously reported (Sani and Abdullahi, 2017; Lacin and Aroguz, 2020).

4.8.2 Adsorption kinetic studies for MB dyes

The Table 4.10 below presents the results of kinetic plots using Pseudo-second-order, Pseudo-first-order and Elovich kinetic models.

Table 4.10: Kinetic parameters for sorption of MB dyes onto Si_3N_4 adsorbents

Model	**Adsorbent**	**SN-1**	**SN-2**	**SN-3**	**SN-4**	**SN-5**	**SN-6**
Pseudo-first-order	$Q_{e, exp} \pm$ S.D (mg/g)	19.06 ± 0.05^{ab}	14.35 ± 0.04^{e}	15.43 ± 0.05^{d}	17.79 ± 0.09^{c}	20.54 ± 0.07^{a}	14.49 ± 0.04^{de}
	$Q_{e, cal} \pm$ S.D (mg/g)	1.50 ± 0.03^{cd}	1.88 ± 0.01^{c}	1.26 ± 0.08^{d}	1.07 ± 0.04^{d}	5.90 ± 0.09^{a}	3.87 ± 0.05^{b}
	K_1 (min^{-1})	2.70×10^{-3}	5.80×10^{-3}	1.60×10^{-3}	2.80×10^{-3}	9.70×10^{-3}	7.00×10^{-4}
	R^2	0.2370	0.1093	0.0908	0.0327	0.4048	0.1174
Pseudo-second-order	$Q_{e, cal} \pm$ S.D (mg/g)	19.08 ± 0.02^{a}	13.70 ± 0.09^{cd}	14.86 ± 0.03^{c}	16.37 ± 0.07^{b}	19.88 ± 0.03^{a}	14.06 ± 0.08^{c}
	K_2 (mg/g/min)	9.06×10^{-2}	5.38×10^{-2}	1.47×10^{-1}	5.26×10^{-1}	1.19×10^{-2}	8.57×10^{-2}
	R^2	0.9984	0.9946	0.9954	0.9936	0.9968	0.9957
Elovich	∝ (mg/g/min)	1.05×10^{-9}	2.65×10^{-15}	2.68×10^{-5}	3.42×10^{-4}	1.48×10^{-7}	3.07×10^{-25}
	β (g/mg)	6.17×10^{-1}	8.29×10^{-1}	5.55×10^{-1}	4.72×10^{-1}	6.33×10^{-1}	8.82×10^{-1}
	R^2	0.4503	0.6764	0.5586	0.4571	0.7682	0.8064
Best fit model		Pseudo-second-order					

mean values with same letter (s) within the same row are not significantly different (One-way ANOVA, Fisher LSD-test, $\alpha = 0.05$)

From the results above (Table 4.10), the correlation coefficient (R^2) values for Pseudo-second-order are close to unity (1) than those for the Elovich and Pseudo-first-order kinetic models. Additionally, the calculated uptake capacity ($Q_{e,\ cal}$) values from the Pseudo-second-order are close to the uptake capacity ($Q_{e,\ exp}$) values obtained experimentally. The rate constant (K_2) values were higher than the K_1 and $\propto$ rate constants. This is as indicated by appendices X B, XI B and XII B.

The closeness of $Q_{e,\ cal}$ and $Q_{e,\ exp}$ with higher R^2 values (> 0.99) and higher K_2 values indicated that the model best fit the experimental data for MB dyes removal compared to other kinetic models. Therefore, the findings demonstrated chemisorption as the rate determining step in MB dyes uptake onto the Si_3N_4 adsorbents (Alharby *et al.,* 2021). Staroń *et al.* (2019) made similar observations on MB dyes adsorption by *raphia* fibers adsorbent.

4.8.3 Adsorption kinetic studies for CR dyes

The time data plots of $\ln(q_e - q_t)$ against time (Pseudo-first-order), q_t versus $\ln_t$ (Elovich) and t/q_t against time (Pseudo-second-order) for CR dyes sorption onto Si_3N_4 adsorbents were employed to determine the kinetic constants and parameters. The outcomes are presented in Table 4.11.

Table 4.11: Kinetic parameters for sorption of CR dyes onto Si_3N_4 adsorbents

Model	Adsorbent	SN-1	SN-2	SN-3	SN-4	SN-5	SN-6
Pseudo-first-order	$Q_{e,\ exp} \pm$ S.D (mg/g)	19.25 ± 0.12^{d}	29.50 ± 0.05^{a}	27.51 ± 0.07^{b}	18.61 ± 0.01^{de}	23.31 ± 0.03^{c}	23.57 ± 0.04^{c}
	$Q_{e,\ cal} \pm$ S.D (mg/g)	3.05 ± 0.02^{c}	10.27 ± 0.00^{a}	4.57 ± 0.05^{b}	1.74 ± 0.08^{d}	3.42 ± 0.01^{c}	3.62 ± 0.03^{bc}
	K_1 (min^{-1})	6.90×10^{-3}	3.70×10^{-3}	8.10×10^{-3}	2.30×10^{-3}	4.70×10^{-3}	9.10×10^{-3}
	R^2	0.6587	0.4486	0.3599	0.5563	0.5139	0.6839
Pseudo-second-order	$Q_{e,\ cal} \pm$ S.D (mg/g)	18.59 ± 0.04^{d}	29.85 ± 0.11^{a}	26.25 ± 0.07^{b}	18.28 ± 0.02^{d}	22.32 ± 0.04^{c}	22.94 ± 0.01^{c}
	K_2 (mg/g/min)	2.94×10^{-2}	1.20×10^{-2}	1.65×10^{-2}	5.87×10^{-1}	1.30×10^{-1}	1.93×10^{-2}
	R^2	0.9984	0.9964	0.9972	0.9942	0.9979	0.9994
Elovich	$\propto$ (mg/g/min)	9.12×10^{-3}	1.84×10^{-4}	1.44×10^{-5}	6.50×10^{-7}	6.66×10^{-13}	1.05×10^{-12}
	β (g/mg)	3.50×10^{-1}	4.85×10^{-1}	4.96×10^{-1}	5.68×10^{-1}	6.40×10^{-1}	6.85×10^{-1}
	R^2	0.5259	0.8380	0.7111	0.5241	0.2268	0.7231
Best fit model		Pseudo-second-order					

mean values with same letter (s) within the same row are not significantly different
(One-way ANOVA, Fisher LSD-test, $\alpha = 0.05$)

The results in Table 4.11 showed low R^2, $\propto$ and K_1 values for Elovich and Pseudo-first-order models in comparison to those of Pseudo-second-order. This implies that the uptake of CR dyes onto Si_3N_4 adsorbents did not fit the models. The Pseudo-second-order R^2 values were > 0.99 for all the adsorbents as constructed in appendices X C, XI C and XII C. This implied that the experimental kinetic data best fitted the model indicating that the sorption of CR dyes onto the adsorbents was chemisorption in nature (Elwakeel *et al.*, 2020). Ojedokun and Bello (2017) observed similar phenomena in adsorption of CR dyes onto guava leaf-based activated carbon.

The kinetic results for the MO, MB and CR sorption studies onto Si_3N_4 adsorbents was explained by Pseudo-second-order model with $R^2 > 0.9$. This indicated that the chemisorption controlled the dyes uptake as the rate limiting step mainly by ion exchange between the adsorbent sites and the dye ions.

The kinetic results showed higher $Q_{e,\ cal}$ and $Q_{e,\ exp}$ for CR dyes for all the adsorbents. This could be due to the adsorbents’ higher affinity for the dye ions.

4.9 Desorption studies

The desorption studies of MO, CR and MB dyes for the first cycle were carried out on Si_3N_4 adsorbents (50 mg/L and 30 mg) using 1.0×10^{-1} M NaOH, 1.0×10^{-1} M CH_3COOH, distilled water and 1.0×10^{-1} M HCl eluents and findings presented in Figures 4.22 A, B and C.

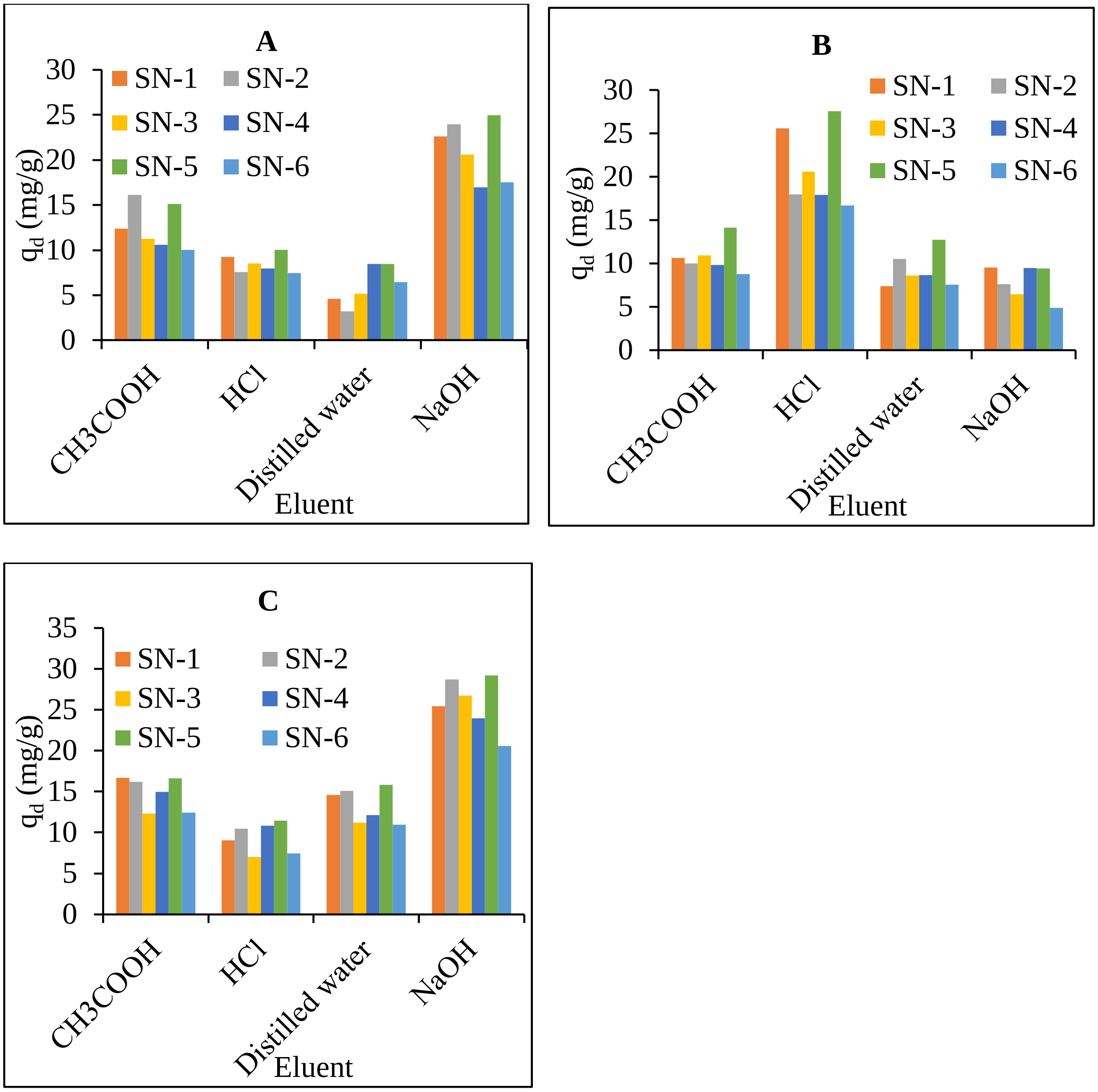

Figure 4.22: Desorption of MO (A), MB (B) and CR (C) dyes from Si_3N_4 loaded adsorbents

From the results in Figures 4.22, the highest desorption capacity (q_d) of 29.17 ± 0.00 mg/g (CR) and 24.97 ± 0.00 mg/g (MO) was achieved with 1.0×10^{-1} M NaOH eluent for all adsorbents with the highest reported in SN-5 adsorbent as constructed by appendices XIII A and XIII C. This revealed that OH^- ions was involved in desorbing the dye molecules from the adsorbent by creating electrostatic repulsions with sulphonate ($–SO_3^-$) groups for silazane ($Si_2=NH_2^+$) groups. This is as shown in the Equation 4.3.

$$Si_2=NH_2^+\text{-}O_3^-S\text{-}Dye + OH^- \longrightarrow Si_2=NH_2^+\text{-}OH^- + Dye\text{-}SO_3^- \qquad (4.3)$$

This implies that ion exchange mechanism was involved in the adsorption and desorption of MO and CR dyes (Parimelazhagan *et al.,* 2022).

The desorption capacity of 25.57 ± 0.00 mg/g (SN-1), 17.97 ± 0.00 mg/g (SN-2), 20.57 ± 0.01 mg/g (SN-3), 17.89 ± 0.00 mg/g (SN-4), 27.60 ± 0.00 mg/g (SN-5) and 16.69 ± 0.00 mg/g (SN-6) was obtained for MB dyes with 1.0×10^{-1} M HCl as more suitable eluent in in regeneration of the dye loaded adsorbents. This is as shown in appendix XIII B. The presence of H^+ ions in the MB dye solution destroys the electrostatic interaction between the silanolate groups ($Si\text{-}O^-$) and the cationic MB dye ions making it to be preferentially complexed at the Si_3N_4 adsorbent surface. The results are similar to those recorded by Munagapati and Kim (2016), El-Kousy *et al.* (2020) and Oyarce *et al.* (2021).

Further desorption studies for CR and MO dyes were performed using 1.0×10^{-1} M NaOH eluent and 1.0×10^{-1} M HCl (for MB dyes) with adsorption/desorption cycles being done upto 6th time. The SN-5 adsorbent showed the highest adsorption-desorption capacity (first cycle) and was used for the subsequent cycles and the outcomes are presented in sub-section 4.9.1.

4.9.1 Adsorption-desorption studies using Si_3N_4 adsorbents

The recovery and re-usability potential of SN-5 adsorbent was studied for MO, CR and MB dyes. The outcomes are shown in Figure 4.23.

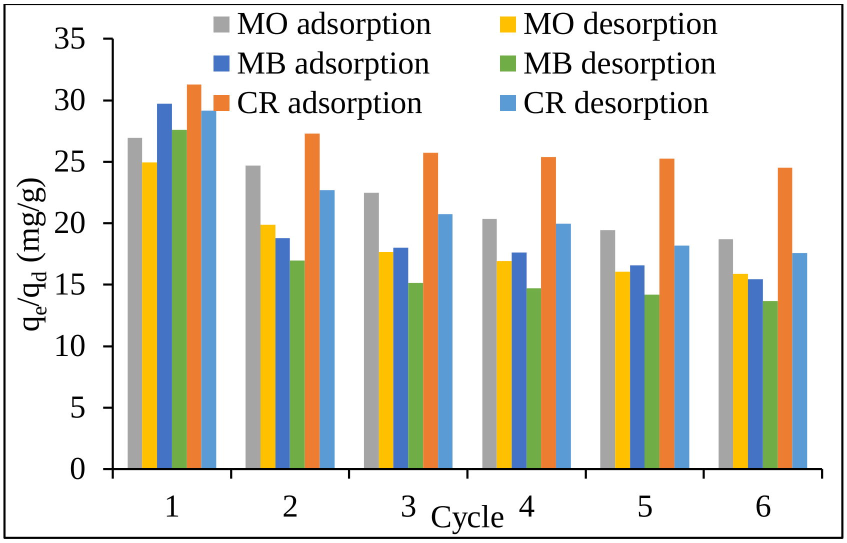

Figure 4.23: Adsorption-desorption cycles for SN-5 adsorbent

The findings in Figure 4.23 indicated that adsorption and desorption capacity of SN-5 adsorbent for MO, MB and CR dyes decreased with increase in cycles. There was slight decrease in both dye adsorption and desorption capacities from the first upto sixth cycle for the MO, MB and CR dyes respectively as constructed in appendix XIV. The decrease in the uptake capacity was due to the ignorable mass of the adsorbent that got lost during the adsorption-desorption processes (Munagapati and Kim, 2016).

The adsorption-desorption experiments showed that Si_3N_4 adsorbents can be re-used repeatedly for MO, MB and CR dyes adsorption and desorption. Therefore, it can be applied in column adsorption studies to test on their applicability in textile dye wastewater treatment.

4.10 Fixed-bed column adsorption studies

The column uptake studies of MO, MB and CR dyes were investigated using SN-5 adsorbent. The outcomes are discussed in sub-section 4.10.1, 4.10.2 and 4.10.3.

4.10.1 Effect of volumetric flow rate on adsorption of MO, MB and CR dyes

The impact of volumetric flow rate on MO, CR and MB dyes sorption onto SN-5 adsorbent is as presented by Figures 4.24 A, B, and C.

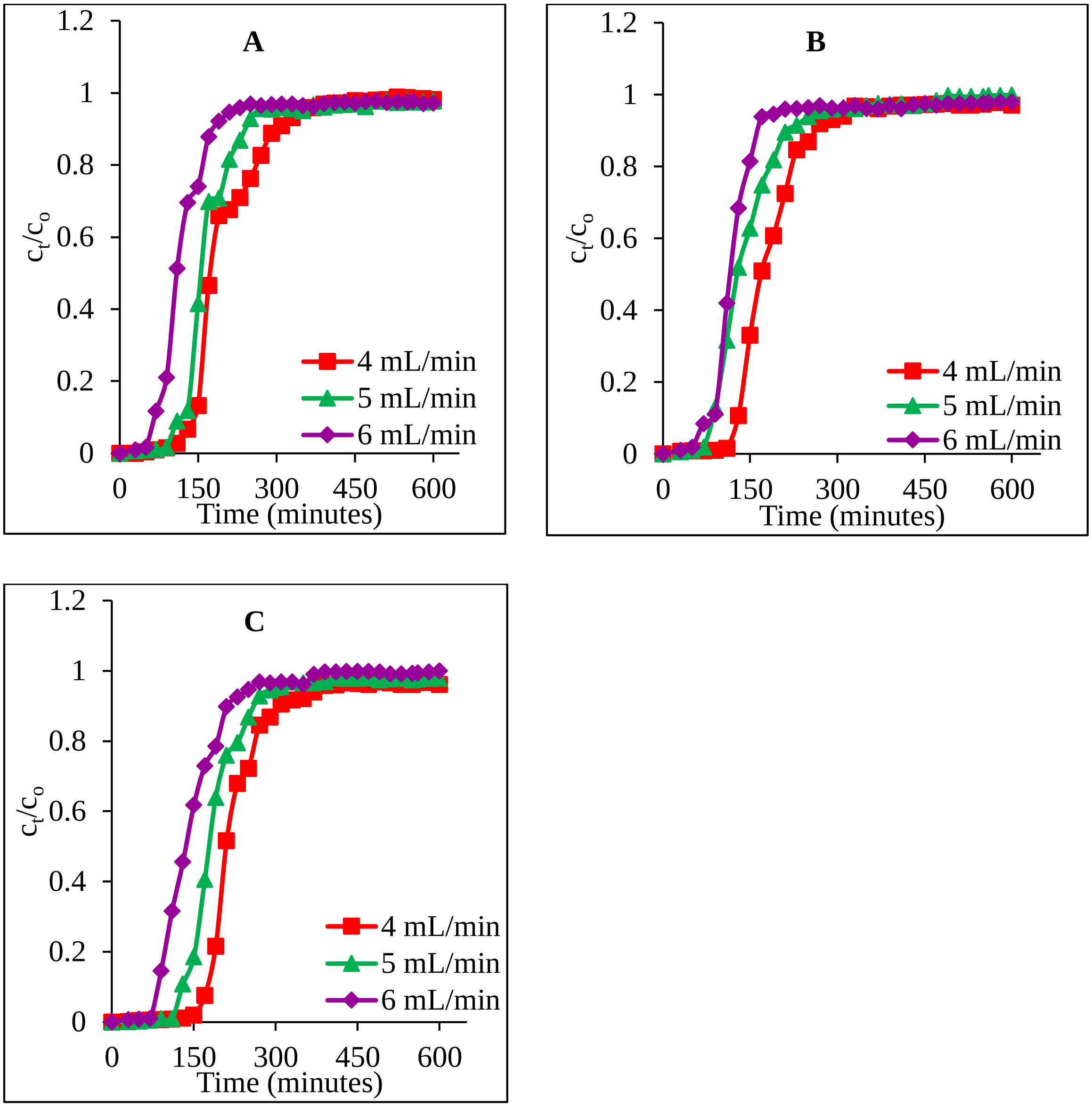

Figure 4.24: Effect of volumetric flow rate on sorption of MO (A), MB (B) and CR (C) dyes onto SN-5 adsorbent (at C_0 = 50 mg/L, Z = 3 cm)

From the results in Figures 4.24, the optimal value of 4 mL/min was attained for MO, MB and CR dyes sorption onto the adsorbent. The breakthrough times were low at a high volumetric flow rate with breakthrough curves becoming steeper. Increase in volumetric flow rate from 4, 5 to 6 mL/min, decreased the breakthrough times (t_b) and saturation times (t_s). That is, 130 minutes to 70 minutes and 350 minutes to 210 minutes; 140 minutes to 70 minutes and 320 minutes to 190 minutes and 180 minutes to 90 minutes and 390 minutes to 240 minutes for MO, MB and CR dyes respectively.

This resulted to a decrease in column adsorption capacity to 42.79 ± 0.04 (MO), 37.38 ± 0.17 mg/g (MB) and 47.33 ± 0.03 mg/g (CR). This is as shown in appendix XV A, XV B and XV C. This could be because of the fact that, at higher volumetric flow rate values, the time of contact of the dyes with the adsorbent surface is not enough (Patel, 2018). This makes the molecules have inadequate time for their interaction with the adsorbent sites leaving the column before saturation occurs (Banerjee *et al.*, 2017). The increase in volumetric flow rate also affects the film diffusion, which lowers the mass transfer force from the aqueous phase to the solid phase (Hummadi *et al.*, 2022). The outcomes agree with those reported by Bennani *et al.* (2015) during their MB dyes column uptake using Moroccan clay adsorbent.

4.10.2 Effect of bed height on adsorption of MO, MB and CR dyes

The breakthrough curves for column uptake of MO, MB and CR dyes onto SN-5 adsorbent were obtained at varied column heights (3, 5 and 7 cm). The findings are as shown in Figure 4.25 A, 4.25 B and 4.25 C.

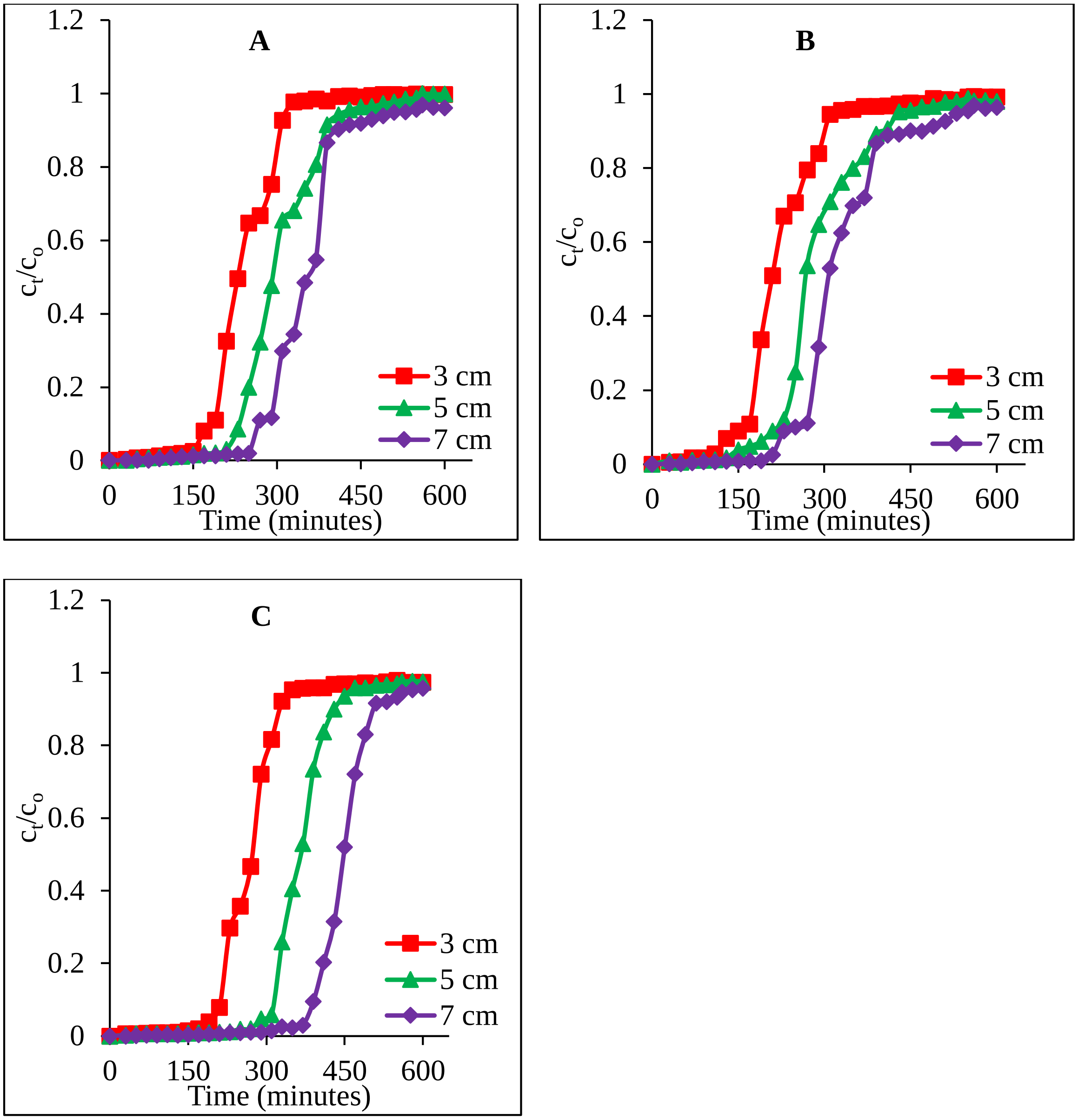

Figure 4.25: Effect of bed height on sorption of MO (A), MB (B) and CR (C) dyes onto SN-5 adsorbent (at $C_0 = 50$ mg/L, Q = 4 mL/min)

The results in Figure 4.25 showed that maximum column capacity for MO, MB and CR dyes was obtained at optimal bed height of 7 cm. The breakthrough times (t_b) increased from 170 minutes to 230 minutes, 130 minutes to 210 minutes and 210 minutes to 370 minutes for MO, MB and CR dyes respectively with increased column height from 3 cm to 7 cm. This also led to an increase in times at which the column becomes saturated and an increase in column capacity. That is, from 310 minutes, 430 minutes to 540 minutes (MO), 320 minutes, 440 minutes to 550 minutes (MB) and 340 minutes, 470 minutes to 580 minutes (CR).

Also, the column sorption capacity increased from 43.88 ± 0.07 to 48.21 ± 0.04 mg/g (MO), 45.79 ± 0.04 to 48.75 ± 0.06 mg/g (MB) and 48.15 ± 0.01 to 51.14 ± 0.06 mg/g (CR) with increase in column height. This is as construed in appendices XV A, XV B and XV C. The findings demonstrated that the breakthrough point took longer with increasing the bed height. At a column height of 3 cm, the adsorbent load in the fixed-bed column is low, hence a smaller bed capacity, which over time, became saturated and as a result, less dyes were adsorbed (Jain *et al.*, 2020). As the column height is raised from 3 cm to 7 cm, a decreased breakthrough curve slope is observed. This resulted to a rapid mass transfer zone (Jaime *et al.*, 2018). This was because of a large adsorbent surface area which led to more binding sites for MO, MB and CR dyes adsorption resulting in higher column capacity (Bharathi and Ramesh, 2013; Yahuza *et al.*, 2017). The findings are coherent with those reported by Nica *et al.* (2020) on MB sorption studies onto cellulose cellet adsorbent.

4.10.3 Effect of influent concentration on adsorption of MO, MB and CR dyes

The impact of concentration on MO, MB and CR dyes column uptake onto SN-5 adsorbent is presented in Figure 4.26 A, B and C by keeping the volumetric flow rate at 4 mL/min and bed height at 7 cm.

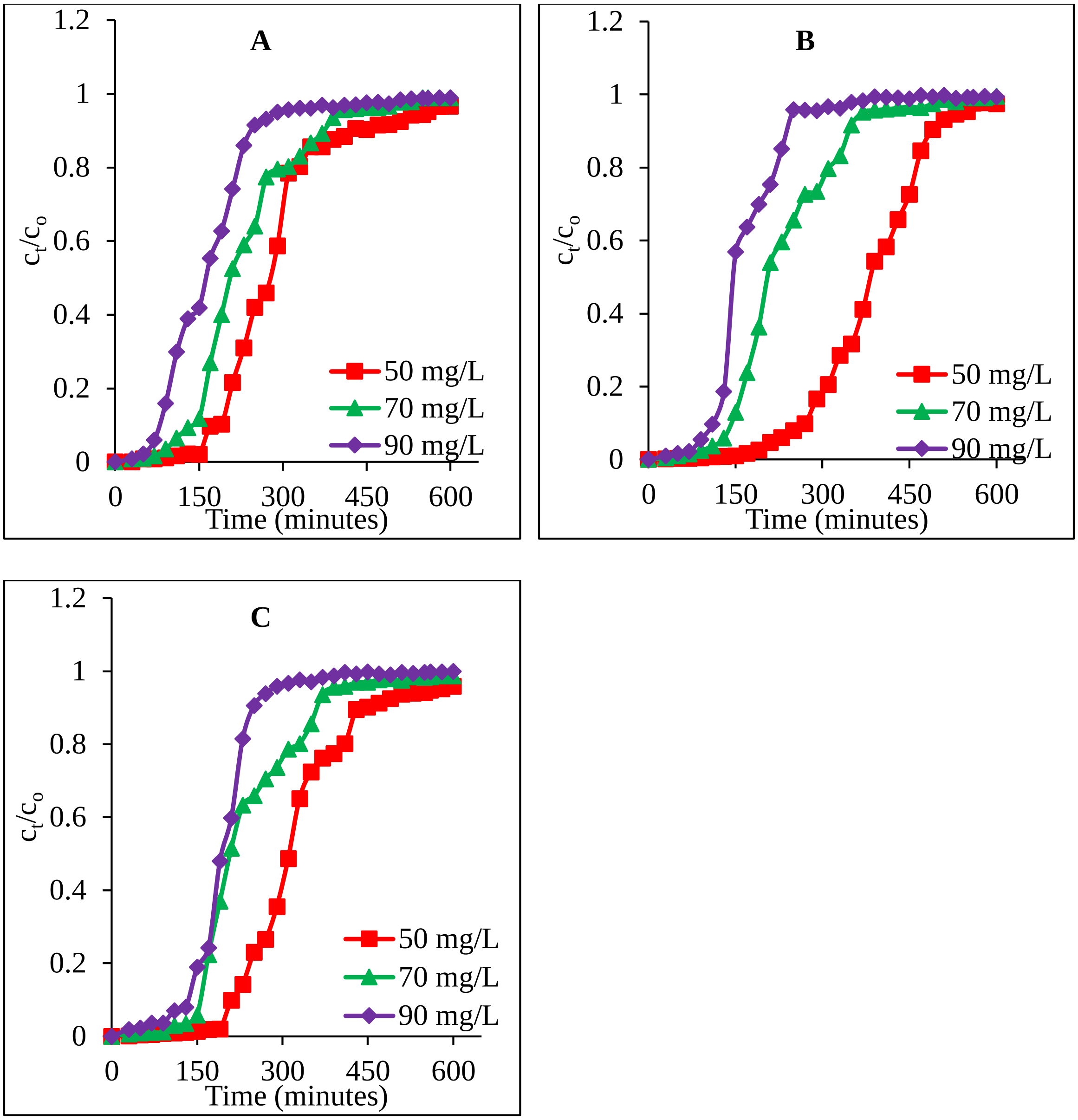

Figure 4.26: Effect of influent concentration on adsorption of MO (A), MB (B) and CR (C) dyes onto SN-5 adsorbent (at Z = 7 cm, Q = 4 mL/min)

From the findings above (Figure 4.26), the MO, CR and MB dyes column uptake onto the SN-5 adsorbent was maximum at 50 mg/L optimal concentration. The breakthrough curves illustrated a decrease in breakthrough (t_b) and saturation times (t_s) as the concentration was varied from 50, 70 to 90 mg/L. That is, from 150 minutes to 70 minutes (MO), 230 minutes to 90 minutes (MB) and 190 minutes to 110 minutes (CR).

Also, from 570 minutes to 290 minutes for MO dyes, 550 minutes to 250 minutes for MB dyes and 590 minutes to 300 minutes for CR dyes.

Maximum column capacity at 50 mg/L was 50.76 ± 0.17 mg/g, 47.01 ± 0.14 mg/g and 52.56 ± 0.04 mg/g for MO, MB and CR dyes respectively. This is as expounded in appendices XV A, XV B and XV C. Low dye concentration makes the saturation time and diffusion rate longer (Ali and Mohammed, 2021). The breakthrough curves became dispersed and breakthrough occurred slowly but sharper breakthrough curves were obtained as the influent concentration increased (Al-Husseiny, 2014). This showed that, at lower inlet concentration, more dye molecules interact with the adsorbent sites leading to higher volume of treated water (Mohammad *et al.,* 2016). Increasing the influent concentration leads to a rapid binding sites saturation due to a higher driving force of dyes lowering the column adsorption (Hummadi *et al.,* 2022). This imply that the adsorbent will be exhausted within a short period of time with less dyes uptake. The outcomes are in tandem with those reported in the study using different adsorbents (Reddy and Nirmala, 2014; Patel *et al.,* 2019).

4.11 Kinetics of column adsorption

The kinetic plots of $\ln\left(\frac{C_o}{C_t} - 1\right)$ against time (Thomas), $\ln\left(\frac{C_t}{C_o}\right)$ against time (Adams-Bohart) and $\ln\left(\frac{C_t}{C_o - C_t}\right)$ against time (Yoon-Nelson) (Equation 2.14, 2.15, 2.16, 2.17 and 2.18) were used to calculate the model constants (k_{TH}, k_{YN} and K_{AB}), maximum bed capacity (Q_o) and breakthrough times at $C_t/C_0 \approx 0.5$ ($\tau_{0.5}$). The outcomes are presented in Table 4.12.

Table 4.12: Column kinetic model constants and correlation coefficients (R^2) for MO, MB and CR dyes sorption onto SN-5 adsorbent

	Thomas				**Yoon-Nelson**					
Dye	**$Q_{o,\ exp}$ ± S.D (mg/g)**	**$Q_{o,\ cal}$ ± S.D (mg/g)**	**K_{TH} (ml/mg/min)**	**R^2**	**K_{YN} (min^{-1})**	**$t_{0.5,\ exp}$ (min)**	**$\tau_{0.5,\ cal}$ (min)**	**$Q_{o,\ 0.5,\ exp}$ ± S.D (mg/g)**	**$Q_{o,\ 0.5,\ cal}$ ± S.D (mg/g)**	**R^2**
MO	50.76 ± 0.17^{b}	45.37 ± 0.12^{c}	2.02×10^{-4}	0.9106	1.42×10^{-2}	300	311.42	27.27 ± 0.23^{b}	28.31 ± 0.09^{b}	0.9324
MB	47.01 ± 0.14^{c}	48.09 ± 0.18^{a}	2.46×10^{-4}	0.9959	2.07×10^{-2}	290	304.20	26.36 ± 0.08^{c}	27.65 ± 0.13^{c}	0.9602
CR	52.56 ± 0.04^{a}	47.63 ± 0.02^{b}	2.38×10^{-4}	0.9545	1.80×10^{-2}	310	334.71	28.18 ± 0.15^{a}	30.43 ± 0.06^{a}	0.9521

		Adams-Bohart		
Dye	**K_{AB} (L/mg/min)**	**N_o (mg/L)**	**$Q_{o,\ cal}$ ± S.D (mg/g)**	**R^2**
MO	1.96×10^{-4}	15126.43 ± 0.07^{c}	15.13 ± 0.07^{c}	0.5944
MB	2.32×10^{-4}	18386.37 ± 0.09^{a}	18.39 ± 0.09^{a}	0.7303
CR	2.80×10^{-5}	17555.31 ± 0.13^{b}	17.56 ± 0.13^{b}	0.4435

mean values with same letter (s) within the same row are not significantly different
(One-way ANOVA, Fisher LSD-test, $\alpha = 0.05$)

From the results in Table 4.12, the column data obtained from the breakthrough curves for MO, MB and CR dyes showed conformity with Yoon-Nelson and Thomas as suitable models in describing fixed-bed column operations ($R^2 > 0.91$). This is as indicated by appendix XVI A, XVII and XVIII. This was corroborated by the closeness of $Q_{o,\ cal}$ with $Q_{o,\ exp}$ at saturation. That is, 50.76 ± 0.17 and 45.37 ± 0.12 mg/g (MO); 47.01 ± 0.14 and 48.09 ± 0.18 mg/g (MB); 52.56 ± 0.04 and 47.63 ± 0.02 mg/g (CR). This was also confirmed by closeness of $Q_{o,\ cal}$ with $Q_{o,\ exp}$ at 50 % column breakthrough.

Also, the rate constants (K_{TH} and K_{YN}) values were higher than the K_{AB} rate constants. This showed that column sorption mechanism of MO, CR and MB dyes onto the SN-5 adsorbent was a monolayer chemical adsorption mechanism (Zhang *et al.*, 2011). This agrees with batch experiment results. The time required for a 50 % adsorbate breakthrough calculated by Yoon-Nelson model compare to those obtained experimentally (appendix XV A, XV B and XV C). The results mirror those reported by Mohammad *et al.* (2016), Silva *et al.* (2020) and Babazadeh *et al.* (2021) using tea wastes, H_3PO_4-activated carbon fibers and chitosan-clinoptilolite adsorbents.

4.12 Column performance using environmental water samples

The column performance using spiked water samples was done at optimized parameters (4 mL/min and 7 cm) for the SN-5 adsorbent. The obtained breakthrough curves were employed to predict the performance of the Si_3N_4 adsorbent. The findings are presented in Figures 4.27 A, 4.27 B and 4.27 C.

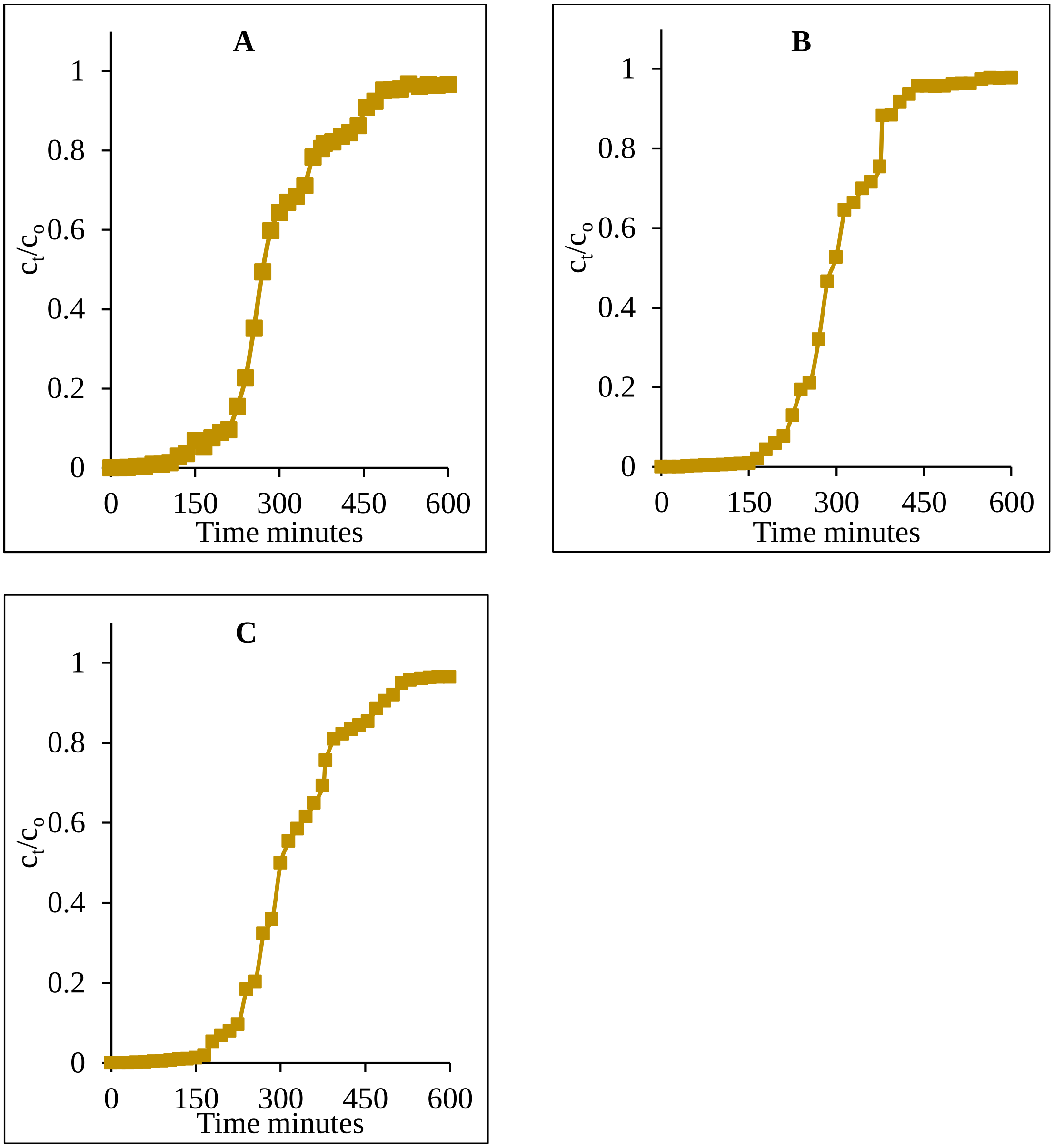

Figure 4.27: Column adsorption of MO (A), MB (B) and CR (C) dyes from spiked water samples onto SN-5 adsorbent (at Q = 4 mL/min, Z = 7 cm)

The results in Figures 4.27 showed that the breakthrough and saturation times for SN-5 adsorbent was 140 minutes and 485 minutes (MO), 195 minutes and 440 minutes (MB) and 180 minutes and 530 minutes (CR). The amount of dyes adsorbed ($Q_{o,\ exp}$) at saturation time was 41.85 ± 0.12 mg/g (MO), 38.92 ± 0.08 mg/g (MB) and 46.38 ± 0.05 mg/g (CR). The findings demonstrated that SN-5 adsorbent took less time to breakthrough and saturation for the spiked water samples than the model solutions with a lower column adsorption capacity. This is as construed in appendix XIX. This could be because of the existence of other interfering inorganic and organic species in the water samples which competed for the available adsorbent sites with the dye molecules resulting to faster saturation of the adsorbent sites (Mahmoud *et al.*, 2019).

The column time data for the breakthrough curves of MO, MB and CR dyes were modelled using Thomas model and outcomes are presented in Table 4.13.

Table 4.13: Thomas parameters of SN-5 adsorbent for MO, MB and CR dyes sorption from spiked water samples

	Parameters					
Dye	**Found in environmental water sample (mg/L)**	**Found in spiked water sample (mg/L)**	**k_{TH} (mL/mg/min)**	**$Q_{o,\ exp}$ ± S.D (mg/g)**	**$Q_{o,\ cal}$ ± S.D (mg/g)**	**R^2**
MO	0.9694	3.5067	3.04×10^{-4}	41.85 ± 0.12^b	34.26 ± 0.09^b	0.9520
MB	1.6450	2.9902	4.12×10^{-4}	38.92 ± 0.08^c	31.80 ± 0.24^c	0.9535
CR	1.0945	2.9686	3.15×10^{-4}	46.38 ± 0.05^a	41.07 ± 0.11^a	0.9782

mean values with same letter (s) within the same row are not significantly different (One-way ANOVA, Fisher LSD-test, $\alpha = 0.05$)

The results in Table 4.13 showed that Thomas plots gave R^2 values of 0.9520, 0.9535 and 0.9782 for MO, MB and CR dyes respectively showing a good data fit as construed by appendix XVI B. Low standard deviation (< 1) demonstrated a good precision, most efficient and reliable recovery process for routine analysis of water samples (Mohd *et al.*, 2020). The results showed SN-5 as a promising adsorbent in dye wastewater treatment.

4.13 Column regeneration

To evaluate the column efficacy of the SN-5 adsorbent, the regeneration efficiency in each of the column adsorption-desorption cycle was determined. The SN-5 adsorbent loaded column was regenerated using 1.0 × 10^{-1} M NaOH or 1.0 × 10^{-1} M HCl eluents for four cycles during the column uptake of MO, CR and MB dyes. The desorption curves are presented by Figures 4.28 A, 4.28 B and 4.28 C.

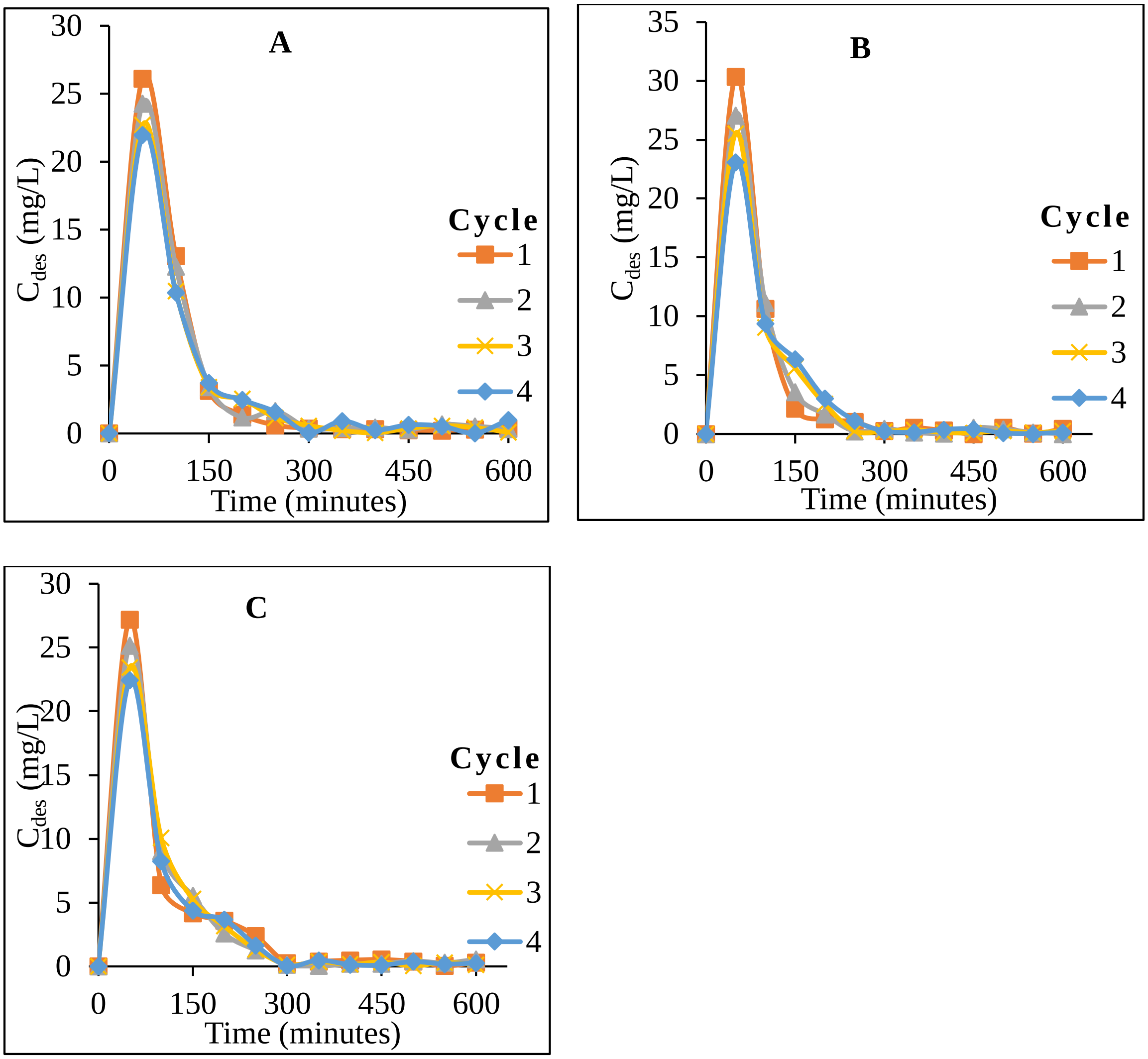

Figure 4.28: Column desorption curves for MO (A), MB (B) and CR (C) dyes (Q = 4 mL/min, Z = 7 cm)

From the results in Figure 4.28, the desorption process for all the four cycles showed a trend of a sharp increase, then a decrease. It was also seen that overall desorption process took about 8 hours for all the dyes after which further elution process was insignificant. A concentration of 26.12 ± 0.07 mg/L (MO), 30.36 ± 0.04 mg/L (MB) and 27.16 ± 0.13 mg/L (CR) was desorbed at a contact time of 50 minutes in the first desorption process. At the beginning of the desorption, higher concentration of the dyes was eluted but decreased as time progressed. This could be due to more accumulation of dyes loaded on the adsorbent (Reddy and Nirmala, 2014).

The total volume of wastewater treated over the four cycles was 6580 mL (MO), 5800 mL (MB) and 6400 mL (CR). The breakthrough times (t_b), saturation times (t_s), column capacity (Q_o) and regeneration efficiency (%) are presented in Table 4.14.

Table 4.14: Regeneration efficiency of SN-5 adsorbent for MO, MB and CR dyes

Dye	**Adsorption cycle**	**t_b (minutes)**	**t_s (minutes)**	**Column capacity, (Q_o, mg/g ± S.D)**	**Regeneration efficiency (% R ± S.D)**
MO	1	140	485	41.85 ± 0.12^a	55.04 ± 0.09^a
	2	120	430	36.45 ± 0.08^b	52.04 ± 0.03^b
	3	90	380	30.36 ± 0.05^c	51.66 ± 0.16^c
	4	80	350	27.77 ± 0.17^d	50.34 ± 0.04^d
MB	1	195	440	38.92 ± 0.08^a	62.41 ± 0.06^a
	2	150	380	32.73 ± 0.08^b	57.10 ± 0.01^b
	3	110	330	27.91 ± 0.02^c	54.90 ± 0.04^c
	4	90	300	25.16 ± 0.13^d	50.05 ± 0.27^d
CR	1	180	530	46.38 ± 0.05^a	56.43 ± 0.17^a
	2	150	410	35.29 ± 0.24^b	53.11 ± 0.08^b
	3	105	360	29.49 ± 0.09^c	52.05 ± 0.06^c
	4	90	300	23.79 ± 0.06^d	51.39 ± 0.01^d

mean values with same letter (s) within the same row are not significantly different (One-way ANOVA, Fisher LSD-test, $\alpha = 0.05$)

From the findings in Table 4.14, column regeneration experiments revealed that Q_o, t_b, t_s and % R decreased with advanced progressive column adsorption/desorption cycles. This could be due to a minimal loss of adsorbent particles because of it being re-used repeatedly (Dovi *et al.*, 2021). The results indicated that the fixed-bed column gets saturated early and that the column capacity decreased slightly as the adsorption-desorption cycles advanced upto the 4th cycle as shown by appendices XX and XXI. The regeneration efficiency was > 50 % (upto 4th cycle) for all the dyes. The results demonstrated that SN-5 adsorbent can be re-used repeatedly for textile dye wastewater treatment with minimal loss.

CHAPTER FIVE

CONCLUSIONS AND RECOMMENDATIONS

5.1 Conclusions

The research study aim was to explore the adsorptive potential of Si_3N_4 adsorbent derived from extracted silica from sand, biochar from coffee husks and macadamia nutshells for column uptake studies of selected dyes from a model and environmental water samples. The Marine National Park sand (MNPS), Bamburi Beach sand (BBS) and Crescent Island Crater sand (CICS) contain quartz (SiO_2), calcite ($CaCO_3$), microcline (K (Al, Fe) Si_3O_8) and clinochlore ($(Mg, Fe)_6(Si, Al)_4O_{10}(OH)_8)$) as revealed by the findings from XRD, XRF and FT-IR characterization. The extracted silica (ES) percentage yield was 35.01 ± 0.11 % (ES-1), 40.49 ± 0.06 % (ES-2) and 31.95 ± 0.26 % (ES-3). The silica content increased to 90.16 ± 0.47 %, 94.75 ± 0.48 % and 84.34 ± 0.45 % respectively. The XRD diffractograms showed a highly pure and amorphous extracted silica. The outcomes of the FT-IR analysis showed siloxane (Si-O-Si) and silanol (Si-OH) as important groups of the extracted silica.

The proximate analysis of biochar samples contained 16.73 ± 2.01 % (CHB) and 21.88 ± 5.28 % (MNB) of fixed carbon content. The FT-IR results of RCH, RMN and their respective biochar samples showed hydroxyl (-OH), carboxylate ($-COO^-$) (raw) and aromatic carbon bonds (C=C) (raw and biochar) as the main functional groups. The XRD results showed the presence of highly amorphous cellulosic materials (RCH and RMN) and biochar carbon structure (CHB and MNB). The SEM results of the biochar samples demonstrated a rougher and porous surface compared to their respective raw biomass samples. Also, the EDX results showed an increase in final carbon content of CHB and MNB to 70.1 % and 75.0 % respectively with negligent ash contents.

The FT-IR results of Si_3N_4 adsorbents showed functional groups of Silicon-Nitrogen (Si-N), Silanol (Si-OH) and Silicon-Nitrogen-Silicon (Si-N-Si), which were hydroxylated in water to silazane groups ($Si_2=NH_2^+$) and silanolate ($Si-O^-$) adsorbent sites for MO, MB and CR dyes removal. The XRD results showed α-Si_3N_4 and β- Si_3N_4 as major and minor phases respectively. The SEM micrographs showed rod-like and fiber-like Si_3N_4 structures with porous surfaces. The EDX spectra showed silicon and nitrogen components of Si_3N_4 adsorbents. The TGA results showed that the adsorbent was thermally stable as the temperature was raised to 600 °C.

The sorption of MO, MB and CR dyes was greatly influenced by initial concentration, agitation time, adsorbent dosage and pH. The maximum uptake was attained at an optimal dosage (30 mg), concentration (50 mg/L), agitation time (50 minutes) and pH of 1.00 (for MO and CR) and 11.00 for MB.

The maximum capacity was 26.93 ± 0.03 mg/g (SN-5), 29.74 ± 0.04 mg/g (SN-5) and 31.77 ± 0.15 mg/g (SN-2) for MO, MB and CR dyes respectively. The isotherm plots best fitted Langmuir and Dubinin-Radushkevich (D-R) models ($R^2 > 0.9$). The kinetic results conformed Pseudo-second-order model with $R^2 > 0.98$ which was preferable in describing the dyes uptake rate. The equilibrium and kinetic results implied that chemisorption predominated the CR, MO and MB dyes uptake onto the Si_3N_4 adsorbents.

The batch desorption studies showed highest desorption capacity of 24.97 ± 0.00 mg/g and 29.17 ± 0.00 mg/g (SN-5) was obtained with 1.0×10^{-1} M NaOH eluent for MO and CR dyes; 27.60 ± 0.00 mg/g (SN-5) with 1.0×10^{-1} M HCl best eluent for MB dyes. The desorption findings showed that the SN-5 adsorbent can be recovered and re-used easily with minimal adsorbent loss.

The SN-5 adsorbent performance for MO, CR and MB dyes uptake in a fixed-bed column was obtained at an optimal value of 50 mg/L, 4 mL/min and 7 cm. The results demonstrated that Yoon-Nelson and Thomas models ($R^2 > 0.91$) were more applicable in explaining the column dynamics which implied a monolayer chemical adsorption mechanism.

The column performance was investigated for SN-5 adsorbent using spiked water samples from river Athi. The SN-5 adsorbent gave a column capacity of 41.85 ± 0.12 mg/g (MO), 46.38 ± 0.05 mg/g (CR) and 38.92 ± 0.08 mg/g (MB). The column regeneration gave a regeneration efficiency of > 50 % (upto 4th cycle) for all the dyes.

The batch and column results showed the highest uptake capacity of Si_3N_4 adsorbents for CR dyes removal. That is, 31.77 ± 0.15 mg/g and 29.50 ± 0.05 mg/g for SN-2 (equilibrium and kinetic results). Also, 52.56 ± 0.04 mg/g and 46.38 ± 0.05 mg/g for fixed-bed column uptake using model and environmental water samples respectively.

5.2 Recommendations

5.2.1 Recommendations from this study

i. The research findings have shown the potential of Si_3N_4 adsorbent in textile dye wastewater treatment. Therefore, it is recommended that pilot-scale and industrial-scale trials be conducted to evaluate performance under real wastewater treatment conditions.

ii. The process uses abundant and low-cost raw materials—sand, coffee husks, and macadamia nutshells—making it environmentally and economically sustainable. It is recommended that local agricultural and mineral wastes be utilized for large-scale adsorbent synthesis.

iii. Encourage household or small-scale textile units to adopt Si_3N_4-based filtration columns for dye removal before wastewater discharge.

5.2.2 Recommendations for further studies

i. The sand from other regions should be investigated on their effectiveness on silica extraction for the synthesis of Si_3N_4 adsorbents.

ii. The process parameters of silica/carbon ratio, temperature, reaction time and nitrogen content on the synthesis of Si_3N_4 adsorbents using the raw materials should be investigated.

iii. Investigations on the effect of interfering species and water turbidity on the uptake of CR, MO and MB dyes from model water should be carried out.

iv. The potential of Si_3N_4 adsorbents in sorption of other textile dyes, phenolic compounds, nitrates, phosphates, heavy metal ions and microbes among others should be investigated.

v. Studies on the shelf life of Si_3N_4 adsorbents should be conducted.

vi. Studies on comparison of the Si_3N_4 adsorbents with the available commercial adsorbents on fixed-bed column performance using environmental water samples should be investigated.

REFERENCES

Abbas, S., Ahmad, Z. and Akbar, Q. (2019). Removal of para chlorophenol (PCP) from wastewater using aluminium/graphite electrode by electrochemical method. *International Journal of Scientific Research in Chemical Sciences*, 6 (5): 7-12.

Abbas, A., Abd, S. and Himdan, T. (2018). Kinetic study of methyl green dye adsorption from aqueous solution by bauxite clay at different temperatures. *Ibn Al-Haitham Journal for Pure & Applied Sciences*, 31 (1): 58-66.

Abdelhak, M., Ahmed, K., Abdelkader, B., Brahim, Z. and Rachid, K. (2014). Algerian Sahara sand dunes characterization. *Silicon*, 6: 149-154.

Abd Mutalib, M., Rahman, M.A., Othman M., Ismail, A. and Jaafar, J. (2017). Scanning Electron Microscopy (SEM) and Energy Dispersive X-Ray (EDX) spectroscopy. In membrane characterization. *Elsevier*, 9: 161-179.

Abdulhameed, A., Mbuvi, H., Changamu, E. and Maingi, F. (2018). Synthesis of silicon nitride from rice husk and sugarcane bagasse ashes. *Journal of Water technology and Treatment methods*, 1 (1): 106-111.

Abdul Rahim, A., Mohsin, H., Chin, K., Johari, K. and Saman, N. (2021). Promising low-cost adsorbent from desiccated coconut waste for removal of congo red dye from aqueous solution. *Water, Air & Soil Pollution*, 232 (9): 357-367.

Aboussabek, A., Boukarma, L., El Qdhy, S., Ousaa, A., Zerbet, M. and Chiban, M. (2024). Experimental investigation, kinetics and statistical modelling of methylene blue removal onto clay@Fe_2O_3: Batch, fixed bed column adsorption and photo-fenton degradation studies. *Case Studies in Chemical and Environmental Engineering*, 9 (5): 1-15.

Abualnaja, K., Alprol, A., Abu-Saied, M., Mansour, A. and Ashour, M. (2021). Studying the Adsorptive behavior of poly (acrylonitrile-co-styrene) and carbon nanotubes (nanocomposites) impregnated with adsorbent materials towards methyl orange dye. *Nanomaterials*, 11 (5): 1144-1165.

Adamu, A., Mbuvi, H.M and Evans, O.C. (2017). Removal of fluoride ion by silicon nitride powder. *International Journal of Water and Wastewater Treatment*, 3 (1): 1-7.

Adegoke, K. and Bello, O. (2015). Dye sequestration using agricultural wastes as adsorbents. *Water Resources and Industry*, 12: 8-24.

Adekanye, T., Dada, O. and Kolapo, J. (2022). Pyrolysis of maize cob at different temperatures for biochar production: Proximate, ultimate and spectroscopic characterisation. *Research in Agricultural Engineering*, 68 (1): 27-34.

Affat, S. (2021). Classifications, advantages, disadvantages, toxicity effects of natural and synthetic dyes: A review. *University of Thi-Qar Journal of Science*, 8 (1): 130-135.

Afriani, F., Evi, J., Mahardika, R., Rafsanjani, R. and Tiandho, Y. (2019). Purification of silica from tin tailing by acid leaching methods. *Advances in Engineering Research*, 167: 5-7.

Ahmad, R. and Ansari, K. (2021). Comparative study for adsorption of congo red and methylene blue dye on chitosan modified hybrid nanocomposite. *Process Biochemistry*, 108: 90-102.

Ahmad, A., Khan, N., Giri, B.S., Chowdhary, P. and Chaturvedi, P. (2020). Removal of methylene blue dye using rice husk, cow dung and sludge biochar: Characterization, application, and kinetic studies. *Bioresource Technology*, 306: 1-5.

Ahmad, R. and Mirza, A. (2017). Inulin-folic acid/bentonite: A novel nanocomposite for confiscation of Cu (II) from synthetic and industrial wastewater, *Journal of Molecular Liquids*, 241: 489-499.

Aigbe, U., Ukhurebor, K., Onyancha, R., Osibote, O., Darmokoesoemo, H. and Kusuma, H. (2021). Fly ash-based adsorbent for adsorption of heavy metals and dyes from aqueous solution: a review. *Journal of Materials Research and Technology,* 14: 2751-2774.

Akash, M. and Rehman, K. (2020). Essentials of pharmaceutical analysis: Thermo Gravimetric Analysis. *Springer*, 19: 215-222.

Akbar, N., Rosman, N., Hambali, S. and Abu Bakar, A. (2020). Adsorption of methylene blue by banana stem adsorbent in a continuous fixed bed column study. *Earth and Environmental Science*, 616 (1): 1-5.

Alardhi, S., Albayati, T. and Alrubaye, J. (2020). Adsorption of the methyl green dye pollutant from aqueous solution using mesoporous materials MCM-41 in a fixed-bed column. *Heliyon*, 6 (1): 1-7.

Albayati, T., Alwan, G.M. and Mahdy, O.S. (2017). High performance methyl orange capture on magnetic nanoporous MCM-41 prepared by incipient wetness impregnation method. *Korean Journal of Chemical Engineering*, 34 (1): 259-265.

Al-Alwadhi, Y.M., Pradhan, S., McKay, G., Al-Ansari, T. and Mackey, H. (2022). Coffee waste biochar: A widely available and low-cost biomass for producing carbonaceous water treatment adsorbents. *Chemical Engineering Transactions*, 92: 319-324.

Al-Husseiny, H.A. (2014). Adsorption of methylene blue dye using low cost adsorbent of sawdust: Batch and continues studies. *Journal of Babylon University/Engineering Sciences*, 22 (2): 296-310.

Al-Mahbashi, N., Kutty, S., Bilad, M., Huda, N., Kobun, R., Noor, A., Jagaba, A.H., Al-Nini, A., Ghaleb, A. and Al-dhawi, B. (2022). Bench-scale fixed-bed column study for the removal of dye-contaminated effluent using sewage-sludge-based biochar. *Sustainability*, 14 (11): 6484-6499.

Al-Salihi, S., Jasim, A.M., Fidalgo, M. and Xing, Y. (2022). Removal of congo red dyes from aqueous solutions by porous γ-alumina nanoshells. *Chemosphere*, 286: 1-9.

Alghamdi, W. and El Mannoubi, I. (2021). Investigation of seeds and peels of *Citrullus colocynthis* as efficient natural adsorbent for methylene blue dye. *Processes*, 9 (8): 1279-1297.

Alharby, N., Almutairi, R. and Mohamed, N. (2021). Adsorption behavior of methylene blue dye by novel crosslinked O-CM chitosan hydrogel in aqueous solution: Kinetics, isotherm and thermodynamics. *Polymers*, 13 (21): 3659-3686.

Ali, H. and Mohammed, A. (2021). Removal of congo red from aqueous solution by circulating fluidized bed (CFB). *Association of Arab Universities Journal of Engineering Sciences*, 28 (2):1-7.

Ali, H. and Mohammed, A. (2020). Elimination of congo red dyes from aqueous solution using *Eichhornia crassipes*. *Iraqi Journal of Chemical and Petroleum Engineering*, 21 (4): 21-32.

Alpay, B. (2014). Investigations of the productions of silicon nitride from Turkish rice husk. Master's Thesis. *Middle East Technical University*.
https://hdl.handle.net/11511/23342

Alvarez, J., Lopez, G., Amutio, M., Bilbao, J. and Olazar, M. (2016). Preparation of adsorbents from sewage sludge pyrolytic char by carbon dioxide activation. *Process Safety and Environmental Protection*, 103: 76-86.

Alyosef, H., Ibrahim, S., Welscher, J., Inayat, A., Eilert, A., Denecke, R., Schwieger, W., Münster, T., Kloess, G., Einicke, W. and Enke, D. (2014). Effect of acid treatment on the chemical composition and the structure of Egyptian diatomite. *International Journal of Mineral Processing*, 132: 17-25.

Aminu, I., Gumel, S.M., Ahmad, W. and Idris, A. (2020). Adsorption isotherms and kinetic studies of congo-red removal from wastewater using activated carbon prepared from Jujube seed. *American Journal of Analytical Chemistry*, 11 (1): 47-59.

Andriayani, Muis, Y. and Nasution, D.Y. (2021). Chemical reduction of silica into silicon from extracted quartz sand using sodium hydroxide and hydrochloric acid solutions. *AIP Conference Proceedings*, 2342 (1): 1-6.

Anim, D. and Ofori-Asenso, R. (2020). Water scarcity and COVID-19 in sub-saharan Africa. *The Journal of Infection*, 81 (2): e108-e109.

Antolik, A. and Daria, J. (2021). Assessment of the alkali-silica reactivity potential in granitic rocks. *Construction and Building Materials*, 295: 1-12.

Anuar, M., Fen, Y., Emilia, R. and Khaidir, M. (2018) Synthesis and structural properties of coconut husk as potential silica source. *Results in Physics*, 11: 1-4.

Aroke, U., Momoh, R., Hamidu, L. and Buhari, U. (2020). Removal of azo dye methyl orange in aqueous solution by kaolinite clay: Equilibrium isotherms, kinetics and error analyses. *Saudi Journal of Engineering and Technology*, 5 (11): 422-433.

Arora, C., Sahu, D., Bharti, D., Vinita, T., Soni, S. and Sharma, S. (2019). Adsorption of hazardous dye crystal violet from industrial waste using low-cost adsorbent *Chenopodium album*. *Desalination and Water Treatment*, 167: 324-332.

Arslan, S., Eyvaz, M., Gürbulak, E. and Yüksel, E. (2016). A review of state of the art technologies in dye containing wastewater treatment the textile industry case. In textile wastewater treatment. *Intech Open*, 1: 1-10.

Arunmetha, S., Karthik, A., Srither, R., Vinoth, M., Suriyaprabha, R., Manivasakan, P. and Rajendran, V. (2015). Size-dependent physicochemical properties of mesoporous nanosilica produced from natural quartz sand using three different methods. *RSC Advances*, 5 (59): 47390-47397.

Awsiuk, K., Budkowski, A., Psarouli, A., Petrou, P., Bernasik, A., Kakabakos, S., Rysza, J. and Raptis, I. (2013). Protein adsorption and covalent bonding to silicon nitride surfaces modified with organo-silanes: Comparison using AFM, angle-resolved XPS and multivariate ToF-SIMS analysis. *Colloids and Surfaces B: Biointerfaces*, 110: 217-224.

Ayalew, A. and Aragaw, T. (2020). Utilization of treated coffee husk as low-cost bio-sorbent for adsorption of methylene blue. *Adsorption Science & Technology*, 38 (5): 205-222.

Aywa, J.O. (2017). Suitability of Athi River water for irrigation within Athi River town and its environs. Master’s Thesis. *South Eastern Kenya University*.
http://repository.seku.ac.ke/handle/123456789/3463

Aziz, N., Othman, N., Ibrahim, N., Yunus, Z. and Setiawan, M. (2019). Optimization of pH and contact time of media in removing calcium and magnesium from groundwater. *International Journal of Integrated Engineering*, 11 (9): 63-72.

Azzahra, A., Yusefin, E.S., Salima, G., Mudita, M., Febriani, N.A. and Nandiyanto, A. (2020). Synthesis of nanosilica materials from various sources using various methods. *Journal of Applied Science and Environmental Studies*, 3 (4): 254-278.

Babazadeh, M., Abolghasemi, H., Esmaeili, M., Ehsani, A. and Badiei, A. (2021). Comprehensive batch and continuous methyl orange removal studies using surfactant modified chitosan-clinoptilolite composite. *Separation and Purification Technology*, 267: 1-19.

Baharlouei, A., Jalilnejad, E. and Sirousazar, M. (2018). Fixed-bed column performance of methylene blue biosorption by *Luffa cylindrica*: Statistical and mathematical modeling. *Chemical Engineering Communications,* 205 (11): 1537-1554.

Bahrudin, N., Nawi, M., Jawad, A. and Sabar, S. (2020). Adsorption characteristics and mechanistic study of immobilized chitosan-montmorillonite composite for methyl orange removal. *Journal of Polymers and the Environment*, 28 (7): 1901-1913.

Banerjee, S., Debsarkar, A. and Datta, S. (2017). Removal of basic dyes from aqueous solution by adsorption using rice husk ash-A fixed bed column study. *International Journal of Advanced Engineering, Management and Science*, 3 (4): 325-330.

Beddiaf, S., Chihi, S. and Leghrieb, Y. (2015). The determination of some crystallographic parameters of quartz, in the sand dunes of Ouargla, Algeria. *Journal of African Earth Sciences*, 106: 129-133.

Bellifa, A., Makhlouf, M. and Boumila, Z. (2017). Comparative study of the adsorption of methyl orange by bentonite and activated carbon. *Acta Physica Polonica A*, 132 (3): 466-468.

Benchaa, S., Gheriani, R., Achouri, A., Bouguettaia, H. and Mechri, M. (2021). Structural characterizations of dune sand and construction sand of Sidi Slimane and Zaouia El Abidia areas in the Touggourt region in southeast Algeria. *Arabian Journal of Geosciences,* 14 (22): 1-11.

Bennani, K.A., Mounir, B., Hachkar, M., Bakasse, M. and Yaacoubi, A. (2015). Adsorption of cationic dyes onto Moroccan clay: Application for industrial wastewater treatment. *Journal of Material and Environmental Science,* 6 (9): 2483-2500.

Benzekri, M., Benderdouche, N., Bestani, B., Douara, N. and Duclaux, L. (2018). Valorization of olive stones into a granular activated carbon for the removal of methylene blue in batch and fixed bed modes. *Journal of Materials and Environmental Sciences*, 9 (1): 272-284.

Bharathi, K.S. and Ramesh, S.P. (2013). Fixed-bed column studies on biosorption of crystal violet from aqueous solution by *Citrullus lanatus* rind and *Cyperus rotundus*. *Applied Water Science*, 3: 673-687.

Bidu, J., Bruggen, B., Rwiza, M. and Njau, K. (2021). Current status of textile wastewater management practices and effluent characteristics in Tanzania. *Water Science Technology*, 83 (10): 2363-2376.

Biesuz, M., Bettotti, P., Signorini, S., Bortolotti, M., Campostrini, R., Bahri, M., Ersen, O., Speranza, G., Lale, A., Bernard, S. and Sorarù, G.D. (2019). First synthesis of silicon nanoscrystals in amorphous silicon nitride from a preceramic polymer. *Nanotechnology*, 30 (25): 255601-255620.

Biswas, R., Khan, P., Mukherjee, S., Mukhopadhyay, A., Ghosh, J. and Muraleedharan, K. (2018). Study of short range structure of amorphous silica from PDF using Ag radiation in laboratory XRD system, RAMAN and NEXAFS. *Journal of Non-Crystalline Solids*, 488: 1-9.

Boretti, A. (2022). Covid 19 pandemic as a further driver of water scarcity in Africa. *GeoJournal*, 87 (2): 787-814.

Boateng, G., Collins, S., Mbullo, P., Wekesa, P., Onono, M., Neilands, T. and Young, S. (2018). A novel household water insecurity scale: Procedures and psychometric analysis among postpartum women in western Kenya. *PloS one*, 13 (6): 1-28.

Boualem, A., Leontie, L., Lopera, S. and Hamzaoui, S. (2021). Synthesis and characterization of mesoporous silica from Algerian river sand for solar grade silicon: Effect of alkaline concentration on the porosity and purity of silica powder. *Silicon*, 14 (10): 5231-5240.

Bousbih, R., Haddadi, I., Zina, H., Alatawi, N. and Ezzaouia, H. (2020). Purification of Tabuk silica using chemical attack and thermal treatment. *Journal of Non-Oxide Glasses*, 12 (3): 27-30.

Bushra, B. and Remya, N. (2020). Biochar from pyrolysis of rice husk biomass—characteristics, modification and environmental application. *Biomass Conversion and Biorefinery*, 10: 1-12.

Çatlıoğlu, F., Akay, S., Turunç, E., Gözmen, B., Anastopoulos, I., Kayan, B. and Kalderis, D. (2021). Preparation and application of Fe-modified banana peel in the adsorption of methylene blue: Process optimization using response surface methodology. *Environmental Nanotechnology, Monitoring & Management*, 16: 1-11.

Cazako, C., Inal, K., Burr, A., Georgi, F. and Cauro, R. (2018). Hypothetic impact of chemical bonding on the moisture resistance of amorphous $Si_XN_YH_Z$ by plasma-enhanced chemical vapor decomposition. *Metallurgical Research & Technology*, 115 (4): 406-411.

Chafi, M., Akazdam, S., Asrir, C., Sebbahi, L., Gourich, B., Barka, N. and Essahli, M. (2016). Continuous fixed bed reactor application for decolourization of textile effluent by adsorption on NaOH treated eggshell. *International Journal of Materials and Textile Engineering*, 9 (10): 1242-1248.

Chakraborty, S., Sharmin, S., Rony, S.R., Ahmad, S. and Sohrab, M. (2018). Stability-indicating UV/Vis spectrophotometric method for diazepam, development and validation. *Indian Journal of Pharmaceutical Sciences*, 80 (2): 366-373.

Chang, R., Sohi, S.P., Jing, F., Liu, Y. and Chen, J. (2019). A comparative study on biochar properties and Cd adsorption behavior under effects of ageing processes of leaching, acidification and oxidation. *Environmental Pollution*, 254: 1-12.

Chang, J., Ma, J., Ma, Q., Zhang, D., Qiao, N., Hu, M. and Ma, H. (2016). Adsorption of methylene blue onto Fe_3O_4/activated montmorillonite nanocomposite. *Applied Clay Science*, 119: 132-140.

Cheah, W., Hosseini, S., Khan, M., Chuah, T. and Choong, T. (2013). Acid modified carbon coated monolith for methyl orange adsorption. *Chemical Engineering Journal*, 215: 747-754.

Chen, C., Sun, K., Huang, C., Yang, M., Fan, M., Wang, A., Zhang, G., Li, B., Jiang, J., Xu, W. and Liu, J. (2023). Investigation on the mechanism of structural reconstruction of biochars derived from lignin and cellulose during graphitization under high temperature. *Biochar*, 5 (1): 51-64.

Chen, X. (2015). Modeling of experimental adsorption isotherm data. *Information*, 6 (1): 14-22.

Chen, Y., Furmann, A., Mastalerz, M. and Schimmelmann, A. (2014). Quantitative analysis of shales by KBr-FTIR and micro-FTIR. *Fuel*, 116: 538-549.

Cheng, Y., Luo, F., Jiang, Y., Li, F. and Wei, C. (2018). The effect of calcination temperature on the structure and activity of TiO_2/SiO_2 composite catalysts derived from titanium sulfate and fly ash acid sludge. *Colloids and Surfaces A*, 554: 81-85.

Cheruiyot, G., Wanyonyi, W., Kiplimo, J. and Maina, E. (2019). Adsorption of toxic crystal violet dye using coffee husks. Equilibrium, kinetics and thermodynamics study. *Scientific African*, 5: 1-11.

Chowdhury, Z., Hamid, S. and Zain, S. (2015). Evaluating design parameters for breakthrough curve analysis and kinetics of fixed bed columns for Cu (II) cations using lignocellulosic wastes. *BioResources*, 10 (1): 732-749.

Conrad, E., Nnaemeka, O. and Enenebeaku, E. (2016). Adsorption of congo red dye from aqueous solution using agricultural waste. *IOSR Journal of Applied Chemistry*, 9 (9): 39-51.

Cui, H., Abu-Siada, A., Li, S. and Islam, S. (2017). Correlation between dissolved gases and oil spectral response. *1st international conference on electrical materials and power equipment*. IEEE. Pp. 28-32.

Cui, J., Li, B., Zou, C., Zhang, C. and Wang, S. (2015). Direct synthesis of α-silicon nitride nanowires from silicon monoxide on alumina. *Nanomaterials and Nanotechnology*, 5: 32-37.

Cundari, L., Afrah, B, Utami, D. and Matondang, N. (2019). Adsorption model in removal of direct synthetic dyes in aqueous solution onto tea waste. *Journal of Physics: Conference Series,* 1167: 1-9.

Daneshvar, E., Vzirzadeh, A., Niazi, A., Kousha, M. and Naushad, M. (2017). Desorption of methylene blue dye from brown macroalga: Effects of operating parameters, isotherm study and kinetic modeling. *Journal of Cleaner Production*, 152: 443-453.

Das, R., Ali, M. and Hamid, S. (2014). Current applications of X-Ray powder diffraction-A review. *Review on Advanced Materials Science,* 38 (2): 95-109.

Dastgerdi, Z.H., Meshkat, S.S. and Jalili, H. (2020). Investigation of an adsorptive indigo carmine dye removal via packed bed column: Experiments and computational fluid dynamics simulation. *AUT Journal of Mechanical Engineering*, 4 (3): 315-330.

Ding, W., Habineza, A., Zeng, X., Yana, Z., Yana, J. and Yang, G. (2022). Adsorption of methylene blue and methyl orange on nano zero-valent iron (nZVI) coated biochar: Column adsorption experiments. *Desalination and Water Treatment*, 260: 169-178.

Dinu, M., Lazar, M. and Dragan, E. (2017). Dual ionic cross-linked alginate/clinoptilolite composite microbeads with improved stability and enhanced sorption properties for methylene blue. *Reactive and Functional Polymers*, 116: 31-40.

Dlamini, M., Bhaumik, M., Pillay, K. and Maity, A. (2021). Polyaniline nanofibers, a nanostructured conducting polymer for the remediation of methyl orange dye from aqueous solutions in fixed-bed column studies. *Heliyon*, 7 (10): 1-13.

Dotto, G. and McKay, G. (2020). Current scenario and challenges in adsorption for water treatment. *Journal of Environmental Chemical Engineering*, 8 (4): 1-6.

Dovi, E., Aryee, A., Kani, A.N., Mpatani, F., Li, J., Li, Z., Qu, L. and Han, R. (2021). Functionalization of walnut shell by grafting amine groups to enhance the adsorption of congo red from water in batch and fixed-bed column modes. *Journal of Environmental Chemical Engineering*, 9 (5): 1-14.

Drozdov, A., Zemnukhova, L., Panasenko, A., Polyakova, N., Slobodyuk, A., Ustinov, A., Didenko, N. and Tyurin, S. (2021). Silicon compounds in sponges. *Applied sciences*, 11 (14): 6587-6609.

Duguma, L., Muthee, K., Carsan, S., Muriuki, J., Bulitta, B., Ayana, A., Kibugi, R. and Suleman, K. (2022). Innovation pathways in the coffee sector in Ethiopia and Kenya. *World Agroforestry*, 6: 1-22.

Duhan, M. and Kaur, R. (2019). Adsorptive removal of methyl orange with polyaniline nanofibers: An unconventional adsorbent for water treatment. *Environmental Technology*, 41 (23): 2977-2990.

Egbosiuba, T., Abdulkareem, A., Kovo, A., Afolabi, E., Tijani, J.O., Auta, M. and Roos, W. (2020). Ultrasonic enhanced adsorption of methylene blue onto the optimized surface area of activated carbon: Adsorption isotherm, kinetics and thermodynamics. *Chemical Engineering Research and Design*, 153: 315-336.

El-Didamony, H., El-Fadaly, E., Amer, A. and Abazeed, I. (2020). Synthesis and characterization of low cost nanosilica from sodium silicate solution and their applications in ceramic engobes. *Journal of the Spanish Ceramic and Glass Society*, 59 (1): 31-43.

El-Kousy, S., El-Shorbagy, H. and El-Ghaffar, M. (2020). Chitosan/montmorillonite composites for fast removal of methylene blue from aqueous solutions. *Materials Chemistry and Physics*, 254: 1-57.

El-Sawy, A., Gemeay, A.H., Helal, A.S. and Salem, M.A. (2021). Catalytic degradation of methylene blue in aqueous solution by H_2O_2 and SiO_2-NH_2-Cu(II)@SiO_2 nanoparticles as catalyst. *Journal of Molecular Liquids*, 341: 1-15.

Elwakeel, K., Elgarahy, A. Elshoubaky, G. and Mohammad, S. (2020). Microwave assist sorption of crystal violet and congo red dyes onto amphoteric sorbent based on upcycled Sepia shells. *Journal of Environmental Health Science and Engineering*, 18: 35-50.

Eshun, J., Wang, L., Ansah, E., Shahbazi, A., Schimmel, K., Kabadi, V. and Aravamudhan, S. (2019). Characterization of the physicochemical and structural evolution of biomass particles during combined pyrolysis and CO_2 gasification. *Journal of the Energy Institute*, 92 (1): 82-93.

Export Processing Zone Authority (EPZA) (2016). Project Report for a Proposed Construction of Phase 2 EPZA Waste Water Treatment Plan. Vol. 1, Kenya.

Fachini, J., de Figueiredo, C., Joaquim, J., Rosa, S., da Silva, J. and do Vale, A. (2021). Novel K-enriched organomineral fertilizer from sewage sludge-biochar: Chemical, physical and mineralogical characterization. *Waste Management*, 135: 98-108.

Fadhil, O. and Eisa, M. (2019). Removal of methyl orange from aqueous solutions by adsorption using corn leaves as adsorbent material. *Journal of Engineering*, 25 (4): 55-69.

Faghihzadeh, F., Anaya, N., Schifman, L. and Oyanedel-Craver, V. (2016). Fourier Transform Infrared Spectroscopy to assess molecular-level changes in microorganisms exposed to nanoparticles. *Nanotechnology for Environmental Engineering*, 1 (1): 1-16.

Farghali, M., Abo-Aly, M. and Salaheldin, T. (2021). Modified mesoporous zeolite-A/reduced graphene oxide nanocomposite for dual removal of methylene blue and Pb^{2+} ions from wastewater. *Inorganic Chemistry Communications*, 126: 1-16.

Farias, R., Buarque, H., Cruz, M., Cardoso, L., Gondim, T. and Paulo, V. (2018). Adsorption of congo red dye from aqueous solution onto amino-functionalized silica gel. *Sanitary Engineering Journal*, 23 (6): 1053-1060.

Fardhyanti, D., Putri, R., Fianti, O., Simalago, A. and Akhir, A. (2018). Synthesis of silica powder from sugarcane bagasse ash and its application as adsorbent in adsorptive-distillation of ethanol-water solution. *MATEC Web of Conferences*, 237: 1-6.

Farzana, R., Rajarao, R., Mansuri, I. and Sahajwalla, V. (2018). Sustainable synthesis of silicon nitride nanowires using waste carbon fibre reinforced polymer (CFRP). *Journal of Cleaner Production*, 188: 371-377.

Fayomi, J., Popoola, A., Popoola, O.M., Oladijo, O. and Fayomi, O. (2020). Understanding the microstructural evolution, mechanical properties, and tribological behavior of AA8011-reinforced nano-Si_3N_4 for automobile application. *The International Journal of Advanced Manufacturing Technology*, 111 (1): 53-62.

Firdaus, M., Madina, F., Sasti, Y., Elvia, R., Ishmah, S., Eddy, D. and Cid-Andres, A. (2020). Silica extraction from beach sand for dyes removal: Isotherms, kinetics and thermodynamics. *Rasayan Journal of Chemistry*, 13 (1): 249-254.

Fortunate, P. and Misael, S. (2016). Removal of methyl orange from water by adsorption onto modified local clay (Kaolinite). *Physical Chemistry*, 6 (2): 39-48.

Gadekar, M. and Ahammed, M. (2016). Coagulation/flocculation process for dye removal using water treatment residuals: Modelling through artificial neural networks. *Desalination and Water Treatment*, 57 (55): 26392-26400.

Gallop, S., Kennedy, D., Loureiro, C., Naylor, L., Muñoz-Pérez, J., Jackson, D. and Fellowes, T. (2020). Geologically controlled sandy beaches: Their geomorphology, morphodynamics and classification. *Science of the Total Environment*, 731: 1-96.

Gawande, S., Belwalkar, N. and Mane, A. (2017). Adsorption and its isotherm-theory. *International Journal of Engineering Research*, 6 (6): 312-316.

Gerçel, Ö. (2015). Removal of textile dye from aqueous solution by electrochemical method. *Separation Science and Technology*, 51 (4): 711-717.

Ghosh, G., Chakraborty, T., Zaman, S., Nahar, M. and Kabir, A. (2020). Removal of methyl orange dye from aqueous solution by a low cost activated carbon prepared from mahagoni (*Swietenia mahagoni*) bark. *Pollution*, 6 (1): 171-184.

Giwa, A., Dindi, A. and Kujawa, J. (2018). Membrane bioreactors and electrochemical processes for treatment of wastewaters containing heavy metal ions, organics, micropollutants and dyes: Recent developments, *Journal of Hazardous Materials*, 370: 172-195.

Gollakota, A., Munagapati, V.S., Volli, V., Gautam, S., Wen, J. and Shu, C. (2021). Coal bottom ash derived zeolite (SSZ-13) for the sorption of synthetic anion Alizarin Red S (ARS) dye. *Journal of Hazardous Materials,* 416: 1-13.

Gonciarz, L., Urbaniak, M., Kaca, W. and Chmiela, M. (2020). Use of Fourier-Transform Infrared spectroscopy (FT-IR) for monitoring experimental *Helicobacter pylori* infection and related inflammatory response in guinea pig model. *International Journal of Molecular Sciences*, 22 (1): 281-297.

Gopal, N., Asaithambi, M., Sivakumar, P. and Sivakumar, V. (2016). Continuous fixed bed adsorption studies of Rhodamine-B dye using polymer bound adsorbent. *Indian Journal of Chemical Technology*, 23: 53-58.

Goswami, R. and Dey, A. (2022). Synthesis and application of treated activated carbon for cationic dye removal from modelled aqueous solution. *Arabian Journal of Chemistry*, 15 (11): 1-21.

Goutam, S.P., Saxena, G., Roy, D., Yadav, A.K. and Bharagava, R.N. (2020). Green synthesis of nanoparticles and their applications in water and wastewater treatment. Bioremediation of industrial waste for environmental safety. *Springer*, 16: 349-379.

Gupta, V., Suhas, Tyagi, I., Agarwal, S., Singh, R., Chaudhary, M., Harit, A. and Kushwaha, S. (2016). Column operation studies for the removal of dyes and phenols using a low cost adsorbent. *Global Journal of Environmental Science and Management*, 2 (1): 1-10.

Gurung, A., Adhikari, S., Chauhan, R., Thakuri, S., Nakarmi, S., Ghale, S., Dongol, B.S. and Rijal, D. (2019). Water crises in a water-rich country: case studies from rural watersheds of Nepal's mid-hills. *Water Policy,* 21 (4): 826-847.

Gusain, R., Kumar, N. and Ray, S. (2020). Recent advances in carbon nanomaterial-based adsorbents for water purification. *Coordination Chemistry Reviews*, 405: 1-56.

Hachani, R., Sabir, H., Sana, N., Zohra, K. and Nesrine, N. (2017). Performance study of a low-cost adsorbent-raw date pits-for removal of azo dye in aqueous solution. *Water Environment Research*, 89 (9): 827-839.

Hachem, R., Meftah, N. and Bouaziz, A. (2023). A comparative analysis of the microstructural and physicochemical properties of alluvial and dune sands from northeast Algerian Sahara. *The Journal of Engineering and Exact Sciences*, 9 (6): 1-14.

Hackley, V. and Malghan, S. (1994). The surface chemistry of silicon nitride powder in the presence of dissolved ions. *Journal of Materials Science*, 29: 4420-4430.

Han, W., Jiao, H. and Fox, D. (2018). Scanning Electron Microscopy. In: *Springer Tracts in Modern Physics*, 272: 35-68.

Harshananda, T., Ayisha, T.M., Janani Priyanka, P., Mather, K. and Vijayakumar, R. (2020). Removal of colour from textile effluent by adsorption using banana stem and coffee husk: A review. *IOSR Journal of Mechanical and Civil Engineering*, 17 (4): 32-41.

Hasdemir, S., Tugˇrul, A. and Yilmaz, M. (2012). Evaluation of alkali reactivity of natural sands. *Construction and Building Materials*, 29: 378-385.

Hassan, M. and Carr, C. (2018). A critical review on recent advancements of the removal of reactive dyes from dyehouse effluent by ion-exchange adsorbents. *Chemosphere*, 209: 201-219.

Honorato, A., Pardinho, R., Dragunski, D., Gonçalves Junior, A. and Caetano, J. (2017). Biosorbent of macadamia residue for cationic dye adsorption in aqueous solution. *Acta Scientiarum: Technology*, 39 (1): 97-102.

Hoseini, M., Cocco, S., Casucci, C., Cardelli, V. and Corti, G. (2021). Coffee by-products derived resources. A review. *Biomass and Bioenergy*, 148: 1-10.

Hou, Y., Liang, Y., Hu, H., Tao, Y., Zhou, J. and Cai, J. (2021). Facile preparation of multi-porous biochar from lotus biomass for methyl orange removal: Kinetics, isotherms, and regeneration studies. *Bioresource Technology*, 329: 1-7.

Hu, Q. and Zhang, Z. (2019). Application of Dubinin–Radushkevich isotherm model at the solid/solution interface: A theoretical analysis. *Journal of Molecular Liquids*, 277: 646-648.

Huang, J., Huang, Z., Yi, S., Liu, Y., Fang, M. and Zhang, S. (2013). Fe-catalyzed growth of one-dimensional α-Si_3N_4 nanostructures and their cathodoluminescence properties. *Scientific reports*, 3 (1): 3504-3512.

Huljana, M., Rodiah, S., Al Jabbar, J., Ichsan, C. and Marzuki, H. (2021). Silica-rice husk as adsorbent of Cr (VI) ions prepared through sol-gel method. *Walisongo Journal of Chemistry*, 4 (1): 65-73.

Hummadi, K., Luo, S. and He, S. (2022). Adsorption of methylene blue dye from the aqueous solution *via* bio-adsorption in the inverse fluidized-bed adsorption column using the torrefied rice husk. *Chemosphere*, 287: 1-11.

Hurairah, S., Lajis, N. and Halim, A. (2020). Methylene blue removal from aqueous solution by adsorption on *Archidendron jiringa* seed shells. *Journal of Geoscience and Environment Protection*, 8 (2): 128-143.

Iheanacho, O.C., Nwabanne, J., Obi, C. and Onu, C.E. (2021). Packed bed column adsorption of phenol onto corn cob activated carbon: Linear and nonlinear kinetics modeling. *South African Journal of Chemical Engineering*, 36: 80-93.

Inkson, B.J (2016). Scanning Electron Microscopy (SEM) and Transmission Electron Microscopy (TEM) for materials characterization. Materials characterization using nondestructive evaluation (NDE) methods. *Elsevier*, 2:18-43.

Ishmah, S., Permana, M., Firdaus, M. and Eddy, D. (2020). Extraction of silica from Bengkulu beach sand using alkali fusion method. *PENDIPA Journal of Science Education*, 4 (2): 1-5.

Isiuku, B. and Horsfall, M. (2017). Packed-bed column adsorption of Metanil Yellow (MY) from simulated wastewater using granular NaOH-activated carbon from cassava (*Manihot esculenta*) peels. *World News of Natural Sciences*, 14: 11-35.

Islam, M., Hyder, A., Saenz-Arana, R., Hernandez, C., Guinto, T., Ahsan, M., Bonifacio, A. and Noveron, J. (2019). Removal of methylene blue and tetracycline from water using peanut shell derived adsorbent prepared by sulfuric acid reflux. *Journal of Environmental Chemical Engineering*, 7 (1): 1-40.

Ismail, A., Saputri, N., Dwiatmoko, A., Susanto, B. and Nasikin, M. (2021). A facile approach to synthesis of silica nanoparticles from silica sand and their application as superhydrophobic material. *Journal of Asian Ceramic Societies*, 9 (2): 665-672.

Ismail, A., Widyaningtyas, A., Susanto, B. and Nasikin, M. (2020). Facile synthesis silica nanoparticles from Indonesia silica sand and their physico-chemical properties. *Key Engineering Materials*, 862: 35-39.

Jadhav, S. and Thorat, S. (2022). Adsorption isotherm of crystal violet dye onto biochar prepared from agricultural waste. *Oriental Journal of Chemistry*, 38 (2): 475-481.

Jagdale, P., Ziegler, D., Rovere, M., Tulliani, J.M. and Alberto, T. (2019). Waste coffee ground biochar: A material for humidity sensors. *Sensors*, 19 (4): 801-816.

Jaime, L., Dalia, I., Reyna, G. and Ma, A. (2018). Study of a fixed-bed column in the adsorption of an azo dye from an aqueous medium using a chitosan–glutaraldehyde biosorbent. *Adsorption Science & Technology*, 36 (1): 215-232.

Jain, S., Tamboli, S.R., Sutar, D.S., Jadhav, S., Marathe, J., Shaikh, A. and Prajapati, A. (2020). Batch and continuous studies for adsorption of anionic dye onto waste tea residue: Kinetic, equilibrium, breakthrough and reusability studies. *Journal of Cleaner Production*, 252: 1-35.

Jan, S., Ahmad, Y., Ali, M., Hussain, Z. and Melhi, S. (2022). Adsorptive removal of methylene blue from aqueous solution using sawdust. *Medicon Pharmaceutical Sciences*, 2 (1): 8-16.

Jatoi, A., Baloch, H.A., Mazari, S., Mubarak, N., Sabzoi, N., Aziz, S., Soomro, S., Abro, R. and Shah, S.F. (2021). A review on extractive fermentation via ion exchange adsorption resins opportunities, challenges, and future prospects. *Biomass Conversion and Biorefinery*, 13: 3543-3554.

Jawad, A., Rashid, R., Ishak, M. and Ismail, K. (2018). Adsorptive removal of methylene blue by chemically treated cellulosic waste banana (*Musa sapientum*) peels. *Journal of Taibah University for Science*, 12 (6): 809-819.

Jhansirani, K., Dubey, R., More, M. and Singh, S. (2016). Deposition of silicon nitride films using chemical vapor deposition for photovoltaic applications. *Results in Physics*, 6: 1059-1063.

Ji, H., Huang, Z., Chen, K., Li, W., Gao, Y., Fang, M., Liu, Y. and Wu, X. (2014). Synthesis of Si_3N_4 powder with tunable α/β-Si_3N_4 content from waste silica fume using carbothermal reduction nitridation. *Powder Technology*, 252: 51-55.

Jiang, R., Zhu, H.Y., Fu, Y.Q., Zong, E.M., Jiang, S.T., Li, J.B. Zhu, J.Q. and Zhu, Y.Y. (2021). Magnetic $NiFe_2O_4$/MWCNTs functionalized cellulose bioadsorbent with enhanced adsorption property and rapid separation. *Carbohydrate Polymers*, 252: 1-40.

Jin, X., Xing, P., Zhuang, Y., Kong, J., Jiang, S. and Wei, D. (2019). Effect of Si_3N_4 diluent on direct nitridation of silicon powder. *Ceramics International*, 45 (8): 10943-10950.

Jovanovski, G. and Makreski, P. (2016). Minerals from macedonia. XXX. Complementary use of vibrational spectroscopy and X-Ray powder diffraction for spectra-structural study of some cyclo-, phyllo- and tectosilicate minerals. A review. *Macedonian Journal of Chemistry and Chemical Engineering*, 35 (2): 125-155.

Kabayo, S., Kindala, J., Nkanga, C., Krause, R. and Taba, K. (2019). Preparation and characterization of solid acid catalysts derived from coffee husks. *International Journal of Chemical Science*, 3 (6): 5-13.

Kakhki, R., Rahni, S.Y. and Karimian, A. (2020). Removal of methyl orange from aqueous solutions by a novel, high efficient and low cost copper-modified nanoalum. *Inorganic and Nano-Metal Chemistry*, 51 (9): 1291-1296.

Kalai, S. and Suganthi, N. (2019). Optimization of column studies on the adsorption of congo red dye using phosphoric acid-treated *Eichhornia crassipes*. *International Journal of ChemTech Research*, 12 (5): 188-199.

Kamau, A., Thiong'o, G. and Kakoi, B. (2020). Equilibrium studies for removal of cadmium (II) ions removal from water using activated carbon derived from *Macadamia Intergrifolia* nutshell waste powder. *International Research Journal of Pure & Applied Chemistry*, 21 (23): 185-197.

Kandisa, R., Narayana, S., Gopinadh, R. and Veerabhadram, K. (2018). Kinetic studies on adsorption of methylene blue using natural low cost adsorbent. *Journal of Industrial Pollution Control*, 34 (2): 2054-2058.

Kanyiri, G. and Waswa, F. (2017). Enhancing benefits from biomass wastes within small-medium scale coffee processing factories in Kiambu County, Kenya. *African Journal of Environmental Science and Technology*, 11 (4): 198-206.

Kemp, E., Roseburrough, R., Elliott, E. and Krause, J. (2021). Spatial variability of sediment amorphous silica and its reactivity in a northern Gulf of Mexico estuary and coastal zone. *Gulf and Caribbean Research*, 32 (1): 1-8.

Kenya Investment Authority (KIA) (2021). Investing in Kenya's fibre, textiles and apparel industry. *Ministry of Industrialization, Trade and Enterprise Development*, Kenya.

Khaleque, M. and Roy, D. (2016). Removing reactive dyes from textile effluent using banana fibre. *International Journal of Basic & Applied Sciences*, 16 (1): 14-20.

Khan, A., Naeem, A., Mahmood, T., Ahmad, B., Ahmad, Z., Farooq, M. and Saeed, T. (2022). Mechanistic study on methyl orange and congo red adsorption onto polyvinyl pyrrolidone modified magnesium oxide. *International Journal of Environmental Science and Technology*, 19 (4): 2515-2528.

Khan, A., Naeem, A. and Mahmood, T. (2020). Thermodynamic study of adsorption of methyl orange and congo red from aqueous solutions by PVP-functionalized ZnO. *Russian Journal of Physical Chemistry A*, 94 (8): 1581-1586.

Khan, H., Yerramilli, A., D'Oliveira, A., Alford, T., Boffito, D. and Patience, G.S. (2020). Experimental methods in chemical engineering: X-Ray Diffraction spectroscopy-XRD. *Canadian Journal of Chemical Engineering*, 98 (6): 1255-1266.

Khan, M., Khan, M. and Zafar, S. (2017). Removal of different anionic dyes from aqueous solution by anion exchange membrane. *Membrane Water Treatment*, 8 (3): 259-277.

Khaniabadi, Y.O., Mohammadi, M.J., Shegerd, M., Sadeghi, S., Saeedi, S. and Basiri, H. (2017). Removal of congo red dye from aqueous solutions by a low-cost adsorbent: Activated carbon prepared from aloe vera leaves shell. *Environmental Health Engineering and Management Journal*, 4 (1): 29-35.

Kheloufi, A., Berbar, Y., Kefaifi, A., Medjahed, A. and Kerkar, F. (2011). Improvement of impurities removal from silica sand by using a leaching process. *Chemical Engineering Transactions*, 24: 1513-1518.

Khurram, R., Wang, Z., Ehsan, M.F., Peng, S., Shafiq, M. and Khan, B. (2020). Synthesis and characterization of an α-Fe_2O_3/ZnTe heterostructure for photocatalytic degradation of congo red, methyl orange and methylene blue. *RSC Advances*, 10 (73): 44997-45007.

Kinyanjui, M. (2023). State advertises tenders for 6,710 affordable housing units. *The Star*. https://the-star.co.ke/news/2023-08-02-state-advertises-tenders-for-6710-affordable-housing-units/Accessed on 4th February, 2023.

Kloster, M., de Almeida, A., Muraca, D., Marcovich, N. and Mosiewicki, M. (2023). Chitosan-based magnetic particles as adsorbents for anionic contaminants. *Engineered Science*, 22: 851-872.

Körbahti, B. and Demirbüken, P. (2017). Electrochemical oxidation of resorcinol in aqueous medium using boron-doped diamond anode: Reaction kinetics and process optimization with response surface methodology. *Frontiers in Chemistry*, 5: 75-88.

Kobayashi, S. (2016). IR spectroscopic study of silicon nitride films grown at a low substrate temperature using very high frequency plasma-enhanced chemical vapor deposition. *World Journal of Condensed Matter Physics*, 6 (4): 287-293.

Krishna Murthy, T., Gowrishankar, S., Krishna, R. H., Chandraprabha, M. and Mathew, B. (2020). Magnetic modification of coffee husk hydrochar for adsorptive removal of methylene blue: Isotherms, kinetics and thermodynamic studies. *Environmental Chemistry and Ecotoxicology*, 2: 205-212.

Krishnan, A., Were, A. and Dirk, W. (2019). Integrating Kenya's small firms into leather, textiles and garments value chains. *Ministry of Industry, Trade and Co-Operatives*, Kenya.

Kuddus, A., Islam, R., Tabassum, S. and Ismail, A. (2019). Synthesis of Si NPs from river sand using the mechanochemical process and its applications in metal oxide heterojunction solar cells. *Silicon*, 12: 1723-1733.

Kumar, A., Dixit, U., Singh, K., Gupta, S.P. and Beg, M. (2021). Structure and properties of dyes and pigments. Dyes and pigments-novel applications and waste treatment. *IntechOpen*, 131: 1-19.

Kumar, S., Vardhan, T., Babu, B., Chakravarthy, C., Prabhakar, N., Rao, K. and Tirupathi, K. (2020). Dataset on tribological, characterization and thermal properties of Silicon carbide reinforced polyamide composites for industrial applications. *Data in Brief*, 30: 1-10.

Kumar, P., Joshiba, G., Femina, C., Varshini, P., Priyadharshini, S., Karthick, M. and Jothirani, R. (2019). A critical review on recent developments in the low-cost adsorption of dyes from wastewater. *Desalination and Water Treatment*, 172: 395-416.

Kümmerer, K., Dionysiou, D., Olsson, O. and Fatta-Kassinos, D. (2019). Reducing aquatic micropollutants-Increasing the focus on input prevention and integrated emission management. *Science of the Total Environment*, 652: 836-850.

Lacin, D. and Aroguz, A. (2020). Kinetic studies on adsorption behavior of methyl orange using modified halloysite, as an eco-friendly adsorbent. *SN Applied Sciences*, 2 (12): 1-12.

Lawrinenko, M. and Laird, D.A. (2015). Anion exchange capacity of biochar. *Green Chemistry*, 17 (9): 4628-4636.

Lellis, B., Fávaro, C.Z., Pamphile, J. and Polonio, C. (2019). Effects of textile dyes on health and the environment and bioremediation potential of living organisms. *Biotechnology Research and Innovation*, 3 (2): 275-290.

Lemraski, E., Yari, S., Ali, E.K., Sharafinia, S., Jahangirian, H., Rafiee-Moghaddam, R. and Webster, T.J. (2021). Polyvinyl alcohol/chitosan/silver nanofibers as antibacterial agents and as efficient adsorbents to remove methyl orange from aqueous solutions. *Journal of the Iranian Chemical Society*, 19 (4): 1287-1299.

Lemus, J., Moya, C., Gilarranz, M., Rodriguez, J. and Palomar, J. (2017). Fixed-bed adsorption of ionic liquids onto activated carbon from aqueous phase. *Journal of Environmental Chemical Engineering*, 5 (6): 5347-5351.

Li, F., Cui, W., Tian, Z., Zhang, J., Du, S., Chen, Z., Zhang, S., Chen, K. and Liu, G. (2022). Effect of the diluent on combustion synthesis of silicon nitride. *International Journal of Applied Ceramic Technology*, 19 (6): 2957-2962.

Liang, G., Sun, G., Bi, J., Wang, W., Yang, X. and Li, Y. (2020). Mechanical and dielectric properties of functionalized boron nitride nanosheets/silicon nitride composites. *Ceramics International*, 47 (2): 2058-2067.

Lin, H., Chen, T., Yan, B., Huang, Z., Zhou, Y., Huang, J. and Xiao, X. (2020). A functionalized silicate adsorbent and exploration of its adsorption mechanism. *Molecules*, 25 (8): 1820-1833.

Litefti, K., Freire, M., Stitou, M. and Julia, G. (2019). Adsorption of an anionic dye (Congo red) from aqueous solutions by pine bark. *Scientific Reports*, 9 (1): 1-11.

Liu, J., Cheng, S., Cao, N., Geng, C., He, C., Shi, Q., Xu, C., Ni, J., DuChanois, R., Elimelech, M. and Zhao, H. (2019). Actinia-like multifunctional nanocoagulant for single-step removal of water contaminants. *Nature Nanotechnology*, 14 (1): 64-71.

Liu, Q., Zhou, Y., Wang, M., Zhang, Q., Ji, T., Chen, T. and Yu, D. (2019). Adsorption of methylene blue from aqueous solution onto viscose-based activated carbon fiber felts: Kinetics and equilibrium studies. *Adsorption Science & Technology*, 37 (3): 312-332.

Liu, H., Huang, Z., Zhang, X., Fang, M., Liu, Y., Wu, X. and Min, X. (2018). Large scale synthesis of α-Si_3N_4 nanowires through a kinetically favored chemical vapour deposition process. *Physica E*, 95: 132-138.

Liu, X., Yi, X., Guo, R., Li, Q. and Nomura, T. (2017). Formation mechanisms of Si_3N_4 microstructures during silicon powder nitridation. *Ceramics International*, 43 (18): 16773-16779.

Luthfiah, A., Deawati, Y., Firdaus, M., Rahayu, I. and Eddy, D. (2021). Silica from natural sources: A review on the extraction and potential application as a supporting photocatalytic material for antibacterial activity. *Science and Technology Indonesia*, 6 (3): 144-155.

Ma, X., Zhang, K., Cheng, H., Chen, Z., Wang, F. and Li, S. (2020). Fabrication of self-separable Si_3N_4 microfibers via one step carbothermal reduction and nitridation of rice straw. *Ceramics International*, 46 (18): 29244-29248.

Maghanga, J., Segor, F., Irina, J. and Tole, M. (2017). Effect of process parameters on the electro coagulation of azo dye wastewater in a Kenyan textile factory. *IOSR Journal of Applied Chemistry*, 10 (11): 1-7.

Mahmut, S., Mustafa, G., Ali, Ç. and Gülsüm, T. (2020). Silicon nitride ceramic for all-ceramic dental restorations. *Dental Materials Journal*, 39 (6): 1080-1086.

Mahdadi, N., Chihi, S., Bouguettaia, H., Beddiaf, S. and Mechri, M. (2016). Chromatic classification of Ouargla (Algeria) dunes sand: Determination of main compositions and color causes by using XRD, FTIR and XRF. *Silicon*, 9 (2): 211-221.

Mahmoud, M., Nabil, G., Khalifa, M., El-Mallah, N. and Hassouba, H. (2019). Effective removal of crystal violet and methylene blue dyes from water by surface functionalized zirconium silicate nanocomposite. *Journal of Environmental Chemical Engineering*, 7 (2): 1-17.

Maia, L., Da Silva, A., Carneiro, E., Monticelli, F., Pinhati, F. and Mulinari, D. (2021). Activated carbon from palm fibres used as an adsorbent for methylene blue removal. *Journal of Polymers and the Environment*, 29 (4): 1162-1175.

Maingi, F., Mbuvi, H., Ng'ang'a, M. and Mwangi, H. (2017). Adsorption kinetics and isotherms of methylene blue by geopolymers derived from common clay and rice husk ash. *Physical Chemistry*, 7 (4): 87-97.

Mani, S., Chowdhary, P. and Bharagava, R. (2019). Textile wastewater dyes: Toxicity profile and treatment approaches. Emerging and eco-friendly approaches for waste management. *Springer*, 11: 219-244.

Manrique, R., Vásquez, D., Ceballos, C., Chejne, F. and Amell, A. (2019). Evaluation of the energy density for burning disaggregated and pelletized coffee husks. *ACS Omega*, 4 (2): 2957-2963.

Mansuri, I., Farzana, R., Rajarao, R. and Sahajwalla, V. (2018). Carbon dissolution using waste biomass—A sustainable approach for iron-carbon alloy production. *Metals*, 8 (4): 290-301.

Manzar, M., Waheed, A., Qazi, I., Blaisi, N. and Ullah, N. (2019). Synthesis of a novel epibromohydrin modified crosslinked polyamine resin for highly efficient removal of methyl orange and eriochrome black T. *Journal of the Taiwan Institute of Chemical Engineers*, 97: 424-432.

Marguí, E., Zawisza, B. and Sitko, R. (2014). Trace and ultratrace analysis of liquid samples by X-Ray Fluorescence spectrometry. *Trends in Analytical Chemistry*, 53: 73-83.

Maroufi, S., Mayyas, M., Nekouei, R., Assefi, M. and Sahajwalla, V. (2018). Thermal nanowiring of e-waste: A Sustainable route for synthesizing green Si_3N_4 nanowires. *ACS Sustainable Chemistry & Engineering*, 6 (3): 3765-3772.

Marzbali, M.H. and Esmaieli, M. (2017). Fixed bed adsorption of tetracycline on a mesoporous activated carbon: Experimental study and neuro-fuzzy modeling. *Journal of Applied Research and Technology*, 15 (5): 454-463.

Masakha, E., Moturi, W. and Ogendi, G. (2017). Seasonal and longitudinal variations of water quality in an urban stream: Case study of Sosiani river Uasin Gishu county, Kenya. *Journal of Resources Development and Management*, 33: 1-8.

Mashkoor, F. and Nasar, A. (2019). Magnetized *Tectona grandis* sawdust as a novel adsorbent: preparation, characterization, and utilization for the removal of methylene blue from aqueous solution. *Cellulose*, 27 (5): 2613-2635.

Matharage, H., Jayaweera, M., Bandara, N., Manatunge, J., Jayawardana, D. and Dissanayake, J. (2025). Fixed-bed column studies on the adsorption of bisphenol A from aqueous solutions using chemically activated king coconut biochar. *Discover Chemical Engineering*, 5 (9): 1-19.

Mcyotto, F., Wei, Q., Macharia, D.K, Huang, M., Shen, C. and Chow, C. (2021). Effect of dye structure on color removal efficiency by coagulation. *Chemical Engineering Journal*, 405: 1-13.

Meftah, N., Hani, A. and Merdas, A. (2023). Extraction and physicochemical characterization of highly-pure amorphous silica nanoparticles from locally available dunes sand. *Chemistry Africa*, 6: 1-10.

Meftah, N. and Mahboub, M. (2019). Spectroscopic characterizations of sand dunes minerals of El-Oued (Northeast Algerian Sahara) by FTIR, XRF and XRD analyses. *Silicon*, 12 (1): 147-153.

Meng, X., Scheidemantle, B., Li, M., Wang, Y., Zhao, X., Miguel, T., Singh, P., Pu, Y., Wyman, C., Ozcan, S., Cai, C. and Ragauskas, A. (2020). Synthesis, characterization, and utilization of a lignin-based adsorbent for effective removal of azo dye from aqueous solution. *ACS Omega*, 5 (6): 2865-2877.

Meziani, S., Moussi, A., Mahiou, L. and Outemzabet, R. (2016). Compositional analysis of silicon oxide/silicon nitride thin films. *Materials Science-Poland*, 34 (2): 315-321.

Ministry of Health-Machakos County Government (MOH-MCG) (2023). Governor Wavinya raises the red flag over rising cancer cases in Machakos. https://machakos.go.ke/governor-raises-the-red-flag-over-rising-cancer-cases-in-machakos/ Accessed on: 4th February, 2023.

Ministry of Health (MOH) (2023). The National Cancer Control Strategy (2023-2027). https://iccp-portal.org.pdf.

Mirzaei, D., Zabardasti, A., Mansourpanah, Y., Sadeghi, M. and Farhadi, S. (2020). Efficacy of novel NaX/MgO–TiO_2 zeolite nanocomposite for the adsorption of methyl orange (MO) dye: Isotherm, kinetic and thermodynamic studies. *Journal of Inorganic and Organometallic Polymers and Materials*, 30 (6): 2067-2080.

Mishra, P. and Soni, R. (2016). Analysis of dyeing and printing waste water of Balotara textile industries. *International Journal of Chemical Science*, 14 (4): 1929-1938.

Mittal, H., Kumar, A. and Khanuja, M. (2019). In-situ oxidative polymerization of aniline on hydrothermally synthesized $MoSe_2$ for enhanced photocatalytic degradation of organic dyes. *Journal of Saudi Chemical Society*, 23 (7): 836-845.

Mohammad, F., Mohamad, E., Hossein, A., Alireza, S. and Ehsan, S.P. (2016). Continuous adsorption study of congo red using tea waste in a fixed-bed column. *Desalination and Water Treatment*, 57 (18): 8437-8446.

Mohammadi, A. and Veisi, P. (2018). High adsorption performance of β -cyclodextrin-functionalized multi-walled carbon nanotubes for the removal of organic dyes from water and industrial wastewater. *Journal of Environmental Chemical Engineering*, 6 (4): 4634-4643.

Mohd, N., Azmi A. and Khalik, W. (2020). Central composite design approach for the optimisation of catalytic degradation of methyl orange dye using silica-silver core-shell nanoparticles. *Research Journal of Chemistry and Environment*, 24 (10): 104-111.

Mondal, N. and Kar, S. (2018). Potentiality of banana peel for removal of congo red dye from aqueous solution: Isotherm, kinetics and thermodynamics studies. *Applied Water Science*, 8 (6): 157-168.

Moreira, K., Oliveira, P., de Deus, Ê. and Cabral, A. (2021). Alkali-silica reaction: Understanding the phenomenon. *Journal of Building Pathology and Rehabilitation*, 6 (5): 1-10.

Mourhly, A., Khachani, M., Hamidi, A. E., Kacimi, M., Halim, M. and Arsalane, S. (2015). The synthesis and characterization of low-cost mesoporous silica SiO_2 from local pumice rock. *Nanomaterials and Nanotechnology*, 5: 35-42.

Mu, B., Wang, H., Hao, X. and Wang, Q. (2018). Morphology, mechanical properties and dimensional stability of biomass particles/high density polyethylene composites: Effect of species and composition. *Polymers*, 10 (3): 308-322.

Mulwa, F., Li, Z. and Fangninou, F. (2021). Water scarcity in Kenya: Current status, challenges and future solutions. *Open Access Library Journal*, 8 (1): 1-15.

Muliwa, A., Mecha, A., Grobler, A. and Onyango, M. (2016). Removal of multi-active-blue dye from aqueous phase using magnetic poly-pyrrole nanocomposites: Fixed-bed adsorption studies. *Research Journal of Applied Sciences, Engineering and Technology*, 13 (7): 576-584.

Munagapati, V. and Kim, D. (2016). Adsorption of anionic azo dye congo red from aqueous solution by cationic modified orange peel powder. *Journal of Molecular Liquids*, 220: 540-548.

Munasir, Supardi, Z., Nisa, Z., Kusumawati, D., Putri, N., Taufiq, A. and Hidayat, N. (2018). Phase transition of SiO_2 nanoparticles prepared from natural sand: The calcination temperature effect. *Journal of Physics: Conference Series*, 1093 (1): 1-10.

Munasir, Triwikantoro, Zainuri, M. and Darminto. (2015). Synthesis of SiO_2 nanopowders containing quartz and cristobalite phases from silica sands. *Materials Science-Poland*, 33 (1): 47-55.

Munasir, Sulton, A., Triwikantoro, Zainuri, M. and Darminto. (2013). Synthesis of silica nanopowder produced from Indonesian natural sand via alkali fusion route. *American Institute of Physics*, 1555 (1): 28-31.

Muniyandi, M. and Govindaraj, P. (2021). Potential removal of methylene blue dye from synthetic textile effluent using activated carbon derived from palmyra (palm) shell. *Materials Today: Proceedings*, 47 (1): 299-311.

Muralisankar, I., Agilan, S., Selvakumar, R. and Vairam, S. (2018). Synthesis of Co_3O_4/graphene nanocomposite using paraffin wax for adsorption of methyl violet in water. *IET Nanobiotechnology*, 12 (6): 787-794.

Mutunga, M., Wanyonyi, W. and Ongera, G. (2020). Utilization of macadamia seed husks as a low-cost sorbent for removing cationic dye (basic blue 3 dye) from aqueous solution. *Environmental Chemistry and Ecotoxicology*, 2: 194-200.

Nayak, P. and Datta, A. (2020). Synthesis of SiO_2-nanoparticles from rice husk ash and its comparison with commercial amorphous silica through material characterization. *Silicon*, 13 (4): 1209-1214.

Ndambiri, H., and Rotich, E. (2018). Valuing excess fluoride removal for safe drinking water in Kenya. *Water Policy*, 20 (5): 953-965.

Ndung'u S.N, Wanjau, R. and Nthiga, E. (2022). Fixed bed column studies of selected phenols and dyes using low-cost adsorbents. *Asian Journal of Research in Chemistry*, 15 (3): 189-194.

Ndung'u, S., Nthiga, E., Wanjau, R. and Ndiritu, J. (2021). Adsorption studies of lead (II) ions from a synthetic media using Jackfruit (*Artocarpus heterophyllus L.)* rags: Kinetics, equilibrium and thermodynamic studies. *International Journal of Scientific Research in Chemical Sciences*, 8 (4): 5-12.

Ngulube, T., Gumbo, J., Masindi, V. and Maity, A. (2017). An update on synthetic dyes adsorption onto clay based minerals: A state-of-art. *Journal of Environmental Management*, 191: 35-57.

Nguyen, T., Nguyen, V., Tran, T., Le, T. and Nguyen, N. (2021). Batch and column adsorption of reactive dyes by eggshell powder-chitosan gel core-shell material. *Moroccan Journal of Chemistry*, 9 (1): 18-27.

Nica, I., Biliuta, G., Zaharia, C., Rusu, L., Coseri, S. and Suteu, D. (2020). Fixed-bed column studies for methylene blue removal by cellulose cellets. *Environmental Engineering and Management Journal*, 19 (2): 269-279.

Nie, B., Liu, X., Yang, L., Meng, J. and Li, X. (2015). Pore structure characterization of different rank coals using gas adsorption and scanning electron microscopy. *Fuel*, 158: 908-917.

Niinimäki, K., Peters, G., Dahlbo, H., Perry, P., Rissanen, T. and Gwilt, A. (2020). The environmental price of fast fashion. *Nature Reviews Earth & Environment*, 1 (4): 189-200.

Norsuraya, S., Fazlena, H. and Norhasyimi, R. (2016) Sugarcane bagasse as a renewable source of silica to synthesize santa barbara amorphous-15 (SBA-15). *Procedia Engineering*, 148: 839-846.

Novita, L. and Idris, I. (2022). Effectiveness of silica gel from palm kernel shell ash as a moisture absorber of bottle packaging medicine. *IOP Conference Series Earth and Environmental Science*, 1041 (1): 1-8.

Njeri, J.N., Nthiga, E.W. and Muthakia, G. (2023). The efficacy of coffee husks biochar in the adsorption of methyl red from textile dyeing wastewater. *International Journal of Scientific Research in Chemical Sciences*, 10 (4): 1-9.

Nzuma, V. (2021). NEMA issues stern warning to factories discharging waste into Athi river. *The Standard*. https://standardmedia.co.ke/counties/article/2001427188/nema-issues-stern warning-to-factories-discharging-waste-into-athi-river. Accessed on 25th October, 2021.

Ojedokun, A. and Bello, O. (2017). Kinetic modeling of liquid-phase adsorption of congo red dye using guava leaf-based activated carbon. *Applied Water Science*, 7 (4): 1965-1977.

Olando, G., Olaka, L., Okinda, P.O. and Abuom, P. (2020). Heavy metals in surface sediments of Lake Naivasha, Kenya: Spatial distribution, source identification and ecological risk assessment. *SN Applied Sciences*, 2 (2): 279-292.

Ombuna, C., Mochoge, B. and Mwetu, K. (2017). Contribution of rooftop rainwater harvesting in relation to total water supply in households-A case study, Nairobi County, Kenya. *European Journal of Physical and Agricultural Sciences*, 5 (2): 6-20.

Omer, O.S., Hussein, M., Hussein, B.H. and Mgaidi, A. (2017). Adsorption thermodynamics of cationic dyes (methylene blue and crystal violet) to a natural clay mineral from aqueous solution between 293.15 and 323.15 K. *Arabian Journal of Chemistry*, 11 (5): 615-623.

Omokpariola, D. and Otuosorochi, J. (2020). Adsorption of congo red dye using rice husk. *World Scientific News*, 150: 22-38.

Osiemo, M., Ogendi, G. and M'Erimba, C. (2019). Microbial quality of drinking water and prevalence of water-related diseases in Marigat urban centre, Kenya. *Environmental Health Insights*, 13 (1): 1-7.

Owiti, G. (2022). Outcry as farmers irrigate crops with contaminated water in Athi River. *The Star*.

https://the-star.co.ke/counties/north-eastern/2022-11-07-outcry-as-farmers-irrigate-crops-with-contaminated-water-in-athi-river. Accessed on 7th November, 2022.

Oyarce, E., Butter, B., Santander, P. and Sánchez, J. (2021). Polyelectrolytes applied to remove methylene blue and methyl orange dyes from water via polymer-enhanced ultrafiltration. *Journal of Environmental Chemical Engineering*, 9 (6): 1-42.

Oyedotun, T. (2018). X-Ray Fluorescence (XRF) in the investigation of the composition of earth materials: A review and an overview. *Geology, Ecology, and Landscapes*, 2 (2): 148-154.

Paclijan, S., Franco, S., Abella, R., Lague, J.C. and Tan, N. (2021). Fresh and uncalcined solution blow spinning-spun PAN and PVDF nanofiber membranes for methylene blue dye removal in water. *Journal of Membrane Science and Research*, 7 (3): 173-184.

Parimelazhagan, V., Jeppu, G. and Rampal, N. (2022). Continuous fixed-bed column studies on congo red dye adsorption-desorption using free and immobilized *Nelumbo nucifera* leaf adsorbent. *Polymers*, 14 (1): 54-76.

Parmar, N. and Shukla, S. (2018). Decolourization of dye wastewater by microbial methods-A review. *Indian Journal of Chemical Technology*, 25 (4): 315-323.

Parrillo, A., Sánchez, G. and· Alles, A. (2021). α-Si_3N_4 and Si_2N_2O whiskers from rice husk and industrial rice husk ash. *SN Applied Sciences*, 3 (2): 268-279.

Patawat, C., Silakate, K., Chuan-Udom, S., Supanchaiyamat, N., Hunt, A.J. and Ngernyen, Y. (2020). Preparation of activated carbon from *Dipterocarpus alatus* fruit and its application for methylene blue adsorption. *RSC advances*, 10 (36): 21082-21091.

Patel, H. (2020). Batch and continuous fixed bed adsorption of heavy metals removal using activated charcoal from neem (*Azadirachta indica*) leaf powder. *Scientific Reports*, 10 (1): 16895-16906.

Patel, H. (2019). Fixed-bed column adsorption study: A comprehensive review. *Applied Water Science*, 9 (3): 45-61.

Patel, H., Vashi, R. and Champaneri, V. (2019). Continuous adsorption of methylene blue dye from aqueous solution onto guava leaf powder in fixed bed. *Journal of Applicable Chemistry*, 8 (5): 2246-2254.

Patel, H. (2018). Adsorptive batch and column studies of congo red onto gulmohar leaf powder. *European Journal of Chemistry*, 9 (2): 107-114.

Pavlenko, N., Strokova, V., Kapsuta, M.N. and Netsvet, D. (2014). About application prospectivity of rocks with different geological and morphological features as basic raw component for free-cement binder production. *Applied Mechanics and Materials*, 670: 462-465.

Philippou, K., Anastopoulos, I., Dosche, C. and Pashalidis, I. (2019). Synthesis and characterization of a novel Fe_3O_4-loaded oxidized biochar from pine needles and its application for uranium removal. Kinetic, thermodynamic, and mechanistic analysis. *Journal of Environmental Management*, 252: 1-9.

Pismenskaya, N., Sarapulova, V., Klevtsova, A., Mikhaylin, S. and Bazinet, L. (2020). Adsorption of anthocyanins by cation and anion exchange resins with aromatic and aliphatic polymer matrices. *International Journal of Molecular Sciences*, 21 (21): 7874-7899.

Potter, N. and Brand, N. (2019). Application of micro-XRF to characterize diamond drill-core from lithium-caesium-tantalum pegmatites. *ASEG Extended Abstracts*, 1: 1-4.

Priyadarshini, B., Patra, T. and Sahoo, T. (2020). An efficient and comparative adsorption of congo red and trypan blue dyes on MgO nanoparticles: Kinetics, thermodynamics and isotherm studies. *Journal of Magnesium and Alloys*, 9 (2): 478-488.

Qadri, S., Rath, B., Gorzkowski, E., Wollmershauser, J. and Feng, C. (2016). Nanostructured silicon nitride from wheat and rice husks. *Journal of Applied Physics*, 119 (13): 1-7.

Qiu, B., Li, M., Xu, B., Liu, P., Chen, Q., Xu, B. and Han, Z. (2019). Effects of amino groups on dispersibility of silicon nitride powder in aqueous media. *Ceramics International*, 45 (4): 4268-4273.

Qu, W., He, D., Huang, H., Guo, Y., Tang, Y. and Song, R. (2020). Characterization of amino-crosslinked hypromellose and its adsorption characteristics for methyl orange from water. *Journal of Materials Science*, 55 (17): 7268-7282.

Radoor, S., Karayil, J., Parameswaranpillai, J. and Siengchin, S. (2020). Removal of anionic dye congo red from aqueous environment using polyvinyl alcohol/sodium alginate/ZSM-5 zeolite membrane. *Scientific reports*, 10 (1): 1-15.

Rahmayanti, A., A'yuni, Q., Hartati, H., Purkan, P. and Romanza, I.G. (2020). Synthesis and characterization of silica gel from Lapindo mud Sidoarjo. *IOP Conference Series: Earth and Environmental Science*, 456: 1-7.

Raj, R., Manimozhi, V. and Saravanathamizhan, R. (2020). Activation of petroleum coke using KOH and fixed bed adsorption studies for acid red dye removal from aqueous solution. *Petroleum Science and Technology*, 38 (6): 609-617.

Rajarao, R. and Veena, S. (2016). A cleaner, sustainable approach for synthesizing high purity silicon carbide and silicon nitride nanopowders using macadamia shell waste. *Journal of Cleaner Production*, 133: 1277-1282.

Rampe, M., Lombok, J.Z. and Tiwow, V. (2023). Characterization of silica (SiO_2) based on beach sand from Sulawesi and Sumatra as silicon carbide (SiC) base material. *Journal of Chemical Technology and Metallurgy*, 58 (3): 467-476.

Ratnamala, G.M., Vidya, S.K. and Govindan, S. (2023). Continuous fixed-bed adsorption of reactive azo dye on activated red mud for wastewater treatment-Evaluation of column dynamics and design parameters. *Environmental Science and Pollution Research*, 30: 57058-57075.

Razzaq, S., Akhtar, M., Zulfiqar, S., Zafar, S., Shakir, I., Agboola, P., Haider, S. and Warsi, M. (2021). Adsorption removal of congo red onto L-cysteine/rGO/PANI nanocomposite: Equilibrium, kinetics and thermodynamic studies. *Journal of Taibah University for Science*, 15 (1): 50-62.

Reddy, M. and Nirmala, V. (2014). Bengal gram seed husk as an adsorbent for the removal of dyes from aqueous solutions-column studies. *Arabian Journal of Chemistry*, 12 (7): 1695-1706.

Rocha, F., Gomes, A., Lunardi, C., Kaliaguine, S. and Patience, G.S. (2018). Experimental methods in chemical engineering: Ultraviolet visible spectroscopy | UV-Vis. *The Canadian Journal of Chemical Engineering*, 96 (12): 2512-2517.

Rondina, D., Ymbong, D.V., Cadutdut, M., Nalasa, J., Paradero, J., Mabayo, V. and Arazo, R. (2019). Utilization of a novel activated carbon adsorbent from press mud of sugarcane industry for the optimized removal of methyl orange dye in aqueous solution. *Applied Water Science*, 9 (8): 181-192.

Rosanti, A., Kusumawati, Y., Hidayat, F., Fadlan, A., Wardani, A. and Anggraeni, H. (2022). Adsorption of methylene blue and methyl orange from aqueous solution using orange peel and CTAB-modified orange peel. *Journal of the Turkish Chemical Society*, 9 (1): 237-246.

Sahoo, K., Kumar, A. and Chakraborty, J.P. (2020). A comparative study on valuable products: bio-oil, biochar, non-condensable gases from pyrolysis of agricultural residues. *Journal of Material Cycles and Waste Management*, 23: 186-204.

Saini, J., Garg, V.K. and Gupta, R. (2018). Removal of methylene blue from aqueous solution by $Fe_3O_4@Ag/SiO_2$ nanospheres: Synthesis, characterization and adsorption performance. *Journal of Molecular Liquids*, 250: 413-422.

Sani, S. and Abdullahi, H. (2017). Kinetics and thermodynamics of methyl orange uptake from model effluent by watermelon shells and neem leaves. *International Journal of Advances in Chemical Engineering & Biological Sciences*, 4 (1): 39-47.

Sarkar, A. (2020). Everyday practices of poor urban women to access water: Lived realities from a Nairobi slum. *African Studies*, 79 (2): 212-231.

Sazali, N., Harun, Z. and Sazali, N. (2020). A review on batch and column adsorption of various adsorbent towards the removal of heavy metal. *Journal of Advanced Research in Fluid Mechanics and Thermal Sciences*, 67 (2): 66-88.

Sebeia, N., Jabli, M., Ghith, A. and Saleh, T.A. (2019). Eco-friendly synthesis of *Cynomorium coccineum* extract for controlled production of copper nanoparticles for sorption of methylene blue dye. *Arabian Journal of Chemistry*, 13 (2): 4263-4274.

Selambakkannu, S., Othman, N., Bakar, K. and Karim, Z. (2019). Adsorption studies of packed bed column for the removal of dyes using amine functionalized radiation induced grafted fiber. *SN Applied Sciences*, 1 (2): 1-10.

Şentürk, İ. and Yıldız, M. (2020). Removal of maxilon red GRL dye in continuous system adsorption column using waste pine sawdust. *International Advanced Researches and Engineering Journal*, 4 (2): 154-160.

Setyoningrum, T., Murni, S. and Nandari, W. (2020). Extraction of silica from Kalirejo minerals, Kokap, Kulonprogo, Yogyakarta. *LPPM UPN "Veteran" Yogyakarta Conference Series Proceeding on Engineering and Science Series*, 1 (1): 269-276.

Shackley, M. (2011). An introduction to X-Ray Fluorescence (XRF) analysis in archaeology. *Springer*, 2: 7-44.

Shah, S., Sharma, T., Dar, B. and Bamezai, R. (2021). Adsorptive removal of methyl orange dye from aqueous solution using populous leaves: Insights from kinetics, thermodynamics and computational studies. *Environmental Chemistry and Ecotoxicology*, 3: 172-181.

Shakoor, S. and Nasar, A. (2018). Adsorptive decontamination of synthetic wastewater containing crystal violet dye by employing *Terminalia arjuna* sawdust waste. *Groundwater for Sustainable Development*, 7: 30-38.

Sharifpour, E., Alipanahpour D.E., Asfaram, A., Ghaedi, M. and Goudarzi, A. (2019). Optimizing adsorptive removal of malachite green and methyl orange dyes from simulated wastewater by Mn-doped CuO-Nanoparticles loaded on activated carbon using CCD-RSM: Mechanism, regeneration, isotherm, kinetic, and thermodynamic studies. *Applied Organometallic Chemistry*, 33 (3): 1-14.

Sharma, G., Bhogal, S., Kumar, A., Naushad, M., Sharma, S., Ahamad, T. and Stadler, F.J. (2020). AgO/MgO/FeO@Si_3N_4 nanocomposite with robust adsorption capacity for tetracycline antibiotic removal from aqueous system. *Advanced Powder Technology*, 31 (10): 4310-4318.

Sharma, G., Kumar, A., Sharma, S., Naushad, M., Ahamad, T., Al-Saeedi, S., Al-Senani, G., Al-kadhi, N. and Stadler, F. (2018). Facile fabrication of $Zr_2Ni_1Cu_7$ trimetallic nano-alloy and its composite with Si_3N_4 for visible light assisted photodegradation of methylene blue. *Journal of Molecular Liquids*, 272: 170-179.

Shi, C., Zhu, Y., Qian, H. and Lu, L. (2014). Fabrication of silicon nitride fiber–PMMA composite through free radical polymerization in batch. *Materials Research Bulletin*, 51: 161-166.

Shittu, I., Edathil, A., Alsaeedi, A., Al-Asheh, S., Polychronopoulou, K. and Banat, F. (2019). Development of novel surfactant functionalized porous graphitic carbon as an efficient adsorbent for the removal of methylene blue dye from aqueous solutions. *Journal of Water Process Engineering*, 28: 69-81.

Silva, M., Spessato, L., Silva, T.L., Greice K., Lopes., Zanella, H., Jéssica, T., André, Y., Cazetta, L. and Almeida, V. (2020). H_3PO_4-activated carbon fibers of high surface area from banana tree pseudo-stem fibers: Adsorption studies of methylene blue dye in batch and fixed bed systems. *Journal of Molecular Liquids*, 324: 1-38.

Simonescu, C., Tãtãruş, A., Culiţã, D., Stãnicã, N., Ionescu, I., Butoi, B. and Banici, A. (2021). Comparative study of $CoFe_2O_4$ nanoparticles and $CoFe_2O_4$-chitosan composite for congo red and methyl orange removal by adsorption. *Nanomaterials*, 11: 711-734.

Singh, K. (2020). Spectrophotometer (UV-Visible). *Compendium of Biomedical Instrumentation*, 343: 1815-1824.

Smita, J., Dipika, J. and Shraddha, K. (2016). Polyaniline for removal of methyl orange dye from waste water. *International Journal of Science Engineering and Management*, 3 (5): 1-6.

Song, J., Wang, Y. and Qiu, J. (2018). High adsorption performance of methyl blue from aqueous solution using hyper-branched polyethyleneimine grafted MWCNTs as an adsorbent. *ES Materials & Manufacturing*, 3 (3): 29-37.

Staroń, P., Chwastowski, J. and Banach, M. (2019). Sorption behavior of methylene blue from aqueous solution by raphia fibers. *International Journal of Environmental Science and Technology*, 16 (12): 8449-8460.

Subbaiah, M.V. and Kim, D. (2016). Adsorption of methyl orange from aqueous solution by aminated pumpkin seed powder: Kinetics, isotherms, and thermodynamic studies. *Ecotoxicology and Environmental Safety*, 128: 109-117.

Suman, S. and Gautam, S. (2017). Pyrolysis of coconut husk biomass: Analysis of its biochar properties. *Energy Sources, Part A: Recovery, Utilization, and Environmental Effects*, 39 (8): 761-767.

Sun, N. and Xiao, Z. (2017). Improvement of the thermostability of silicone oil/polystyrene microcapsules by embedding TiO_2/Si_3N_4 nanocomposites as outer shell. *Journal of Materials Science*, 52 (18): 10800-10813.

Tahazadeh, S., Karimi, H., Mohammadi, T., Emrooz, H. and Tofighy, M. (2021). Fabrication of biodegradable cellulose acetate/MOF-derived porous carbon nanocomposite adsorbent for methylene blue removal from aqueous solutions. *Journal of Solid State Chemistry*, 299: 1-13.

Tan, M., Zheng, S., Lv, H., Wang, B., Zhao, Q. and Zhao, B. (2021). Rational design and synthesis of chitosan–quinoa polysaccharide composite aerogel and its adsorption properties for congo red and methylene blue. *New Journal of Chemistry*, 45 (22): 9829-9837.

Tao, J., Xiaomin, X. and Wei, G. (2016). Influence of rice husk on preparing porous silicon nitride ceramics. *Chinese Journal of Environmental Engineering*, 10 (4): 2031-2034.

Thahir, R., Wahab, A., Nafie, N. and Raya, I. (2019). Synthesis of mesoporous silica SBA-15 through surfactant set-up and hydrothermal process. *Rasayan Journal of Chemistry*, 12 (3): 1117-1126.

Thuong, N., Nhi, N., Nhung, V., Bich, H., Quynh, B., Bach, L. and Nguyen, T. (2019). A fixed-bed column study for removal of organic dyes from aqueous solution by pre-treated durian peel waste. *Indonesian Journal of Chemistry*, 19 (2): 486-494.

Tishchenko, I., Ilchenko, O. and Kuzema, P. (2015). TGA-DSC-MS analysis of silicon carbide and of its carbon-silica precursor. *Chemistry, Physics and Technology of Surface*, 6 (2): 216-223.

Titus, D., Samuel, E. and Roopan, S. (2019). Nanoparticle characterization techniques. In green synthesis, characterization and applications of nanoparticles. *Elsevier*, 12: 303-319.

Todkar, B., Deorukhkar, O. and Deshmukh, S.M. (2016). Extraction of silica from rice husk. *International Journal of Engineering Research and Development*, 12 (3): 69-74.

Toumi, I., Djelad, H., Chouli, F. and Benyoucef, A. (2021). Synthesis of PANI@ZnO hybrid material and evaluations in adsorption of congo red and methylene blue dyes: Structural characterization and adsorption performance. *Journal of Inorganic and Organometallic Polymers and Materials*, 32 (1): 112-121.

Tran, C., Vu, H., Tran, N.V., Nguyen, N., Dang, K., Nguyen, A., Le, B., Mai, V., La, D. and Phan, X. (2021). Synthesis of Si_3N_4 powder by powder metallurgy method in atmospheric pressure N_2: A review. *International Journal of Advanced Engineering Research and Science*, 8 (3): 31-37.

Tsai, W., Lin, Y. and Huang, H. (2021). Valorization of rice husk for the production of porous biochar materials. *Fermentation*, 7 (2): 70-81.

Tuli, F.J., Hossain, A., Fazle Kibria, A., Tareq, A., Mamun, S. and Atique Ullah, A. (2020). Removal of methylene blue from water by low-cost activated carbon prepared from tea waste: A study of adsorption isotherm and kinetics. *Environmental Nanotechnology, Monitoring & Management*, 14: 1-8.

United Nations Children's Fund (UNICEF) and World Health Organization (2019). Progress on household drinking water, sanitation and hygiene 2000-2017. Special focus on inequalities. *New York*.

United Nations Environment Program (2018). Exploring the nature of resilience: A trip down Kenya's Athi River. https://unep.org/news-and-stories/story/exploring-nature-resilience-trip-down-kenyas-athi-river. Accessed date: 19th March, 2018.

United Nations World Water Assessment Programme (2017). The United Nations World Water Development Report 2017. Wastewater: The Untapped Resource. *Paris*, UNESCO.
http://unesco.org/new/en/natural-sciences/environment/water/wwap/wwdr/2017-wastewater-the-untapped resource/ Accessed date: 20th July, 2018.

Unugul, T. and Nigiz, F.U. (2020). Preparation and characterization an active carbon adsorbent from waste mandarin peel and determination of adsorption behavior on removal of synthetic dye solutions. *Water, Air & Soil Pollution*, 231 (11): 538-551.

Verma, G. and Mishra, M. (2018). Development and optimization of UV-Vis spectroscopy-A review. *World Journal of Pharmaceutical Research*, 7 (11): 1170-1180.

Vishnu, D., Sure, J., Kim, H., Kim, J., Kumar, R. and Schwandt, C. (2018). Direct electrochemical preparation of nanostructured silicon carbide and its nitridation behavior. *Journal of The Electrochemical Society*, 165 (14): D731-D742.

Wafula, G., Tole, M., Dharani, N. and Nadir, S. (2020). Effectiveness of a wastewater treatment plant located at EPZ in reducing pollutants discharged into river Athi, Kenya. *Journal of Environmental Science and Engineering B*, 9: 261-276.

Waitara, J.K., Kerich, G., Kihoro, J. and Korir, A. (2021). Poisson-gamma and spatial-temporal models: with application to cervical cancer in Kenya's counties. *American Journal of Theoretical and Applied Statistics*, 10 (3): 158-166.

Waithaka, A.W. (2017). Wastewater management in cotton wet processing in Thika cloth mills in Kiambu County, Kenya. Master's Thesis. *Kenyatta University*. https://ir-library.ku.ac.ke/handle/123456789/18061

Wahyudi, A., Amalia, D. and Sariman. (2013). Preparation of nano silica from silica sand through alkali fusion process. *Indonesian Mining Journal*, 16 (3): 149-153.

Wakhungu, M. (2019) An ethnography of policy: Water reuse policy in Kenya. *Water Policy*, 21 (2): 436-448.

Wan, X. (2013). Carbothermal synthesis of Silicon Nitride. Doctoral Dissertation. *The University of New South Wales*. https://hdl.handle.net/1959.4/52988

Wasilwa, L., Nyaga, A., Watani, G., Kasina, M., Ochieng, V., Muriuki, S., Ondabu, N., Gitonga, L., Kiuru, P., Muli, H. and Waitiki, B. (2019). Macadamia nut propagation. *Kenya Agricultural & Livestock Research Organization*.

Wawrzkiewicz, M. and Hubicki, Z. (2016). Anion exchange resins of tri-n-butyl ammonium functional groups for dye baths and textile wastewater treatment. *Solvent Extraction and Ion Exchange*, 34 (6): 558-575.

Wawrzkiewicz, M. and Hubicki, Z. (2015). Anion exchange resins as effective sorbents for removal of acid, reactive, and direct dyes from textile wastewaters. In ion exchange-studies and applications. *Intech Open*, 2: 37-72.

Wongcharee, S., Aravinthan, V. and Erdei, L. (2019). Mesoporous activated carbon-zeolite composite prepared from waste macadamia nut shell and synthetic faujasite. *Chinese Journal of Chemical Engineering*, 27 (1): 226-236.

World Health Organization (2020). International agency for research on cancer, Kenya. *Globocan*. Geneva. https://gco.iarc.who.int/media/globocan/factsheets/populations/404-kenya-fact-sheet.pdf

World Health Organization (2017). Drinking-water fact sheets. *WHO Press*. https://iris.who.int/server/api/core/bitstreams/1b7a285e-3635-45dd-a1a9-6068c8fbe173/content

Wu, L., Liu, X., Lv, G., Zhu, R., Tian, L., Liu, M., Li, Y., Rao, W., Liu, T. and Liao, L. (2021). Study on the adsorption properties of methyl orange by natural one-dimensional nano-mineral materials with different structures. *Scientific Reports*, 11 (1): 10640-10650.

Wu, D., Chen, G., Hu, B. and Deng, H. (2019). Feasibility and energy consumption analysis of phenol removal from salty wastewater by electro-electrodialysis. *Separation and Purification Technology*, 215: 44-50.

Xiao, R., Yang, W., Cong, X., Dong, K., Xu, J., Wang, D. and Yang, X. (2020). Thermogravimetric analysis and reaction kinetics of lignocellulosic biomass pyrolysis. *Energy*, 201: 1-12.

Xiao, J., Li, F., Zhong, Q., Bao, H., Wang, B., Huang, J. and Zhang, Y. (2015). Separation of aluminum and silica from coal gangue by elevated temperature acid leaching for the preparation of alumina and SiC. *Hydrometallurgy*, 155: 118-124.

Xu, Y., Ren, B., Wang, R., Zhang, L., Jiao, T. and Liu, Z. (2019). Facile preparation of rod-like MnO nanomixtures via hydrothermal approach and highly efficient removal of methylene blue for wastewater treatment. *Nanomaterials*, 9 (1): 10-25.

Yaashikaa, P.R., Kumar, P.S., Varjani, S. and Saravanan, A. (2020). A critical review on the biochar production techniques, characterization, stability and applications for circular bioeconomy. *Biotechnology Reports*, 28: 1-15.

Yahuza, K., Ibrahim, M., Ayuba, A. and Hamza, R. (2017). Fixed-bed column adsorption of methyl blue using carbon derived from axle-wood (*Anogeissus leiocarpus*) stem as adsorbent. *Bayero Journal of Pure and Applied Sciences*, 10 (1): 304-310.

Yang, H., Mu, B., Zhang, T., Lu, Y. and Wang, A. (2023). Sustainable utilization of natural sands for cleaner preparation of high-performance nanostructured cobalt blue composite pigments by dolomite induced mechanochemistry. *RSC Sustainability*, 1: 1278-1289.

Yang, C., Li, L., Shi, J., Long, C. and Li, A. (2015). Advanced treatment of textile dyeing secondary effluent using magnetic anion exchange resin and its effect on organic fouling in subsequent RO membrane. *Journal of Hazardous Materials*, 284: 50-57.

Youcef, L., Belaroui, L. and López-Galindo, A. (2019). Adsorption of a cationic methylene blue dye on an Algerian palygorskite. *Applied Clay Science*, 179: 1-10.

Yue, C., Liu, J., Zhang, H., Dai, L., Wei, B. and Chang, Q. (2018). Increasing the hydrophobicity of filter medium particles for oily water treatment using coupling agents. *Heliyon*, 4 (9): 1-14.

Yunnen, C., Ye, W., Chen, L., Guo Lin, Jinxia, N. and Rushan, R. (2017). Continuous fixed-bed column study and adsorption modeling: Removal of arsenate and arsenite in aqueous solution by organic modified spent grains. *Polish Journal of Environmental Studies*, 26 (4): 1847-1854.

Zare, K., Sadegh, H., Shahryari-ghoshekandi, R., Maazinejad, B., Ali, V., Tyagi, I., Agarwal, S. and Gupta, V.K. (2015). Enhanced removal of toxic congo red dye using multi walled carbon nanotubes: Kinetic, equilibrium studies and its comparison with other adsorbents. *Journal of Molecular Liquids*, 212: 266-271.

Zhang, H., Li, Y., Cheng, B., Ding, C. and Zhang, Y. (2020). Synthesis of a starch-based sulfonic ion exchange resin and adsorption of dyestuffs to the resin. *International Journal of Biological Macromolecules*, 161: 561-572.

Zhang, Z., Wang, J., Tang, X., Liu, Y., Han, Z. and Chen, Y. (2019). Comparison study between mesoporous silica nanoscale microsphere and active carbon used as the matrix of shape-stabilized phase change material. *Scientific Reports*, 9 (1): 1-10.

Zhang, X., Lu, M., Idrus, M., Crombie, C. and Jegatheesan, V. (2019) Performance of precipitation and electrocoagulation as pretreatment of silica removal in brackish water and seawater. *Process Safety and Environmental Protection*, 126: 18-24.

Zhang, Z., Li, Y., Du, Q. and Li, Q. (2018). Adsorption of congo red from aqueous solutions by porous soybean curd xerogels. *Polish Journal of Chemical Technology*, 20 (3): 95-102.

Zhang, H., Ogura, H., Umezu, M., Imai, T. and Ishii, M. (2017). Hydration reaction characteristics of CaO from various local limestone samples as chemical heat pump/storage materials. *Journal of Materials Science*, 52 (19): 11360-11369.

Zhang, W., Dong, L., Yan, H., Li, H., Jiang, Z., Kan, X., Yang, H., Li, A. and Cheng, R. (2011). Removal of methylene blue from aqueous solutions by straw based adsorbent in a fixed-bed column. *Chemical Engineering Journal*, 173 (2): 429-436.

Zhao, Y., Shun Dong, S., Hu, P., Zhao, X. and Hong, C. (2021). Recent progress in synthesis, growth mechanisms, properties, and applications of silicon nitride nanowires. *Ceramics International*, 47 (11): 14944-14965.

Zhao, P., Zhang, R. and Wang, J. (2017). Adsorption of methyl orange from aqueous solution using chitosan/diatomite composite. *Water Science and Technology*, 75 (7): 1633-1642.

Zhi, Q., Wang, B., Zhao, S., Zhang, Z., Deng, Y., Zhang, N. and Yang, J. (2019). Synthesis and mechanical properties of highly porous ultrafine-grain Si_3N_4 ceramics via carbothermal reduction-nitridation combined with liquid phase sintering. *Ceramics International*, 45 (17): 21359-21364.

Zhou, Y., Ge, L., Fan, N. and Xia, M. (2018). Adsorption of congo red from aqueous solution onto shrimp shell powder. *Adsorption Science & Technology*, 36 (5): 1310-1330.

Zouaouid, K. and Gheriani, R. (2018). Mineralogical analysis of sand roses and sand dunes samples from two regions of South Algeria. *Silicon*, 11 (3): 1537-1545.

Zulfiqar, U., Subhani, T. and Husain, S.W. (2016). Synthesis of silica nanoparticles from sodium silicate under alkaline conditions. *Journal of Sol-Gel Science and Technology*, 77 (3): 753-758.

APPENDICES

Appendix I: Maximum wavelength absorbance for MO, MB and CR dyes

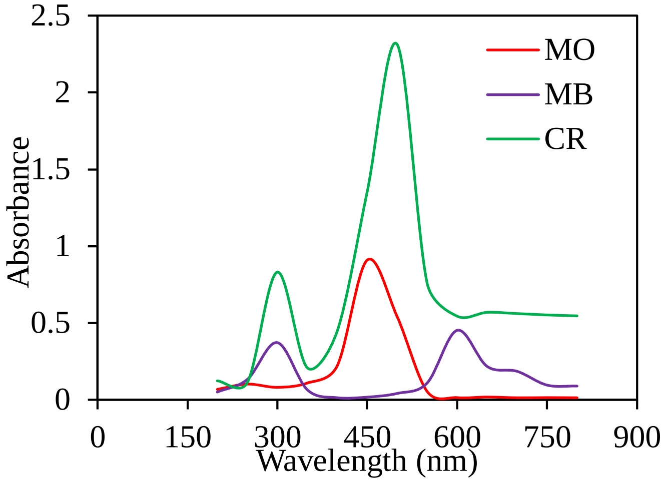

Appendix II: Calibration curves for CR, MO and MB dyes

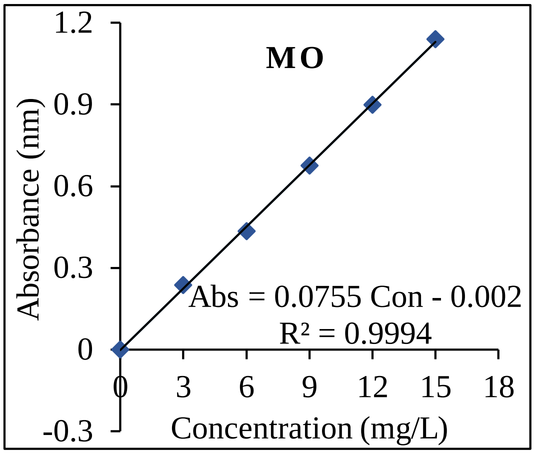

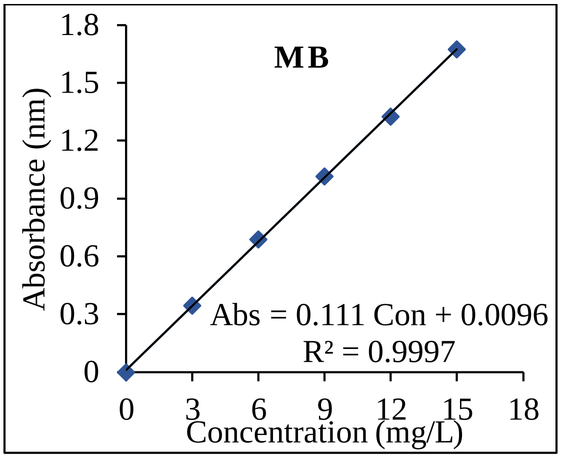

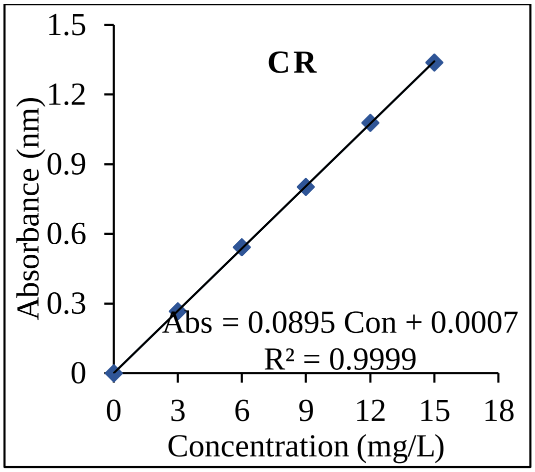

Appendix III A: Effect of varying the pH on removal of MO dyes

pH	SN-1	SN-2	SN-3	SN-4	SN-5	SN-6
			(Mean ± S.D)			
1	13.57 ± 0.06^{d}	14.55 ± 0.03^{c}	13.63 ± 0.04^{d}	14.58 ± 0.01^{c}	15.64 ± 0.14^{b}	16.52 ± 0.05^{a}
3	13.13 ± 0.02^{b}	10.57 ± 0.01^{c}	12.00 ± 0.05^{b}	11.81 ± 0.03^{b}	13.51 ± 0.02^{a}	12.18 ± 0.12^{b}
5	9.70 ± 0.05^{c}	9.67 ± 0.04^{c}	11.45 ± 0.01^{b}	10.26 ± 0.02^{c}	12.64 ± 0.02^{a}	11.84 ± 0.01^{ab}
7	7.91 ± 0.02^{c}	8.18 ± 0.05^{c}	8.73 ± 0.01^{abc}	8.45 ± 0.00^{bc}	9.30 ± 0.04^{ab}	9.53 ± 0.09^{a}
9	6.26 ± 0.05^{b}	6.35 ± 0.01^{b}	6.22 ± 0.02^{b}	6.24 ± 0.01^{b}	8.51 ± 0.17^{a}	8.63 ± 0.08^{a}
11	4.29 ± 0.03^{d}	5.17 ± 0.06^{cd}	5.86 ± 0.00^{bc}	5.25 ± 0.04^{cd}	7.50 ± 0.01^{a}	6.88 ± 0.07^{ab}
13	3.99 ± 0.03^{bc}	4.87 ± 0.05^{b}	4.82 ± 0.01^{b}	3.31 ± 0.07^{c}	6.93 ± 0.01^{a}	6.11 ± 0.06^{a}

mean values with same letter (s) within the same row are not significantly different
(One-way ANOVA, Fisher LSD-test, α = 0.05)

Appendix III B: Effect of varying the pH on removal of MB dyes

pH	SN-1	SN-2	SN-3	SN-4	SN-5	SN-6
			(Mean ± S.D)			
1	7.01 ± 0.05^{a}	5.90 ± 0.04^{c}	5.21 ± 0.07^{c}	7.14 ± 0.08^{a}	6.52 ± 0.01^{ab}	5.69 ± 0.12^{c}
3	7.68 ± 0.02^{ab}	6.70 ± 0.18^{bc}	5.93 ± 0.01^{c}	8.43 ± 0.00^{a}	7.47 ± 0.03^{ab}	8.06 ± 0.06^{a}
5	8.22 ± 0.05^{c}	8.70 ± 0.01^{bc}	7.87 ± 0.01^{c}	9.58 ± 0.07^{ab}	9.50 ± 0.04^{ab}	10.38 ± 0.06^{a}
7	10.99 ± 0.36^{bc}	10.15 ± 0.08^{cd}	8.51 ± 0.02^{e}	9.92 ± 0.05^{d}	11.61 ± 0.03^{ab}	12.15 ± 0.01^{a}
9	11.53 ± 0.07^{bc}	11.34 ± 0.06^{bc}	10.97 ± 0.03^{c}	10.55 ± 0.05^{c}	12.23 ± 0.02^{b}	13.88 ± 0.06^{a}
11	13.93 ± 0.09^{bc}	13.99 ± 0.06^{b}	10.90 ± 0.03^{d}	12.91 ± 0.03^{c}	14.62 ± 0.01^{b}	16.82 ± 0.05^{a}
13	12.60 ± 0.01^{bc}	12.97 ± 0.03^{b}	10.00 ± 0.11^{d}	11.71 ± 0.05^{c}	13.59 ± 0.05^{b}	16.35 ± 0.07^{a}

mean values with same letter (s) within the same row are not significantly different
(One-way ANOVA, Fisher LSD-test, α = 0.05)

Appendix III C: Effect of varying the pH on removal of CR dyes

pH	SN-1	SN-2	SN-3	SN-4	SN-5	SN-6
	(Mean ± S.D)					
1	15.70 ± 0.05^{b}	15.99 ± 0.13^{ab}	14.37 ± 0.08^{c}	16.81 ± 0.05^{a}	15.75 ± 0.07^{b}	14.33 ± 0.03^{c}
3	13.17 ± 0.00^{b}	15.51 ± 0.06^{a}	12.48 ± 0.01^{c}	13.90 ± 0.03^{b}	14.20 ± 0.01^{b}	13.63 ± 0.01^{b}
5	9.45 ± 0.05^{c}	12.48 ± 0.01^{b}	8.74 ± 0.00^{c}	9.27 ± 0.09^{c}	14.01 ± 0.23^{a}	11.70 ± 0.02^{b}
7	8.90 ± 0.12^{b}	7.28 ± 0.03^{c}	7.16 ± 0.05^{c}	8.70 ± 0.01^{b}	12.09 ± 0.01^{a}	8.44 ± 0.01^{b}
9	7.11 ± 0.02^{ab}	5.97 ± 0.01^{c}	6.53 ± 0.02^{bc}	6.55 ± 0.01^{bc}	8.04 ± 0.07^{a}	7.18 ± 0.06^{ab}
11	6.72 ± 0.01^{a}	5.44 ± 0.08^{b}	5.93 ± 0.04^{ab}	5.16 ± 0.03^{b}	5.22 ± 0.00^{b}	5.42 ± 0.13^{b}
13	4.86 ± 0.03^{a}	5.42 ± 0.06^{a}	4.74 ± 0.02^{a}	4.96 ± 0.01^{a}	4.95 ± 0.01^{a}	5.41 ± 0.11^{a}

mean values with same letter (s) within the same row are not significantly different
(One-way ANOVA, Fisher LSD-test, $\alpha = 0.05$)

Appendix IV A: Effect of varying the agitation time on removal of MO dyes

Agitation time (Minutes)	SN-1	SN-2	SN-3	SN-4	SN-5	SN-6
	(Mean ± S.D)					
10	9.78 ± 0.06^{b}	8.99 ± 0.01^{b}	9.63 ± 0.02^{b}	12.32 ± 0.01^{a}	6.35 ± 0.00^{c}	9.24 ± 0.02^{b}
30	10.88 ± 0.02^{c}	10.92 ± 0.01^{c}	10.03 ± 0.01^{c}	15.03 ± 0.05^{a}	10.58 ± 0.01^{c}	13.10 ± 0.00^{b}
50	9.99 ± 0.08^{c}	14.15 ± 0.01^{b}	14.11 ± 0.02^{b}	15.55 ± 0.07^{a}	13.93 ± 0.02^{b}	14.05 ± 0.11^{b}
70	9.76 ± 0.02^{d}	10.80 ± 0.02^{cd}	14.30 ± 0.01^{a}	12.38 ± 0.01^{b}	12.16 ± 0.02^{b}	10.88 ± 0.00^{c}
90	9.49 ± 0.02^{b}	10.13 ± 0.01^{b}	12.75 ± 0.01^{a}	12.06 ± 0.01^{a}	12.86 ± 0.02^{a}	11.84 ± 0.02^{a}
110	9.68 ± 0.03^{d}	10.02 ± 0.00^{cd}	12.12 ± 0.01^{ab}	12.38 ± 0.01^{a}	12.14 ± 0.01^{a}	11.08 ± 0.01^{bc}

mean values with same letter (s) within the same row are not significantly different
(One-way ANOVA, Fisher LSD-test, $\alpha = 0.05$)

Appendix IV B: Effect of varying the agitation time on removal of MB dyes

Agitation time (Minutes)	**SN-1**	**SN-2**	**SN-3**	**SN-4**	**SN-5**	**SN-6**
	(Mean ± S.D)					
10	9.06 ± 0.01^{ab}	9.42 ± 0.04^{a}	9.79 ± 0.01^{a}	8.34 ± 0.04^{b}	5.20 ± 0.02^{c}	9.74 ± 0.02^{a}
30	11.67 ± 0.00^{c}	14.38 ± 0.06^{a}	12.90 ± 0.07^{b}	11.05 ± 0.07^{c}	12.81 ± 0.01^{b}	14.56 ± 0.09^{a}
50	14.15 ± 0.06^{b}	12.88 ± 0.13^{c}	15.78 ± 0.00^{a}	14.09 ± 0.04^{b}	14.44 ± 0.01^{b}	14.42 ± 0.01^{b}
70	12.88 ± 0.01^{cd}	12.48 ± 0.11^{d}	15.21 ± 0.10^{a}	13.94 ± 0.02^{bc}	15.71 ± 0.04^{a}	14.65 ± 0.02^{ab}
90	12.19 ± 0.04^{c}	12.25 ± 0.02^{c}	15.50 ± 0.16^{a}	12.93 ± 0.06^{c}	14.52 ± 0.01^{ab}	14.19 ± 0.07^{b}
110	11.99 ± 0.20^{c}	12.05 ± 0.02^{c}	15.17 ± 0.19^{a}	12.82 ± 0.02^{c}	14.44 ± 0.06^{ab}	14.04 ± 0.01^{b}

mean values with same letter (s) within the same row are not significantly different
(One-way ANOVA, Fisher LSD-test, $\alpha = 0.05$)

Appendix IV C: Effect of varying the agitation time on removal of CR dyes

Agitation time (Minutes)	**SN-1**	**SN-2**	**SN-3**	**SN-4**	**SN-5**	**SN-6**
	(Mean ± S.D)					
10	10.80 ± 0.22^{a}	11.23 ± 0.03^{a}	8.56 ± 0.01^{b}	9.02 ± 0.08^{b}	10.45 ± 0.07^{a}	11.50 ± 0.20^{a}
30	12.58 ± 0.02^{b}	13.38 ± 0.13^{ab}	10.72 ± 0.01^{c}	11.09 ± 0.11^{c}	13.04 ± 0.03^{b}	14.41 ± 0.03^{a}
50	14.26 ± 0.07^{b}	10.59 ± 0.01^{d}	13.06 ± 0.02^{c}	10.07 ± 0.06^{d}	15.05 ± 0.01^{ab}	15.85 ± 0.06^{a}
70	12.95 ± 0.09^{a}	10.01 ± 0.02^{b}	12.23 ± 0.00^{a}	10.00 ± 0.01^{b}	10.66 ± 0.03^{b}	12.15 ± 0.00^{a}
90	12.90 ± 0.05^{a}	10.00 ± 0.02^{b}	12.73 ± 0.18^{a}	10.01 ± 0.01^{b}	10.53 ± 0.31^{b}	10.64 ± 0.11^{b}
110	12.34 ± 0.01^{a}	10.05 ± 0.02^{b}	12.15 ± 0.20^{a}	10.64 ± 0.01^{b}	10.89 ± 0.48^{b}	10.78 ± 0.07^{b}

mean values with same letter (s) within the same row are not significantly different
(One-way ANOVA, Fisher LSD-test, $\alpha = 0.05$)

Appendix V A: Effect of varying the adsorbent dosage on removal of MO dyes

Dosage (mg)	SN-1	SN-2	SN-3	SN-4	SN-5	SN-6
	(Mean ± S.D)					
5	5.24 ± 1.09^{abc}	3.70 ± 0.25^{bcd}	6.96 ± 1.98^{a}	6.78 ± 0.16^{ab}	5.85 ± 0.14^{abc}	3.20 ± 0.06^{cd}
10	7.96 ± 0.28^{ab}	6.60 ± 0.41^{c}	8.63 ± 0.12^{a}	7.14 ± 0.11^{bc}	7.37 ± 0.03^{bc}	6.93 ± 0.04^{bc}
15	9.63 ± 0.21^{ab}	8.46 ± 0.07^{cd}	10.60 ± 0.10^{a}	8.01 ± 0.07^{d}	9.52 ± 0.05^{abc}	9.01 ± 0.01^{bcd}
20	14.57 ± 0.27^{a}	8.42 ± 0.03^{d}	9.60 ± 0.03^{c}	8.55 ± 0.03^{cd}	11.64 ± 0.04^{b}	12.65 ± 0.02^{b}
25	14.06 ± 0.08^{a}	8.34 ± 0.01^{d}	8.55 ± 0.01^{d}	10.56 ± 0.05^{c}	11.02 ± 0.05^{bc}	11.88 ± 0.02^{b}
30	12.13 ± 0.06^{a}	8.30 ± 0.02^{c}	8.01 ± 0.05^{c}	11.97 ± 0.02^{a}	10.32 ± 0.01^{b}	10.54 ± 0.01^{b}
35	11.26 ± 0.01^{a}	8.15 ± 0.01^{b}	7.90 ± 0.02^{b}	11.29 ± 0.00^{a}	10.31 ± 0.02^{a}	10.36 ± 0.02^{a}
40	9.93 ± 0.01^{a}	8.14 ± 0.01^{b}	7.89 ± 0.01^{b}	9.91 ± 0.01^{a}	9.95 ± 0.00^{a}	9.91 ± 0.00^{a}

mean values with same letter (s) within the same row are not significantly different
(One-way ANOVA, Fisher LSD-test, $\alpha = 0.05$)

Appendix V B: Effect of varying the adsorbent dosage on removal of MB dyes

Dosage (mg)	SN-1	SN-2	SN-3	SN-4	SN-5	SN-6
	(Mean ± S.D)					
5	6.96 ± 0.03^{a}	3.59 ± 0.10^{b}	4.59 ± 0.04^{b}	6.37 ± 0.07^{a}	3.96 ± 0.15^{b}	4.00 ± 0.06^{b}
10	8.52 ± 0.20^{a}	4.85 ± 0.12^{c}	6.49 ± 0.01^{b}	8.63 ± 0.03^{a}	6.53 ± 0.04^{b}	5.64 ± 0.11^{bc}
15	10.64 ± 0.03^{a}	6.02 ± 0.08^{d}	7.02 ± 0.02^{cd}	8.01 ± 0.02^{c}	9.53 ± 0.04^{b}	7.02 ± 0.05^{cd}
20	11.53 ± 0.10^{a}	6.89 ± 0.06^{c}	8.86 ± 0.04^{b}	7.87 ± 0.04^{bc}	10.69 ± 0.07^{a}	8.02 ± 0.02^{b}
25	11.86 ± 0.03^{a}	7.21 ± 0.01^{c}	9.46 ± 0.00^{b}	7.70 ± 0.02^{c}	12.45 ± 0.03^{a}	9.49 ± 0.05^{b}
30	12.10 ± 0.01^{a}	7.97 ± 0.01^{c}	10.63 ± 0.01^{b}	7.57 ± 0.02^{c}	12.88 ± 0.01^{a}	9.99 ± 0.00^{b}
35	10.57 ± 0.01^{ab}	7.13 ± 0.01^{d}	10.01 ± 0.00^{bc}	7.60 ± 0.02^{d}	11.11 ± 0.01^{a}	9.45 ± 0.01^{c}
40	9.91 ± 0.00^{a}	6.99 ± 0.01^{b}	9.76 ± 0.01^{a}	7.57 ± 0.01^{b}	9.81 ± 0.02^{a}	9.01 ± 0.01^{a}

mean values with same letter (s) within the same row are not significantly different
(One-way ANOVA, Fisher LSD-test, $\alpha = 0.05$)

Appendix V C: Effect of varying the adsorbent dosage on removal of CR dyes

Dosage (mg)	SN-1	SN-2	SN-3	SN-4	SN-5	SN-6
	(Mean ± S.D)					
5	6.37 ± 0.11^{ab}	4.51 ± 0.16^{c}	5.63 ± 0.16^{b}	3.52 ± 0.33^{d}	6.99 ± 0.23^{a}	2.99 ± 0.52^{d}
10	7.53 ± 0.07^{c}	6.69 ± 0.05^{d}	8.12 ± 0.08^{b}	4.69 ± 0.14^{f}	9.23 ± 0.06^{a}	5.64 ± 0.05^{e}
15	7.96 ± 0.07^{d}	7.25 ± 0.00^{e}	8.69 ± 0.05^{c}	6.52 ± 0.29^{f}	10.54 ± 0.06^{a}	9.36 ± 0.09^{b}
20	8.37 ± 0.02^{c}	8.01 ± 0.03^{d}	9.66 ± 0.02^{b}	7.10 ± 0.02^{e}	11.45 ± 0.10^{a}	11.55 ± 0.02^{a}
25	9.22 ± 0.04^{c}	7.66 ± 0.02^{e}	10.26 ± 0.03^{b}	7.97 ± 0.01^{d}	10.33 ± 0.08^{b}	11.99 ± 0.01^{a}
30	9.00 ± 0.02^{d}	7.62 ± 0.03^{e}	9.86 ± 0.03^{b}	7.51 ± 0.02^{f}	9.55 ± 0.01^{c}	11.04 ± 0.01^{a}
35	8.96 ± 0.02^{d}	7.63 ± 0.02^{e}	9.84 ± 0.01^{b}	7.53 ± 0.04^{f}	9.25 ± 0.03^{c}	11.11 ± 0.01^{a}
40	8.85 ± 0.01^{d}	7.61 ± 0.01^{e}	9.85 ± 0.01^{a}	7.52 ± 0.01^{f}	9.21 ± 0.01^{c}	9.30 ± 0.01^{b}

mean values with same letter (s) within the same row are not significantly different
(One-way ANOVA, Fisher LSD-test, $\alpha = 0.05$)

Appendix VI A: Effect of varying the initial concentration on removal of MO dyes

Concentration (mg L^{-1})	SN-1	SN-2	SN-3	SN-4	SN-5	SN-6
	(Mean ± S.D)					
10	5.88 ± 0.02^{cd}	5.28 ± 0.03^{d}	5.22 ± 0.02^{d}	6.34 ± 0.05^{a}	6.27 ± 0.03^{ab}	4.14 ± 0.04^{c}
30	12.43 ± 0.03^{e}	15.20 ± 0.06^{bc}	14.97 ± 0.02^{c}	19.04 ± 0.07^{a}	16.81 ± 0.04^{b}	13.64 ± 0.06^{d}
50	24.38 ± 0.03^{b}	26.01 ± 0.01^{a}	24.84 ± 0.02^{b}	18.92 ± 0.09^{d}	26.93 ± 0.03^{a}	21.52 ± 0.02^{c}
70	24.06 ± 0.02^{b}	25.43 ± 0.01^{a}	24.44 ± 0.03^{b}	18.60 ± 0.10^{c}	25.56 ± 0.03^{a}	18.49 ± 0.04^{c}
90	23.39 ± 0.02^{ab}	24.23 ± 0.01^{a}	23.16 ± 0.04^{b}	17.14 ± 0.12^{c}	24.13 ± 0.06^{a}	17.28 ± 0.04^{c}
110	21.81 ± 0.06^{c}	22.85 ± 0.06^{bc}	23.07 ± 0.01^{b}	16.61 ± 0.13^{d}	24.35 ± 0.08^{a}	16.17 ± 0.04^{d}
130	20.50 ± 0.01^{c}	22.24 ± 0.02^{b}	21.03 ± 0.05^{c}	16.69 ± 0.06^{d}	24.27 ± 0.06^{a}	15.32 ± 0.03^{e}

mean values with same letter (s) within the same row are not significantly different
(One-way ANOVA, Fisher LSD-test, $\alpha = 0.05$)

Appendix VI B: Effect of varying the initial concentration on removal of MB dyes

Concentration (mg L^{-1})	SN-1	SN-2	SN-3	SN-4	SN-5	SN-6
	(Mean ± S.D)					
10	4.97 ± 0.02^{c}	6.64 ± 0.04^{a}	5.71 ± 0.03^{b}	5.24 ± 0.01^{b}	6.55 ± 0.05^{a}	5.36 ± 0.15^{bc}
30	16.76 ± 0.02^{e}	18.79 ± 0.01^{d}	21.25 ± 0.02^{b}	18.25 ± 0.07^{d}	24.22 ± 0.06^{a}	19.21 ± 0.05^{cd}
50	27.46 ± 0.09^{b}	17.18 ± 0.02^{e}	24.53 ± 0.02^{c}	17.17 ± 0.04^{e}	29.74 ± 0.04^{a}	18.92 ± 0.07^{d}
70	27.38± 0.08^{b}	16.58 ± 0.06^{f}	22.07 ± 0.01^{c}	17.36 ± 0.05^{e}	28.09 ± 0.07^{a}	18.86 ± 0.05^{de}
90	26.27 ± 0.05^{a}	15.42 ± 0.04^{e}	22.23 ± 0.02^{b}	16.03 ± 0.04^{de}	26.62 ± 0.13^{a}	17.70 ± 0.10^{c}
110	26.62 ± 0.00^{a}	15.50 ± 0.04^{ef}	19.39 ± 0.06^{c}	14.44 ± 0.03^{f}	24.62 ± 0.01^{b}	17.20 ± 0.04^{d}
130	24.59 ± 0.18^{a}	15.56 ± 0.06^{d}	19.07 ± 0.11^{b}	14.16 ± 0.03^{e}	23.93 ± 0.05^{a}	17.43 ± 0.02^{c}

mean values with same letter (s) within the same row are not significantly different
(One-way ANOVA, Fisher LSD-test, α = 0.05)

Appendix VI C: Effect of varying the initial concentration on removal of CR dyes

Concentration (mg L^{-1})	SN-1	SN-2	SN-3	SN-4	SN-5	SN-6
	(Mean ± S.D)					
10	5.01 ± 0.38^{ab}	5.53 ± 0.03^{a}	4.60 ± 0.05^{b}	3.41 ± 0.01^{c}	5.93 ± 0.08^{a}	3.06 ± 0.05^{c}
30	18.06 ± 0.12^{a}	15.68 ± 0.11^{c}	16.10 ± 0.04^{bc}	11.79 ± 0.03^{d}	18.82 ± 0.09^{a}	11.25 ± 0.04^{d}
50	29.29 ± 0.03^{bc}	31.77 ± 0.15^{a}	28.87 ± 0.07^{c}	26.27 ± 0.08^{d}	31.27 ± 0.13^{a}	23.29 ± 0.03^{e}
70	27.42 ± 0.20^{b}	30.47 ± 0.12^{a}	26.35 ± 0.19^{cd}	25.95 ± 0.06^{d}	27.22 ± 0.10^{b}	21.23 ± 0.18^{e}
90	26.88 ± 0.23^{b}	29.34 ± 0.09^{a}	25.87 ± 0.21^{c}	23.27 ± 0.02^{d}	26.51 ± 0.11^{b}	19.83 ± 0.06^{e}
110	26.86 ± 0.27^{b}	28.65 ± 0.05^{a}	25.94 ± 0.10^{bc}	22.55 ± 0.06^{d}	25.73 ± 0.16^{c}	19.40 ± 0.06^{e}
130	26.51 ± 0.11^{b}	28.44 ± 0.04^{a}	24.81 ± 0.15^{c}	22.43 ± 0.08^{d}	23.24 ± 0.06^{cd}	18.36 ± 0.11^{e}

mean values with same letter (s) within the same row are not significantly different
(One-way ANOVA, Fisher LSD-test, α = 0.05)

Appendix VII A: Langmuir isotherms for MO dyes

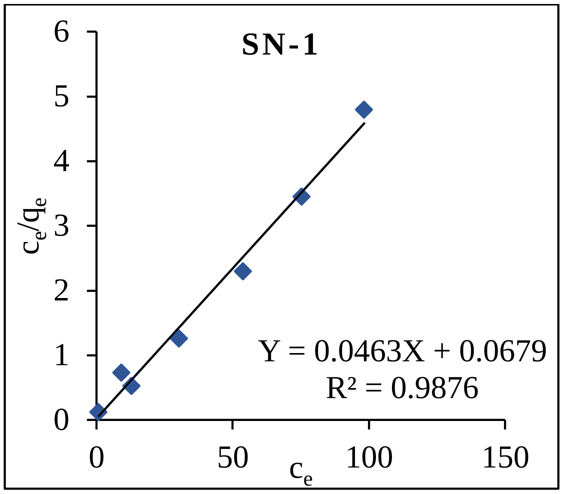

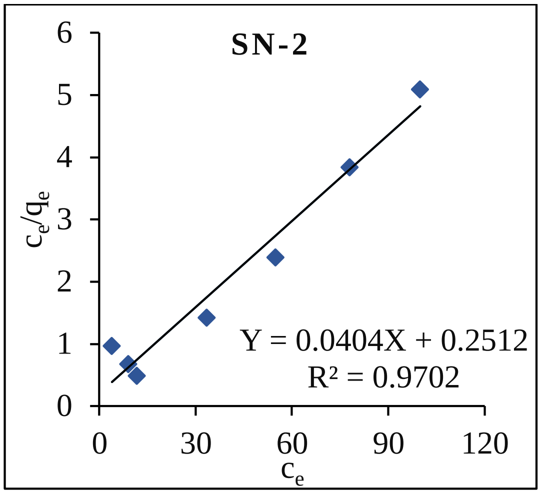

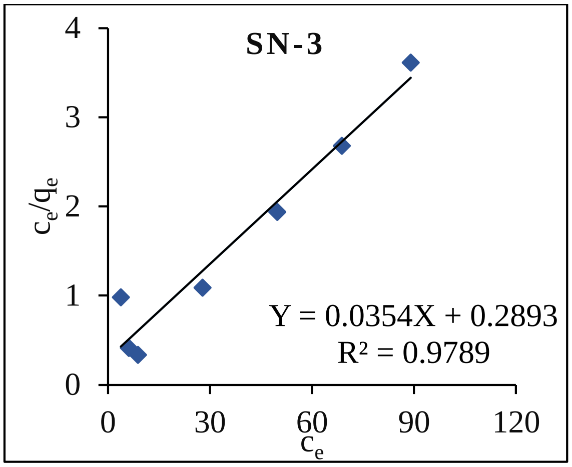

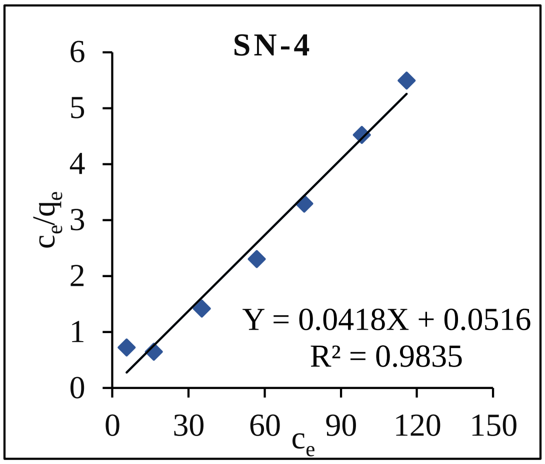

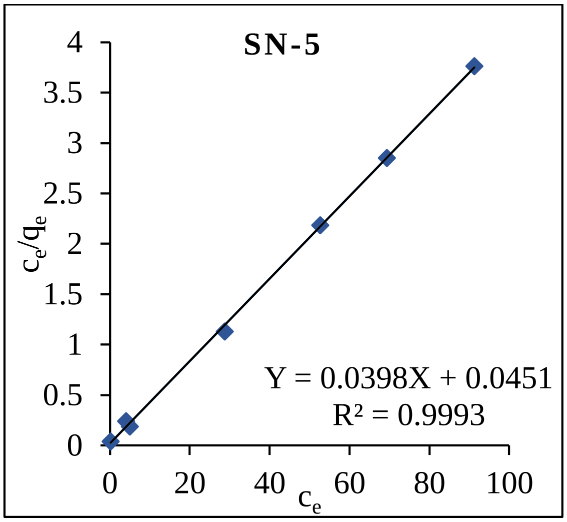

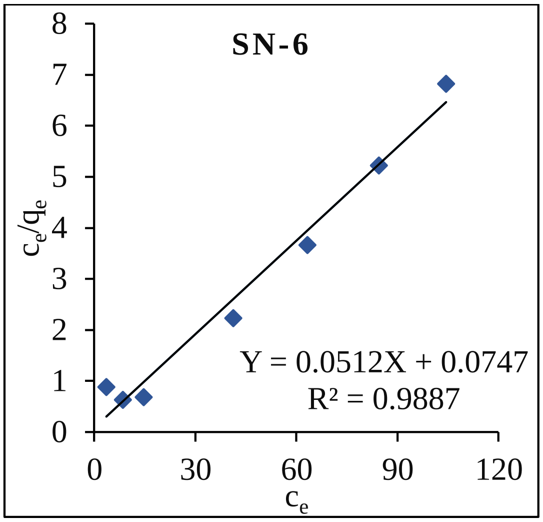

Appendix VII B: Langmuir isotherms for MB dyes

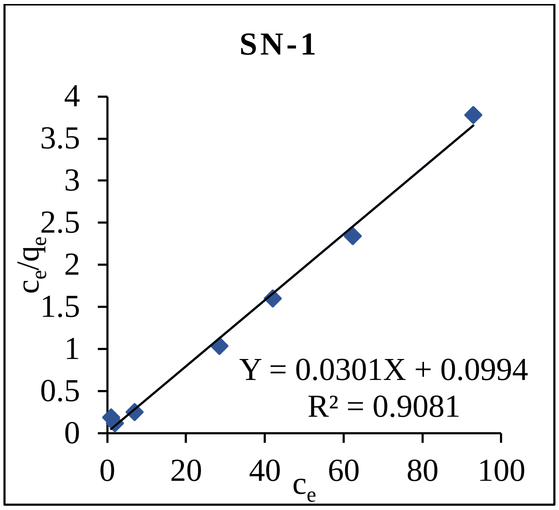

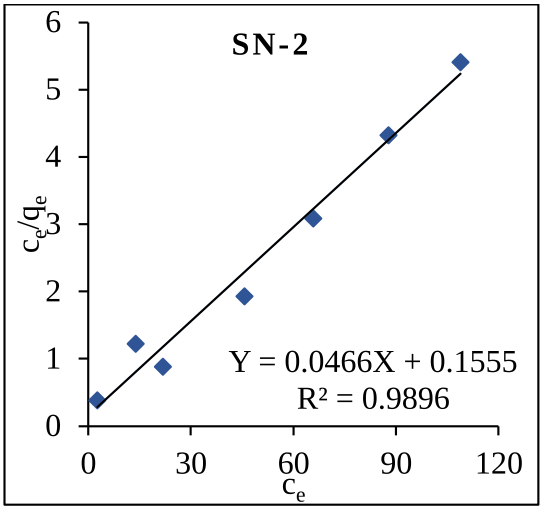

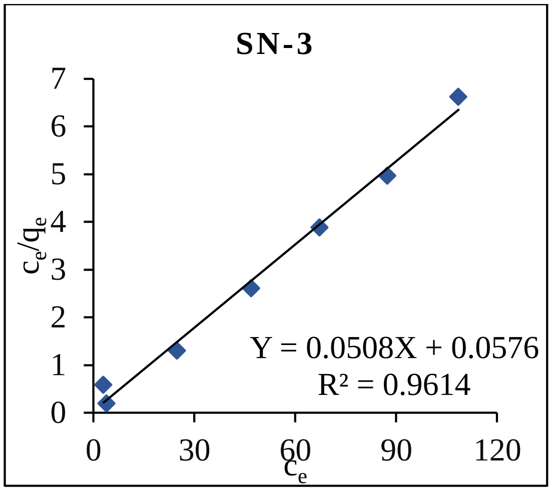

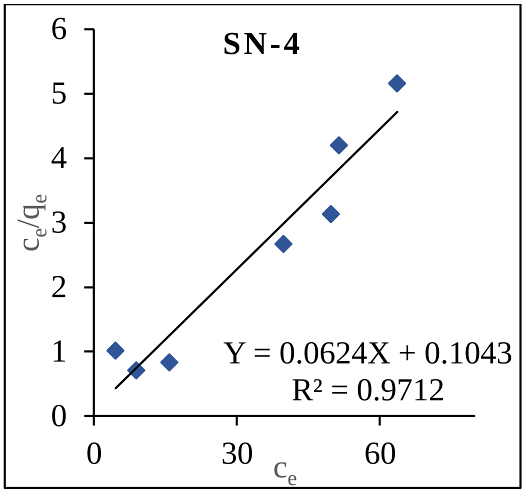

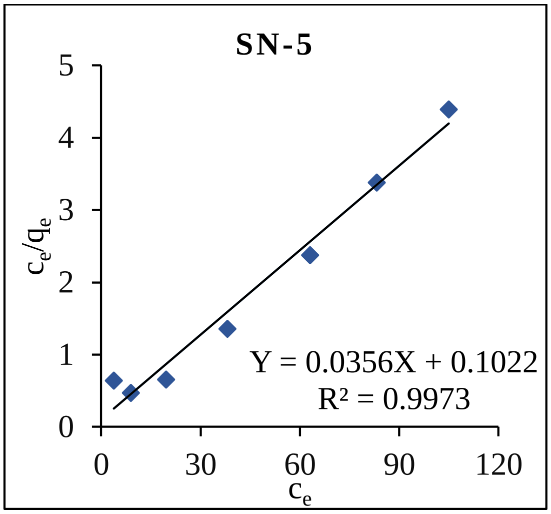

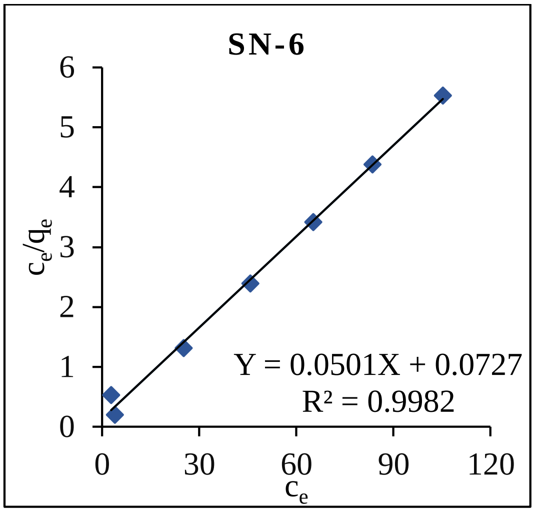

Appendix VII C: Langmuir isotherms for CR dyes

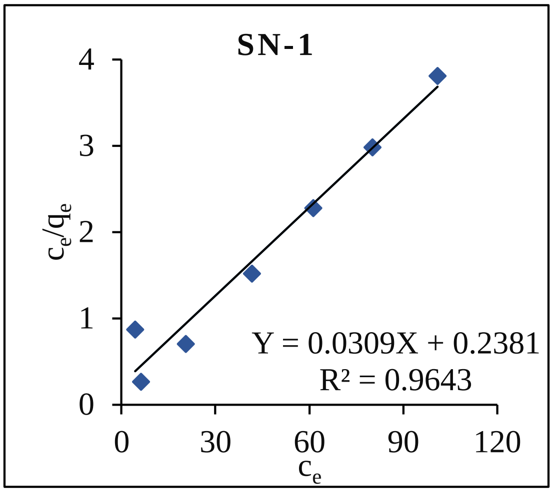

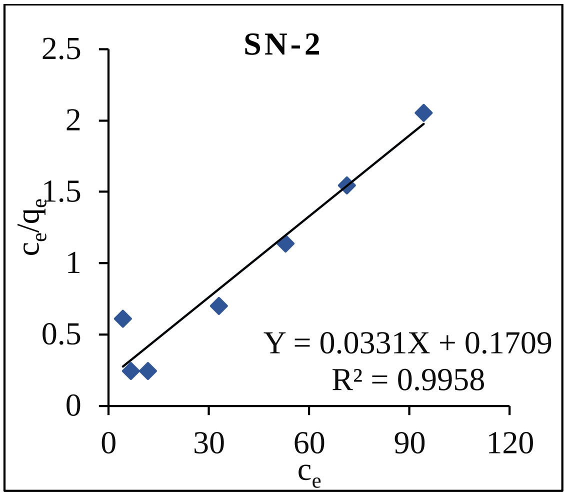

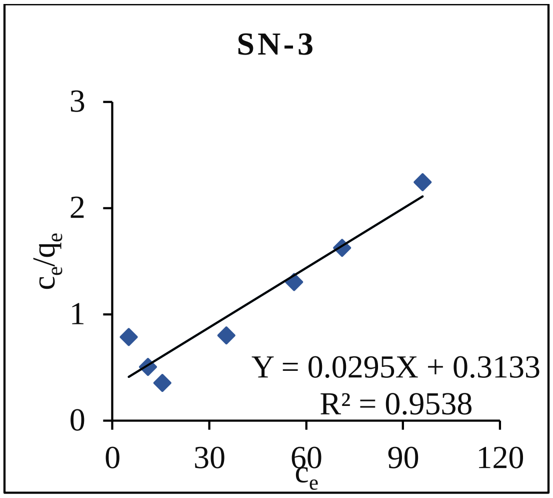

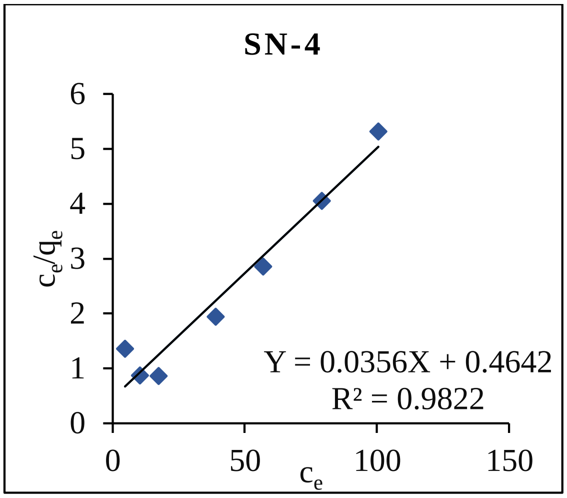

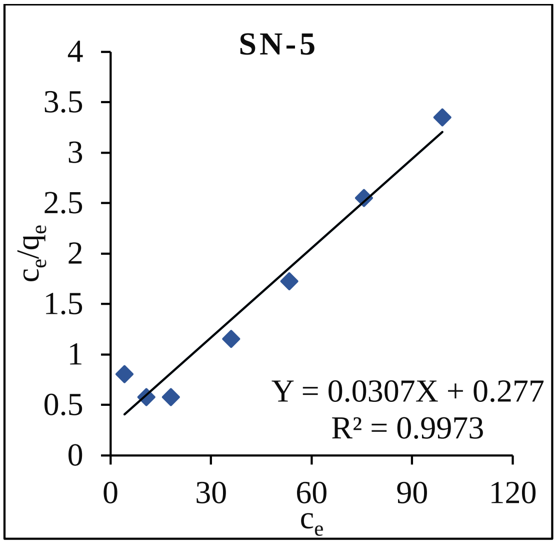

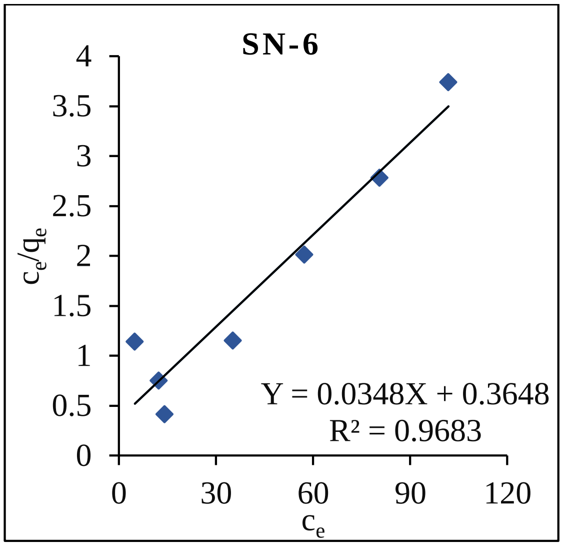

Appendix VIII A: Freundlich isotherms for MO dyes

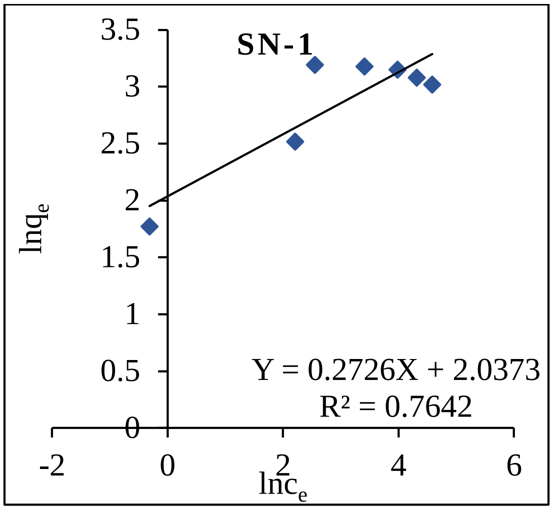

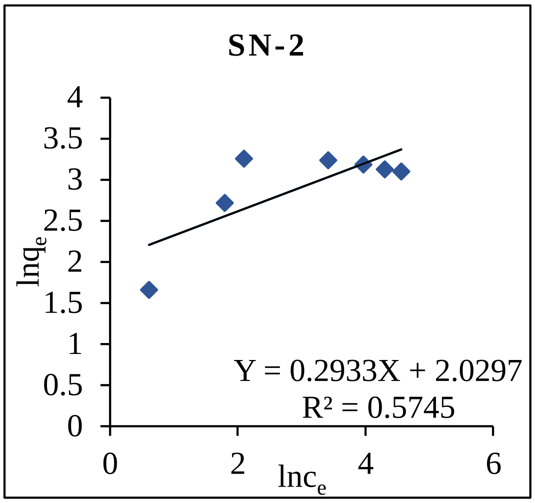

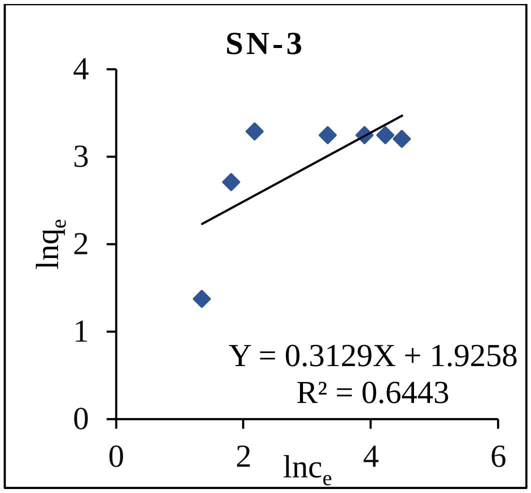

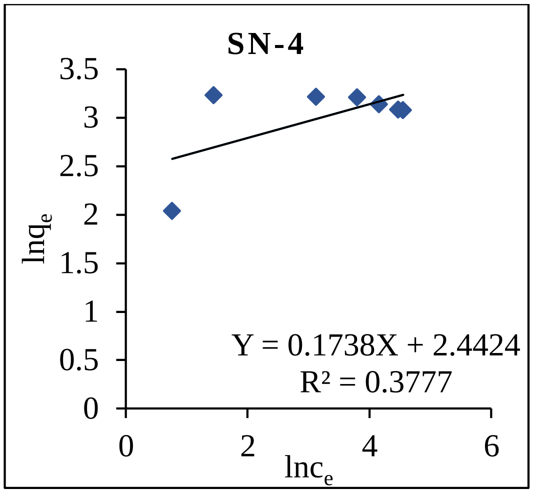

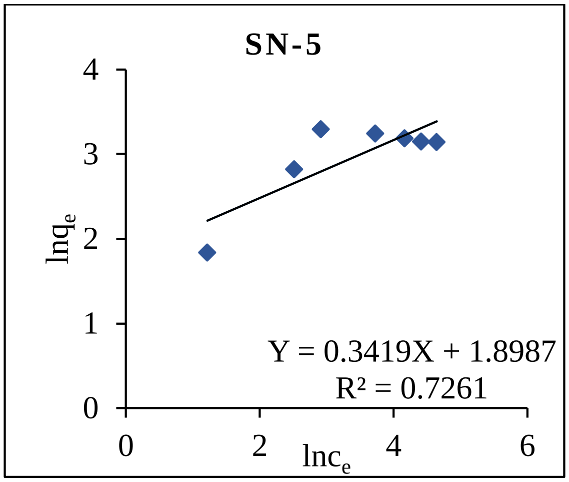

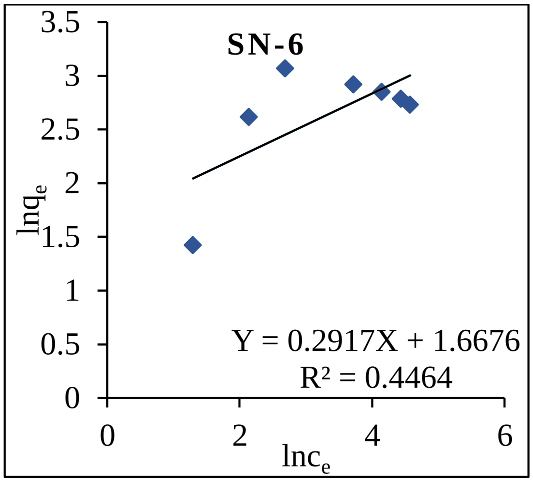

Appendix VIII B: Freundlich isotherms for MB dyes

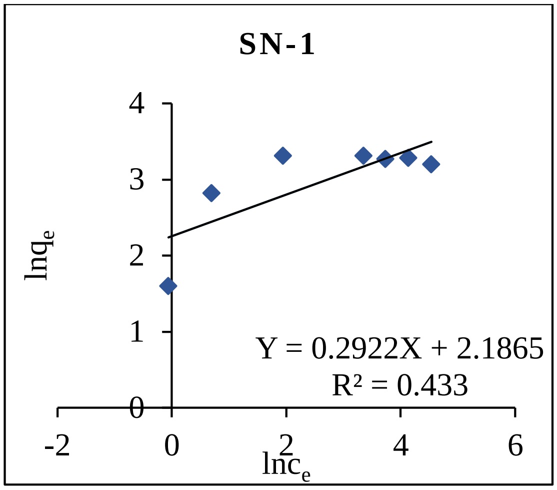

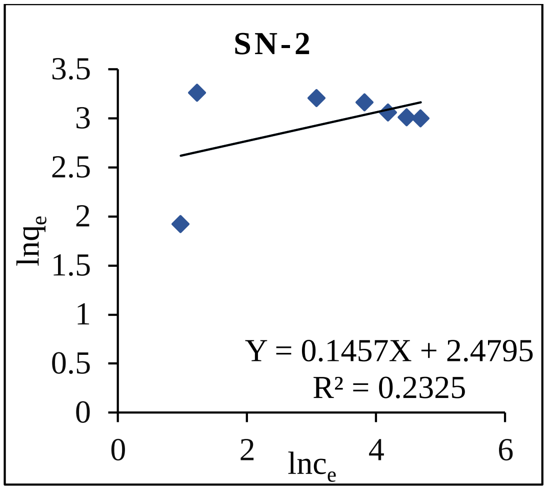

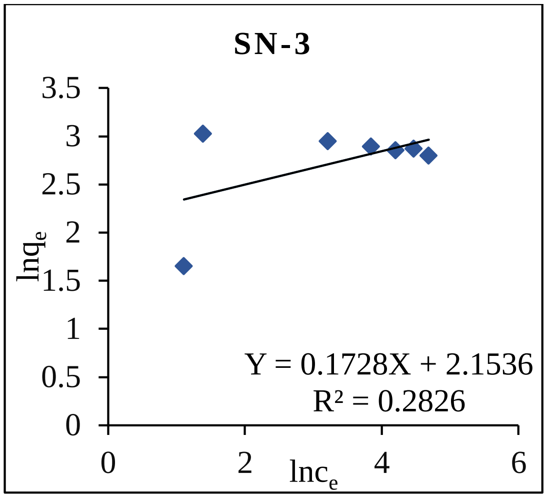

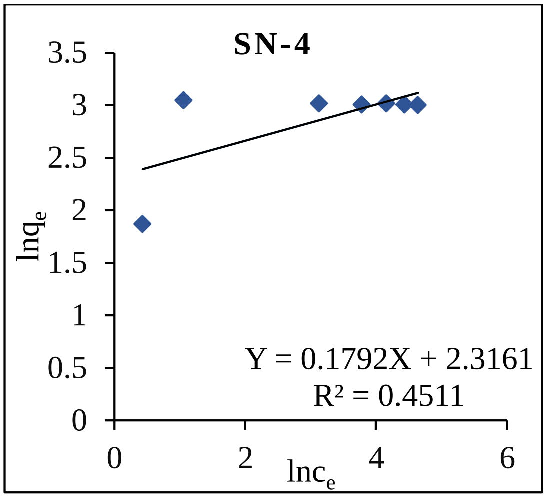

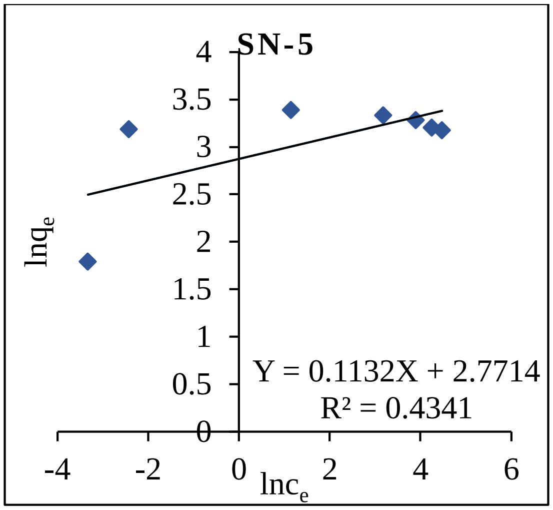

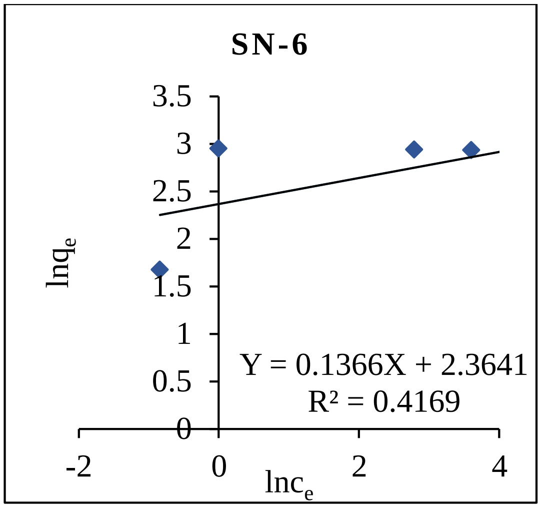

Appendix VIII C: Freundlich isotherms for CR dyes

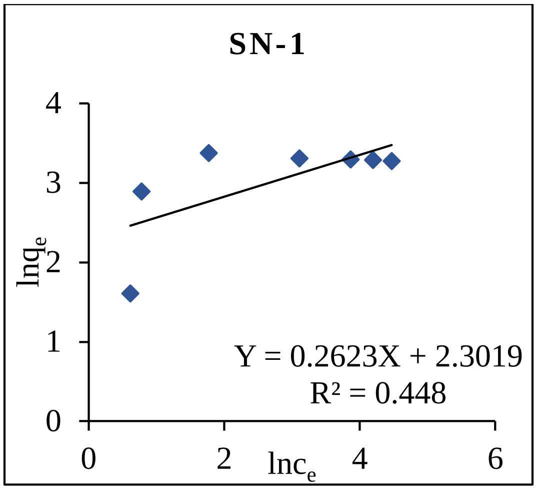

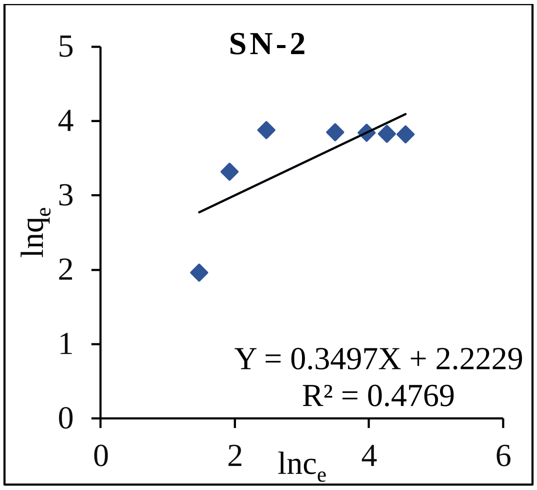

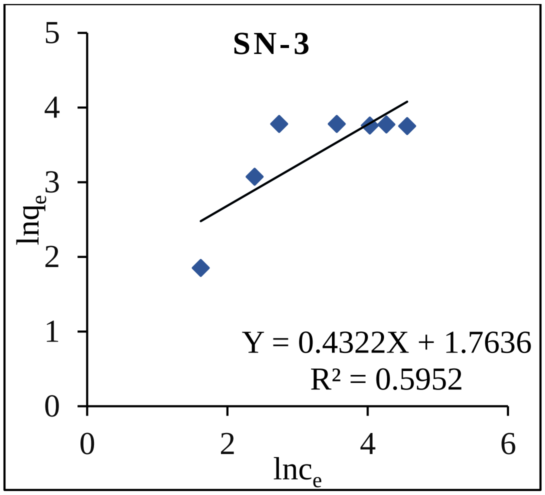

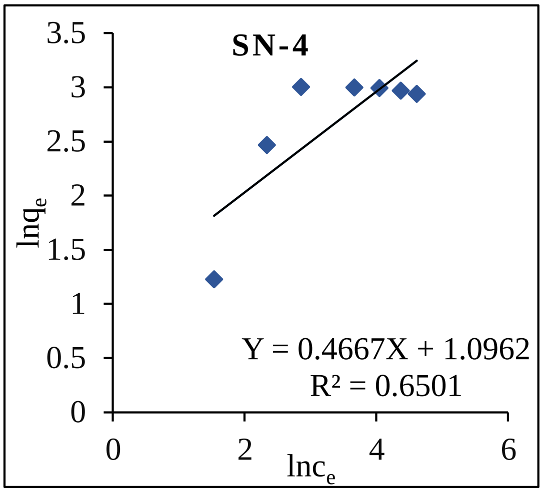

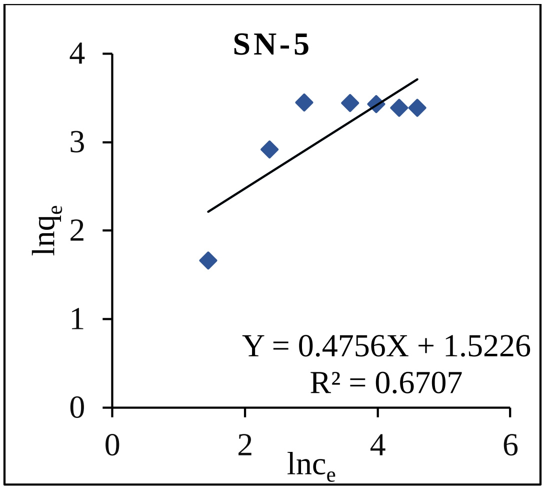

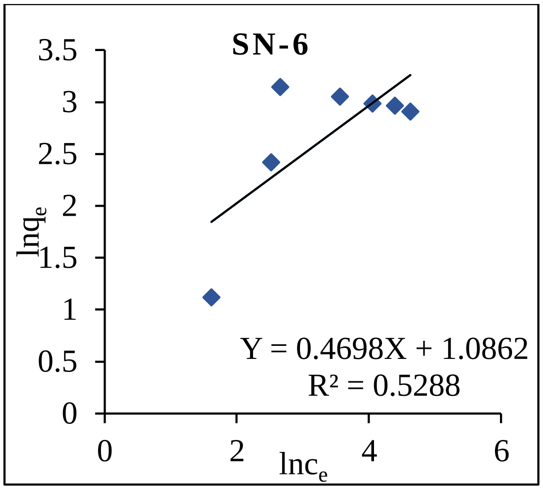

Appendix IX A: Dubinin-Radushkevich isotherms for MO dyes

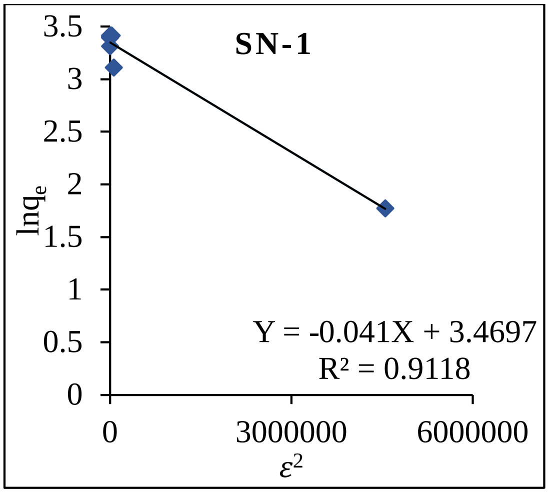

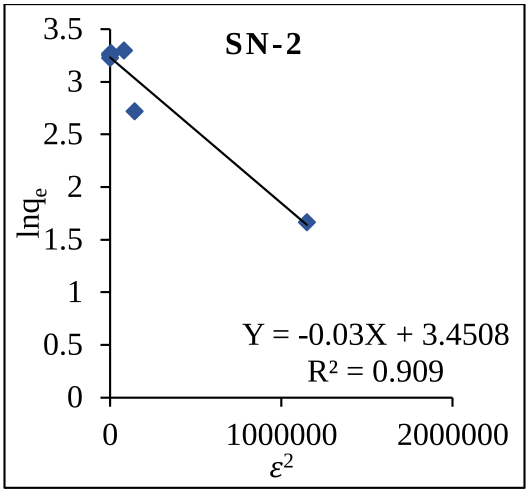

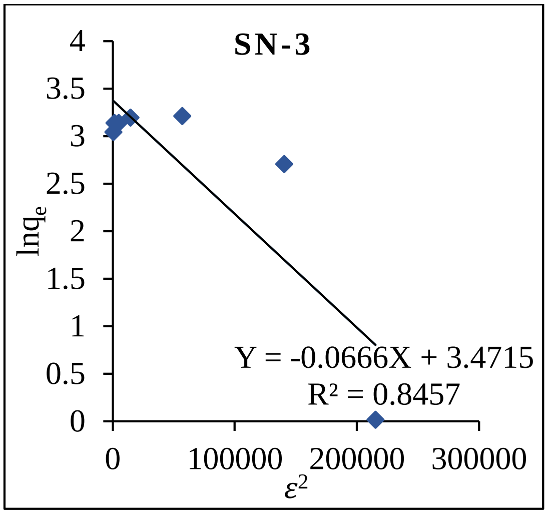

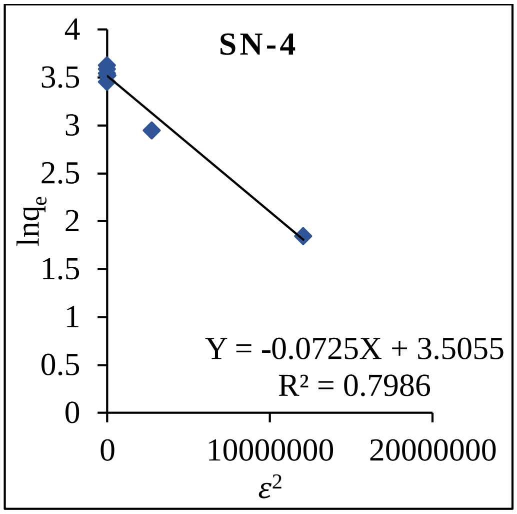

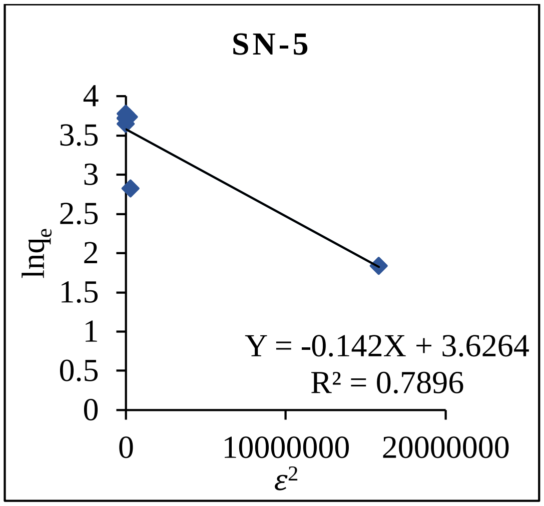

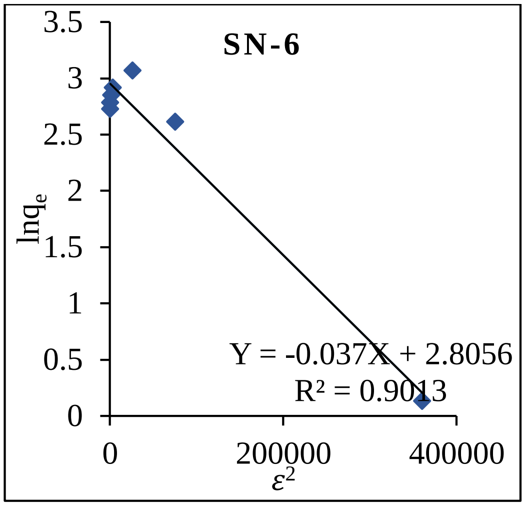

Appendix IX B: Dubinin-Radushkevich isotherms for MB dyes

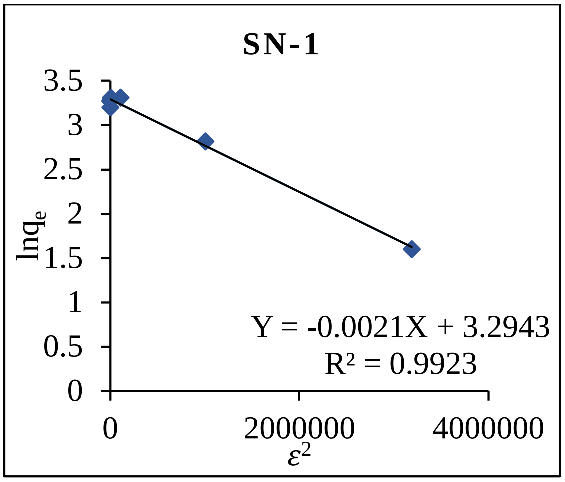

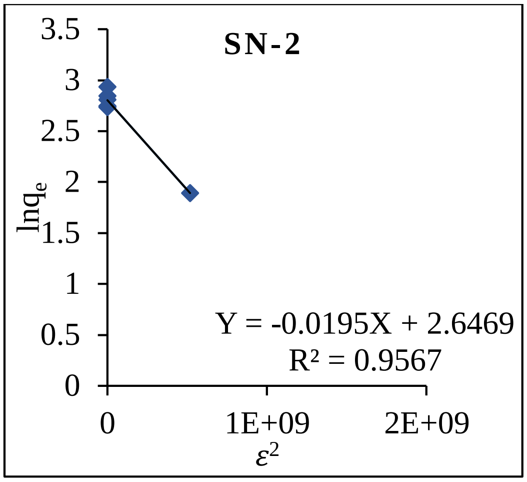

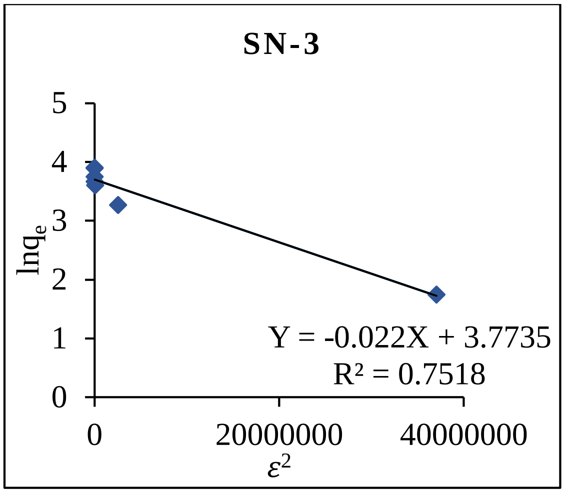

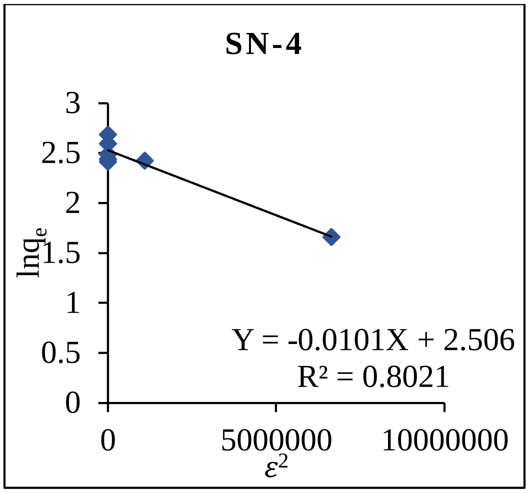

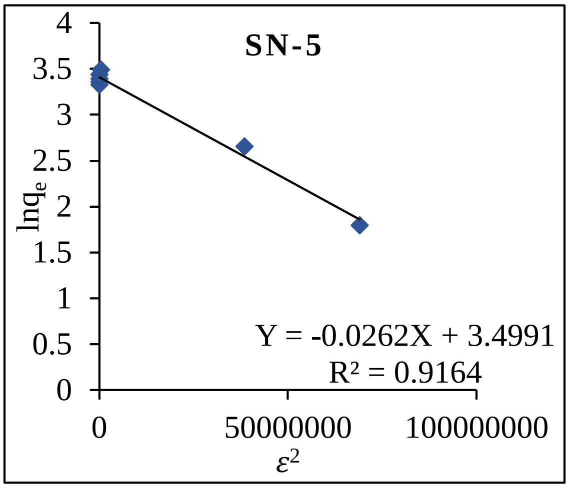

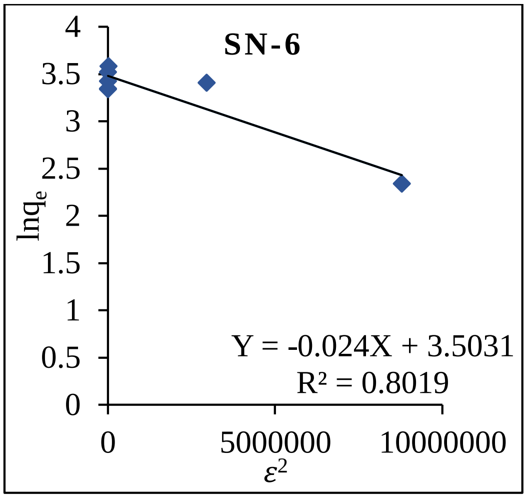

Appendix IX C: Dubinin-Radushkevich isotherms for CR dyes

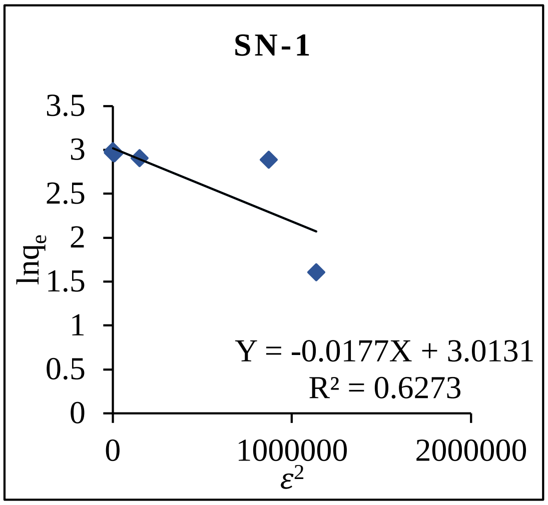

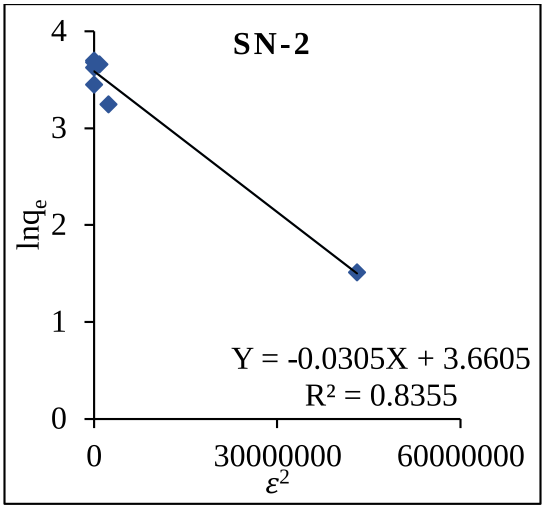

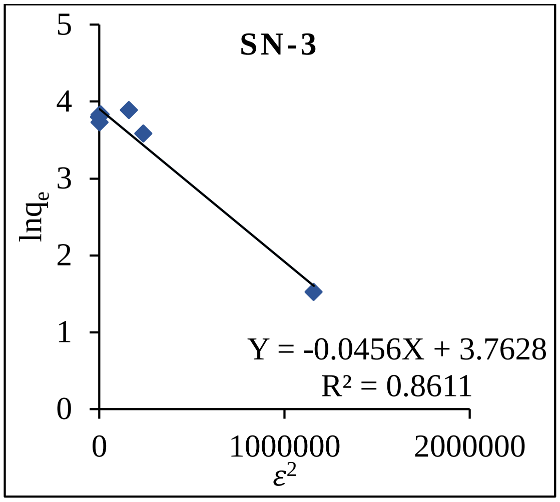

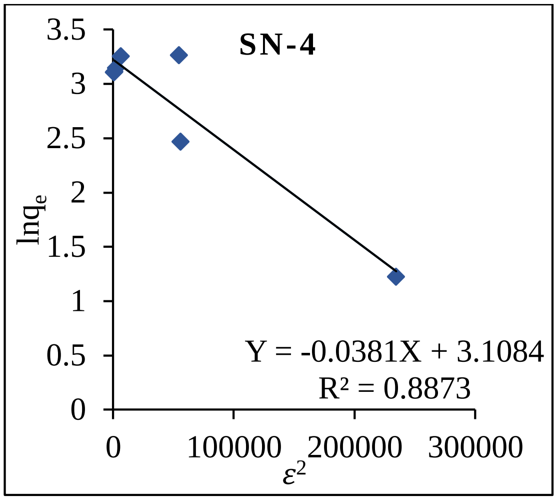

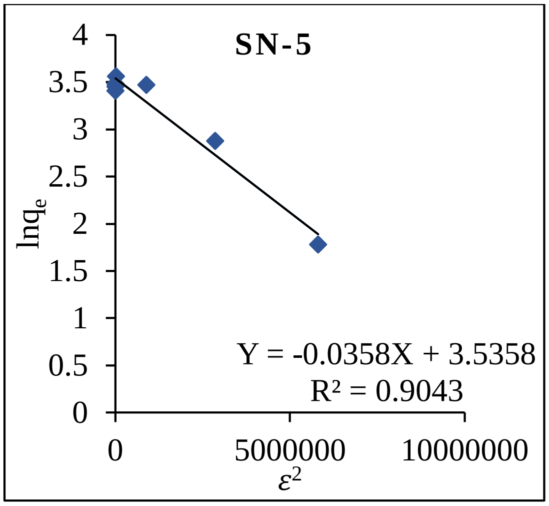

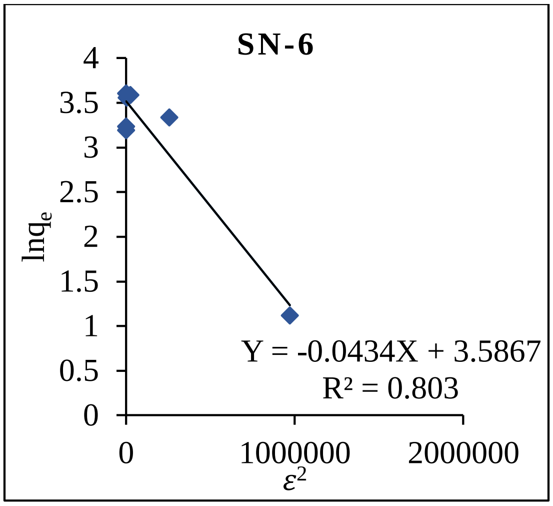

Appendix X A: Pseudo-first-order kinetics for MO dyes

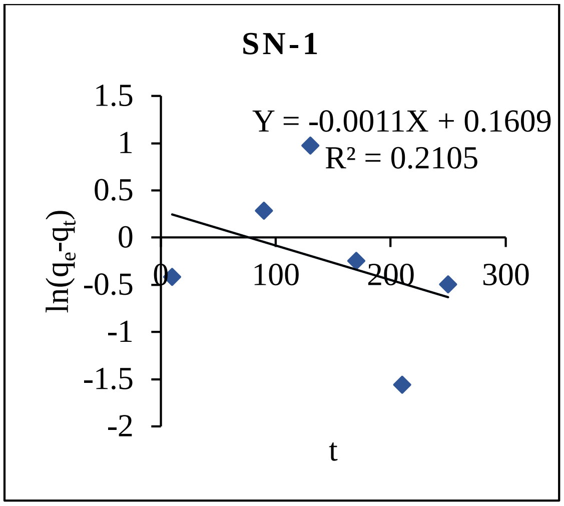
SN-1

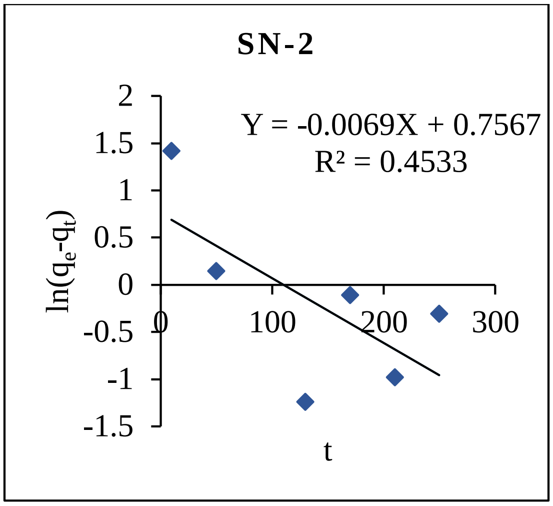
SN-2

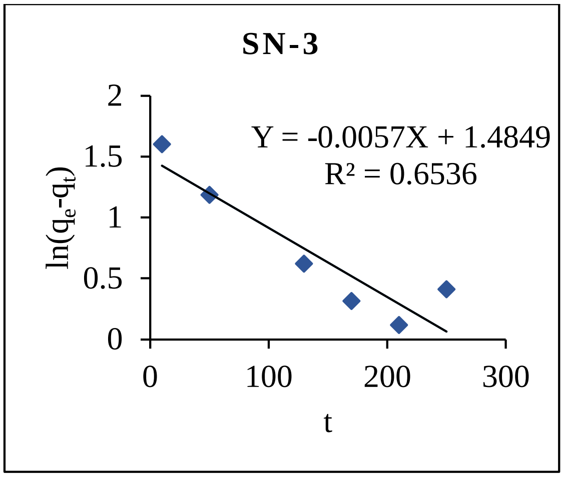
SN-3

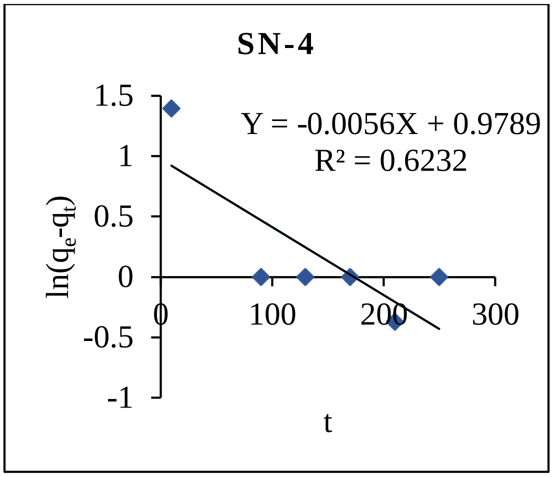
SN-4

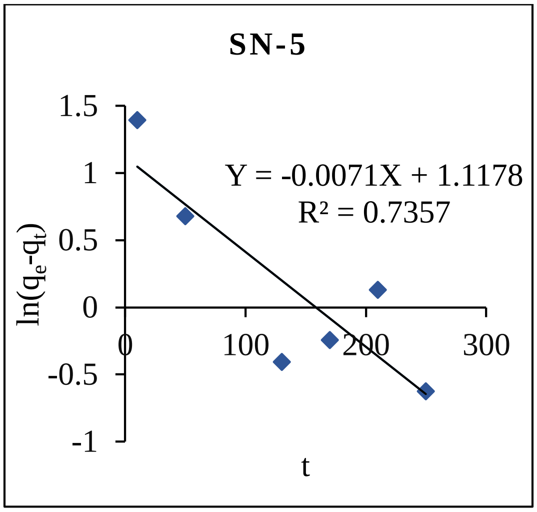
SN-5

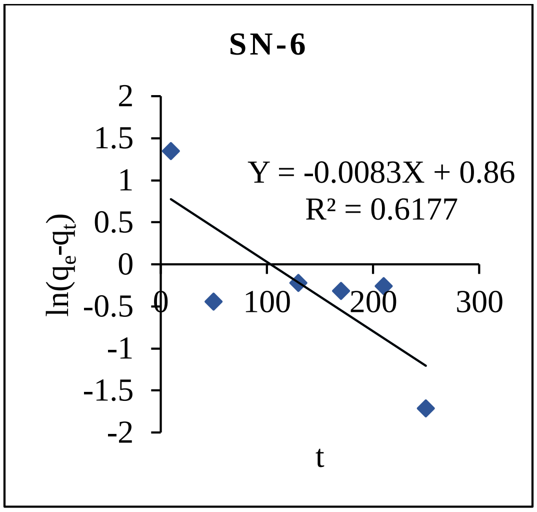
SN-6

Appendix X B: Pseudo-first-order kinetics for MB dyes

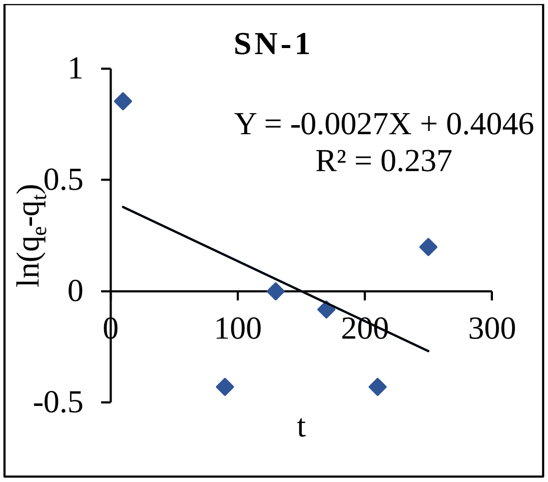
SN-1

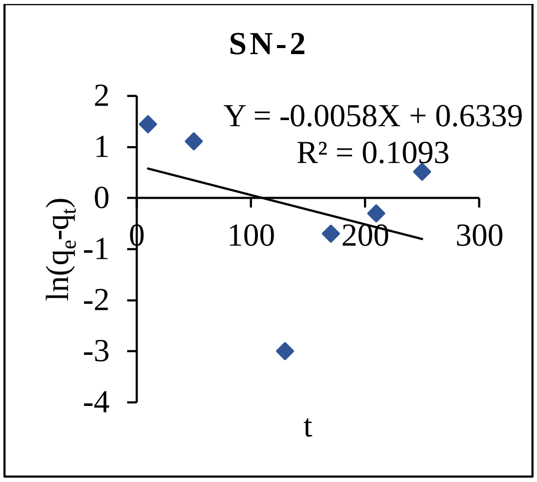
SN-2

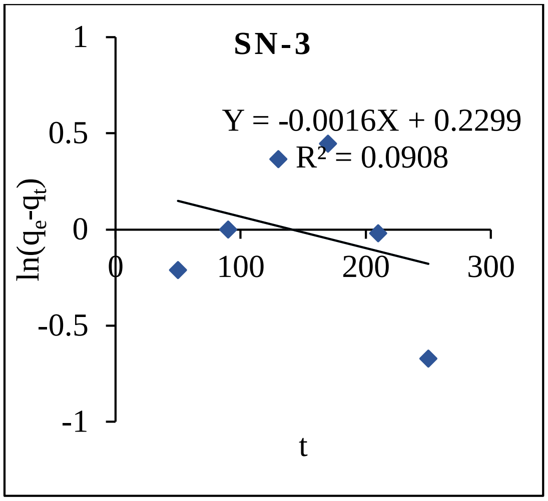
SN-3

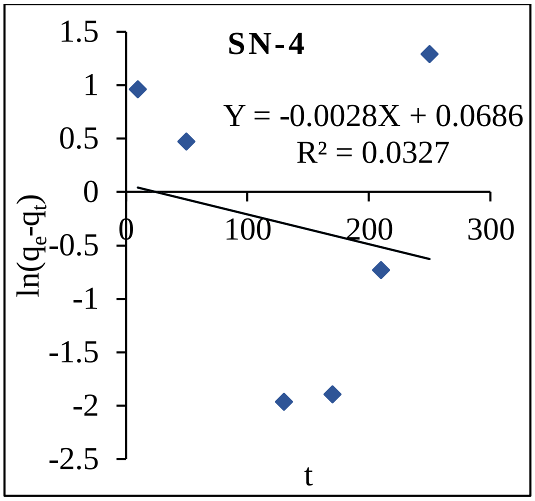
SN-4

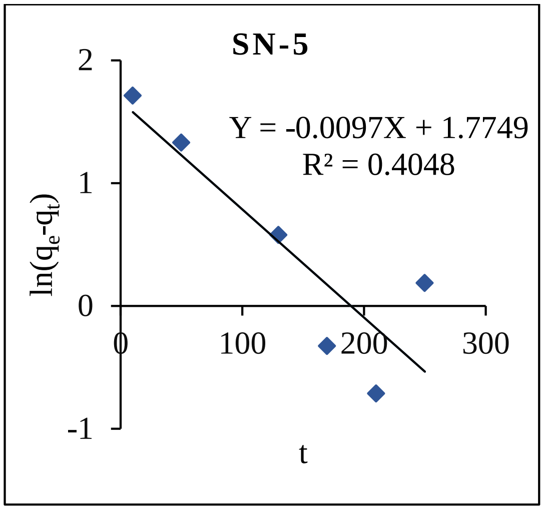
SN-5

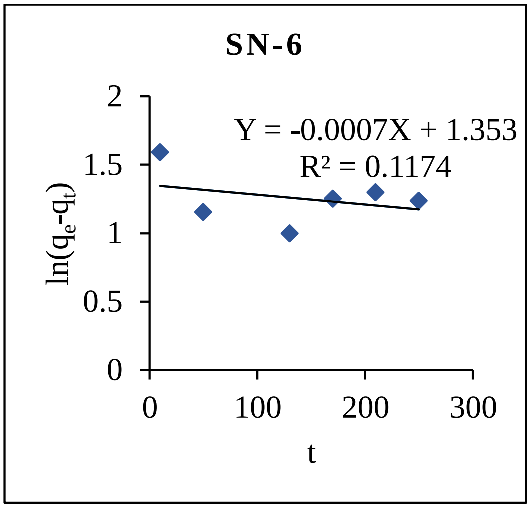
SN-6

Appendix X C: Pseudo-first-order kinetics for CR dyes

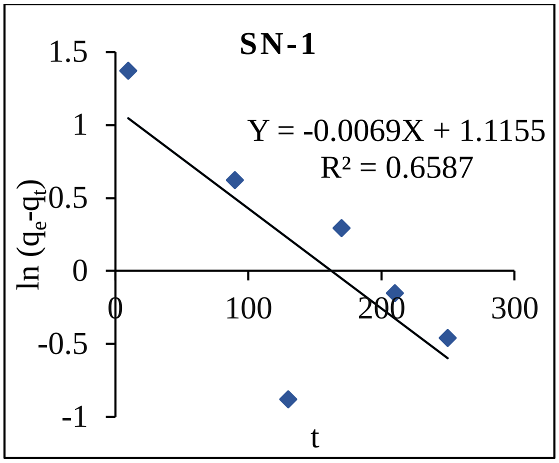

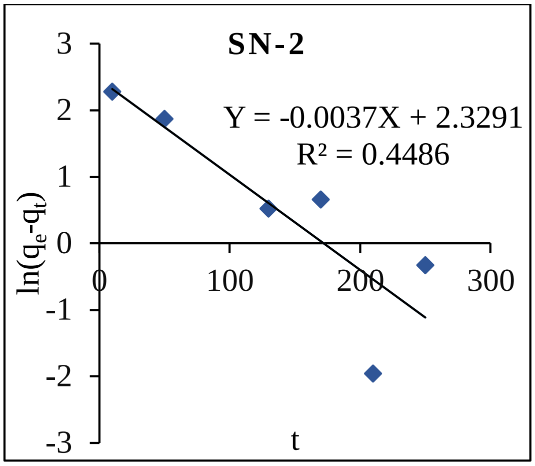

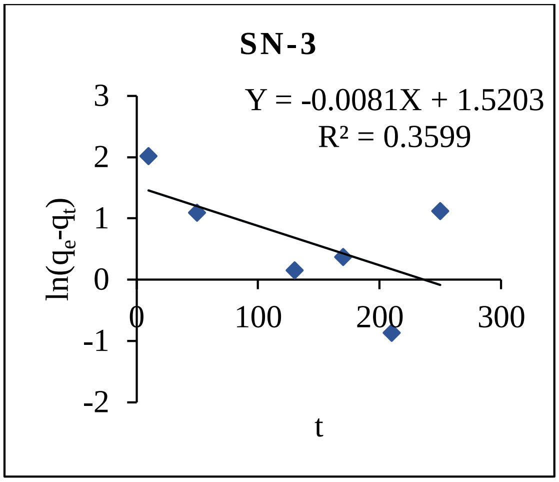

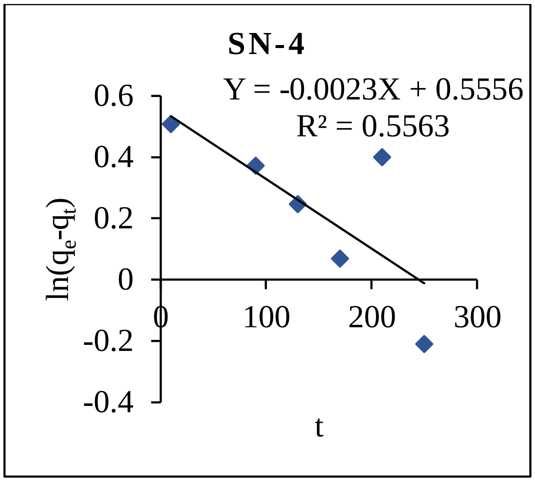

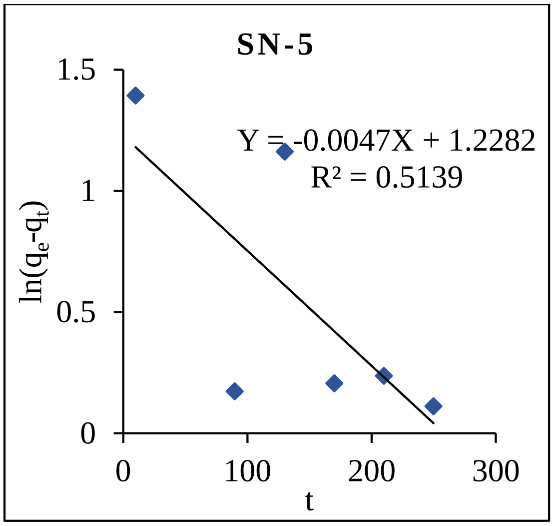

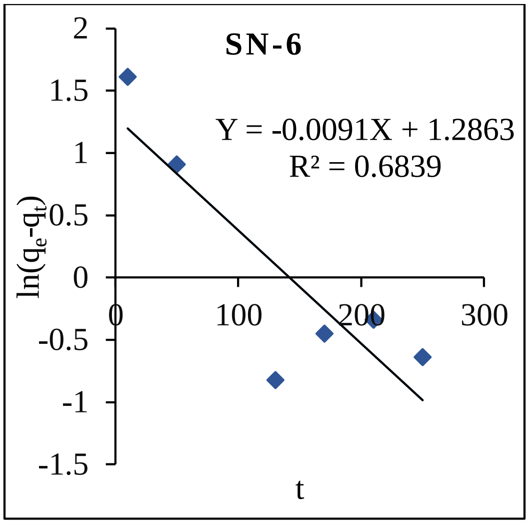

Appendix XI A: Pseudo-second-order kinetics for MO dyes

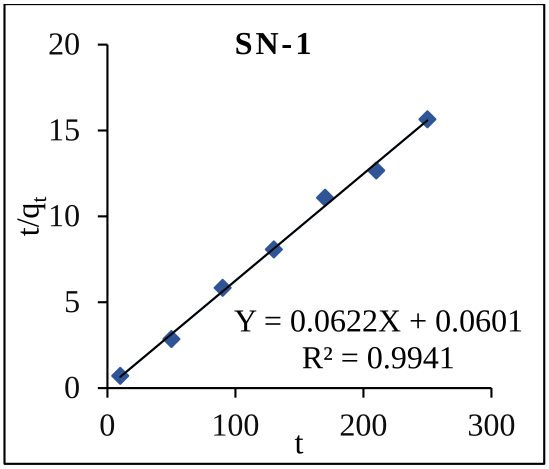

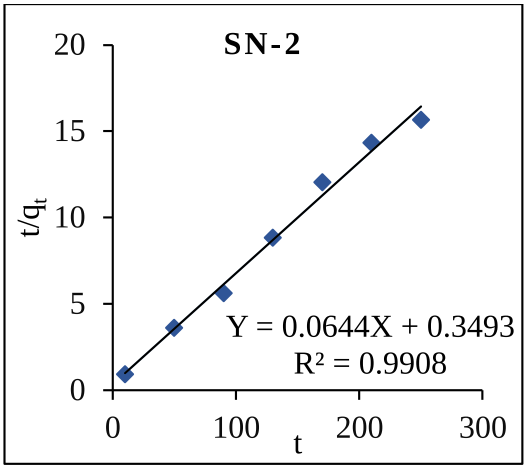

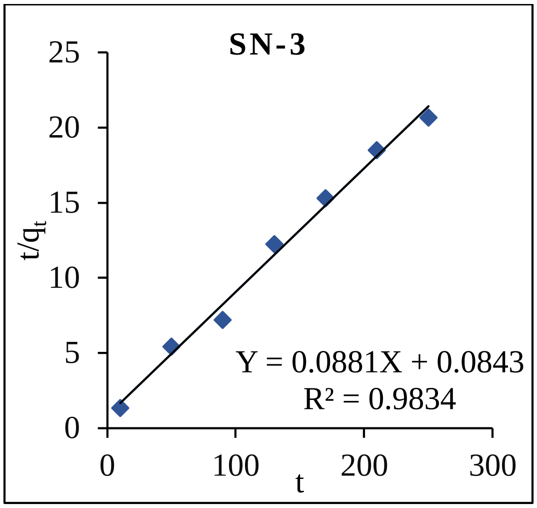

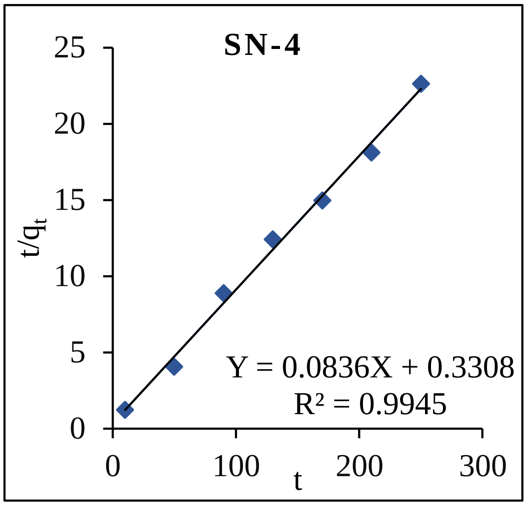

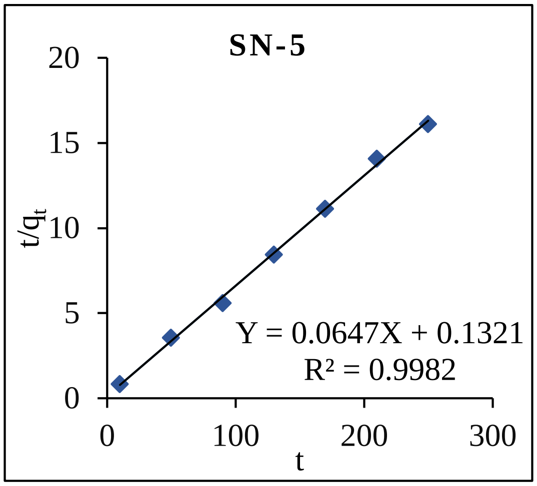

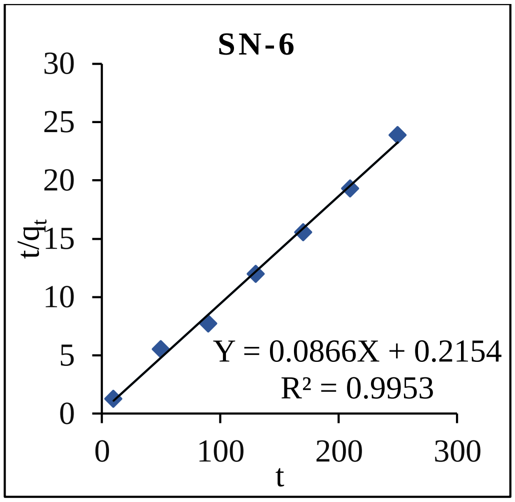

Appendix XI B: Pseudo-second-order kinetics for MB dyes

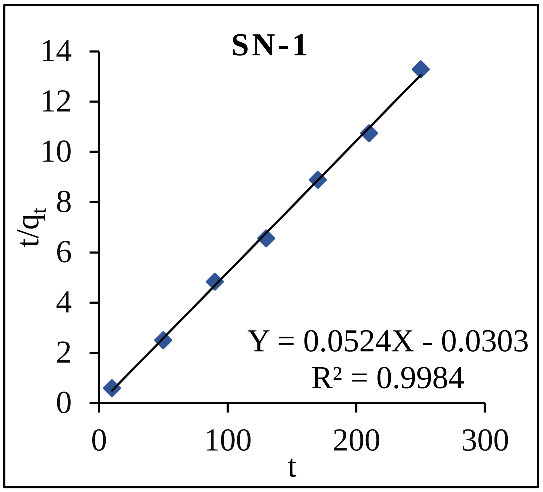

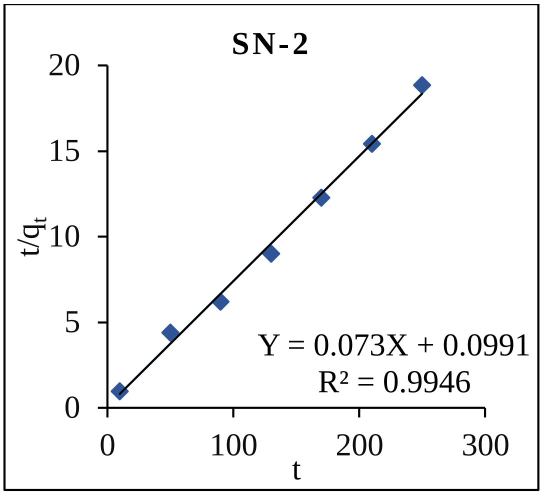

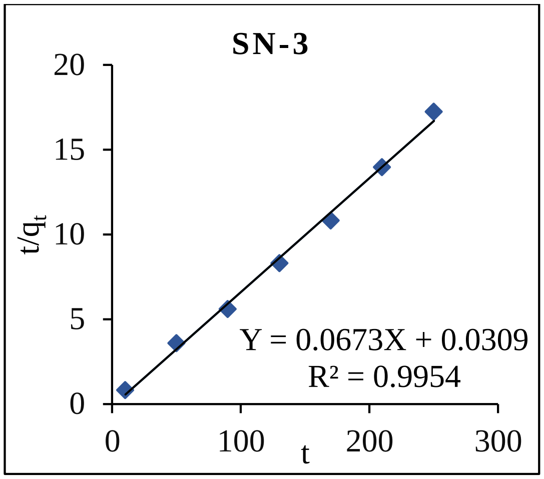

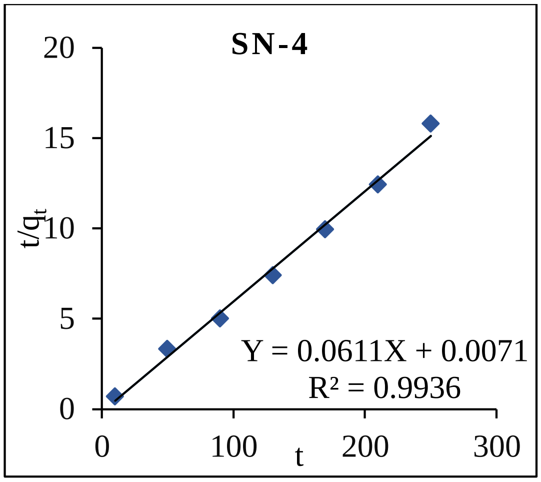

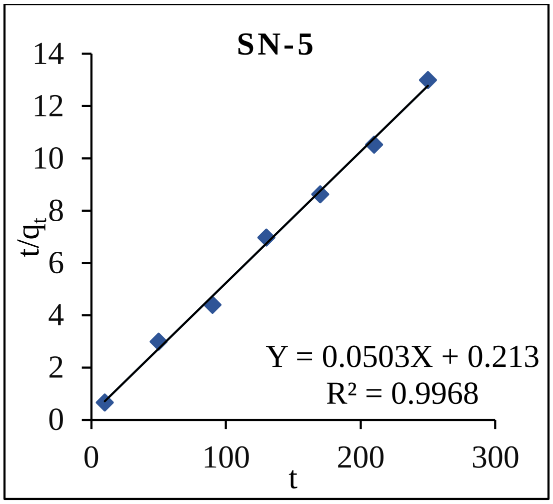

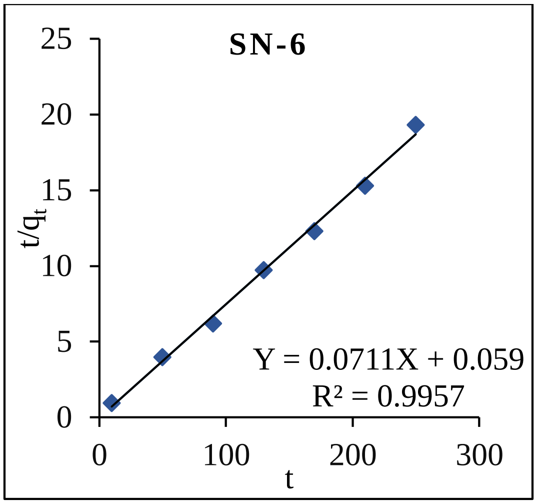

Appendix XI C: Pseudo-second-order kinetics for CR dyes

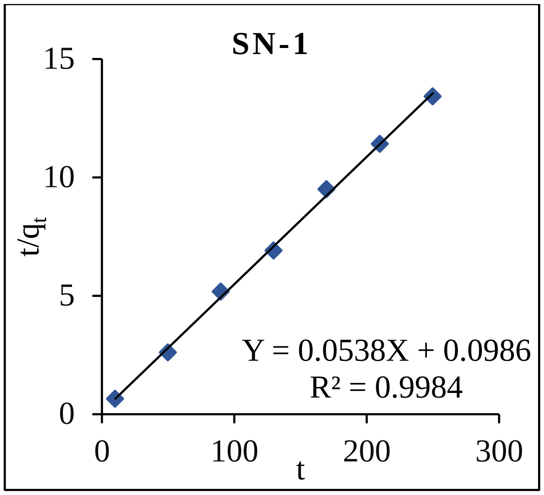

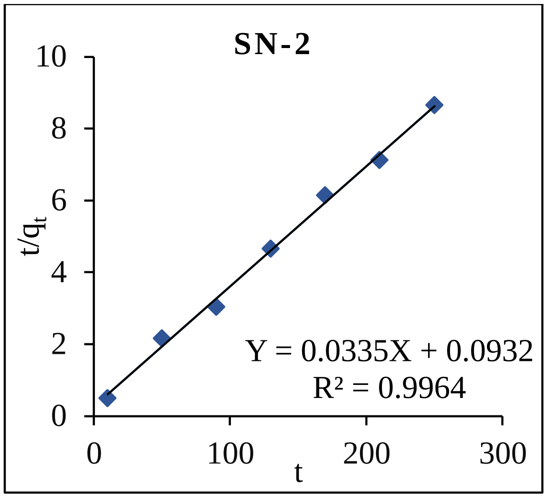

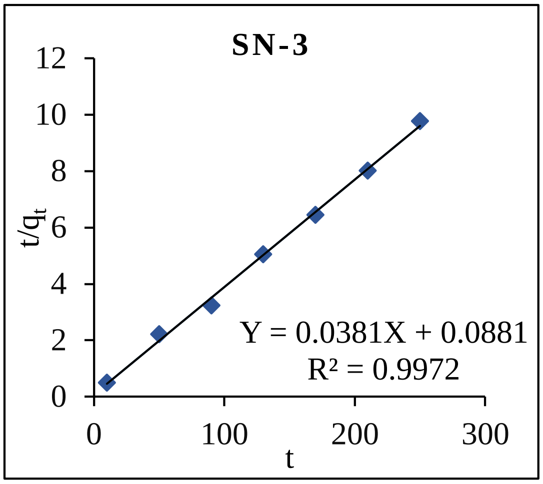

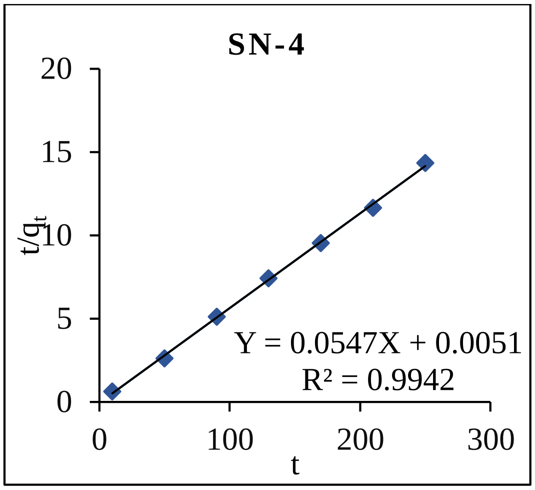

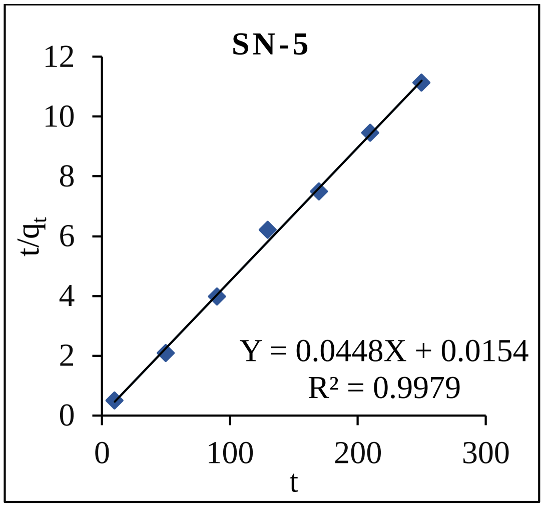

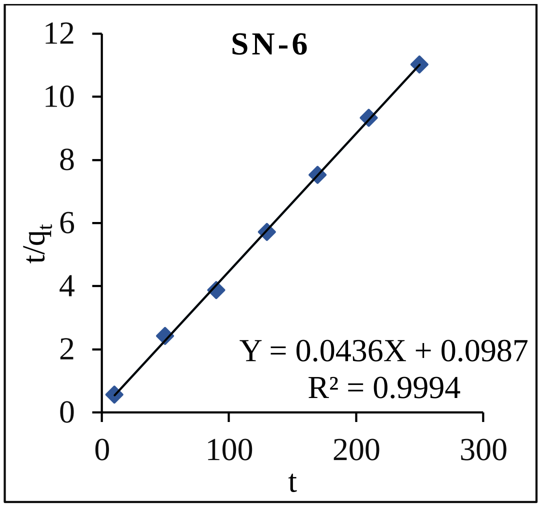

Appendix XII A: Elovich kinetics for MO dyes

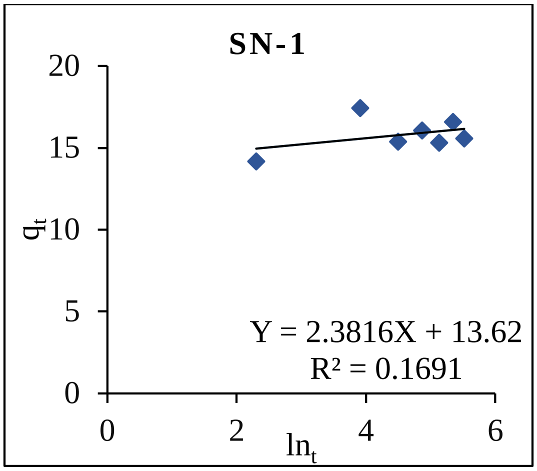

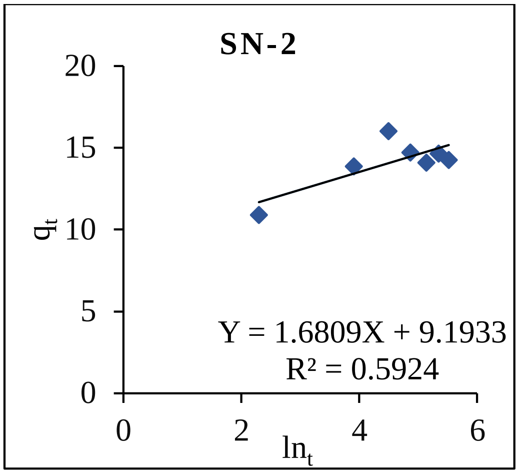

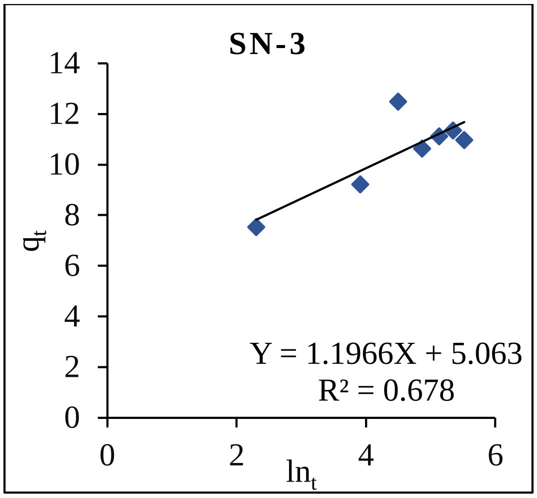

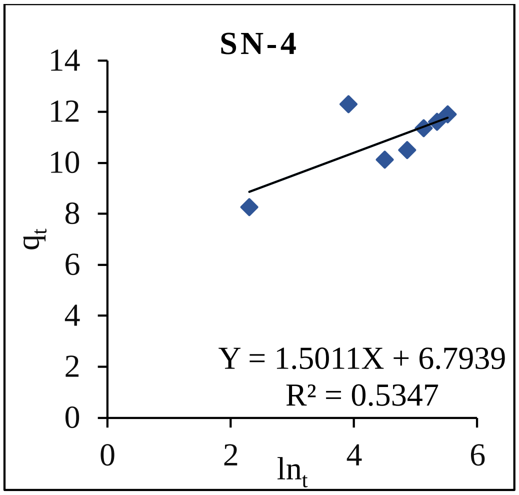

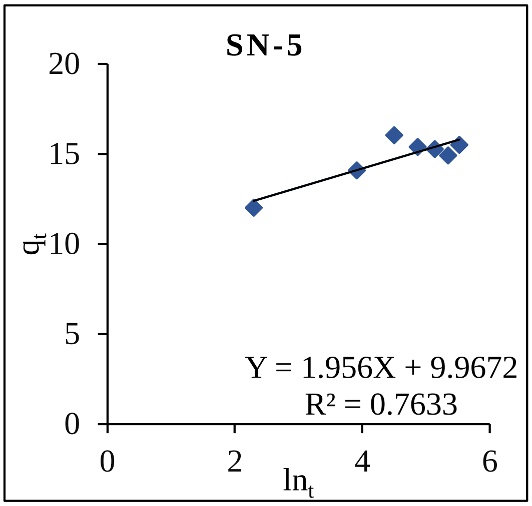

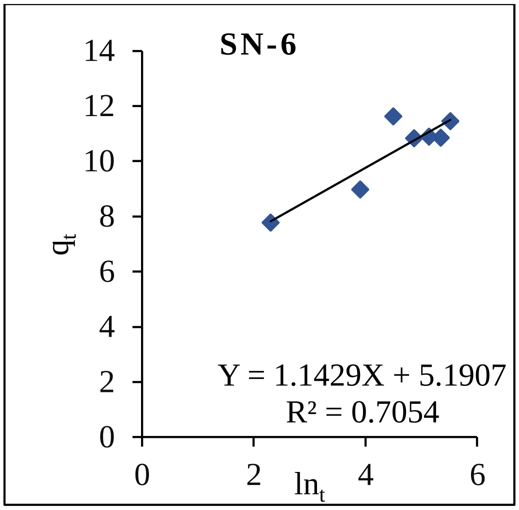

Appendix XII B: Elovich kinetics for MB dyes

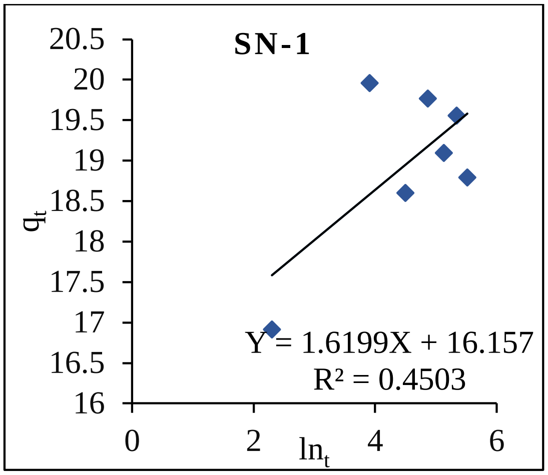

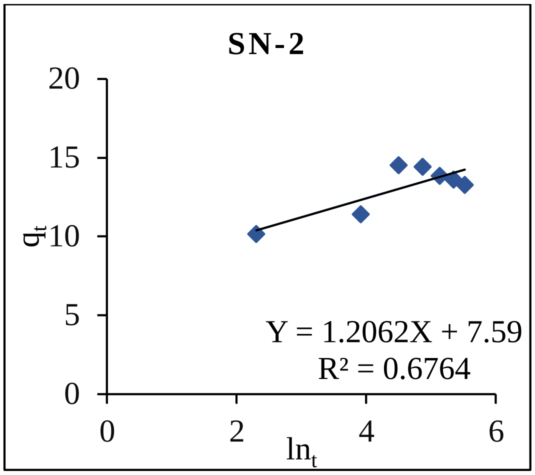

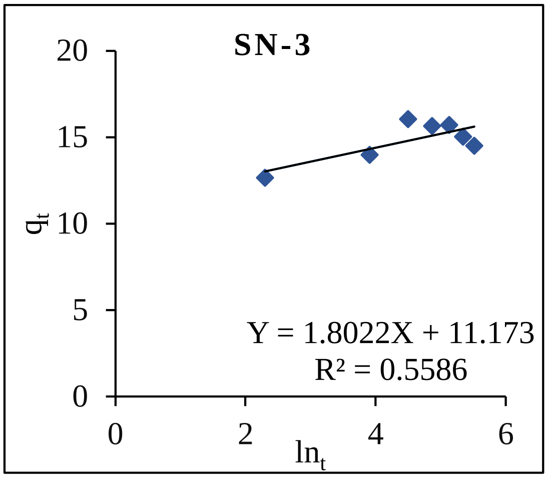

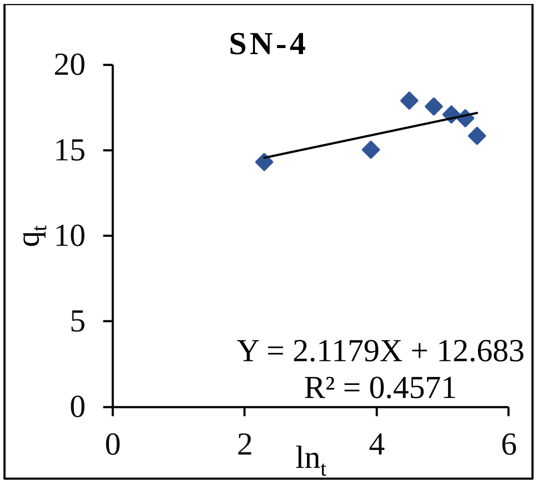

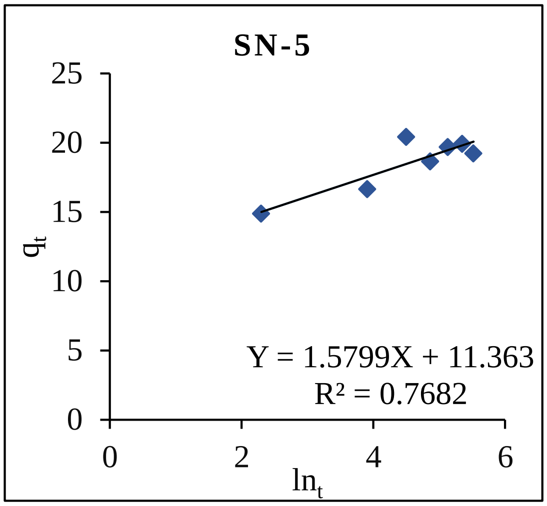

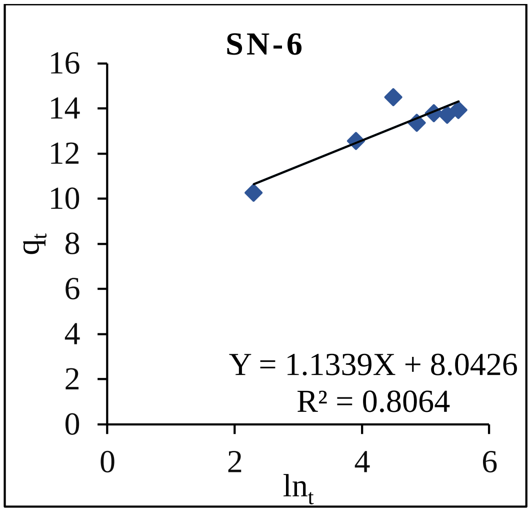

Appendix XII C: Elovich kinetics for CR dyes

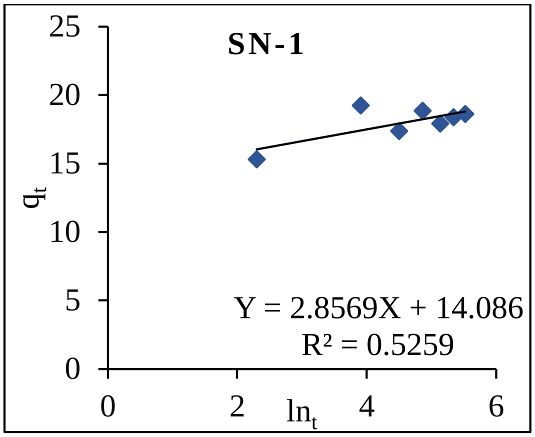

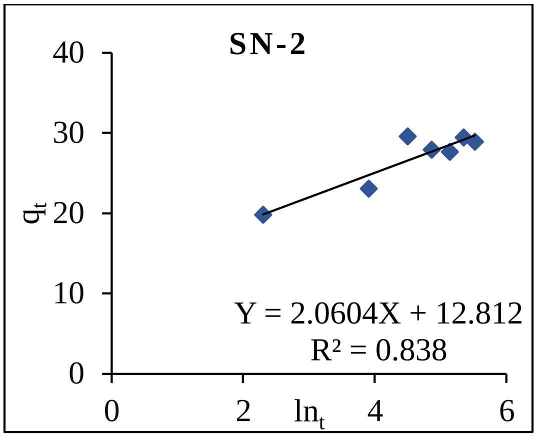

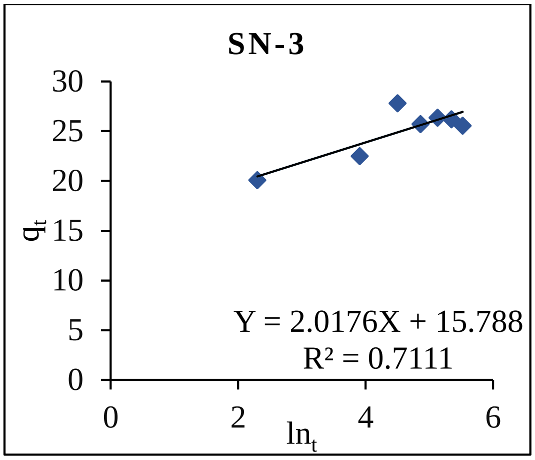

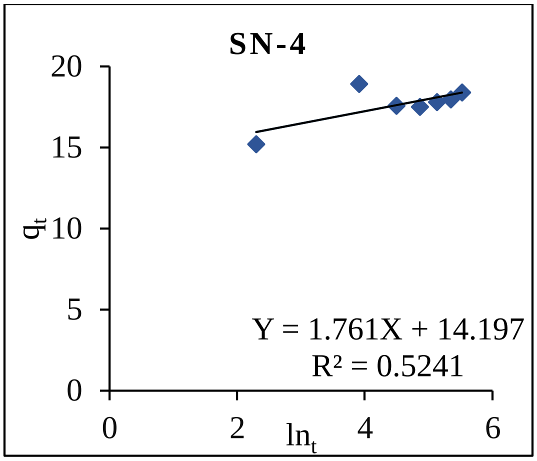

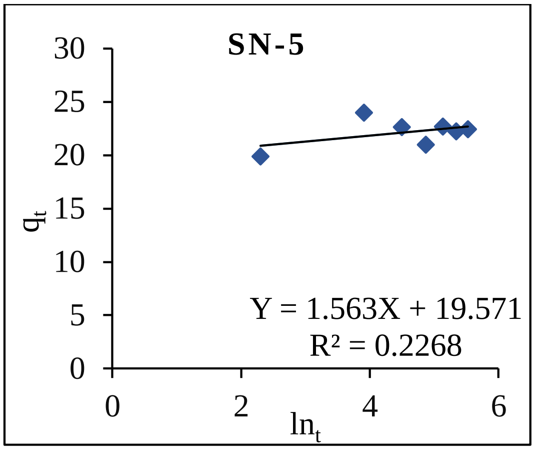

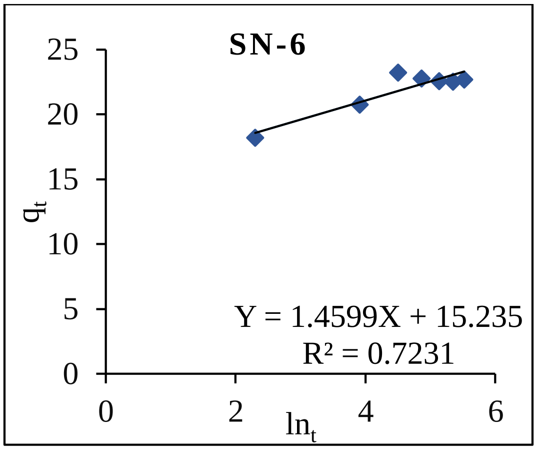

Appendix XIII A: q_d, desorption capacity for MO dyes

Eluent	SN-1	SN-2	SN-3	SN-4	SN-5	SN-6
	(Mean ± S.D)	(Mean ± S.D)	(Mean ± S.D)	(Mean ± S.D)	(Mean ± S.D)	(Mean ± S.D)
1.0 × 10^{-1} M CH_3COOH	12.36 ± 0.00^{c}	16.12 ± 0.01^{a}	11.28 ± 0.01^{de}	10.58 ± 0.00^{e}	15.11 ± 0.01^{b}	10.05 ± 0.00^{e}
1.0 × 10^{-1} M HCl	9.24 ± 0.01^{ab}	7.58 ± 0.00^{c}	8.54 ± 0.00^{bc}	7.99 ± 0.01^{c}	10.03 ± 0.00^{a}	7.46 ± 0.01^{c}
Distilled water	4.62 ± 0.00^{d}	3.19 ± 0.01^{d}	5.19 ± 0.00^{cd}	8.46 ± 0.01^{a}	8.49 ± 0.01^{a}	6.47 ± 0.00^{bc}
1.0 × 10^{-1} M NaOH	22.64 ± 0.01^{b}	23.97 ± 0.00^{ab}	20.63 ± 0.01^{c}	16.96 ± 0.00^{d}	24.97 ± 0.00^{a}	17.52 ± 0.01^{d}

mean values with same letter (s) within the same row are not significantly different
(One-way ANOVA, Fisher LSD-test, $\alpha = 0.05$)

Appendix XIII B: q_d, desorption capacity for MB dyes

Eluent	SN-1	SN-2	SN-3	SN-4	SN-5	SN-6
	(Mean ± S.D)	(Mean ± S.D)	(Mean ± S.D)	(Mean ± S.D)	(Mean ± S.D)	(Mean ± S.D)
1.0 × 10^{-1} M CH_3COOH	10.65 ± 0.00^{bc}	9.97 ± 0.01^{c}	10.94 ± 0.00^{b}	9.84 ± 0.00^{b}	14.14 ± 0.01^{a}	8.79 ± 0.00^{d}
1.0 × 10^{-1} M HCl	25.57 ± 0.00^{b}	17.97 ± 0.00^{de}	20.57 ± 0.01^{c}	17.89 ± 0.00^{d}	27.60 ± 0.00^{a}	16.69 ± 0.00^{e}
Distilled water	7.35 ± 0.01^{d}	10.54 ± 0.00^{b}	8.59 ± 0.00^{c}	8.67 ± 0.00^{c}	12.75 ± 0.01^{a}	7.57 ± 0.00^{d}
1.0 × 10^{-1} M NaOH	9.55 ± 0.00^{a}	7.62 ± 0.01^{b}	6.46 ± 0.00^{bc}	9.46 ± 0.01^{a}	9.43 ± 0.00^{a}	4.89 ± 0.00^{c}

mean values with same letter (s) within the same row are not significantly different
(One-way ANOVA, Fisher LSD-test, $\alpha = 0.05$)

Appendix XIII C: q_d, desorption capacity for CR dyes

Eluent	SN-1	SN-2	SN-3	SN-4	SN-5	SN-6
	(Mean ± S.D)	(Mean ± S.D)	(Mean ± S.D)	(Mean ± S.D)	(Mean ± S.D)	(Mean ± S.D)
1.0 × 10^{-1} M CH_3COOH	16.66 ± 0.00^{a}	16.16 ± 0.00^{a}	12.33 ± 0.00^{c}	14.98 ± 0.00^{b}	16.64 ± 0.00^{a}	12.42 ± 0.00^{c}
1.0 × 10^{-1} M HCl	9.03 ± 0.00^{bc}	10.45 ± 0.00^{b}	7.01 ± 0.00^{d}	10.84 ± 0.00^{ab}	11.47 ± 0.00^{a}	7.41 ± 0.00^{d}
Distilled water	14.58 ± 0.00^{b}	15.07 ± 0.00^{a}	11.17 ± 0.00^{cd}	12.12 ± 0.01^{c}	15.85 ± 0.00^{a}	10.98 ± 0.00^{d}
1.0 × 10^{-1} M NaOH	25.41 ± 0.00^{c}	28.69 ± 0.00^{a}	26.75 ± 0.01^{bc}	23.97 ± 0.01^{d}	29.17 ± 0.00^{a}	20.59 ± 0.00^{e}

mean values with same letter (s) within the same row are not significantly different
(One-way ANOVA, Fisher LSD-test, $\alpha = 0.05$)

Appendix XIV: MO, MB and CR dyes adsorption and desorption capacity for SN-5 adsorbent

Cycle	MO			MB			CR		
	q_e, adsorption (Mean ± S.D)	q_e, desorption (Mean ± S.D)	p-value (α=0.05)	q_e, adsorption (Mean ± S.D)	q_e, desorption (Mean ± S.D)	p-value ($\alpha = 0.05$)	q_e, adsorption (Mean ± S.D)	q_e, desorption (Mean ± S.D)	p-value ($\alpha = 0.05$)
1	26.93 ± 0.03	24.97 ± 0.00	0.0001	29.74 ± 0.04	27.60 ± 0.00	0.0000	31.27 ± 0.15	29.17 ± 0.00	0.0001
2	24.68 ± 0.01	19.89 ± 0.00		18.79 ± 0.00	16.97 ± 0.00		27.30 ± 0.02	22.69 ± 0.00	
3	22.49 ± 0.02	17.64 ± 0.00		18.01 ± 0.01	15.14 ± 0.00		25.71 ± 0.03	20.75 ± 0.00	
4	20.37 ± 0.02	16.93 ± 0.00		17.63 ± 0.02	14.69 ± 0.00		25.38 ± 0.01	19.97 ± 0.00	
5	19.46 ± 0.00	16.04 ± 0.00		16.56 ± 0.00	14.17 ± 0.00		25.25 ± 0.01	18.17 ± 0.00	
6	18.71 ± 0.00	15.89 ± 0.00		15.47 ± 0.02	13.69 ± 0.00		24.53 ± 0.00	17.59 ± 0.00	

mean values with same letter (s) within the same row are not significantly different
(One-way ANOVA, Fisher LSD-test, $\alpha = 0.05$)

Appendix XV A: Column parameters for the breakthrough curves of MO dyes

Parameter	Volumetric flow rate (mL/min)			Bed height (cm)			Influent concentration (mg/L)		
	4	5	6	3	5	7	50	70	90
t_b (min)	130	110	70	170	210	230	150	110	70
t_s (min)	350	270	210	310	430	540	570	410	290
$t_{0.5}$ (min)	180	150	110	230	290	370	300	210	170
V_{eff} (mL)	1400	1350	1260	1240	1720	2160	2280	1640	1160
Q_{exp} ± S.D (mg/g)	50.29 ± 0.02^a	47.28 ± 0.05^b	42.79 ± 0.04^c	43.88 ± 0.07^c	46.33 ± 0.07^b	48.21 ± 0.04^a	50.76 ± 0.17^a	48.76 ± 0.01^b	43.64 ± 0.04^c
M_{total} (mg)	70.00	67.50	63.00	62.00	86.00	108.00	114.00	114.80	104.40
R.E (%)	93.40	91.06	88.30	92.01	96.97	98.21	97.96	93.44	91.96

mean values with same letter (s) within the same row are not significantly different
(One-way ANOVA, Fisher LSD-test, $\alpha = 0.05$)

Appendix XV B: Column parameters for the breakthrough curves of MB dyes

Parameter	**Volumetric flow rate (mL/min)**			**Bed height (cm)**			**Influent concentration (mg/L)**		
	4	**5**	**6**	**3**	**5**	**7**	**50**	**70**	**90**
t_b (min)	140	90	70	130	170	210	230	130	90
t_s (min)	320	250	190	320	440	550	550	380	250
$t_{0.5}$ (min)	170	130	110	210	270	310	290	210	150
V_{eff} (mL)	1280	1250	1140	1280	1760	2200	2200	1520	1000
Q_{exp} ± S.D (mg/g)	43.97 ± 0.09^a	41.87 ± 0.06^b	37.38 ± 0.17^c	45.79 ± 0.04^c	46.55 ± 0.19^{bc}	48.75 ± 0.06^a	47.01 ± 0.14^a	43.33 ± 0.23^b	35.68 ± 0.08^c
M_{total} (mg)	64.00	62.50	57.00	64.00	88.00	110.00	110.00	106.40	90.00
R.E (%)	89.31	87.09	85.25	93.01	95.22	97.50	94.02	89.59	87.22

mean values with same letter (s) within the same row are not significantly different
(One-way ANOVA, Fisher LSD-test, α = 0.05)

Appendix XV C: Column parameters for the breakthrough curves of CR dyes

Parameter	**Volumetric flow rate (mL/min)**			**Bed height (cm)**			**Influent concentration (mg/L)**		
	4	**5**	**6**	**3**	**5**	**7**	**50**	**70**	**90**
t_b (min)	180	130	90	210	310	370	190	150	110
t_s (min)	390	300	240	340	470	580	590	400	300
$t_{0.5}$ (min)	210	170	130	270	370	450	310	210	190
V_{eff} (mL)	1560	1500	1440	1360	1880	2320	2360	1600	1200
Q_{exp} ± S.D (mg/g)	55.45 ± 0.09^a	51.48 ± 0.04^b	47.33 ± 0.03^c	48.15 ± 0.01^c	49.15 ± 0.09^b	51.14 ± 0.06^a	52.56 ± 0.04^a	47.94 ± 0.06^b	45.66 ± 0.01^c
M_{total} (mg)	78.00	75.00	72.00	68.00	94.00	116.00	118.0	112.0	108.0
R.E (%)	92.42	89.23	85.46	92.05	94.12	96.99	97.99	94.17	93.01

mean values with same letter (s) within the same row are not significantly different
(One-way ANOVA, Fisher LSD-test, α = 0.05)

Appendix XVI A: Thomas plots for MO (A), MB (B) and CR (C) dyes

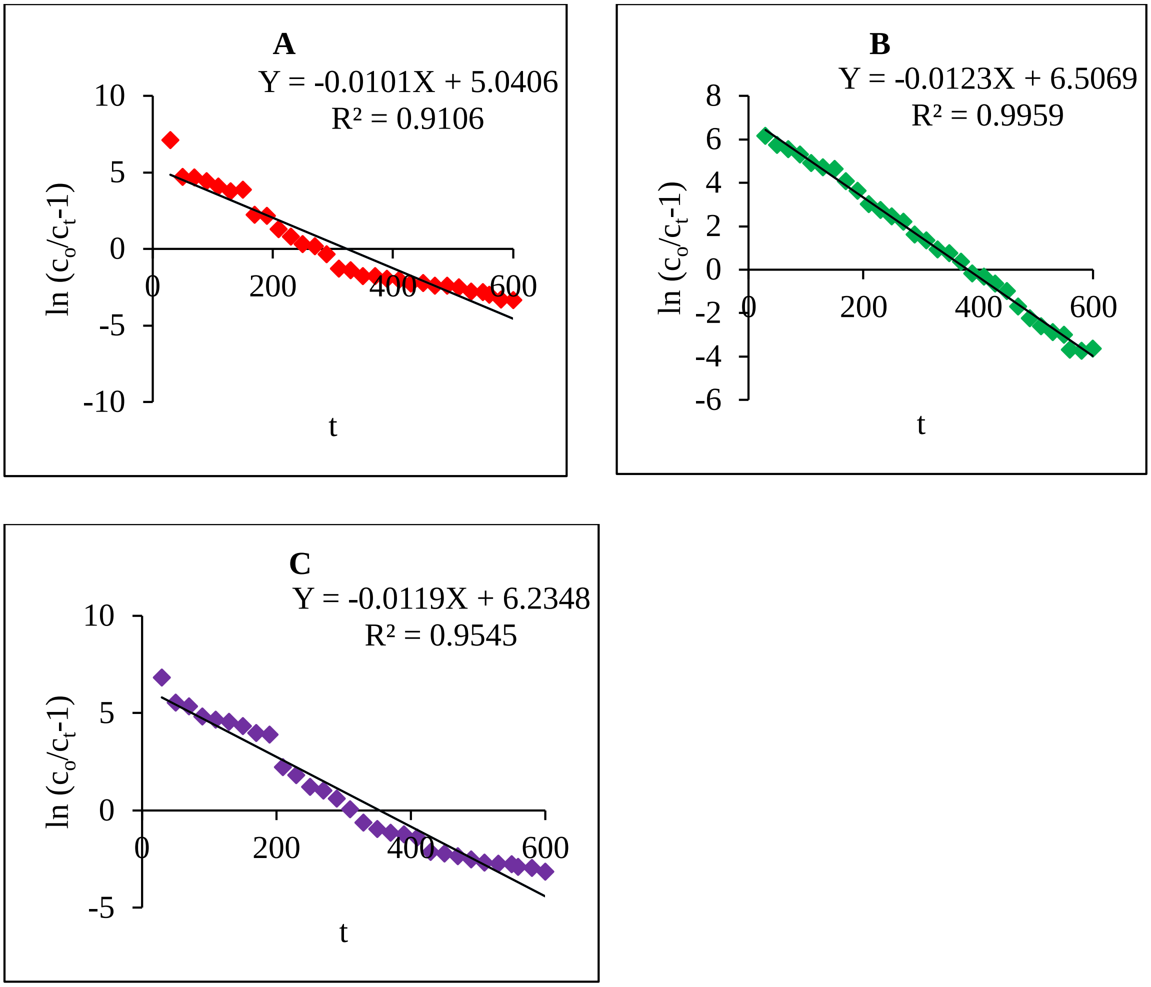

Appendix XVI B: Thomas plots for MO (A), MB (B) and CR (C) dyes using spiked water sample

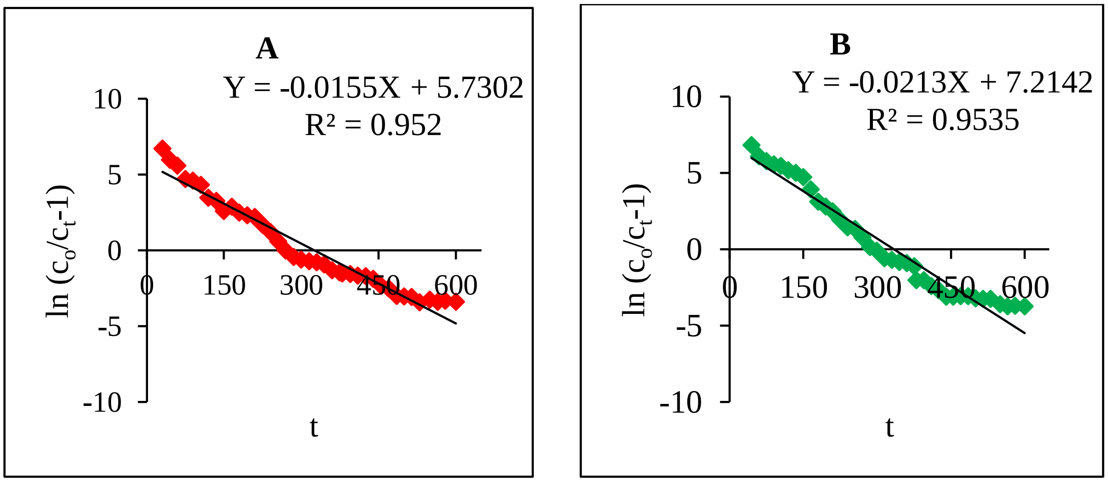

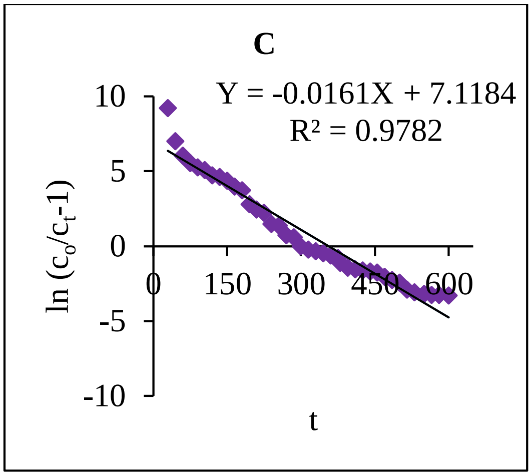

Appendix XVII: Yoon-Nelson plots for MO (A), MB (B) and CR (C) dyes

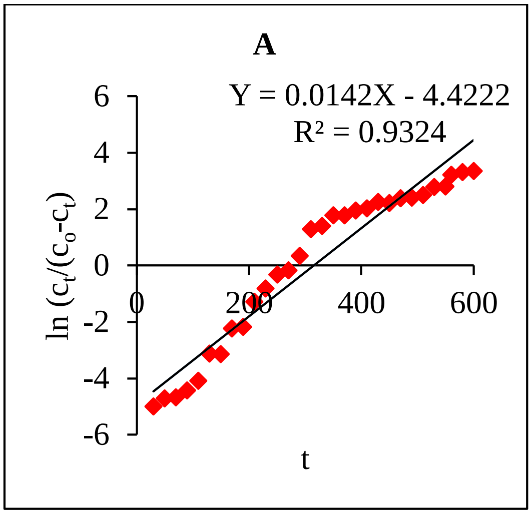

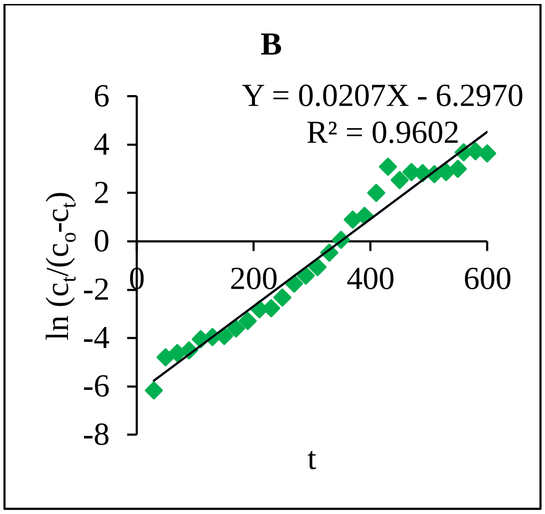

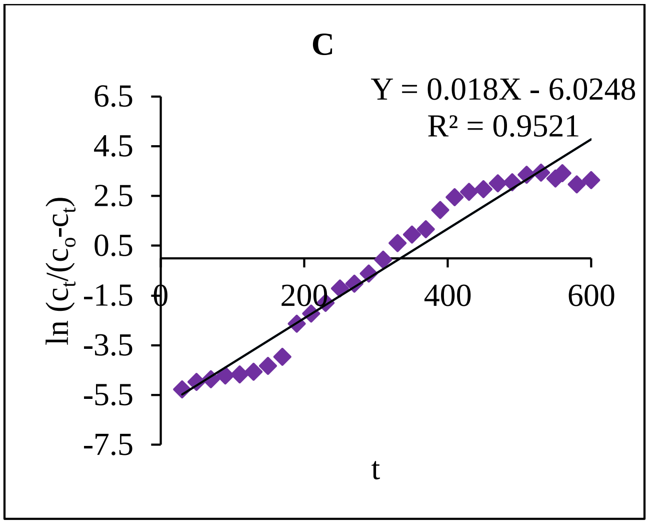

Appendix XVIII: Adams-Bohart plots for MO (A), MB (B) and CR (C) dyes

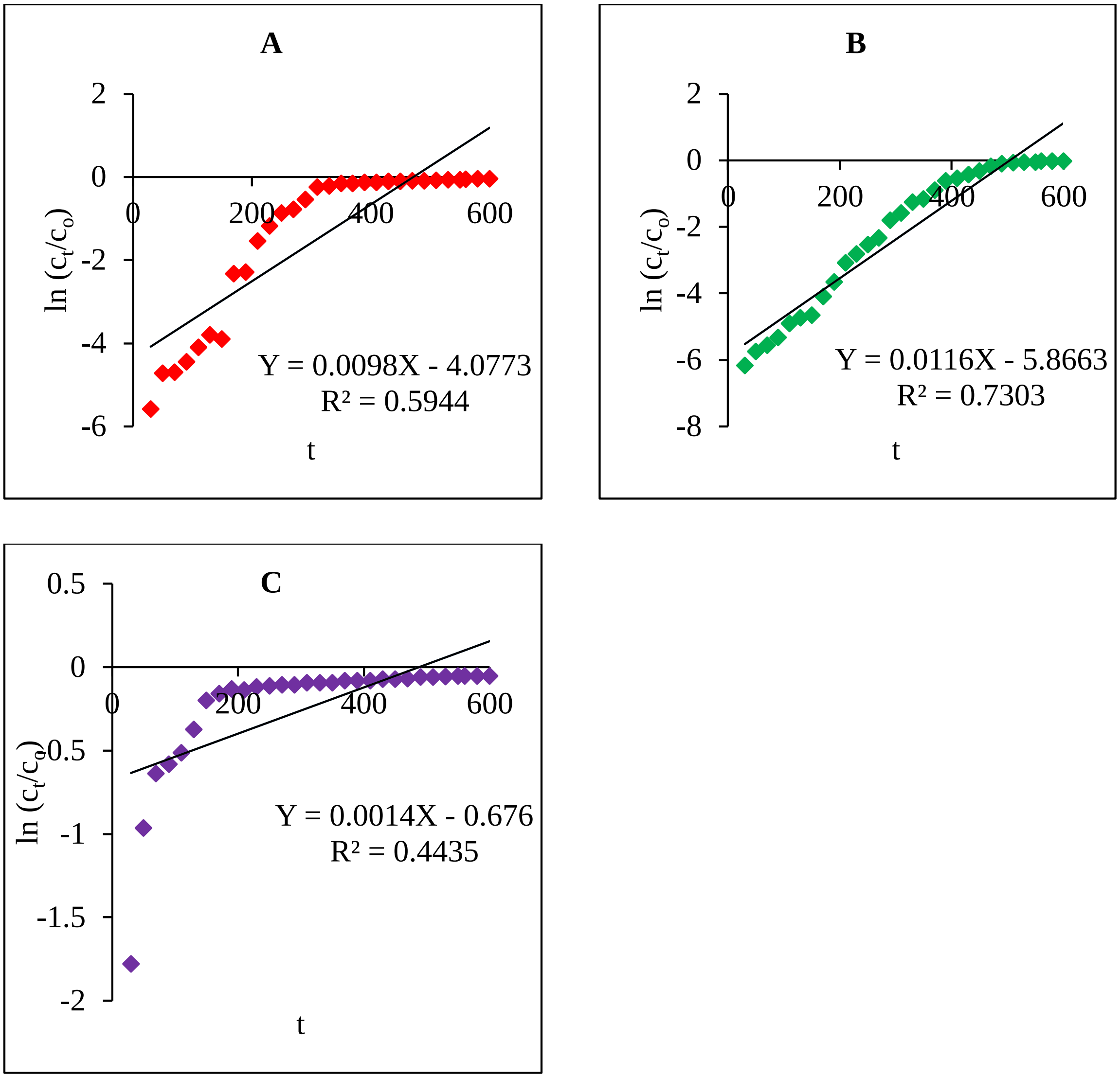

Appendix XIX: Column parameters for the breakthrough curves of MO, MB and CR dyes in spiked water samples

Parameter	MO	MB	CR
t_b (min)	140	195	180
t_s (min)	485	440	530
$t_{0.5}$ (min)	270	285	300
V_{eff} (mL)	1940	1760	2120
Q_{exp} ± S.D (mg/g)	41.85 ± 0.12^{b}	38.92 ± 0.08^{c}	46.38 ± 0.05^{a}
M_{total} (mg)	98.88	90.90	108.32
R.E (%)	93.11	94.20	94.20

mean values with same letter (s) within the same row are not significantly different
(One-way ANOVA, Fisher LSD-test, α = 0.05)

Appendix XX: Column parameters for the column adsorption cycles of MO, MB and CR dyes in spiked water samples

Parameter	MO				MB				CR			
	Adsorption cycle											
	1	2	3	4	1	2	3	4	1	2	3	4
t_b (min)	140	120	90	80	195	150	110	90	180	150	105	90
t_s (min)	485	430	380	350	440	380	330	300	530	410	360	300
$t_{0.5}$ (min)	270	240	210	200	285	220	180	170	300	240	210	180
V_{eff} (mL)	1940	1720	1520	1400	1760	1520	1320	1200	2120	1640	1440	1200
Q_{exp} ± S.D (mg/g)	41.85 ± 0.12^{a}	36.45 ± 0.08^{b}	30.36 ± 0.05^{c}	27.77 ± 0.17^{d}	38.92 ± 0.08^{a}	32.73 ± 0.08^{b}	27.91 ± 0.02^{c}	25.16 ± 0.13^{d}	46.38 ± 0.05^{a}	35.29 ± 0.24^{b}	29.49 ± 0.09^{c}	23.79 ± 0.06^{d}
M_{total} (mg)	98.88	87.67	77.47	71.36	90.90	78.50	68.17	61.97	108.32	83.79	73.58	61.31
R.E (%)	93.11	91.47	86.22	85.61	94.20	91.73	90.07	89.32	94.20	92.66	88.17	85.37

mean values with same letter (s) within the same row are not significantly different
(One-way ANOVA, Fisher LSD-test, α = 0.05)

Appendix XXI: Breakthrough curves for the column adsorption cycles of MO, MB and CR dyes in spiked water samples

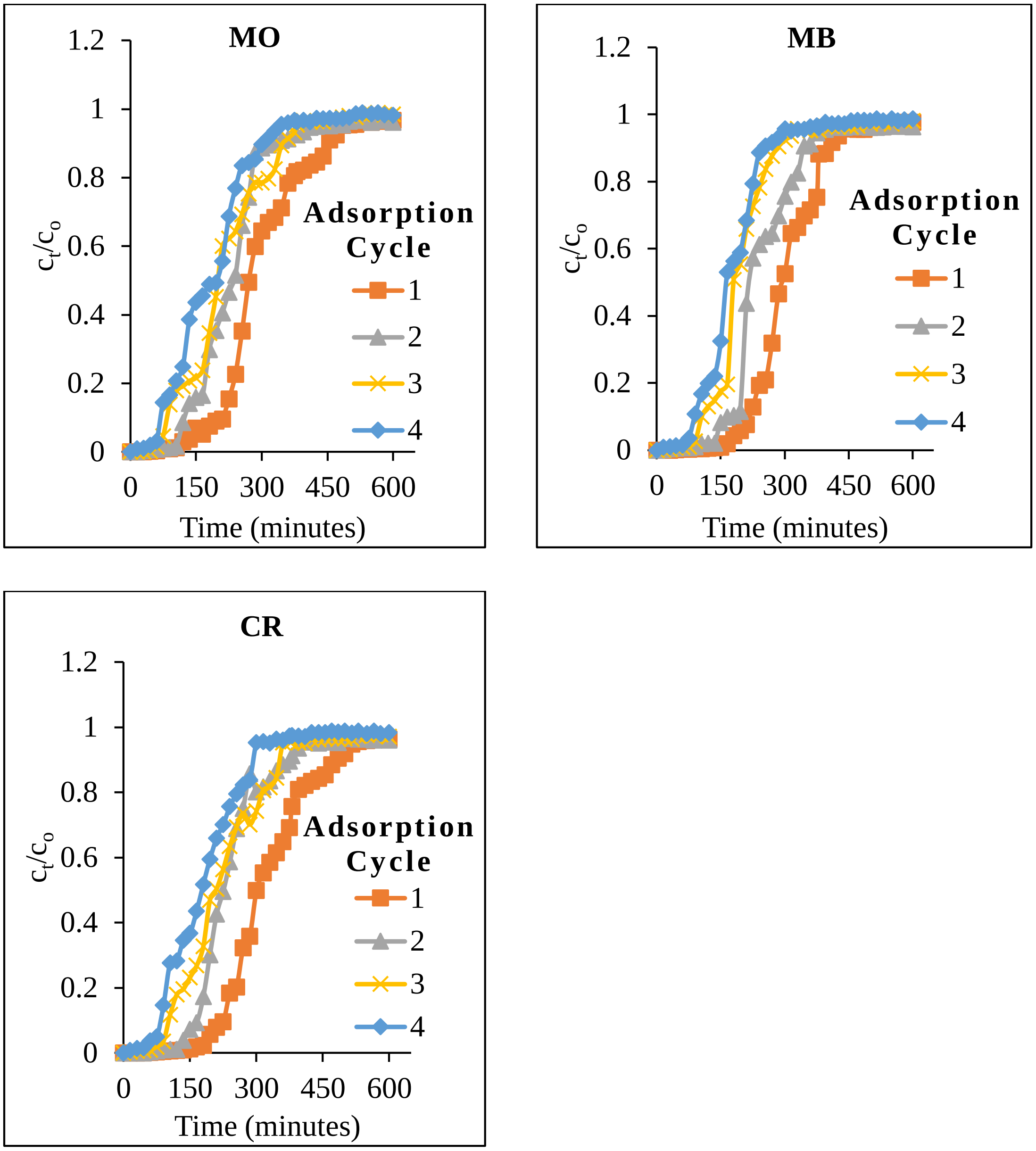

Appendix XXII: Approval of research proposal

KENYATTA UNIVERSITY
GRADUATE SCHOOL

E-mail: dean-graduate@ku.ac.ke
Website: www.ku.ac.ke

P.O. Box 43844, 00100
NAIROBI, KENYA
Tel. 810901 Ext. 57530

Internal Memo

FROM: Dean, Graduate School

DATE: 1st July, 2022

TO: Ndungu S. Ng'ang'a
C/o Department of Chemistry
Kenyatta University

REF: I84/21737/21

SUBJECT: APPROVAL OF RESEARCH PROPOSAL

We acknowledge the receipt of your revised Research Proposal entitled **"Treatment of Textile Dye Wastewater by Silicon Nitride Derived from Sand, Coffee Husk and Macadamia Nut Wastes"** as per recommendations raised by the Graduate School Board of **25th May, 2022.**

You may now proceed with your Data collection, subject to clearance with the National Universities Commission.

As you embark on your data collection, please note that you will be required to submit to Graduate School completed supervision Tracking and Progress Report Forms. The Forms are available at the University's Website under Graduate School webpage downloads.

Also, please ensure that you publish article(s) from your thesis before submitting it to Graduate School for examination as per the Commission for University Education and Kenyatta University guidelines.

By copy of this letter, the Registrar (Academic) is hereby requested to grant you substantive registration for your Ph.D. studies.

Thank you.

04 JUL 2022

JULIA GITU
FOR DEAN, GRADUATE SCHOOL

c.c. Registrar (Academic) Att. Mr. Richard Chweya
Chairman, Department of Chemistry

Supervisor

1. Prof. Ruth Wanjau
   C/o Dept. of Chemistry
   Kenyatta University
2. Dr. Esther Nthiga
   Dedan Kimathi University of Technology
   C/o Department of Chemistry
   Kenyatta University

Committed to Creativity, Excellence & Self-Reliance

Appendix XXIII: Research license

REPUBLIC OF KENYA

NATIONAL COMMISSION FOR
SCIENCE,TECHNOLOGY & INNOVATION

Ref No: **939658**

Date of Issue: **17/January/2023**

RESEARCH LICENSE

This is to Certify that Mr.. SAMUEL NG'ANG'A NDUNG'U of Kenyatta University, has been licensed to conduct research as per the provision of the Science, Technology and Innovation Act, 2013 (Rev.2014) in Nairobi on the topic: TREATMENT OF TEXTILE DYE WASTEWATER BY SILICON NITRIDE DERIVED FROM SAND, COFFEE HUSK AND MACADAMIA NUT WASTES for the period ending : 17/January/2024.

License No: **NACOSTI/P/23/23224**

939658

Applicant Identification Number

Director General
NATIONAL COMMISSION FOR
SCIENCE,TECHNOLOGY &
INNOVATION

Verification QR Code

NOTE: This is a computer generated License. To verify the authenticity of this document,
Scan the QR Code using QR scanner application.

See overleaf for conditions

Appendix XXIV: Refereed publications

Progress in Chemical and Biochemical Research 2024, 7(3), 283-292

Progress in Chemical and Biochemical Research

Journal homepage: www.pcbiochemres.com

Original Research Article

Fixed-Bed Column Adsorption Studies of Methylene Blue Dye from an Aqueous Solution Using Silicon Nitride Adsorbent Synthesized from Sand and Coffee Husk Wastes

Ndung'u Samuel Ng'ang'a[1,*], Nthiga Esther Wanja[2], Wanjau Ruth Nduta[1], Gichumbi Joel Mwangi[3]

[1]Department of Chemistry, Kenyatta University, P.O Box 43844-00100, Nairobi, Kenya
[2]Department of Chemistry, Dedan Kimathi University of Technology, P.O Box 657-10100, Nyeri, Kenya
[3]Department of Physical Sciences, Chuka University, P.O Box 109-60400, Chuka, Kenya

ARTICLEINFO

ARTICLEHISTORY
Submitted: 2024-02-28
Revised: 2024-04-15
Accepted: 2024-06-17
Available Online: 2024-07-11
ID: PCBR-2402-1343
Checked for Plagiarism: Yes
Language Editor Checked: Yes

KEYWORDS
Methylene Blue (MB) Dye
Fixed-Bed
Adsorption
Breakthrough Curves

ABSTRACT

This study presents a fixed-bed column adsorptive behavior of Silicon Nitride (Si_3N_4) adsorbent for Methylene blue dyes. The adsorbent was characterized using XRD and EDX. Effect of parameters such as influent concentrations, volumetric flow rate, and bed height for the column study are explored. The Yoon-Nelson, Thomas, and Adam-Bohart models were used to predict breakthrough curves. The results showed α-Si_3N_4 as the main adsorbent phase with Silicon and Nitrogen as the main elements. A column capacity (47.01 mg/g) was reported at optimal values of 4 mL/min, 7 cm and 50 mg/L. Column dynamic modeling analysis revealed that Thomas and Yoon-Nelson models best fitted the breakthrough curves than Adam-Bohart model. The column performance using spiked water samples Athi showed that Si_3N_4 adsorbent had a lower efficacy than in a model solution with the maximum column adsorption capacity of 38.92 ± 0.04 mg/g. The results revealed the potential of Si_3N_4 adsorbent for decontamination of MB dyes from wastewater.

Citation: N. S. Ng'ang'a, N. E. Wanja, W. R. Nduta, G. J. Mwangi. Fixed-Bed Column Adsorption Studies of Methylene Blue Dye from an Aqueous Solution Using Silicon Nitride Adsorbent Synthesized from Sand and Coffee Husk Wastes. Prog. Chem. Biochem. Res., 7(3) (2024) 283-292
https://doi.org/10.48309/PCBR.2024.446161.1343
https://www.pcbiochemres.com/article_200168.html

---

* Corresponding author: Ndung'u Samuel Ng'ang'a
✉ E-mail: samuelndungu530@gmail.com
☎ Tel number: +254710302380

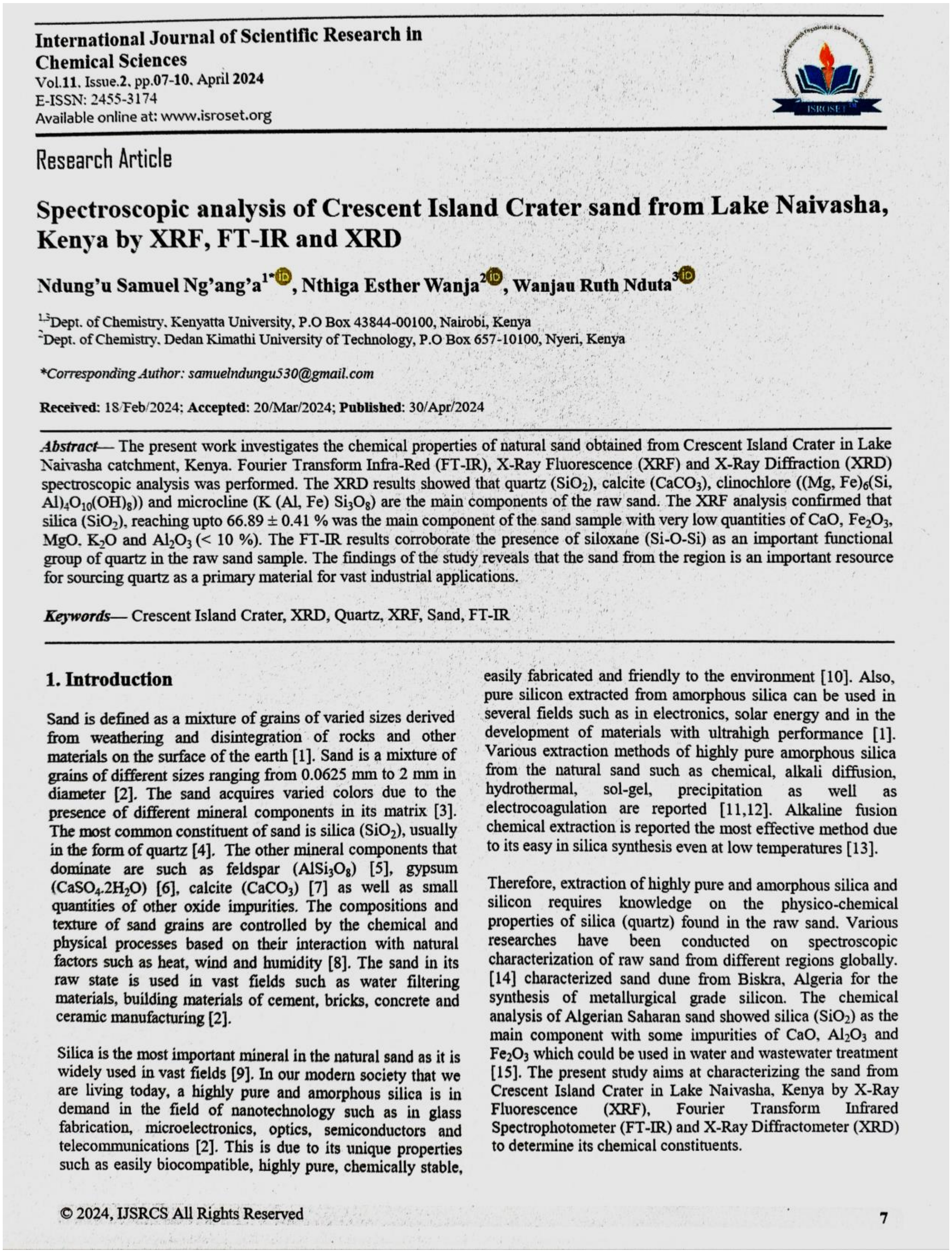

International Journal of Scientific Research in Chemical Sciences
Vol.**11**, Issue.**2**, pp.**07-10**, April **2024**
E-ISSN: 2455-3174
Available online at: www.isroset.org

Research Article

Spectroscopic analysis of Crescent Island Crater sand from Lake Naivasha, Kenya by XRF, FT-IR and XRD

Ndung'u Samuel Ng'ang'a[1*], Nthiga Esther Wanja[2], Wanjau Ruth Nduta[3]

[1,3]Dept. of Chemistry, Kenyatta University, P.O Box 43844-00100, Nairobi, Kenya
[2]Dept. of Chemistry, Dedan Kimathi University of Technology, P.O Box 657-10100, Nyeri, Kenya

Corresponding Author: samuelndungu530@gmail.com

Received: 18/Feb/2024; **Accepted:** 20/Mar/2024; **Published:** 30/Apr/2024

Abstract— The present work investigates the chemical properties of natural sand obtained from Crescent Island Crater in Lake Naivasha catchment, Kenya. Fourier Transform Infra-Red (FT-IR), X-Ray Fluorescence (XRF) and X-Ray Diffraction (XRD) spectroscopic analysis was performed. The XRD results showed that quartz (SiO_2), calcite ($CaCO_3$), clinochlore ($((Mg, Fe)_6(Si, Al)_4O_{10}(OH)_8))$ and microcline (K (Al, Fe) Si_3O_8) are the main components of the raw sand. The XRF analysis confirmed that silica (SiO_2), reaching upto 66.89 ± 0.41 % was the main component of the sand sample with very low quantities of CaO, Fe_2O_3, MgO, K_2O and Al_2O_3 (< 10 %). The FT-IR results corroborate the presence of siloxane (Si-O-Si) as an important functional group of quartz in the raw sand sample. The findings of the study reveals that the sand from the region is an important resource for sourcing quartz as a primary material for vast industrial applications.

Keywords— Crescent Island Crater, XRD, Quartz, XRF, Sand, FT-IR

1. Introduction

Sand is defined as a mixture of grains of varied sizes derived from weathering and disintegration of rocks and other materials on the surface of the earth [1]. Sand is a mixture of grains of different sizes ranging from 0.0625 mm to 2 mm in diameter [2]. The sand acquires varied colors due to the presence of different mineral components in its matrix [3]. The most common constituent of sand is silica (SiO_2), usually in the form of quartz [4]. The other mineral components that dominate are such as feldspar ($AlSi_3O_8$) [5], gypsum ($CaSO_4.2H_2O$) [6], calcite ($CaCO_3$) [7] as well as small quantities of other oxide impurities. The compositions and texture of sand grains are controlled by the chemical and physical processes based on their interaction with natural factors such as heat, wind and humidity [8]. The sand in its raw state is used in vast fields such as water filtering materials, building materials of cement, bricks, concrete and ceramic manufacturing [2].

Silica is the most important mineral in the natural sand as it is widely used in vast fields [9]. In our modern society that we are living today, a highly pure and amorphous silica is in demand in the field of nanotechnology such as in glass fabrication, microelectronics, optics, semiconductors and telecommunications [2]. This is due to its unique properties such as easily biocompatible, highly pure, chemically stable, easily fabricated and friendly to the environment [10]. Also, pure silicon extracted from amorphous silica can be used in several fields such as in electronics, solar energy and in the development of materials with ultrahigh performance [1]. Various extraction methods of highly pure amorphous silica from the natural sand such as chemical, alkali diffusion, hydrothermal, sol-gel, precipitation as well as electrocoagulation are reported [11,12]. Alkaline fusion chemical extraction is reported the most effective method due to its easy in silica synthesis even at low temperatures [13].

Therefore, extraction of highly pure and amorphous silica and silicon requires knowledge on the physico-chemical properties of silica (quartz) found in the raw sand. Various researches have been conducted on spectroscopic characterization of raw sand from different regions globally. [14] characterized sand dune from Biskra, Algeria for the synthesis of metallurgical grade silicon. The chemical analysis of Algerian Saharan sand showed silica (SiO_2) as the main component with some impurities of CaO, Al_2O_3 and Fe_2O_3 which could be used in water and wastewater treatment [15]. The present study aims at characterizing the sand from Crescent Island Crater in Lake Naivasha, Kenya by X-Ray Fluorescence (XRF), Fourier Transform Infrared Spectrophotometer (FT-IR) and X-Ray Diffractometer (XRD) to determine its chemical constituents.

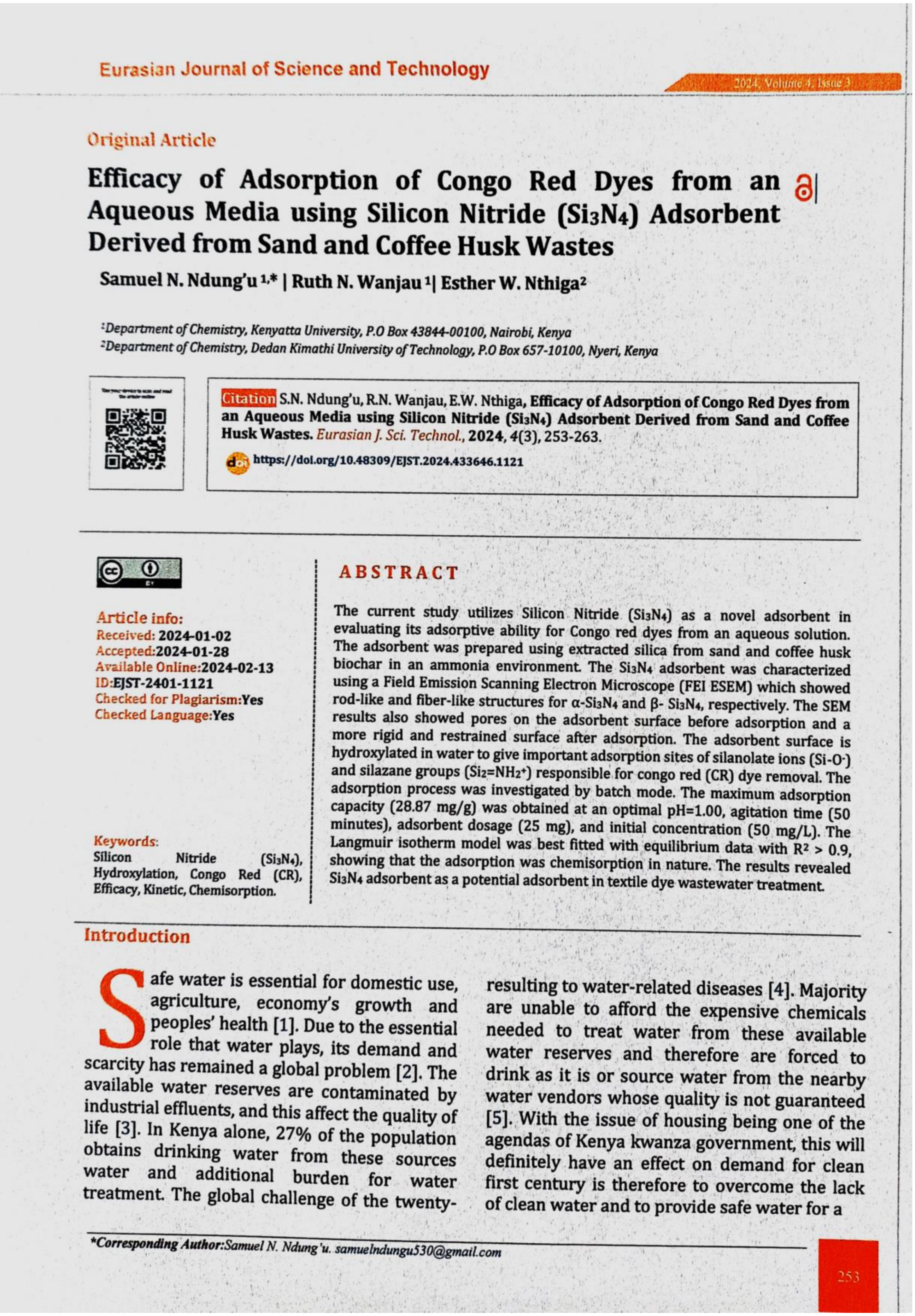

Eurasian Journal of Science and Technology

2024, Volume 4, Issue 3

Original Article

Efficacy of Adsorption of Congo Red Dyes from an Aqueous Media using Silicon Nitride (Si_3N_4) Adsorbent Derived from Sand and Coffee Husk Wastes

Samuel N. Ndung'u [1],* | Ruth N. Wanjau [1]| Esther W. Nthiga [2]

[1]Department of Chemistry, Kenyatta University, P.O Box 43844-00100, Nairobi, Kenya
[2]Department of Chemistry, Dedan Kimathi University of Technology, P.O Box 657-10100, Nyeri, Kenya

Citation S.N. Ndung'u, R.N. Wanjau, E.W. Nthiga, **Efficacy of Adsorption of Congo Red Dyes from an Aqueous Media using Silicon Nitride (Si_3N_4) Adsorbent Derived from Sand and Coffee Husk Wastes.** *Eurasian J. Sci. Technol.*, **2024**, *4*(3), 253-263.

https://doi.org/10.48309/EJST.2024.433646.1121

Article info:
Received: 2024-01-02
Accepted:2024-01-28
Available Online:2024-02-13
ID:EJST-2401-1121
Checked for Plagiarism:Yes
Checked Language:Yes

ABSTRACT

The current study utilizes Silicon Nitride (Si_3N_4) as a novel adsorbent in evaluating its adsorptive ability for Congo red dyes from an aqueous solution. The adsorbent was prepared using extracted silica from sand and coffee husk biochar in an ammonia environment. The Si_3N_4 adsorbent was characterized using a Field Emission Scanning Electron Microscope (FEI ESEM) which showed rod-like and fiber-like structures for α-Si_3N_4 and β- Si_3N_4, respectively. The SEM results also showed pores on the adsorbent surface before adsorption and a more rigid and restrained surface after adsorption. The adsorbent surface is hydroxylated in water to give important adsorption sites of silanolate ions ($Si\text{-}O^-$) and silazane groups ($Si_2{=}NH_2^+$) responsible for congo red (CR) dye removal. The adsorption process was investigated by batch mode. The maximum adsorption capacity (28.87 mg/g) was obtained at an optimal pH=1.00, agitation time (50 minutes), adsorbent dosage (25 mg), and initial concentration (50 mg/L). The Langmuir isotherm model was best fitted with equilibrium data with $R^2 > 0.9$, showing that the adsorption was chemisorption in nature. The results revealed Si_3N_4 adsorbent as a potential adsorbent in textile dye wastewater treatment.

Keywords:
Silicon Nitride (Si_3N_4), Hydroxylation, Congo Red (CR), Efficacy, Kinetic, Chemisorption.

Introduction

Safe water is essential for domestic use, agriculture, economy's growth and peoples' health [1]. Due to the essential role that water plays, its demand and scarcity has remained a global problem [2]. The available water reserves are contaminated by industrial effluents, and this affect the quality of life [3]. In Kenya alone, 27% of the population obtains drinking water from these sources water and additional burden for water treatment. The global challenge of the twenty-first century is therefore to overcome the lack of clean water and to provide safe water for a

resulting to water-related diseases [4]. Majority are unable to afford the expensive chemicals needed to treat water from these available water reserves and therefore are forced to drink as it is or source water from the nearby water vendors whose quality is not guaranteed [5]. With the issue of housing being one of the agendas of Kenya kwanza government, this will definitely have an effect on demand for clean

***Corresponding Author:**Samuel N. Ndung'u. samuelndungu530@gmail.com*

African Journal of Pure & Applied Sciences

ISSN: 2710-0758
DOI 10.33886/ajpas.v4i3.426

Journal homepage: http://journal.ku.ac.ke/index.php/AJPAS

Research Article

Open Access

Characterization of amorphous silicon nitride prepared from sand and coffee husk wastes by carbothermal reduction-nitridation

Ndung'u S.N.[1*], Nthiga E.W.[2], Wanjau R.N.[1]

[1]Department of Chemistry, Kenyatta University, P.O Box 43844-00100, Nairobi, Kenya.
[2]Department of Chemistry, Dedan Kimathi University of Technology, P.O Box 657-10100, Nyeri, Kenya.
[1*]Corresponding author: samuelndungu530@gmail.com, samuelndungu53@yahoo.com

Received 8th July , 2023/ Accepted 9th Sept2023, Published online 31st December, 2023

How to cite:
Ndung'u, S., Nthiga, E., & Wanjau, R. (2023). Characterization of amorphous silicon nitride prepared from sand and coffee husk wastes by carbothermal reduction-nitridation. *African Journal of Pure and Applied Sciences*, 4(3), i-j. https://doi.org/10.33886/ajpas.v4i3.426

ABSTRACT

The continued coffee demand in Kenya has amplified the generation of its husk wastes causing disposal problems. This has led to serious pollution to the environment. Therefore, developing a greener and cost-effective ways to handle these wastes is necessary. The current study entailed the use of extracted silica and coffee husk biochar as novel precursor materials for the synthesis of silicon nitride (Si_3N_4) composite in an ammonia environment. The silica was extracted from raw sand by alkali fusion route. The biochar was prepared by pyrolytic treatment of raw coffee husk biomass at 300 °C for 5 hours followed by acid leaching. The sand, extracted silica, raw and biochar samples and silicon nitride composites were characterized using X-Ray Fluorescence (XRF), Fourier Transform Infrared (FT-IR), X-Ray Diffractometer (XRD), Scanning Electron Microscope (SEM), Energy Dispersive X-Ray (EDX) and Thermogravimetric Analyzer (TGA). The results showed that the raw sand contain quartz, calcite, microcline and clinochlore. The results for the extracted silica showed a highly amorphous silica containing hydroxyl (-OH) and siloxane (Si-O-Si) functional groups. The alkali fusion process increased the silica content to > 92 % from 83 % with oxide impurities reduced to < 1 %. The characterization of biochar samples showed a highly amorphous, porous carbon structure with aromatic carbon bonds (C=C) and a negligible ash content. The characterization of Si_3N_4 powder showed thermally stable, porous and highly amorphous material with ⊠-Si_3N_4 and ⊠- Si_3N_4 phases. The FT-IR results showed Silicon-Nitrogen-Silicon (Si-N-Si), silanol (Si-OH), Silicon-Nitrogen (Si-N) and Silicon-Silicon (Si-Si) as important functional groups present in silicon nitride composite material. The results revealed a greener approach of Si_3N_4 synthesis for application in vast industrial fields.

Key words: Extracted silica (ES), Silicon nitride (Si_3N_4), Bamburi Beach Sand (BBS), Coffee husk biochar (CHB), α- Si_3N_4, β- Si_3N_4

INTRODUCTION

Silicon nitride material is employed in vast fields due to its outstanding thermomechanical properties, corrosion resistance, high thermal conductivity and chemical inertness amongst others (Pan, 2014). The structure has a rigid structure with strong covalent bonds (Sharma *et al.*, 2018). These features make the material suitable in many applications such as in optoelectronic devices, automotive engine parts, nanocomposites and ball bearings amongst others (Farzana *et al.*, 2018). Silicon nitride occurs in two phases, an alpha (α) form (trigonal) which is stable at lower temperatures and a beta (β) form (hexagonal) stable at higher temperatures (Parrillo *et al.*, 2021).

Various techniques such as metallurgy method (Tran *et al.*, 2021), oxide-assisted growth (Zhao *et al.*, 2021), direct nitridation of silicon (Jin *et al.*, 2019), electrochemical method (Vishnu *et al.*, 2018), chemical vapour deposition (Liu *et al.*, 2018) and carbothermal reduction-nitridation of amorphous silica (Abdulhameed *et al.*, 2018) among

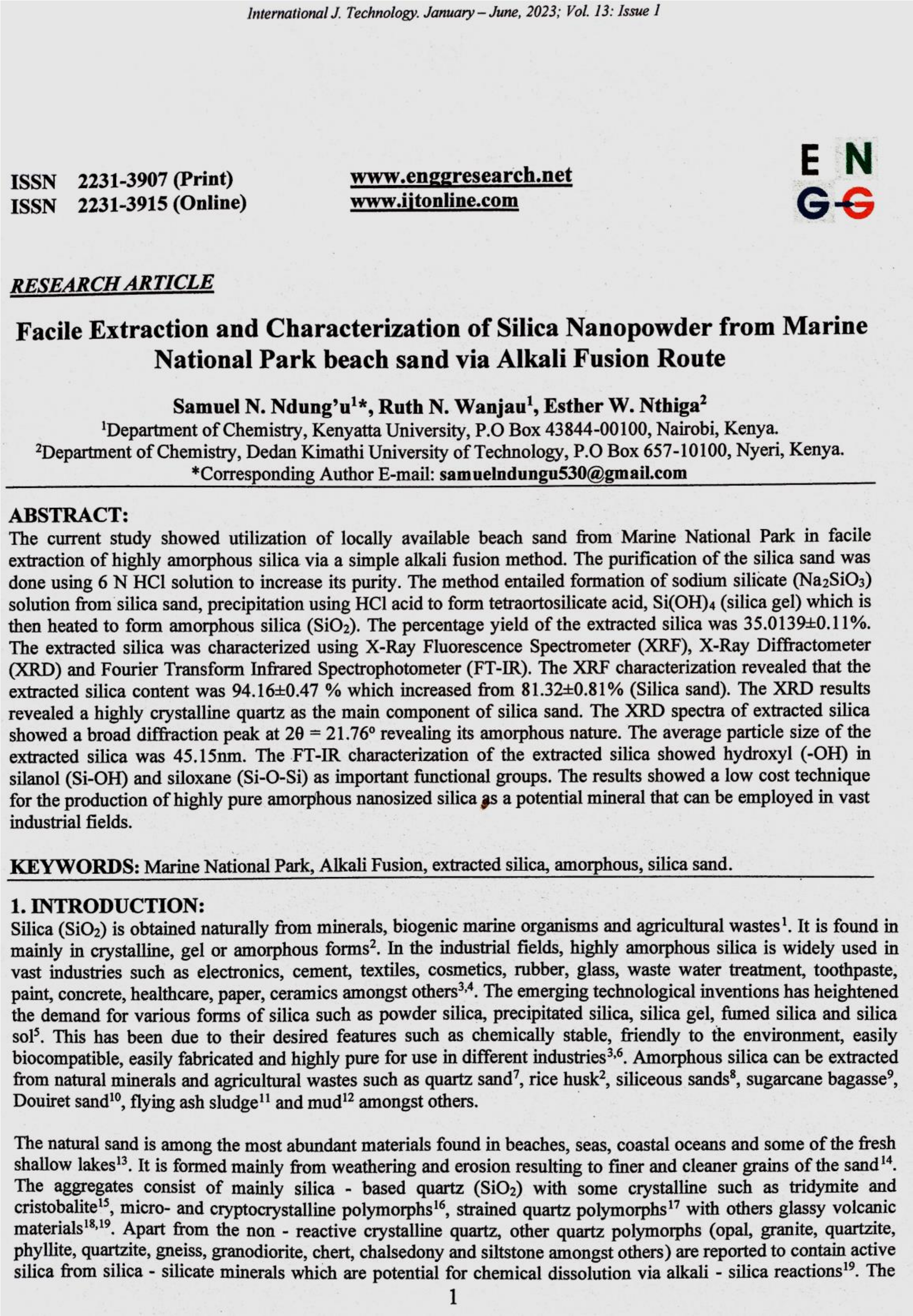

International J. Technology. January – June, 2023; Vol. 13: Issue 1

ISSN 2231-3907 (Print)
ISSN 2231-3915 (Online)

www.enggresearch.net
www.ijtonline.com

RESEARCH ARTICLE

Facile Extraction and Characterization of Silica Nanopowder from Marine National Park beach sand via Alkali Fusion Route

Samuel N. Ndung'u[1]*, Ruth N. Wanjau[1], Esther W. Nthiga[2]
[1]Department of Chemistry, Kenyatta University, P.O Box 43844-00100, Nairobi, Kenya.
[2]Department of Chemistry, Dedan Kimathi University of Technology, P.O Box 657-10100, Nyeri, Kenya.
*Corresponding Author E-mail: **samuelndungu530@gmail.com**

ABSTRACT:

The current study showed utilization of locally available beach sand from Marine National Park in facile extraction of highly amorphous silica via a simple alkali fusion method. The purification of the silica sand was done using 6 N HCl solution to increase its purity. The method entailed formation of sodium silicate (Na_2SiO_3) solution from silica sand, precipitation using HCl acid to form tetraortosilicate acid, $Si(OH)_4$ (silica gel) which is then heated to form amorphous silica (SiO_2). The percentage yield of the extracted silica was 35.0139±0.11%. The extracted silica was characterized using X-Ray Fluorescence Spectrometer (XRF), X-Ray Diffractometer (XRD) and Fourier Transform Infrared Spectrophotometer (FT-IR). The XRF characterization revealed that the extracted silica content was 94.16±0.47 % which increased from 81.32±0.81% (Silica sand). The XRD results revealed a highly crystalline quartz as the main component of silica sand. The XRD spectra of extracted silica showed a broad diffraction peak at $2\theta = 21.76^\circ$ revealing its amorphous nature. The average particle size of the extracted silica was 45.15nm. The FT-IR characterization of the extracted silica showed hydroxyl (-OH) in silanol (Si-OH) and siloxane (Si-O-Si) as important functional groups. The results showed a low cost technique for the production of highly pure amorphous nanosized silica as a potential mineral that can be employed in vast industrial fields.

KEYWORDS: Marine National Park, Alkali Fusion, extracted silica, amorphous, silica sand.

1. INTRODUCTION:

Silica (SiO_2) is obtained naturally from minerals, biogenic marine organisms and agricultural wastes[1]. It is found in mainly in crystalline, gel or amorphous forms[2]. In the industrial fields, highly amorphous silica is widely used in vast industries such as electronics, cement, textiles, cosmetics, rubber, glass, waste water treatment, toothpaste, paint, concrete, healthcare, paper, ceramics amongst others[3,4]. The emerging technological inventions has heightened the demand for various forms of silica such as powder silica, precipitated silica, silica gel, fumed silica and silica sol[5]. This has been due to their desired features such as chemically stable, friendly to the environment, easily biocompatible, easily fabricated and highly pure for use in different industries[3,6]. Amorphous silica can be extracted from natural minerals and agricultural wastes such as quartz sand[7], rice husk[2], siliceous sands[8], sugarcane bagasse[9], Douiret sand[10], flying ash sludge[11] and mud[12] amongst others.

The natural sand is among the most abundant materials found in beaches, seas, coastal oceans and some of the fresh shallow lakes[13]. It is formed mainly from weathering and erosion resulting to finer and cleaner grains of the sand[14]. The aggregates consist of mainly silica - based quartz (SiO_2) with some crystalline such as tridymite and cristobalite[15], micro- and cryptocrystalline polymorphs[16], strained quartz polymorphs[17] with others glassy volcanic materials[18,19]. Apart from the non - reactive crystalline quartz, other quartz polymorphs (opal, granite, quartzite, phyllite, quartzite, gneiss, granodiorite, chert, chalsedony and siltstone amongst others) are reported to contain active silica from silica - silicate minerals which are potential for chemical dissolution via alkali - silica reactions[19]. The

Appendix XXV: Conference Presentations

1. **Ndung'u Samuel Ng'ang'a** (presenter). Fixed-Bed Column Treatment of Textile Dye Wastewater by Silicon Nitride Derived from Sand, Coffee Husk and Macadamia Nutshells. The Inaugural National Bi-Annual Postgraduate Students Conference organized by The National Research Fund (NRF), in collaboration with Maasai Mara University. Theme: Innovation for Sustainable Development: Postgraduate Research for Societal Transformation. 28th – 30th May, 2025. Venue: *Maasai Mara University*, Narok, Kenya.

2. Dr. Nthiga E.W., **Ndung'u S.N.** (presenter) and Prof. Wanjau R.N. Characterization of amorphous silicon nitride prepared from sand and coffee husk wastes by carbothermal reduction-nitridation. 8th DeKUT International Conference on Science, Technology and Entrepreneurship. Theme: Leveraging Science, Technology, Innovation and Entrepreneurship for Sustainability and Development. 6th – 8th November, 2024. *Dedan Kimathi University of Technology*, Nyeri, Kenya.

3. **Samuel N. Ndung'u** (presenter), Ruth N. Wanjau and Esther W. Nthiga. A flash and poster presentation on the "Efficacy of adsorption of congo red dyes from an aqueous media using silicon nitride (Si_3N_4) adsorbent derived from sand and coffee husk wastes. Pan Africa Chemistry Network Congress 2024 organized by Royal Society of Chemistry (RSC). Theme: Sustainability. 29th – 31st October, 2024. *The University of Nairobi*, Kenya.

4. Dr. Esther W. Nthiga, **Samuel N. Ndung'u** (Presenter) and Prof. Ruth N. Wanjau. Facile extraction and characterization of silica nanopowder from Marine National Park beach sand from Malindi, Kilifi County, Kenya via Alkali Fusion route. 7th DeKUT International Conference on Science, Technology, Innovation and Entrepreneurship. Theme: Leveraging Science, Technology, Innovation and Entrepreneurship for Sustainable development. 8th – 10th November, 2023. *Dedan Kimathi University of Technology*, Nyeri, Kenya.